Chapter 4: AEROSOL PROPERTIES

James W. Fleming, Ph.D. and
Ronald S. Sheinson, Ph.D.,
U.S. Naval Research Laboratory

TABLE OF CONTENTS

4.1 INTRODUCTION

From the beginning of the Next Generation Fire Suppression Technology Program (NGP), it was expected there would be condensed phase compounds that might offer sufficiently efficient fire protection that could be considered as replacements for halon 1301. These compounds would be delivered to the fire as aerosols. An aerosol is a suspension of small diameter solid particles and/or liquid droplets in a gas. Fog and dust clouds are examples of liquid and solid aerosols, respectively. The term particle is often used to refer to the individual solid components or the individual liquid drops that make up the aerosol.

The realm of fire suppressant aerosols includes two-phase fluid combinations of air with water, halogenated organic chemicals, or solids such as alkali metal compounds or transition metal salts. Because of the influence of gravity, the size of the individual liquid droplets or solid particles must be sufficiently small in order to be carried or suspended by a finite flow of air. Unlike gaseous fire suppression agents, aerosol agents must rely on their environment and delivery method in order to remain suspended and reach the fire location.

Complementing the understanding of the chemical action of fire suppression compounds as described in Chapter 3 with an understanding of the role of the colligative properties of aerosols was recognized as a central factor to the search for suitable replacements. However, the published data describing the fire suppression behavior of aerosols were often difficult to interpret, especially for larger-scale fire tests. It was difficult to separate possible chemical suppression effects from the physical effects which are almost always present. It was known that the aerosol particle size was an important parameter in suppression effectiveness although a quantitative understanding as to the exact role particle size played was hard to determine. In short, the phenomenon of fire suppression using aerosols needed further exploration.

The NGP research described in this chapter was undertaken to address the lack of quantitative information on aerosol suppression behavior. Studies targeted the effects of aerosol size, aerosol droplet or particle velocity behavior in various flow fields, the physical and chemical properties of liquid and powder aerosols, and the predictive capabilities of aerosol suppression behavior. Most of the research predates the NGP focus on aircraft fire protection (Chapter 1) and is directed at a wider range of halon replacement applications.

4.2 PREVIOUS KNOWLEDGE

4.2.1 Water

Certainly the fire fighting agent that has been used the longest is water (Chapter 1). The interactions of water droplets of various diameters with flames have been studied for almost four decades.[1,2,3,4,5] Many of the early studies examined the effectiveness of water sprays on liquid fires. The suppression of liquid fuel

counterflow flames by water was experimentally investigated by Seshadri[6] using very small droplets that vaporized completely. McCaffrey[7] in the 1980s examined the effect of water introduced in the form of a mist of small droplets on natural gas diffusion flames of various sizes. He introduced the mist outside the base of the flame, where it was entrained along with the fuel. Mass flows of water mist approximately equal to the fuel flows extinguished the flame. In this instance, fine water mist was as effective as halon 1301. In 1977, the U.S. Naval Research Laboratory (NRL) examined some of the advantages of water mist for shipboard use.[8] In addition to pointing out the physical roles (oxygen dilution and high molar heat absorption), the report also noted that aqueous solution of salts would form fine solid particles upon evaporation of the water.

Although there was consensus in the community on the fundamental fire suppression mechanism of water, little detailed quantitative information on the various physical effects operating or any possible chemical effects of water mist was available. Such information underpins the ability to identify when a water-based suppression should be considered, how best to deliver the water, and how one might enhance the fire suppression ability of water mist. Aerosol fire suppression understanding was in its infancy at the beginning of the NGP.

4.2.2 Powders

In addition to the liquid aerosol properties that affect suppression (heat capacity, vaporization and possible additional chemical suppression pathways) powder aerosols possess additional properties that impact fire extinguishment including crystal decrepitation, decomposition, and surface mediated reaction.[9] In interpreting fire suppression results for early studies with various dry powders,[10,11,12] researchers were able to utilize the surface area of the particles to explain thermal vs. chemical effectiveness of finely divided particles.

Rosser et al.[13] examined the effect of finely divided metal salts on the burning velocity of premixed hydrocarbon-air flames in the early 1960s. While several of the powders they studied were not effective, several compounds of sodium, potassium, and copper were effective. They observed that the measured inhibition correlated with the degree of particle evaporation. Successive steps were identified for successful suppression: particle heating, particle evaporation, particle decomposition, and chemical flame inhibition by the added metal compounds.

Fischer et al.[14] at NRL in the early 1980s studied methane flame extinction in a laboratory scale Bunsen burner flame apparatus for a number of powders including monoammonium phosphate, potassium bicarbonate, potassium chloride, sodium bicarbonate, and Monnex™ (primarily $K_2C_2N_2H_3O_3$). Extinguishment efficiency increased rapidly with decreasing powder particle diameter with transition diameters ranging from 40 μm to 60 μm depending on the specific inorganic salt compound. Of the powders studied, Monnex™ displayed the largest size, ~ 60 μm, for onset of higher efficiency (probably related to the tendency of Monnex™ to undergo decrepitation).

In the early 1980s, Ewing, Hughes, and Carhart[15] at NRL developed an empirical predictor for the flame suppression effectiveness of liquid, gaseous, and solid agents. They observed a large increase in suppression efficiency with decreasing particle size. They concluded that suppression of a methane fire was achieved predominantly by heat extraction from the flame by means of heat capacity sinks and endothermic reaction sinks, such as vaporization, dissociation, and decomposition for the powders they

investigated. They generalized that the extinguishing potential of a powder agent could be predicted from its thermodynamic properties. In later tests, Ewing et al.[16] extinguished heptane pan fires in a 420 L test chamber. Both $NaHCO_3$ and $KHCO_3$ agents were applied to the fires via a pressurized discharge nozzle. From the tests, a critical size below which particles fully decomposed in their fire scenario was determined for each agent. In a companion effort, Fischer and Leonard[17] performed extinction studies on 21 agents in a premixed flame and also observed a distinct transition region from effective to ineffective particle sizes. Similar experiments were performed by Chattaway et al.[18] in evaluating the efficiency of very small aerosol particulates.

Knuth, Ni, and Seeger[19] studied the flame inhibition effectiveness of several dry chemicals, including $KHCO_3$ and $NaHCO_3$, solely in the 38μm to 43 μm size range, by adding powders to a counterflow diffusion flame and measuring species and temperature profiles. Their conclusions were primarily based on the decrease in flame temperature and production of the major combustion product species, H_2O and CO_2. The powders tested were then ranked in increasing reaction-inhibition effectiveness: Al_2O_3 (least effective), $NaHCO_3$, $KHCO_3$, $NH_4H_2PO_4$, and KCl (most effective). Hamins et al.[20] used a counterflow burner to study extinction of liquid pool fires of n-heptane and JP-8 by 13 gaseous agents and sodium bicarbonate. Powder sample in three nominal size ranges were tested: 0 μm to 10 μm, 10 μm to 20μm, and 20 μm to 30 μm. Results were not reported for powders above 30 μm. They concluded that the 0 μm to 10 μm size range was the most effective, followed by the 20 μm to 30 μm and then the 10 μm to 20 μm range. No explanation for the non-monotonic behavior of effectiveness with size was proposed. Using a cup burner, Hamins showed that, on a mass basis, small $NaHCO_3$ particles (sub-10-μm diameter particles) which act both as a physical and a chemical suppressant, are three times more effective than halon 1301 (CF_3Br) and five times more effective than nitrogen.[21]

4.2.3 Combined Agents - Water Additives

A brief, general discussion on the uses of water additives for fire fighting can be found in Wahl.[22] The general intent of adding salts to water was to improve the thermophysical properties of neat water. An example is the lowering of the normal freezing point of water so that it can be used at sub-zero temperatures. For fire suppression, it had long been recognized that additives could significantly reduce the mass of water needed to quench flames.

Monson et al.[23,24] investigated various water additives for fire fighting. Several formulations were identified, which included the following aqueous solutions: 24 % by mass of LiCl, 5 % LiCl, 26 % $CaCl_2$, 10 % $Ca(NO_3)_2$, 27 % $CaCl_2$, and 5 % $FeCl_3$, 29 % $CaCl_2$. Only the first of these formulations was actually tested for fire suppression effectiveness. Using a spray nozzle directed at a wood crib fire, the solution extinguished the fire 1.4 times faster than neat water applied at the same rate.

In a series of reports, Grove and co-workers[25,26,27,28,29,30,31,32,33] evaluated the effect of the addition of a viscosity modifier, a surfactant, and/or an opacifier to water on improving the fire suppression effectiveness of water (applied in the form of a spray). The purpose of using a viscosity modifier was to improve the blanketing and runoff properties of water. The opacifier additives were used to mitigate the radiative feedback from the fire to the burning fuel surface. The surfactant was used to facilitate the dispersion of opacifiers in water. Based on the experimental results of their scaled model Class A (solid fuel) fires, it was concluded that:

- The major contribution to the improvement of the fire suppression effectiveness was attributed to the viscosity modifier.
- Viscous water produced more rapid initial control of the fires than neat water.
- The rate of extinguishment of the fires was more rapid with viscous water; the extinguishment time decreased as the viscosity of water was increased.
- The danger of re-ignition was reduced when the fires were extinguished with viscous water, as a result of less water runoff.
- Reduced runoff of viscous water provided better water utilization for fire control and minimized collateral water damage.
- The addition of an opacifier to viscous water further improved the fire fighting properties of water.
- The surfactants used in the study had very little effect on the improvement of the extinguishing properties of water.

In an attempt to improve the effectiveness of water to control and suppress forest fires, Davis et al.[34,35] added several viscosity modifiers to plain water. The results from their controlled field and laboratory fire tests also indicated that fire suppression effectiveness was related to the viscosity of water.

Fine spray solutions of sodium and potassium carbonates and bicarbonates were studied by Friedrich [36] to evaluate the effectiveness of these aqueous solutions in suppressing liquid pool fires. Concentrations ranging from a mass fraction of 0.01 to 0.1 were used in the study, which involved the application of the solution from a spray nozzle located at a fixed distance from the liquid pool. The salt solutions with the highest concentration exhibited the highest effectiveness; however, no improvement in the effectiveness was observed when the concentration was less than a mass fraction of 0.05. No comparison of the fire suppression effectiveness among various salt solutions was given in the cited reference. The author attributed the increase in fire suppression effectiveness of these aqueous solutions to the chemical inhibition ability of the salts and suggested that other compounds such as the oxalates would probably be more effective than the carbonates (albeit low solubility in water and toxicity are potential issues).

Investigation of very high mass fraction additives to water was motivated by the need for fire suppression at low theater temperatures. At the Army Research Laboratory, Elkins studied the use of ethylene glycol anti-freeze as an additive to water.[37] At a volume fraction of 0.3, the ethylene glycol/water solution was found to be approximately three to four times *less* effective (in terms of extinguishment time) than pure water. The author recommended that the concentration of ethylene glycol should not exceed a volume fraction of 0.3, lest the solution lose its fire fighting capability.

The fire suppression effectiveness of aqueous solutions of KBr, KCl, NH_4Cl, Na_2CO_3, $NaHCO_3$, K_2CO_3, $KHCO_3$, and HCOOK of various concentrations were examined by Kida.[38] The solutions were sprayed vertically downward to a small hexane pool fire, and the extinction times were measured. Despite large scatter in the data, a 0.20 volume fraction $KHCO_3$ solution was found, on the average, to be at least twice as effective (in terms of the extinction times) as pure water. The performance of the other aqueous solutions was not reported in the cited reference.

In a United Kingdom Patent by Ball et al.,[39] potential water additives such as phosphates, carbonates, amino compounds, citrates, anti-freeze agents, and surfactants were suggested to increase the solubility of CO_2 in water for fire suppression applications.

Finnerty et al.[40] evaluated the fire suppression effectiveness of 13 water additives using an airless paint sprayer and a small JP-8 pan fire. Solutions of potassium lactate (0.60 mass fraction) and potassium acetate (also at 0.60 mass fraction) were found to be superior to the other additives and at least four times more effective than pure water in terms of extinguishment time. Although these two solutions had the same overall fire suppression efficiency, the acetate has a sufficiently higher normal freezing point as to render it undesirable for low temperature applications. The superior performance of the potassium lactate and acetate solutions was further demonstrated using the dispersed liquid agent fire screen apparatus developed by NIST[41] under the NGP (Chapter 6).

The significant enhancement in flame suppression ability of aqueous NaOH solutions (almost a factor of five for 17.5 % of NaOH by mass in water)[40] was found to be consistent with previous experiments reported by Zheng et al.[42] for premixed counterflow flames using aqueous NaCl solutions.

Experiments by Mitani and Niioka [43] considered inhibition of premixed flames with ultra fine water droplets (less than 2.4 μm mean diameter) containing NaOH and $NaHCO_3$, indicating a flame inhibition/ extinction with addition of chemical agents. In particular, their slower $C_2H_4/O_2/N_2$ premixed flame experiments (as opposed to faster $H_2/O_2/N_2$ flames) showed distinct chemical inhibition effects, but the saturation effects due to condensation of the inhibitor species were not explored. Zheng et al.[42] documented a significant enhancement in counterflow premixed flame suppression from fine droplets of solutions of water/ NaCl over that of pure water.

Fire suppression studies relevant for protecting shipboard machinery spaces conducted by the British Royal Navy in Great Britain examined the suppression effect of adding proprietary wetting agents, Aqueous Film Forming Foam (AFFF), and Film Forming Fluoro Proteins (FFFP) to water sprays.[44] They found that the additives did shorten the fire extinguishing times over neat water, yet the surface tension lowering actually resulted in a slight *increase* in the mean droplet size of the resulting water spray. In this case, the foam forming attributes and possible chemical suppression properties of the additives likely played a more significant role in the suppression effectiveness than the influence of the additive on the surface tension and subsequent droplet formation of the liquid.

4.2.4 Burning Surfaces

There have been numerous studies on flame spread velocities in opposed and counter flow configurations during the last three decades.[45,46,47,48,49,50,51] These studies have shown that the flame spread velocity depends on the fuel thickness, flow configuration, oxygen concentration, and the size of the wind tunnel. Therefore, for flame suppression studies, it is best to obtain data with and without the suppressant in the same facility.

Studies describing spray-target interactions have primarily focused on application of paint coatings to surfaces.[52,53] These studies have shown that high gas phase strain rates where the spray impinges on the target dramatically affect turbulent transport of small droplets (diameter less than 25 μm), and hence the deposition of the droplets on the intended surface. In addition, the deposited droplet size distribution can be significantly different from that of the initial spray. Finally, droplet transport is dependent on initial

droplet momentum, aerodynamic drag, and the gravitational force, with aerodynamic drag being dominant.

Many studies have been performed that quantify the vaporization process of both single and multiple droplet arrays impacting on hot surfaces.[54,55] These studies have identified the need for spatially and temporally resolved data describing the droplet trajectory as it approaches a hot surface (including buoyancy effects), as well as the temperature distribution of the surface material. The NGP studies addressing the interaction of droplets with surfaces are described in Section 4.6 and 4.7.

4.2.5 Large-scale Studies

Need for Testing at Realistic Scale

A candidate halon replacement (in-kind, i.e., vaporizing liquid) or alternative (not in-kind, e.g., aerosol, such as water mist or fine powder) may demonstrate great promise based on laboratory or small-scale evaluations. Implementation effectiveness will hinge on a number of additional considerations including applicability, compatibility, stability, shelf-life, toxicity, and dispersal. Performance against a full-scale, realistic threat and long-term certification is often needed to provide confidence that what looked good in the laboratory will work reliably in practice.

In practice, gaseous fire suppressants deployed as total flooding agents are generally expected and required to disperse throughout a space. Even so, there will remain distribution inhomogeneities due to finite agent release locations and the effects of obstacles. NRL studies in a real-size simulated ship machinery space (840 m^3) found that, even for a very carefully designed gaseous agent discharge system, there were agent concentration inhomogeneities of at least ± 20 % that impacted the fire extinguishment time.[56] For fire suppression agents that are solids or liquids at the application temperature, dissemination and distribution challenges become much more difficult than for gaseous agents.

Liquid Aerosols - Water Mist

Full-scale total flooding water mist extinguishment tests, including mists with additives such as AFFF, were conducted by NRL in the early 1980s in 83 m^3 and 324 m^3 highly instrumented compartments.[57] The testing demonstrated the effectiveness of a fresh water mist with a high fraction of droplet diameters under 50 μm in diameter. Fixed arrays of commercial nozzles, mainly Bete Fog Nozzles, were evaluated at discharge pressures up to 2 MPa (300 psi). Suppression challenges were included in a variety of Class A (solid) and Class B (liquid) fuels in compartments configured as very obstructed and cluttered machinery spaces or torpedo rooms. Except for occasional malfunctions, all Class B fires were extinguished in 15 s to 40 s. Some Class A fires in the 324 m^3 compartment were fully extinguished with one or two bursts of water mist of 1 min to 2 min duration. The flames from other Class A fires were extinguished, but smoldering continued. Flaming combustion reappeared after the water mist system was turned off. Even with slow extinguishment, significant cooling was achieved; the fires were "slowed down" and re-entry by protected firefighters would have been possible. Even for the largest tests, the total quantities of water used for extinguishment were usually less than 190 L to 265 L (50 gal to 70 gal). For comparison, a conventional 38 mm (1½ in) fire hose delivers about 380 L/min (100 gal/min), and a single hose would hardly begin to quench these fires, especially in the obstructed geometries. With the

water mist, cleanup was minimal. The experience showed the great merit of water mist for total flooding applications and the potential for optimization.

Solid Aerosols - Powders

Early NRL studies in the 1950s provided quantitative data on the effectiveness advantage of potassium bicarbonate ($KHCO_3$) over sodium bicarbonate ($NaHCO_3$), and addressed practical techniques for allowing better implementation of powders. In large-scale powder studies in the 1980s, Ewing et al. at NRL found that the increased efficiency with decreasing powder particle size observed in small, bench top experiments was also valid when extinguishing large heptane pool fires (0.29 m^2 and 2.32 m^2).[58,59] Momentum factors for getting the particles into the flame sheet were considered.

Pyrogenic Generated Aerosols

Pyrogenic generation of fire suppression agents is one method of generating and dispersing aerosol agents in large-scale. The "Halon 90 - Second Conference on the Fire Protecting Halons and the Environment" in Geneva on 1-3 October 1990 presented Russian fine solid aerosol fire suppressant efforts via videos of pyrotechnic devices in operation. These combustion devices released a very hot product stream that produced very small solid aerosol particles by condensation. Also presented were a number of Russian pyrotechnic aerosol efforts, including work by Russian émigrés and further studies in Israel and the USA. Initial U.S. Navy evaluation at the Spectronix Israeli site in August 1992 confirmed that the buoyancy of the exothermically produced aerosol is a significant distribution issue in employing a heterogeneous fuel/oxidant propellant product as a total flooding agent in large spaces.

Follow-up experiments at NRL measured aerosol generation temperatures and pressures and evaluated two approaches to removing heat: passive water bath and water spray generators. Fire threats included n-heptane pool fires of various sizes. In the 56 m^3 (2000 ft^3), 4.3 m (14 ft) tall instrumented compartment tests,[60] aerosol concentrations were determined from optical density measurements at three heights: 0.5 m, 2.0 m, and 4.1 m (1.7 ft, 6.7 ft, and 13.5 ft).

In tests of uncooled aerosol generation, 1/4 to 1/3 of the solid agent containing pyrotechnic material was aerosolized with over 200 L of CO_2 per kg of original material. There was also considerable energy emitted. Visible flame plumes 30 cm long exited the generator horizontally, but then quickly rose almost vertically due to buoyancy effects. The highest and middle optical probes were quickly engulfed using 1 kg of material. Only after almost 90 s did the aerosol cloud descend to within 0.5 m of the floor. The aerosol densities took over 4 min to equilibrate and maintain these levels at the three heights. There was little visible residue.[61]

Rapidly bubbling the hot aerosol through water for cooling produced both a rising buoyant plume and a dropping cooled cloud. The two layers did not coalesce until after 2 min, and the aerosol densities were lower with water removal of the aerosol.

The generators utilizing water spray cooling dispensed agent horizontally for over 1 m. However, the 1 kg aerosol charge was not cooled sufficiently by 1.6 L water injection and exited the generator at close to 1000 ºC. The horizontal momentum thrust dissipated and buoyancy forces still dominated dispersion. Thus, the elevated temperatures of pyrotechnic-produced aerosols remained a concern.

Large-scale fire extinguishment tests evaluated both liquid and solid aerosols. Hot gas generators were found to extinguish 0.23 m^2 pan fires in 45 s with 4 kg of pyrotechnic material, equivalent to 71 g of solid fire extinguishing agent per m^3. Water bath cooled generators could not extinguish the fires with 3 kg of material; extinguishment required 5 kg and more than 115 s (equivalent to 89 g/m^3). In contrast, the water spray cooled generators extinguished a 0.23 m^2 pool fire in 65 s using just 3 kg of agent (equivalent to 54 g/m^3).

Larger, 1.1 m^2 pan fires were extinguished more quickly and required powder concentrations as low as 15 g/m^3. However, the larger pan fires were partially self-inhibited by oxygen depletion and were thus easier to extinguish. Even then, aerosol generation and fire extinguishment took significant lengths of time. Much faster generator mixture burning rates are possible with other compositions. However, the increased energy release rates can exceed pressure and temperature safety level requirements, requiring greatly improved aerosol cooling mechanisms to obtain uniform distributions.

Researchers did note that dry chemical fire extinguishing powders exhibited suppression vs. size behavior similar to water aerosols. For a fixed mass of extinguishant, larger particles were found to be less effective and were observed to fall out faster than smaller ones. Very small pyrotechnically generated particles, with estimated diameters ranging from 0.5 μm to 4 μm, propelled at a fire, should be easily swept away by fire-generated convection currents. The small particle size and high concentration aerosol cloud should also cause concern in occupied enclosures. Particles less than 5 μm in diameter can penetrate deep into the lung and cause pulmonary complications, physically clogging the small pulmonary air paths. Some aerosol formulations that have been pursued, while possibly more efficient as fire extinguishants, may generate more toxic and abrasive products. A U.S. Navy toxicological evaluation of a pyrotechnic fire extinguishing formulation with rats showed short-term breathing difficulties although no residual health effects were observed. For the protected area, the hygroscopic nature of some aerosol residues may lead to corrosion and electrical problems.

Addional pyrotechnic approaches were pursued in England, the U.S., and the former Soviet Union. Detailed results were often not available due to the proprietary nature of the materials tested. Solid energy absorbers, evaluated by various producers, increased weight penalties. "VNIIPO" (Moscow) studied nine different types of pyrotechnic-generated aerosol units from "GABAR," "GRANIT," "PERM," "SOYUS," and "Technology," in October 1993. Tests were conducted on 5A and 13B challenges in a 64 m^3 volume. Only the two GABAR single units succeeded in extinguishing both test fires and preventing reignition.[62] Dr. Baratov claimed his GABAR company units addressed the concerns of ignition of combustibles by hot propellant exhaust, cooled aerosol generation for better total volume distribution, and effectiveness on smoldering combustion. One U.S. Army test series on tank engine compartment fires found a pyrotechnic agent successfully extinguished the fire only to later reignite it. The weights of the heat abstracting units can be considerably more than the pyrotechnic charge weights. Still, total system weight was low compared to the pressure vessels and piping of halon-like systems.

Achieving homogeneous distribution can be a significant implementation problem for pyrogenic approaches in large spaces. However, such fire suppression strategies may be quite satisfactory for smaller spaces with lower ceiling heights, such as small rooms, cabinets or storage closets.

4.2.6 Modeling

For most of the 20th century, there were few basic models that described details of aerosol/flame interactions for non-combustible aerosols. Prior to the NGP, there were no detailed models describing the size reduction and evaporation of droplets in flames, or their effect on surface reaction kinetics. Even models that predict what size droplets could reach burning surfaces were not generally available. Understandably, there was interest in understanding the overall performance of larger-scale water mist systems.[42,63] In 1955, Braidech et al.[1] concluded that, in most cases, the efficacy of water mist is predominantly due to the oxygen displacement effect of the water evaporating, rather than to thermal cooling. In the late 1990s, modeling research began to examine the interactions of droplets with flames. Chen et al.[64] considered the motion of droplets in a non-premixed counterflow field. They considered both n-heptane and water droplets. For the droplet sizes considered, Chen et al. showed that a droplet can penetrate through the stagnation plane established by the gaseous streams and reverse its trajectory at some point in the opposing side of the flow. Prasad et al.[65] modeled water mist suppression of diffusion flames, including the dependence on the droplet trajectories into the flame.

4.3 THE NATURE OF AEROSOLS

4.3.1 Quantitative Descriptors

Particle Diameter

Aerosols are almost never monodisperse (all drops/particles of exactly the same size). Real aerosols can be nearly monodisperse, but more typically exhibit a range of particle sizes. A mean or average diameter is useful for providing specific information relating to a particular phenomenon controlling the process under investigation.[66] (See Table 4–1) These definitions are strictly true only for spherical aerosol particles or liquid drops.

Table 4–1. Mean Diameter Definitions, Symbols, and Notations used to Describe Aerosol Size Distributions.

Mean Diameter Basis	Symbol	Notation
Arithmetic or length	D_{10}	$\Sigma N_i D_i / \Sigma N_i$
Surface area	D_{20}	$(\Sigma N_i D^2_i / \Sigma N_i D_i)^{1/2}$
Volume	D_{30}	$(\Sigma N_i D^3_i / \Sigma N_i)^{1/3}$
Sauter (SMD)	D_{32}	$\Sigma N_i D^3_i / \Sigma N_i D^2_i$

The arithmetic or length mean, D_{10}, is simply the mean diameter of the spherical particles. The Sauter Mean Diameter (SMD) is that diameter for a single particle whose ratio of volume to surface area is the same as that of the entire aerosol. While D_{10} and the SMD values can be used to compare the mean diameters or surface area ratios of various aerosols, they do not convey information regarding the distribution of particle sizes.

Aerosols can be also be described by defining a mass accumulation diameter such that all droplets below this diameter make up a certain percentage of the total mass of the aerosol. For instance, $D_{0.5}$ is that droplet size such that half (0.5) of the liquid volume is in droplets of smaller diameter. The $D_{0.5}$ diameter

is also referred to as the mass median diameter (MMD). Other common mass accumulation diameters are for 10 %, $D_{0.1}$, and for 90 %, $D_{0.9}$.

Particle Size Distribution

Aerosols with similar D_{10} values, $D_{0.5}$ values, D_{30} values, or SMDs can have very different size distributions. Since aerosols of different size can exhibit different degrees of fire suppression effectiveness, characterization of the range of sizes or size distribution is necessary to compare the suppression performance of different aerosols and to make valid comparisons between experimental observations and modeling predictions. Several mathematical expressions for size distributions have been proposed, although each of them has some shortcomings. The expression to use is the one that best characterizes the relevant properties of the mist under study.

A simple and practical method for displaying droplet size information is to plot a histogram where the number of droplets in a defined size bin is plotted for that bin. In practice, the minimum size plotted is dictated by the physical limitation of the instrument settings. A water mist histogram (obtained with a phase Doppler interferometer as discussed below) is presented in Figure 4-1. Values for the mean diameters defined in Table 4–1 for this mist are indicated in the table. In the limit of small bin size, the histogram becomes a frequency or size distribution.

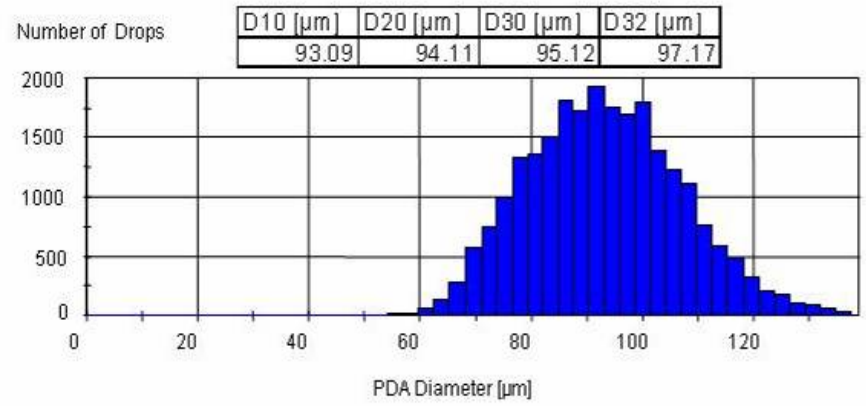

Figure 4-1. Water Mist Size Histogram and Values of Several Mean Diameters.

Two commonly used functional expressions describe the droplets as (a) a Gaussian distribution or (b) a mass accumulation.[67] These simple expressions cannot be used to describe bi- or multi-modal distributions. For these, linear combinations of the different single expressions are sometimes used.

The Gaussian or normal distribution with respect to the natural logarithm (lognormal) of the diameter is given in Equation (4−1). This expression is often sufficient to fit observed experimental droplet size distributions, where d_{mn} is the number geometric mean droplet diameter D_{10}, and s is the corresponding standard deviation describing the spread in the distribution.

$$N(d) = \frac{0.399}{s * d} \exp\left(\frac{\{\log(d) - \log(d_{mn})\}^2}{2s^2} \right) \tag{4-1}$$

The Rosin-Rammler equation (mass accumulation expression) describes the aerosol by relating the mass of aerosol material contained in particles up to a certain diameter. The Rosin-Rammler expression is given in Equation (4−2). In this expression, *a* and *b* are constants related to a mean diameter and the spread, respectively.

$$N(d) = \frac{b}{a^b} d^{b-4} \exp\left(\left(\frac{d}{a} \right)^b \right) \tag{4-2}$$

Note that each expression includes two parameters to describe the distribution. One advantage of using the Rosin-Rammler expression is that all of the representative diameters (e.g. $D_{0.1}$, $D_{0.5}$, etc.) can be related to each other through the spread.

Both of these two mathematical descriptions of the histogram in Figure 4-1 are presented in Figure 4-2. The values of the two parameters are: D_{10} = 93 μm, s=0.15 (lognormal) and a=101, b=9.4 (Rosin-Rammler). Both expressions qualitatively describe the mist, although the lognormal expression is a better match for this mist in both the peak position and spread in the distribution.

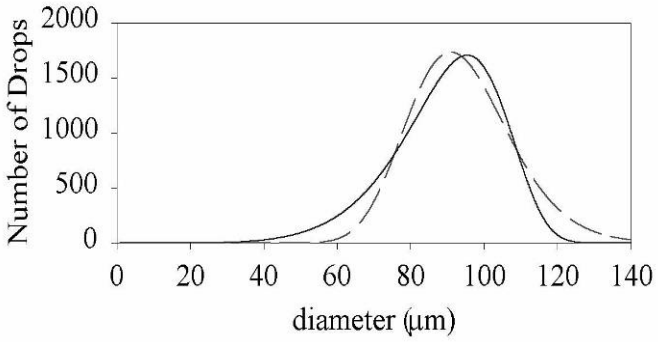

Figure 4-2. Lognormal (dashed line) and Rosin-Rammler (solid line) Expressions Fit to the Water Mist Histogram Presented in Figure 4-1.

4.3.2 Generation Techniques

Generating, controlling, and measuring aerosols are challenging but necessary tasks for studying fire suppression as well as evaluating fire suppression systems. Although concentration standards are straightforward for gases, there is no aerosol standard. An aerosol generation system that could reproducibly produce a uniform distribution of a monodisperse (or polydisperse) aerosol would be extremely useful.

Aerosols of liquid droplets can be produced using ultrasonic agitation of the liquid, either disrupting the liquid surface or modulation of a liquid jet stream. NGP studies employed both methods; the specifics are outlined in Chapters 7 and 8. Assisted breakup of liquid jets can produce aerosol droplet size distributions that are narrow, approaching a single, monodisperse droplet size for all of the drops. This

generation method is ideal for small, bench-top studies only requiring a small number of drops. The number of droplets produced is in general not sufficient for large-scale suppression applications.

Powder aerosol samples are typically produced by physically crushing solid samples, followed by size separation using various sieving protocols. Sample crushing often results in a range of particle shapes in a given size bin, where individual shape differences will depend on the nature of the powder and the crushing/sieving protocol. Sample drying is often required to improve the flow properties, especially for very small particles. Small concentrations of flow enhancers such as silica can improve flow properties.

Large masses of powder particles can be generated using pyrogenic methods discussed in Section 4.2.5. Particle size and composition (including the addition of chemical suppressant moieties) can be varied depending on the type of generator and the particular propellant formula. Because of the high particle momentum and often high gas temperatures exiting the generators, pyrogenic powder aerosol generation techniques are rarely practical for bench-scale studies. However, in large-scale applications, the high particle momentum can be very useful in aiding agent dispersal.

4.3.3 Quantification of Aerosols

Gaseous fire suppression agents can generally be monitored and controlled by regulating the volumetric flow of the agent. Gaseous agents generally distribute throughout the measurement volume so that agent spatial distribution issues are generally dictated by the physical constraints of the application geometry. Aerosol agents will not uniformly fill the application space, especially very large, obstructed spaces. In order to determine the amount of aerosol agent in the application area, measurement techniques must be employed that are applicable and can provide relevant, valid information. Relevant information includes data on how the aerosol is distributed spatially in the application area, especially in and around any fires that may be present.

4.3.4 Aerosol Size and Velocity Characterization

One of the most challenging aspects of working with aerosols is characterizing the aerosol that has been generated in order to obtain relevant, quantitative information. Such quantitative information, even on a relative basis, is required in order to make valid suppression effectiveness comparisons. A general discussion of the characterization methods used in NGP aerosol fire suppression studies is outlined below. Specific details are given in the individual studies.

Diffraction Method

Diffraction-based systems are capable of providing size information (either mass or volume) of an aerosol.[68] The experimental layout is fairly simple, as shown in Figure 4-3. A coherent light source (i.e., a laser) and a two-dimensional detector (i.e., a linear array of detectors or a charge coupled device, CCD, camera) are needed. The laser light, directed at the detector, passes through the sample volume containing the aerosol. Laser light diffracts around individual droplets in the aerosol (Fraunhofer diffraction). The light intensity pattern falling on the camera is a superposition of all of the single droplet diffraction patterns. By deconvoluting the diffracted intensity from the ensemble of drops, the mass or volume distribution can be derived. Diffraction methods do not rely on a spherical droplet or particle,

although the determination of volume or mass must assume some shape. The ease of set-up and straightforward calibration requirement make diffraction methods attractive.

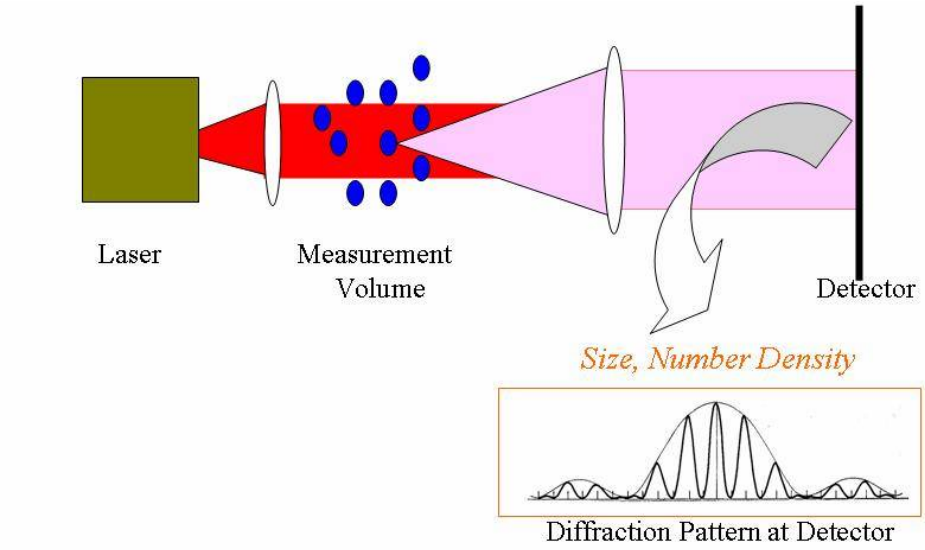

Figure 4-3. Schematic Diagram for Diffraction-based Particle Sizing.

Diffraction methods lack the spatial resolution of other optical approaches. They measure everything that lies in the beam path. Because they rely on diffraction, higher power laser sources are often needed. Diffraction methods also do not provide velocity information, and thus cannot provide flux information directly. Although the lack of velocity information is an issue, diffraction methods can provide droplet size distribution and density information. An effective mass flux can be estimated for well-characterized flows.

Phase Doppler Interferometry Method

Phase Doppler Interferometry (PDI, also referred to as phase Dopler anemometry, PDA) is an established technique that can provide velocity information or both velocity and size for individual, spherical particles.[69] PDI systems which only provide velocity information are called Laser Doppler Velocimetry (LDV) systems. PDI measurement times can be as short as 1 μs, so that statistically significant size histograms can be generated in less than a second depending on the particle number density. Droplet sizes from ~ 1 μm to several mm can be measured, although not with a single system configuration.

PDI droplet sizing relies on the phase difference between two signals originating from the same point and arriving at two spatially separated detectors. Each signal is generated by a droplet passing through a set of parallel grating lines produced from the overlap of coherent laser beams. The technique is depicted schematically in Figure 4-4 with a representation for the ellipsoidal "grating" measurement volume. PDI determined diameters are only strictly valid for spherical drops. A third detector, providing a second phase difference, is used to check the sphericity assumption.

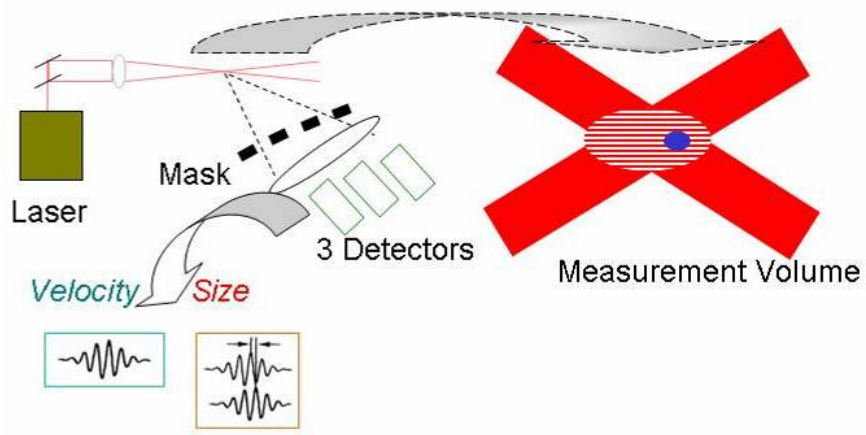

Figure 4-4. Diagram for 1-D Phase Doppler Interferometry System for Obtaining Size and Velocity of "Spherical" Aerosol Particles.

The size of the ellipsoidal measurement volume depends on the wavelength of the laser, the beam diameter at focus, and the crossing angle. Typical measurement volumes are ≈ 1 mm long by 0.2 mm diameter for droplet sizes relevant to water mist suppression. Only a single droplet can be present in this volume during the measurement period for the measurement to be valid. This requirement can be problematic for very large number densities (e.g., > ≈ 10^4 drops/cm^3 for uniformly dispersed 50 μm diameter drops).

The laser wavelength and beam-crossing angle control the grating line spacing. Passage of the droplet through the grating generates a Doppler burst pattern containing the droplet 1-D velocity information perpendicular to the fringes. Additional hardware is required for 2-D and 3-D velocity information. The grating fringe spacing must be reasonable for the droplet size in order to determine a valid burst pattern and provide the corresponding velocity. For closely spaced lines and large drops, there may not be sufficient modulation in the signal to qualify as a valid burst. Large spacings and small droplets may not provide enough modulations for the phase shift validation. PDI signals can originate from light reflected from the droplet surface or refracted through the drop. The angle of the refracted light exiting the droplet is dependent on the liquid index of refraction that must be known. Reflected light does not depend on the index of refraction but signals are generally much weaker. The choice of scattering angle will determine which scattering mode is dominant. When a single scattering mode is dominant there will be a linear correlation of the droplet diameter with the phase difference. If more than one scattering mode significantly contributes to the signal, the phase angle/diameter relationship will not be linear. For water droplets in air, first order refraction dominates light scattered at 30º in the forward direction. A scattering angle of 30º was used for measuring water droplets in the NGP studies.

Uncertainties in the PDI size determinations associated with the scattering angle and refractive index are generally less than a few percent. Because of the finite range for the detector and the non-linear dependence of the scattering intensity on the droplet size, the usable dynamic range dictates a droplet size dependent precision in the determination of the sizes. Additional potential limiting factors are the laser power, detector gain setting, and S/N ratio. These combined effects typically limit the uncertainty for a PDI size determination to at least 0.5 % of the full-scale reading. Velocity uncertainties depend on the processor settings, primarily the need to divide the velocity space into a finite number of bins. Binning depends on the size range to be measured, which depends on the optical configuration used. In addition to the dependence on processor settings, uncertainties in the velocity determination depend also on the

instrument A/D resolution, fringe spacing uncertainty, and sampling frequency. Velocity uncertainties can be as high as ± 25 %.

The mass flux determination relies on the droplet size, velocity, and the probe volume. The droplet number density also relies on the probe volume. However, the probe volume is droplet size dependent, requiring a correction for both number density and mass flux. The dynamic range for a single PDI system configuration is typically 40:1. This value depends on several factors, including the optical system, laser power, detector gain and dynamic range, and system S/N ratio. Obtaining accurate size information becomes a compromise between the size resolution desired and the range of droplet sizes that can be determined.

Imaging Method

Capturing an image of the aerosol particle can provide both size and velocity information. Unlike diffraction-based techniques, imaging techniques can be used to "size" non-spherical particles or spherical objects such as drops. Imaging techniques have been used extensively to study and understand sprays and spray formation and development.[70] In its basic form, an imaging configuration is fairly simple, as shown in Figure 4-5. It consists of a light source and a recording medium, either photographic film or more typically a CCD camera. The light source is normally a laser, which provides sufficient spectral brightness in a short time period to "freeze" the motion of the drop. Droplets can either be back illuminated in shadow method, as indicated in Figure 4-5, or illuminated from the front. The shadow method is more often used, as the droplet size dependent back-reflected light can complicate data collection. In the shadow method, droplet images appear as dark spots on a light background. The 2-D velocity information in the image plane can be determined from timing droplet exposure "tracks" or by double pulsing the light source, creating two images of the same droplet displaced according to its velocity and the illumination time delay. The two images can be in the same camera frame or in sequential frames. Software algorithms correlate the images, permitting both speed and trajectory information. Algorithms permit false shadow rejection from images that remain in the same location frame after frame (e.g., a spot on a lens or window).

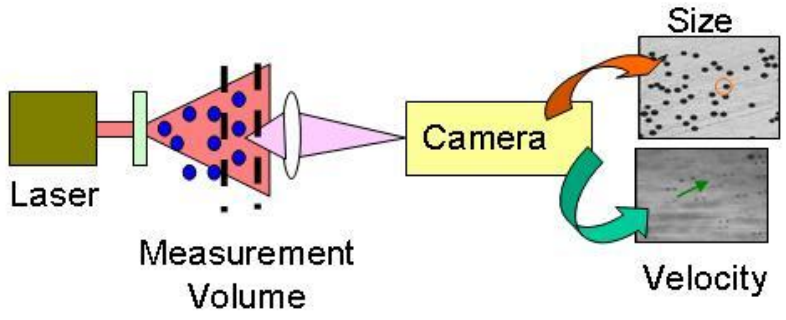

Figure 4-5. Schematic Diagram for Imaging-based Particle Sizing.

Although cameras with photographic film can be used, CCD cameras provide greater flexibility. Cameras can be digital or analog. Digital imaging requires a large data storage capacity if the raw images are saved. This may limit the time for continuous data collection. Images can be processed either on-line or off-line. On-line image processing generally saves time but unless the images are also stored, valuable information may be lost. Off-line processing requires that the raw images be stored. Analog cameras

with tape storage (usually super VHS) offer the advantage of long data collection times (several hours). Acquiring the raw images and performing off-line data reduction is an added time expense, but can be an advantage. Repeated data reduction using different fitting parameters can sometimes identify issues with the data collection or point out systematic problems.

Droplets from a few μm to several mm may be imaged but the total size range requires a change of optics. The measurement region that can be imaged depends on the magnification but is typically 1 mm^2 for detecting ~ 4 μm to 300 μm diameter drops. Similar to microscope optics, imaging magnification factors must be greater than one, requiring that the distance of the droplets from the focusing lens be much shorter than the distance of the image from the lens. In practice, this means that the sample volume must lie fairly close to the collection lens for the smallest droplets.

Size and velocity measurement accuracy is controlled by the lens focusing system, the media resolution (photographic grain limit or camera pixel resolution), and the determination of degree of focus. Since the data obtained are a mixture of in-focus and out-of-focus images, image analysis schemes must be employed to decide which images are valid and then render sizes. The degree of focus impacts both the location of the droplet edges and also the determination of the measurement volume.

The uncertainty in the measurement volume is the largest source of uncertainty for imaging detection. Both the droplet number density and mass flux determination are impacted by this uncertainty. The derived particle volume depends on the size of the drop but fortunately, computers can aid in eliminating the human bias in the decision-making. The key to achieving a reasonable accuracy lies in the calibration and validation processes.

Particle Image Velocimetry (PIV) is the macroscopic analog of droplet size imaging.[71] In PIV, the marker particle image is not resolved since size resolution is not desired. Marker particles are illuminated with two temporally delayed laser sheets. Small particles, typically < 1 μm, are used to insure that the marker particles validly represent the flow field. Large areas ($\geq$ 1 m by 1 m, depending on the spectral brightness of the laser source and the collection optics) can be characterized. By recording two shots in the same frame or in sequential frames, both speed and direction of movement of the particle can be derived through image analysis. PIV is typically used to monitor bulk gas or liquid flows. It can also be used to monitor the flow behavior of larger aerosol particles that, because of their size, do not follow the flow field streamlines. As is shown in this chapter, suppression aerosol particle velocity (speed and trajectory) controls the overall aerosol effectiveness. Such velocity information becomes key in understanding the suppression mechanism for aerosol agents.

4.3.5 Aerosol Properties Affecting Behavior

Evaporation/decomposition behavior

Rosser et al.[13] and Mitani and Niioka,[43] based on observations for particle suppression behavior in premixed flames, described the flame suppression mechanism in terms of particle size and residence times. Generalizing these findings to both liquids and solids, four steps with their characteristic times relevant to suppression behavior of an aerosol (liquid droplet or solid particle) can be assumed:

Step I: aerosol heating,

Step II: aerosol evaporation (solid or liquid) and/or decomposition (primarily solids),

Step III: generation of the inhibitor radical species in the gas phase, and

Step IV: inhibition of the gas-phase combustion process.

Optimum inhibition efficiency requires completion of all four steps. The slower steps determine the extent of inhibition and what aspects of the condensed phased suppression mechanism contribute to the inhibition process. The times for Steps III and IV involving gas-phase reactions are typically much shorter than the drop/particle heating times or the decomposition/evaporation times for Steps I and II.

Heating of the aerosol in Step I needs to raise the temperature to the aerosol's boiling/decomposition temperature. The particle heating will depend on the size of the particle, the particle thermal conductivity and that of the surrounding gas, and the gas temperature. Flames temperatures encountered are typically ≈ 1800 K. Assuming the aerosol particles are small, the heating time for Step I is typically short, << 1 ms.

The evaporation of the aerosol particle in Step II involves losing mass (vapor) to the surroundings. Several models have been proposed for treating the evaporation of liquid drops, depending on what regimes are relevant and what assumptions are appropriate. One model suitable for the experimental conditions under consideration here is[72]

$$d^2(t) = d_0^2 - Kt \tag{4-3}$$

where K, the evaporation constant, is given by

$$K = \frac{8\lambda}{\rho c_p} \ln\left[1 + (T - T_{boil})\frac{c_p}{h_{vap}}\right] \tag{4-4}$$

The time for complete evaporation to occur can be estimated from:

$$t_{vap} = \frac{d_0^{\,2}}{K} \tag{4-5}$$

Equation (4−3) is referred to as the d-square law for droplet evaporation and predicts the droplet diameter, d, at any time, t, in terms of the original droplet diameter, d_0. The mass transfer is dependent on the temperature, T, and thermal conductivity, λ, of the surrounding gas as well as on the properties of the drop: heat capacity at constant pressure, c_p; density, ρ; enthalpy of evaporation, h_{vap}; and boiling point, T_{boil}. According to Equation (4−5), the time required for the droplet to evaporate completely is dependent on the original diameter of the drop.

Evaporation times for water as a function of droplet size for temperatures ranging from 1100 k to 2200 K are shown in Figure 4-6. The evaporation time for a 30 μm diameter water droplet in an air stream at 2100 K is predicted to be ≈ 2.5 ms. The thermal conductivity data for air are from Kays and Crawford.[73]

Whether the droplet will have sufficient time to evaporate partially or completely will depend on how long the droplet resides in the higher temperature region. This time depends on the specifics of the flow field configuration.

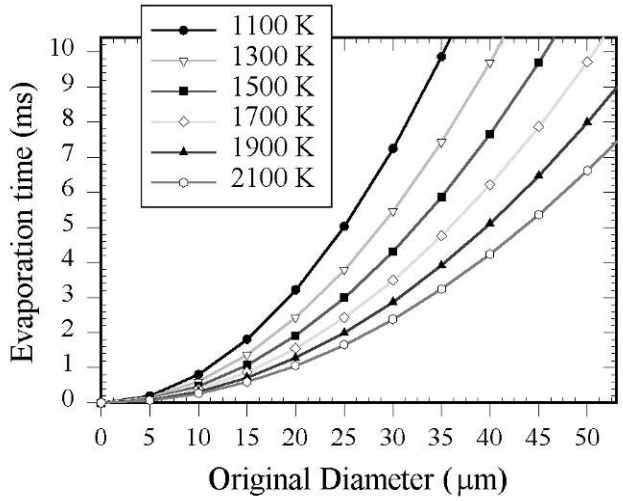

Figure 4-6. Predicted Evaporation Times using Equations (4−3) through (4−5) for Water Droplets in Air at the Indicated Temperature as a Function of Initial Droplet Diameter.

Flow Entrainment

Generation of the aerosol is only a first step in producing an aerosol suitable for further study. For flame studies, the aerosols must be seeded or entrained into a flow that hopefully results in as uniform a distribution as practical. Both uniformity in the particle mass flow as well as uniformity of the distribution of particle sizes representative of the entire distribution are needed to be able to make valid comparisons and quantitative evaluations. In order to entrain the aerosol particle in the carrier gas flow with a minimal difference in the particle and gas velocities, the gas flow velocity must equal or exceed the particle's terminal settling velocity[74] in that gas.

The terminal settling velocity assuming Stokes flow for a spherical particle can be expressed as

$$v_T = gd^2 \frac{\left(\rho_P - \rho_{gas}\right)}{18\eta_{gas}} \tag{4-6}$$

The terminal velocity, v_T, depends on the acceleration due to gravity, g, the density difference between the particle, ρ_p, and the carrier gas, ρ_{gas}, and the viscosity of the carrier gas, η_{gas}. Values of v_T for water droplets and sodium bicarbonate particles, two aerosols studied in the NGP program, are shown in Figure 4-7. Terminal settling velocities are centimeters per second depending on diameter and have a quadratic dependence on particle diameter.

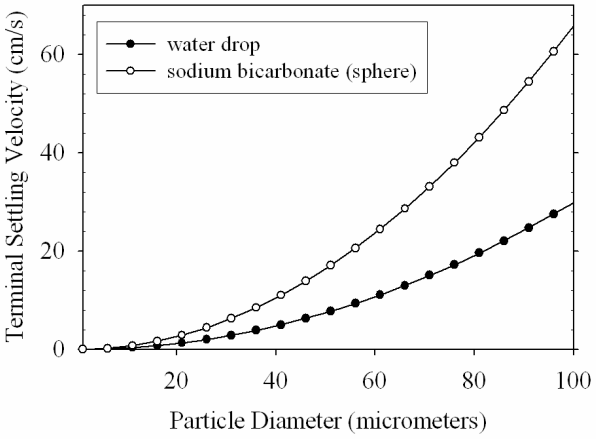

Figure 4-7 Predicted Terminal Settling Velocity for Water Droplets and Sodium Bicarbonate Particles in Air at 20 ºC.

Entrainment velocities adequate for studying water droplets may be insufficient for studying the same size sodium bicarbonate particles. Thus, the particle terminal settling velocity put limits on the size of aerosol particles that can be entrained and/or delivered to the experiment in a primarily vertical flow. For aerosols whose size distributions are non-monodisperse, low entrainment velocities can result in particle size discrimination. In some cases, velocity discrimination can be used to restrict the aerosol particle sizes introduced to the experiment. Thus, entrainment flow conditions must be considered when carrying out experiments as well as in the interpretation of data.

Particles moving in a flow with a thermal gradient will also tend to experience a thermophorectic force pushing them in the direction of lower temperature. The effect is greater for smaller particles and large temperature gradients. High temperature environments are exactly the conditions that favor rapid disappearance of the condensed phase aerosol agents due to evaporation or decomposition.

4.4 THE NATURE OF FLAMES

4.4.1 Flame Characteristics

Suppression of fires involves heat extraction, oxygen reduction, and, for chemical agents, kinetic effects at the molecular level that involve heat production and the concentration and distribution of key flame and inhibitor species. Despite the studies carried out prior to the NGP, considerable uncertainties existed in the assessment of aerosol suppression pathways, especially in the quantitative interpretation of suppression behavior. Early literature alluded to a dependence of aerosol suppression effectiveness on the fundamental aerosol size (liquid droplets or solid particles), and properties (composition, thermal stability, reactivity). In addition, the application environment (flow field, flow orientation, flame temperature) of the various fires investigated imposed characteristic residence times controlling the performance of the aerosols. Thus, characterizing these flame conditions is necessary to interpret and understand the aerosol suppression results.

For a system that undergoes combustion, the fuel and oxidizer can either be premixed (combined) or non-premixed (kept separate) upon entering the reaction region. Real fires often exhibit a combination of both mixing protocols. Figure 4-8 compares gaseous flame configurations to each other and the variation in the flow field complexity needed to describe and understand them. In general, the greater the complexity of the flow field, the more computationally challenging it is to include both the details of the flow and the details of the chemistry in the modeling treatment of the flame process. This is even more apparent in multiphase flow problems, such as the interaction of solids or liquids with gaseous flames. In order to understand the extinction mechanism of aerosols and approach a quantitative understanding of the aerosol/flame interaction, NGP researchers studied a number of flames depicted in Figure 4-8. This sometimes required a re-examination of key experiments in the literature with the focus on minimizing the number of parameters that might vary and exploring the dependence of several of these parameters on the overall suppression performance. Researchers paid close attention to the control of experimental parameters that could influence the results. In this way, the new data could be used more directly to validate the predictions of multi-phase flame suppression codes as well as aid in their development. The next sections address the different flame configurations explored under the NGP aerosol studies, discuss the metrics used to determine suppression effectiveness, and explore the nature and impact of the imposed residence times on the suppression properties of the aerosols investigated.

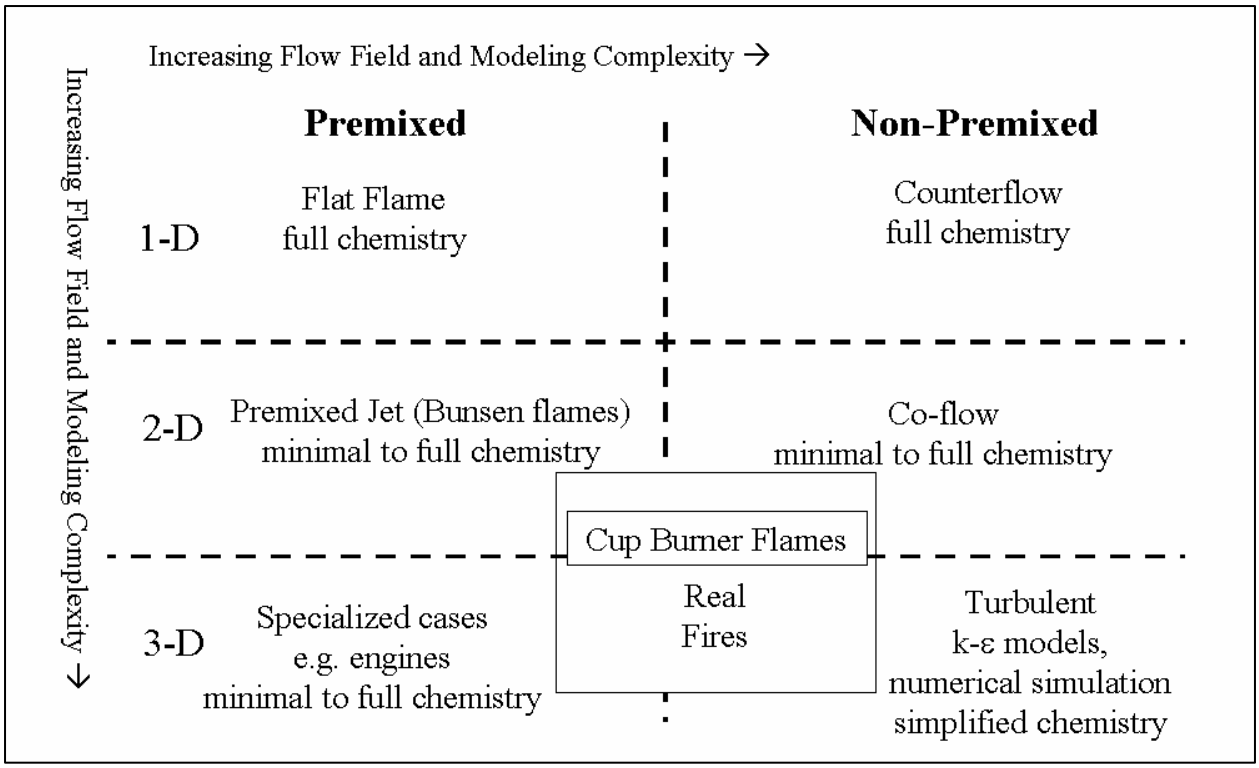

Figure 4-8. Relationship of Flame Dimensionality and Modeling Complexity.

4.4.2 Premixed Bunsen Type Flames

Premixed flames offer the least complicated flow field for gaseous flames since they can be configured to give flat, essentially one-dimensional flames. Two such flames are shown schematically in Figure 4-9 from Reference 75. The ideal one dimensional flat flame shown at the left can be experimentally achieved with gaseous reactants and gaseous suppression agents. This configuration is difficult to achieve when aerosols must be introduced uniformly into the flame. Experimentally seeding aerosols into the premixed flow and maintaining the flat, one-dimensional geometry is very difficult.

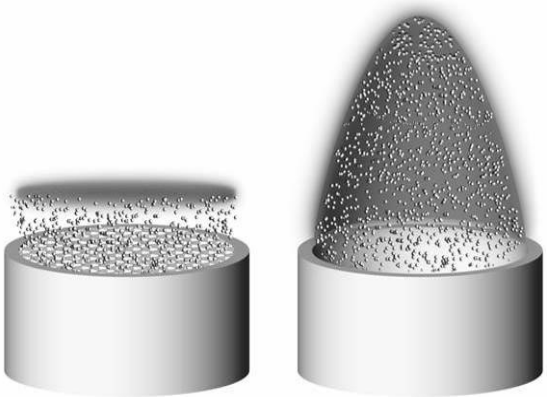

Figure 4-9. Representations of Aerosol Suppressed Premixed Flames: (left) Ideal Mist Inhibited Flat Flame as Simulated in 1-D Modeling; (right) Bunsen-type Flame Typically Studied Experimentally.

The air/fuel flow in a premixed Bunsen-type flame, shown on the right, can be fairly easily seeded with aerosols. The figure shows introduction of the aerosol which are seeded into the premixed gases. This is the experimental flame more typically studied with aerosols.

The laminar burning velocity is a fundamental property of a flammable gas mixture and is frequently used as an indicator of the effectiveness of an inhibiting agent.[76] There are various methods to measure laminar burning velocity.[77] Each method involves recording some aspect related to the burning region. The visible flame emission can be converted into a total burning surface area as can schlieren images of density gradients in the flame region due to regions of varying temperature. Both have been used to quantify the burning velocity. Although each gives a slightly different absolute surface area, they provide the same information when comparing suppressed flames to the unsuppressed flame. Ratio comparison minimizes systematic differences between various methods for burning surface derivation.

4.4.3 Non-premixed Flames

Counterflow

The counterflow or opposed flow flame configuration provides an excellent experimental and modeling arrangement to study the effects of aerosols on a flame and the effects of high temperature environments on the aerosol.[64,78 79] This configuration has been used to study the effect of aerosols on premixed flames by using two opposing premixed fuel and oxidizer flows.[64] Advantages of the counterflow arrangement include the ability to investigate variable flow residence times and potentially to separate chemical from physical effects.

The counterflow flame configuration is depicted schematically in Figure 4-10. The delivery tubes can be converging nozzles or straight tubes. The counterflow burner can be used to study gaseous and aerosol agents. In the non-premixed mode, fuel is introduced through one inlet and oxidizer though the other.

Non-premixed flames of hydrocarbon fuels in air burn near the fuel/air stagnation plane in a region that contains the stoichiometric composition for complete combustion. For hydrocarbon fuels, the flame resides on the air side of the stagnation plane, as depicted in Figure 4-10. The fuel can enter from the top or bottom for non-premixed flames, with air introduced from the opposite tube. The aerosol can be added to either the fuel or the air. Air side introduction of the aerosol is relevant to total flooding fire suppression scenarios and is the configuration most often studied. Transport and composition dependent suppression effects can be studied by comparing extinction results of air-introduced aerosols with results obtained when the aerosol is introduced into the fuel.

Representative centerline temperature and axial velocity profiles are indicated, as is the strain rate, a, the maximum gradient in the axial velocity on the air side of the flame. In this flow field, stable flames can be maintained if sufficient amounts of heat and flame radicals generated from the combustion process can be conducted to the unreacted fuel and air as they flow into the reaction zone. Extinction occurs when the flow is too fast to maintain the flame. Under these conditions, the flame strain rate exceeds a critical value referred to as the *extinction strain rate*. Suppression agents lower the extinction strain rate and this reduction is a direct measure of the suppression effectiveness. The flame strain rate can be estimated from the global strain rate.[80] Since the global strain rate can vary between burner designs, the local strain rate, determined by experimentally measuring the local velocity field, is used for absolute comparisons.

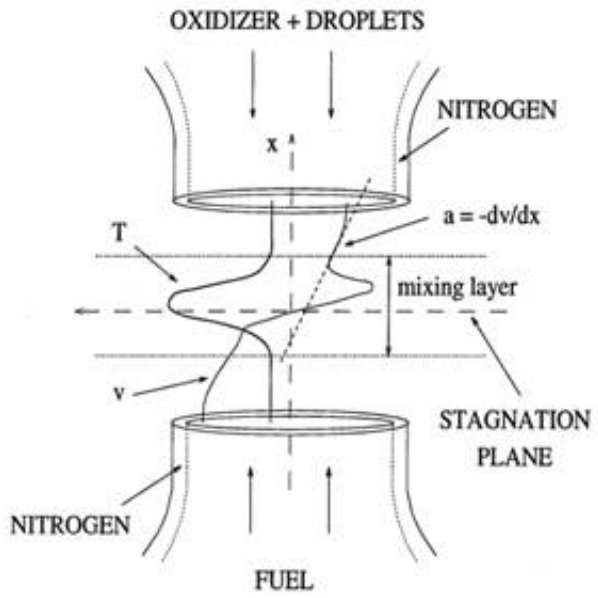

Figure 4-10. Experimental Schematic for Studying the Effects of Aerosols on the Extinction Strain Rate of Counterflow Non-Premixed Flames.[81]

The reciprocal of the strain rate can be used to estimate a characteristic residence time for an aerosol particle in this flow field. Depending on burner design, the local strain rate can range from ~ 10 s^{-1} to the value for extinction in the absence of any inhibitor (~ 600 s^{-1} for propane/air flames). Thus, the particle residence time can be varied by an order of magnitude. Chen et al.[64] note that for certain conditions the aerosol particles can often be trapped and oscillate in the opposing streams, thereby increasing their effective residence times.

Another design for studying suppression of non-premixed flames in opposed flow is the Tsuji burner.[41] Gaseous fuel is introduced through a porous tube perpendicular to the air flow as seen in Figure 4-11. NIST incorporated a variant of this design to develop a suitable NGP screening test for condensed phase agents.[82] Details of that work can be found in Chapter 8.

In the Tsuji configuration, flames can be established in the forward, stagnation region or downstream of the air flow in the fuel tube wake. In the forward direction, the two-dimensional flames are very stable and can be accessed readily with various diagnostic probes. The Tsuji flame established in this flow field also lends itself to modeling. Since the fuel and oxidizer flows can be independently controlled, flame strain rate can also be easily varied and studied. The air stream velocity required to blow-off the forward, stagnation flame is used to evaluate suppressant effectiveness.

In the Tsuji configuration, as in the premixed and opposed flow configurations introduced above, aerosols introduced with the air stream (or their decomposition products) are restricted to enter the flame. This flow arrangement assures the optimum effectiveness for the added agent. Aerosol particles that are too large to completely evaporate or decompose in the flame could potentially collide with the porous fuel tube, requiring periodic tube cleaning or replacement.

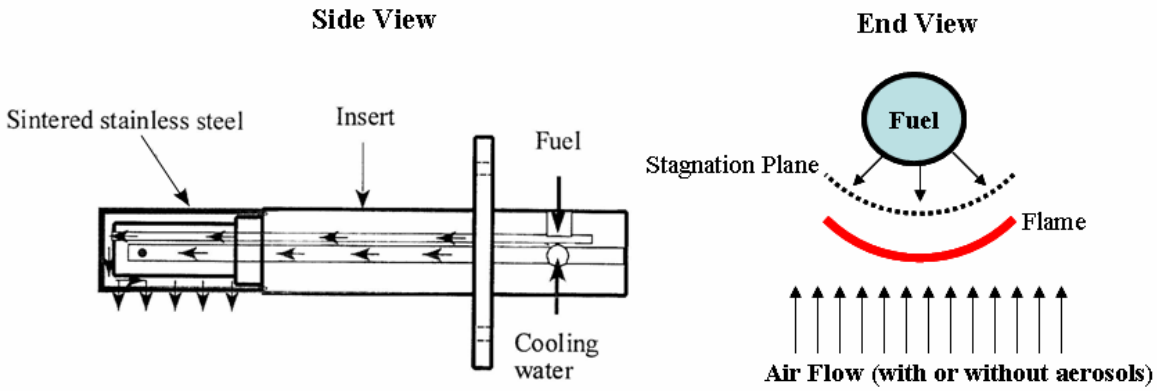

Figure 4-11. Schematic of Tsuji Burner (left[41]) and Flame Configuration (right).

Cup Burner Co-flow Flames

Cup burner flame extinction results are commonly used in the fire protection industry for suppression agent effectiveness ranking as well as for suppression system design guidance. The cup burner flame is a non-premixed flame stabilized on a cylindrical cup that holds liquid fuel or delivers a low-velocity gas jet. A surrounding laminar co-flow of air carries the suppression agent of interest.[83] The majority of the agents studied have been gaseous.

Cup burner flames have many similarities to real fires: initial separation of reactants, flame flickering, and regions of varying strain rates. These similarities make cup burner extinction results useful for suppression agent ranking and for evaluating extinction requirements in real fire scenarios. These similarities also make the cup burner flames challenging for studying aerosol suppressants. Nonetheless, researchers had investigated the suppression behavior and effectiveness of condensed-phase particles in cup burner flames prior to the NGP. (See the work of Hamins et al.[20,21])

A cup burner apparatus modified to study the suppression properties of water mist is shown in Figure 4-12.[84] Water droplet entrainment and flow conditioning occur in the lower section, water quantification occurs in the middle section, and the flame is located in the uppermost section.

Under the NGP, Linteris et al. studied the effects of various metallic compounds on cup burner flames. Several of the metallic compounds were found to be less effective than expected, surprisingly less effective compared to their performance in premixed or opposed flow flames. Even though the agents are introduced in the gas phase, their poor fire suppression effectiveness has been attributed to the formation of condensed phase particles in the cup burner flow field. Details of that work are presented in Chapter 3.

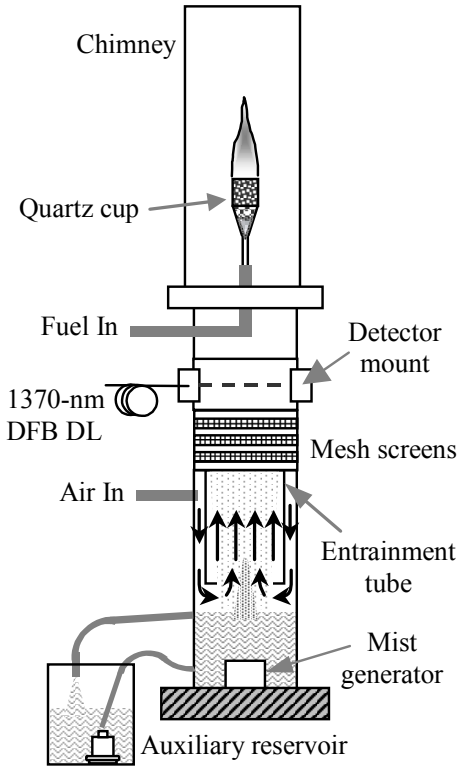

Figure 4-12. Cup Burner Apparatus Modified for Water Mist Suppression Studies. [84]

4.5 AEROSOL FLAME SUPPRESSION STUDIES

4.5.1 Water, a Physical Suppression Agent

Water Mist Studies in Premixed Flames

Experimental

NGP researchers at NRL studied the flame suppression properties of water mist as a function of droplet size, measuring the effectiveness of the mist on reducing the burning velocity of methane/air flames.[85] Mists were generated using various methods. Droplets smaller than 1 μm in diameter were generated using a venturi-based nebulizer (TSI Model 3076). A schematic of the nebulizer is shown in Figure 4-13. Pressurized air, flowing through a small orifice, produced a high velocity air jet. The resulting pressure drop drew liquid from a reservoir through a small tube and entrained it in the air jet, breaking the liquid into drops. Larger droplets impacted the nebulizer wall and returned to the reservoir. Droplets small enough to remain entrained in the air flow were carried from the nebulizer. The amount of mist exiting the nebulizer was determined by measuring the change in mass of the liquid reservoir with time for a fixed air flow. Mists of polydisperse droplets in the range of 1 μm to 20 μm were produced using a second venturi-based nebulizer (Airlife Nebulizer with Air Entrainment and Heater Adapter), requiring a minimum air flow of ≈ 2.9 L/min to generate drops.

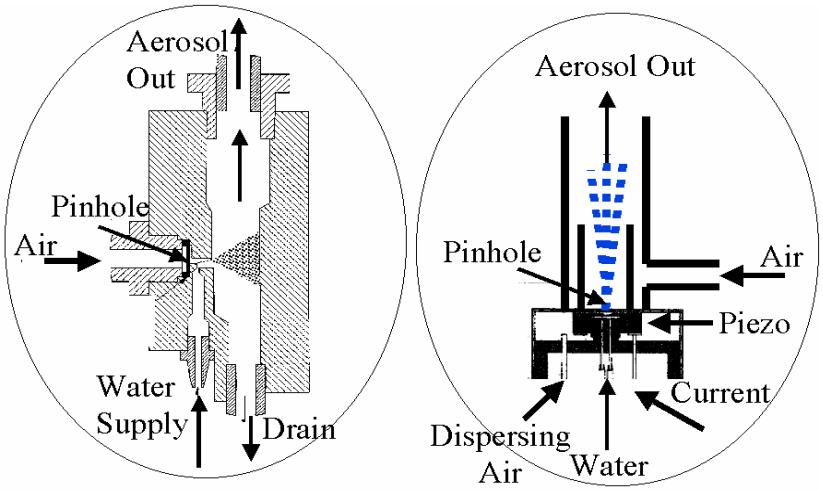

Figure 4-13. Schematic of Water Aerosol Generation Methods. (left) Venturi-Based Atomizer For Generation Of Sub-Micron Diameter Water Drops; (right) Vibrating Orifice Aerosol Generator for Generating Monodisperse Water Droplets > 15 μm Diameter.

Monodisperse droplets of larger size (> 15 μm diameter) were generated using a vibrating orifice aerosol generator (VOAG, TSI Inc. Model 3450). A schematic of the droplet generator is shown in Figure 4-13 (left). To generate the mist, liquid was forced through a pinhole using either a syringe pump or a plastic bag under pressure. Limited control over the liquid flow was accomplished using either method. The size of the pinhole ultimately determined how much liquid could be delivered to the burner. The pinhole was acoustically excited by a piezoelectric ceramic driven at specific frequencies to break up the liquid jet into a stream of extremely monodisperse drops. The droplet size depended on the pinhole diameter, the liquid flow, the forcing frequency, and the liquid properties. A dispersion cap was used to distribute the droplet stream uniformly into a three-dimensional mist. This sacrificed some of the size monodispersity as shown in Figure 4-14 for the three water mists that were studied. In the absence of the dispersion cap and dispersing air, all droplets occupied a single PDPA size bin.

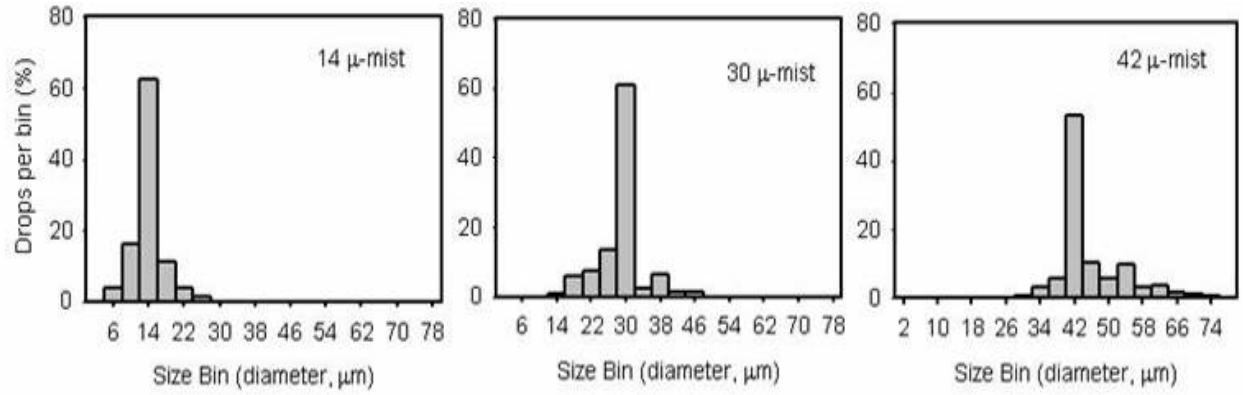

Figure 4-14. PDPA-determined Droplet Diameter Histogram 2 mm above the Air Tube Exit for Three Water Mists.[85]

Droplet size, velocity, and number density for droplets greater than ≈ 2 μm in diameter were measured using a phase Doppler interferometry system (Phase Doppler Particle Anemometer – PDPA, Dantec Measurement Technology). For droplets smaller than ≈ 1 μm diameter, water concentration in the

reactant stream was monitored by 90° scattering of a Helium-Neon laser at a wavelength of 0.6328 μm as shown in Figure 4-15. The scattered laser light was detected with a photomultiplier tube (PMT) using a narrow-line optical filter. The laser beam was modulated at 1 kHz by passing the beam through a rotating slotted wheel. The laser beam was positioned just above the burner exit. A reference beam was split off just before the burner and monitored by a photodiode. The scattered and reference signals were processed with a lock-in amplifier (EG&G Instruments, Model 7265 DSP) and integrated over a period of 0.5 s. The scattering intensity was calibrated to a mist delivery rate by correlating the scattering signal with the change in water mass of the reservoir.

The total flame surface area derived by visible flame imaging was used to quantify the reduction in burning velocity as a function of added mist for suppressed premixed conical flames. A schematic of the arrangement is shown in Figure 4-15.

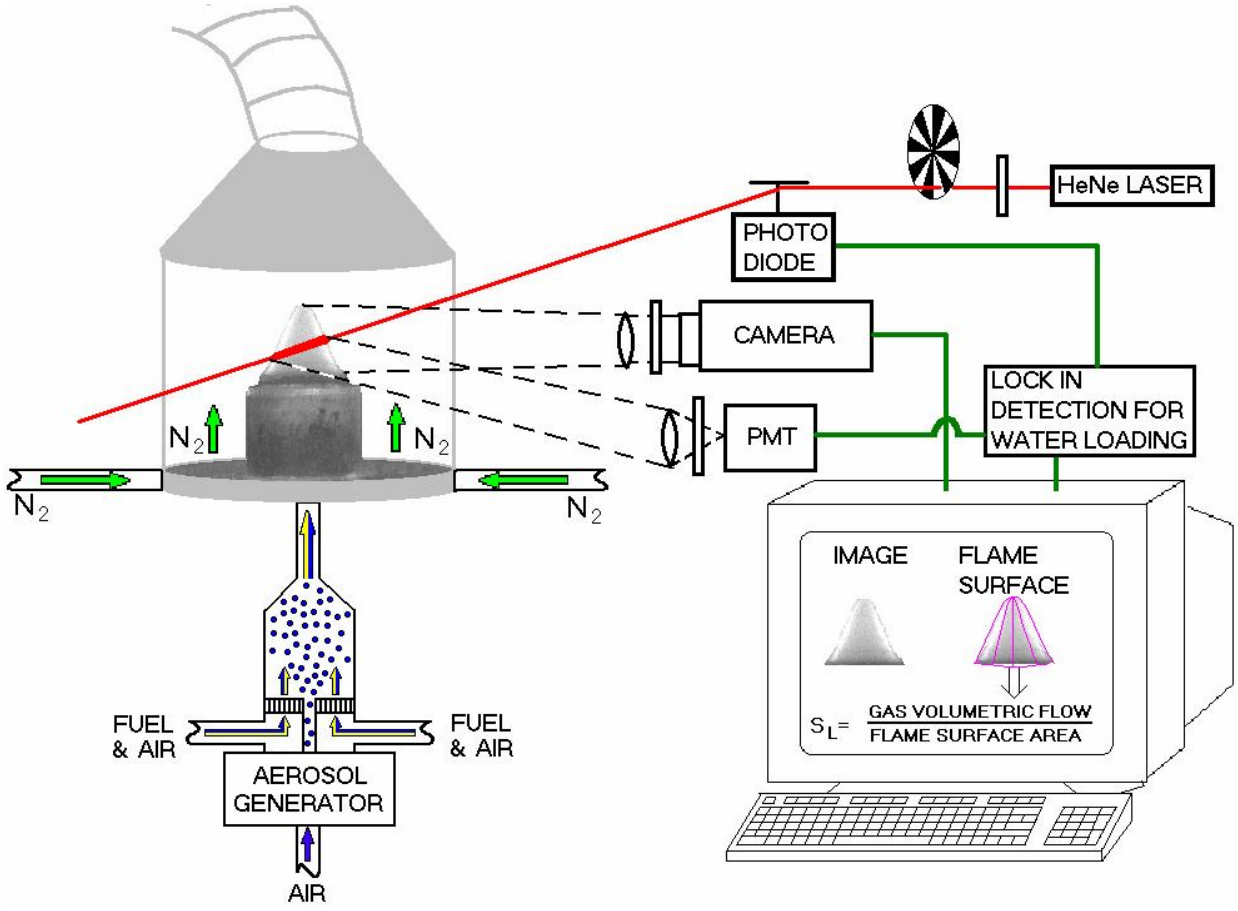

Figure 4-15. Schematic for Liquid Aerosol Inhibited Burning Velocity Determination in Premixed Flames.[75]

The burner was a converging nozzle with an exit diameter of 1.0 cm. An entrainment device to straighten the flow and uniformly seed droplets in the premixed gas flow utilized a perforated disk. The sub-micron size mist droplets were small enough to pass through the ≈ 0.16 cm diameter perforation holes. Larger droplets (> 5 μm diameter) were introduced through an opening in the middle of the perforated disk. The burner was enclosed inside a 13 cm diameter inner diameter acrylic tube that allowed optical access to the

flame. The acrylic chamber was vented to an exhaust hood through a conical metal covering open at the top. A nitrogen flow of approximately 3 L/min was introduced through a sintered disk in the bottom of the chamber. This purged the chamber of excess oxygen and product gases. Flame images were recorded using a CCD camera and a value for the total flame surface was determined by fitting the shape and then mathematically generating a three dimensional surface. Burning velocities were determined by comparing the total flame surface to the volumetric flow of gases in the burner. Light from a modulated He-Ne laser, scattered from the aerosol in the premixed flow and detected with a lock-in detector, was used to determine the amount of water aerosol in the form of small droplets introduced into the flame. PDPA was used to quantify the water concentration for mists of larger drops.

Burning velocities for the inhibited flames were reported relative to the uninhibited burning velocity, thereby minimizing systematic errors in determining an absolute value for the burning velocity. Relative values derived from schlieren images for some of the flames were in good agreement with values derived from the visible flame surface. The presence of the aerosol reduced the flame burning velocity, which resulted in a taller flame with a larger flame surface area for a fixed fuel-air flow. To minimize any systematic effects due to varying flame height, fuel and air flows were adjusted to maintain a stoichiometric mixture and a flame height of 1.0 cm ± 0.15 cm. The measured burning velocities of nitrogen-inhibited flames were found to be insensitive to flame height over this range.

Modeling

Both theoretical[86,87] and computational[88,89] models have been developed to predict premixed flame structure and extinction characteristics as a function of water-mist properties. NGP modeling of sub-micron mists in premixed flames was done in collaboration with Prof. Robert Kee at the Colorado School of Mines. The suppression effects of gas-phase agents were modeled using PREMIX[90] and OPPDIFF.[91] The chemical reaction mechanism and the associated thermodynamic and transport properties were taken from GRI-Mech 3.0,[92] but with the nitrogen chemistry removed. The inhibition effects of water aerosols on premixed flames were calculated using a multiphase combustion model.[89] The multi-phase model solves the conservation equations for mass, momentum, and energy for the water droplets within a Lagrangian framework. One-dimensional conservation equations in an Eulerian framework were used to solve the physics of the gas-phase flame propagation. Coupling of the two phases was achieved through addition of drop-evaporation related source terms in the PREMIX software. Boundary conditions for the drop-evaporation dynamics were obtained from the PREMIX solution.

Figure 4-16 illustrates the predicted dependence of the burning velocity on droplet size and water loading.[89] For small drops, the burning velocity decreases monotonically as a function of water loading. For sufficiently small drops, the burning velocity becomes independent of droplet size but still depends on water loading. For stoichiometric, methane-air, premixed flames, this small-droplet limit is achieved for a droplet diameter of approximately 10 μm.[89]

Results and Discussion

Figure 4-17(a) shows the image of a premixed methane-air flame with no mist. Figure 4-17(b) shows mist of nominal 0.3 μm drops as they exit the burner nozzle in the absence of the flame. The drops are illuminated with a doubled Nd:YAG laser sheet. In Figure 4-17(c), both the illuminated drops and the flame image are shown although no mist drops are observed leaving the visible flame zone. The inhibition effect of this mist on the flame normalized burning velocity is plotted in Figure 4-18. Details

of the experiment and results are reported in Reference 93 Also shown are the inhibition effect of N_2, CF_4, and CF_3Br. The CF_3Br data are modeling results considering full chemistry.[76,94] On a mass basis, the inhibition effectiveness of water mist was comparable to that of CF_3Br.

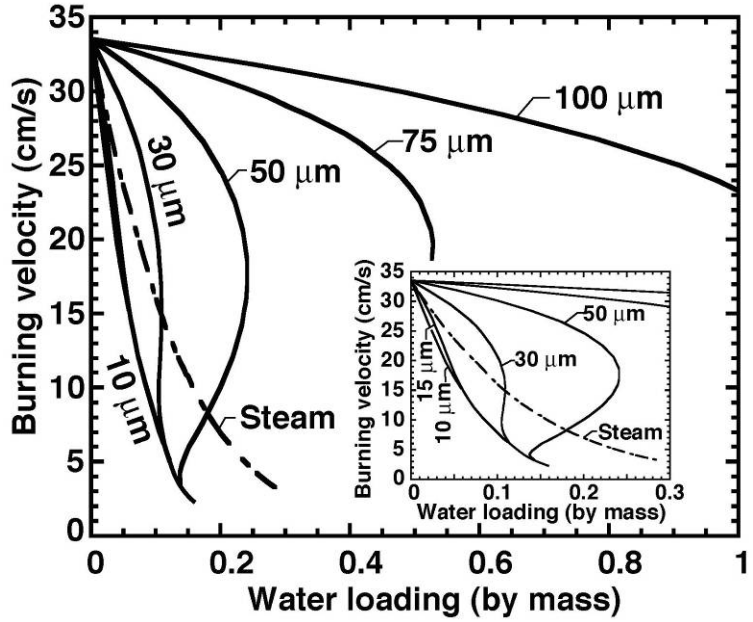

Figure 4-16. Predicted Burning Velocity for a Stoichiometric, Premixed, Methane-air Flame as a Function of Initial Droplet Diameter and Water Mass Loading. (Reference 90)[89]

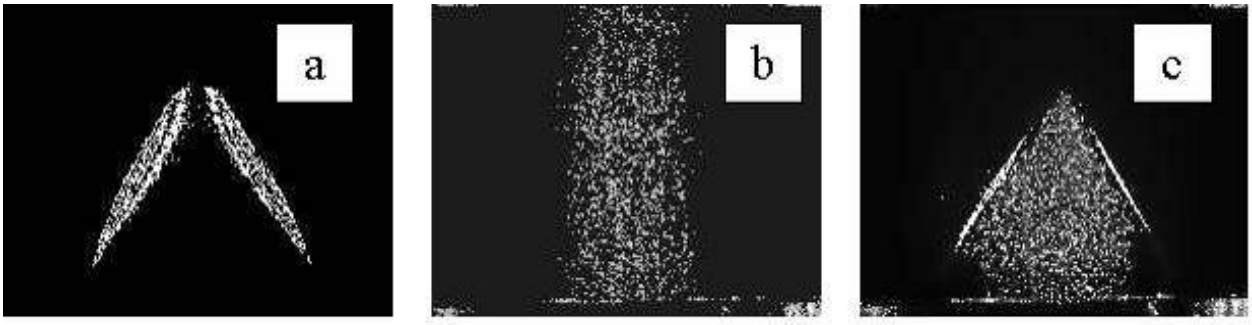

Figure 4-17. (a) Image of Premixed Methane-air Flame Stabilized on Burner; (b) Image of Water Mist (no flame) as it Exits the Burner; (c) Image of Laser-illuminated Water Mist and Methane-air Flame Showing Disappearance of the Mist at the Flame Boundary. (Reference 93)

A summary of an evaluation of the thermodynamic properties of the agents investigated in Figure 4-18 is listed in Table 4–2. Columns 2 and 3 list the sensible enthalpy, per unit mass and per mole, respectively, required to raise the temperature of each agent from 300 K to 1600 K.[95] On a mass basis, N_2 and CF_4 should contribute similarly to the inhibition. The sensible enthalpy for water mist, including the heat of vaporization at 101 kPa (1 atm), is almost twice that of water vapor and 3.5 times higher than for the same mass of N_2 or CF_4. These predictions are consistent with the experimental observations. The mass of inhibitor required to reduce the burning velocity by a fixed amount (20 % was chosen here) is listed in Column 4 and the molar amount in Column 5.

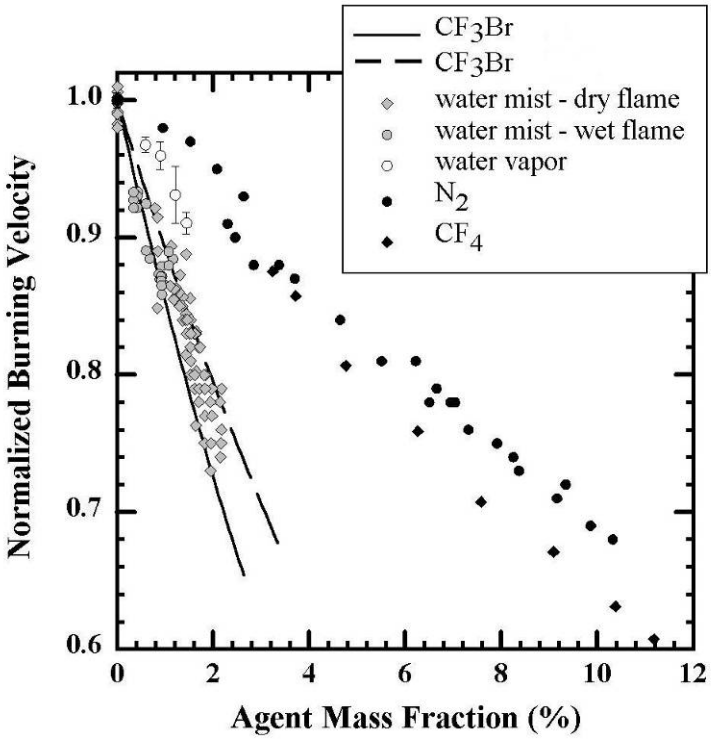

Figure 4-18. Normalized Burning Velocity Reduction vs. Mass of Added Inhibitor for an Inhibited Methane-Air Premixed Flame. (Reference 93)

The mass of liquid water needed to reduce the burning velocity by 20 % is one-third that required for N_2 or CF_4, which is in good agreement with the thermodynamic estimate. The value for water is comparable to published measurements for CF_3Br. Thus, small water droplets acting thermally exhibit a comparable effectiveness on a mass basis in premixed flames as CF_3Br with its chemical effect. Modeling prediction of the small-droplet limiting behavior is presented in Figure 4-19 along with the experimental results of Figure 4-18. The sub-micron mist inhibition results are in excellent agreement with modeling predictions of Yang and Kee, requiring no adjustable parameters.[93] Water vapor was both observed and predicted to be less effective than water aerosols of droplet diameters smaller than ≈ 15 μm. An increase in the effectiveness of liquid water is predicted as the droplet size is reduced to ≈ 10 μm. Below this size limit, no increase in suppression effectiveness with decreasing droplet size is predicted. This limiting droplet size correlates with those droplets that completely evaporate in this flow field and is consistent with the observations in Figure 4-17.

Table 4–2. Thermodynamic Quantities for Physical Suppressants Compared to CF_3Br.

Agent	$(H_f^{1600K} - H_f^{300K})^a$		Mass Fraction to Reduce Burning Velocity by 20 %	Mole Fraction to Reduce Burning Velocity by 20 %
	kJ/g	kJ/mol		
N_2	1.5	42	0.063 ± 0.004	0.062 ± 0.004
CF_4	1.4	122	0.055 ± 0.004	0.019 ± 0.002
H_2O (vapor)	2.9	53	0.033 ± 0.002	0.050 ± 0.003
H_2O (mist)	5.2	93	0.017 ± 0.001	0.026 ± 0.002
CF_3Br	0.85	126	0.019 [b]	0.004 [b]

[a] Calculated from data in Chase et al.[95]
[b] Data from Noto et al.[96]

PDPA measurements for larger droplets as a function of position above the burner were recorded for the methane-air premixed flame: diameter vs. position are shown in Figure 4-20(a) and number density vs. position in Figure 4-20(b). Droplets larger than 27 μm in diameter (generated using the VOAG) were reasonably monodisperse and survived travel through this flame (peak temperature ≈ 2100 K, determined using a radiation-corrected, coated Pt/Pt-Rh thermocouple). The smaller droplets generated with a nebulizer (average diameter 6 μm, Dv0.9 < 10 μm) completely evaporated at the flame front. Thus, the experimental droplet size for onset of complete evaporation in this flame is between 6 μm and 27 μm. These measurements are consistent with the predicted nominal 10 μm limiting droplet size of the multi-phase model.

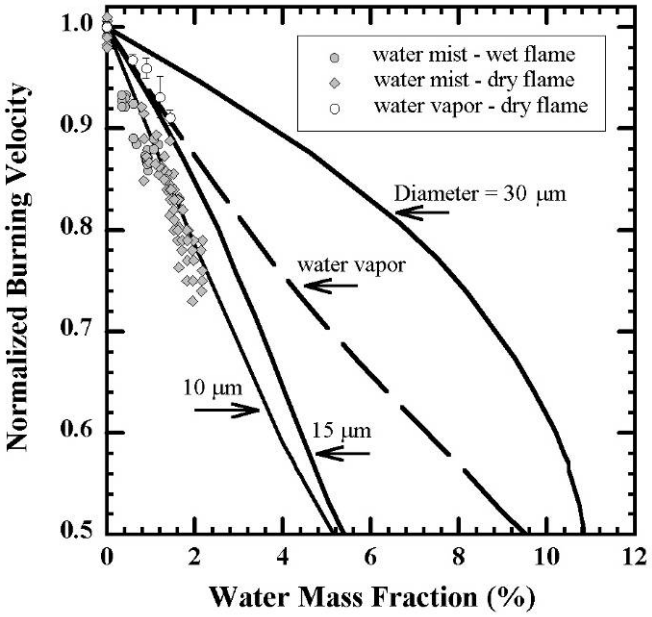

Figure 4-19. Premixed Methane-air Burning Velocity as a Function of Agent Mass Fraction, Normalized by the Uninhibited Burning Velocity. Water data from Figure 4-18 (symbols), multiphase flame modeling results for humidified flames inhibited with mists of indicated drop size (solid lines), and PREMIX modeling results for humidified flames inhibited with additional water vapor (dashed line).[93]

Modeling predictions for the experimental conditions presented in Figure 4-20 are shown in Figure 4-21. Droplet size vs. position is shown in Figure 4-21a, and relative droplet number density vs. position is shown in Figure 4-21b. The water mass fraction is 0.05. (The 0 mm position is the 300 K left boundary for the freely propagating flame solution.) Droplet size behavior is in reasonable agreement in the post flame region. However, the experimental droplet number density decay rates are much slower than the model predicts; note that the distance plotted in Figure 4-20b is four times that of Figure 4-21b. The source of the difference lies in the different residence times of the droplets in the flame. In the experiments, droplets are traveling at the same speed as the gas phase, about 140 cm/s. In the one-dimensional, freely propagating flame model, droplets also travel at the same speed as the gas phase, but this is about 30 cm/s. Thus, the prediction of a higher evaporation rate (shorter evaporation time) for the longer residence time in the model is consistent. Experiments to quantify the effect of larger droplets on the burning velocity are needed.

The model predicts a turning-point behavior for the effect of moderate and larger sized droplets (above 25 μm for stoichiometric, premixed, methane flames) on burning velocity as seen in Figure 4-16. At the turning point, the derivative of burning velocity with respect to the water mass loading is infinite. Turning points are caused by the droplet dynamics within the flame. Specifically, longer droplet residence time in a suppressed flame causes further increase of efficiency in flame suppression. Mathematically, at a turning point, an infinitesimally small increase of water mass loading causes the

burning velocity to fall to the lower branch of the suppression curve. Such very-low-burning-velocity branches are experimentally not achievable due to the various heat-loss mechanisms that would prevent these flames from stabilizing. Therefore, it may be safe to interpret such turning points as flame extinction points.

The theoretical and computational analyses predict that the burning-velocity curves join together in the lower-burning-velocity region. This behavior can be attributed to a greater droplet residence time in the slow-burning flames. If the burning velocity is sufficiently low, any droplet can totally evaporate within the flame, leading to equivalent efficiency for flame suppression.

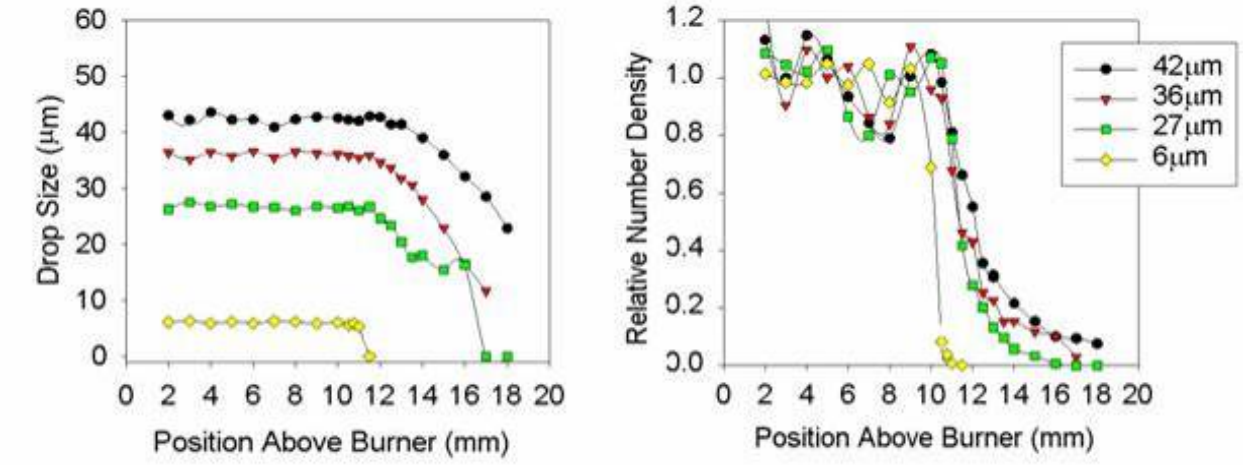

Figure 4-20. Experimental Measurements of Water Droplet Diameter and Number Density in a Stoichiometric Premixed Methane-air Flame as a Function of Height above the Burner Exit.[75]

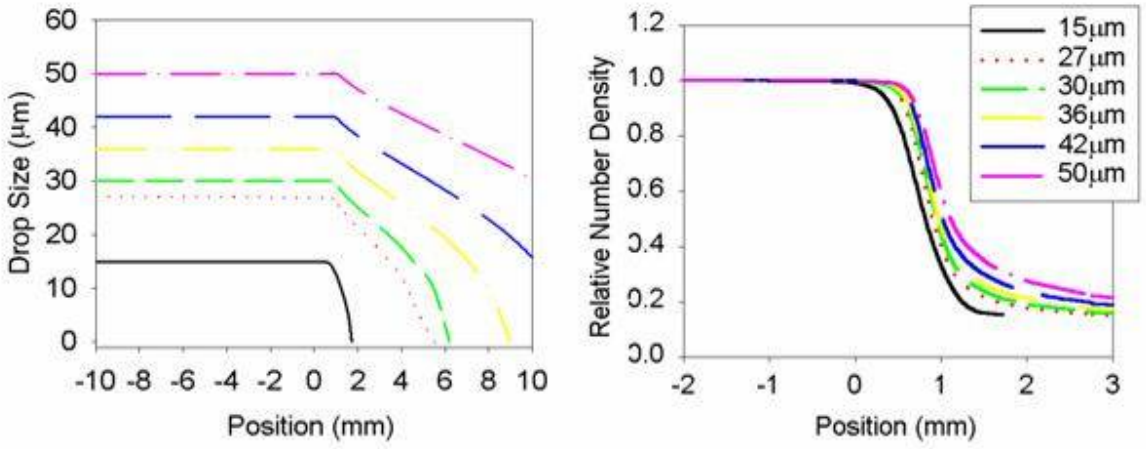

Figure 4-21. Multi-phase Predictions of Water Mist Droplet Diameter and Number Density in a Stoichiometric Premixed Methane-air Flame.[75]

The turning points predicted for larger droplets seen in Figure 4-16 can be important in fire suppression. Unfortunately, no direct observation or measurement of such behavior for inhibited premixed flames has been reported. The challenges to realizing such experiments include the generation of the monodisperse mists, the high water-mass loading required at turning points, and controlling the non-ideal conditions such as buoyancy and heat loss to the environment. Experiments that focus on the inhibition effects of larger droplets are needed.

Understanding the inhibited flame structure and droplet dynamics provided considerable insight into the mechanisms of flame suppression. The computational model predicted temperature, species concentration, number density, and droplet history profiles throughout the flame. These variables represent the underlying factors that control the overall burning velocity. Therefore, detailed measurements of flame structure were extraordinarily valuable. Unfortunately, both creating the flame and developing the required diagnostics are significant challenges. For these studies, flame structure, burning velocity, and extinction characteristics were modeled as an ideal flat flame. The experiment was a Bunsen-like configuration that allowed droplets to be introduced through the open tube. The burning velocity in these flames was inferred from analysis of the flame area. In addition, flame profile data were measured, for example, on the centerline. This configuration and modeling approach are valid for sub-micron droplets that fully evaporate prior to entering the flame. However, for larger droplets or particles, data from such experiments cannot be compared directly to one-dimensional flat-flame models. The gas and particle/droplet velocities, for example, were much greater in the Bunsen-like flame. It appears that there are two choices for modeling the inhibition effect of larger particles/droplets in premixed flames: configure a "flat" premixed, burner-stabilized flame that can be seeded with large water particles/drops, or directly model the three-dimensional Bunsen-like flame. The success of uniformly seeding particles/droplets into a flat flame is highly unlikely considering the particle/droplet sizes to be studied. Success seems more likely for alternative modeling approaches. This area is one that still requires further development.

Modeling of Counterflow, Non-premixed Flames[i]

One of the NGP objectives was to understand the trajectories of condensed-phase, monodisperse aerosols in a reacting counterflow field and investigate their effect on the flame extinction condition. Several modeling approaches were explored to aid in the understanding of the observed suppression behavior. One publicly available code advertised as capable of modeling suppression of counterflow flames by aerosols is RUN-1DL (Rogg and Wang, Cambridge, England). Available documentation on the treatment of droplets was very sparse. The code as delivered only treated a single droplet stream and was not immediately capable of modeling flame conditions involving an ensemble of water drops. Further development and code modification to model the range of NGP experimental conditions were deemed too time consuming in light of the limited documentation.

PHOENICS (CHAM, London), a finite volume code for calculating fluid flow, was also considered for modeling the interaction of droplets in the counterflow flame. NRL staff had previously used this to model the flow field in this counterflow burner.[97] PHOENICS was configured to treat the full flame chemistry. Stable gas-phase flames could be modeled. The calculation was very sensitive to the

i The model described here was developed and predictions made before much of the experimental data was available. Subsequent experimental work presented later in this chapter benefited greatly from the modeling studies. The experimental studies in large part validated the modeling approach and subsequent predictions.

inclusion of the aerosol/flame interaction due to the time and spatial scale dynamic ranges. Further development and code modification were not pursued as part of this project.

Chelliah and co-workers at the University of Virginia developed a two-phase hybrid Eulerian–Lagrangian formulation for treating the interaction of droplets and counterflow non-premixed flames.[80,98,99] The details of the hybrid Eulerian-Lagrangian formulation and the solution algorithm developed to predict the interaction between water mist and a laminar counterflow flame are described in Reference 80. The model predictions were validated against experimental non-premixed counterflow flame extinction conditions and low-pressure flame structure data for both propane and methane flames, as well as indirect comparison to experimental methane-air burning velocity results.[100] A reduced chemical kinetic mechanism was used, which was derived from a much more comprehensive one proposed by Wang and co-workers.[101,102] The Wang mechanism had been validated based on global flame propagation/extinction experiments and flame structure measurements for a variety of fuels.[101] For water mist suppression of propane or methane counterflow flames, extinction strain rate predictions using both mechanisms agreeded within 5 s^{-1}. Both mechanisms predicted a non-premixed propane-air flame extinction strain rate of ≈ 580 s^{-1}, in excellent agreement with the experimental measurements.

For the model, water droplets were introduced into the air stream. The water droplet loadings were small, i.e., the mass of liquid water was less than 3 % of the air flow. Thus, the ratio of droplet separation distance to droplet diameter was greater than 20, and collisional effects between droplets were neglected. The reduced gas-phase chemical kinetics mechanism involed 17 species and 39 elementary reactions with variable thermochemical and transport data. The discretized gas phase equations were solved using an algorithm that includes Newton and fixed point iteration steps.

The flow configuration was shown earlier in Figure 4-10. When ignited, a steady laminar flame was established within the mixing layer. The exit velocity profiles of both air and fuel streams were assumed to be of the plug flow type. The droplets were introduced though the upper nozzle at a steady rate with the air stream and were assumed to be monodisperse. Droplet velocities at the nozzle exit were assumed to be the same as that of air. (For the two-phase system considered here, the gas velocity can differ from that of droplets.) The response of droplet trajectories for different flow strain rates was addressed by varying the nozzle exit velocities of methane and air streams. For plug flow boundary conditions (corresponding to viscous, rotational flow formulation), the flow strain rate, a, is defined as the negative of the axial velocity gradient of the gas in the air side (i.e., 2dv/dx), just outside the mixing layer (Figure 4-10). At flame extinction, the critical value of the flow strain rate was identified here as a_{ext}. In the experiments, the outer air flow was known to deviate slightly from the plug flow boundary conditions,[103] but explicit detailed laser Doppler velocimetry data at the boundary can be easily implemented in the model.

Effect of Water Vapor on Flame Extinction

In a real-life fire situation, or in laboratory experiments, when water droplets are introduced into a dry air stream, there will be some evaporation. Consequently, the fraction of oxygen displaced (or diluted) by the water vapor can reduce the flame strength, or the extinction strain rate, a_{ext}, of the counterflow flame considered here. Figure 4-22 shows a comparison of the predicted variation of maximum flame temperature, T_{max}, for a methane-air flame as a function of the flow strain rate, a, for some selected water vapor concentrations. The circle symbol corresponds to a dry case, whereas the star symbol correspond to a fully saturated case at a room temperature of 300 K and atmospheric pressure (i.e., partial pressure of

water $p_{H2O,sat}$ = 0.0351 atm or, in mass fractions, $Y_{H2O,u}$ = 0.0222, with $Y_{O2,u}$ = 0.2278 and $Y_{N2,u}$ = 0.7500). Based on this figure, if the asymptotic value of highest strain rate for each case is taken as the extinction strain rate, a_{ext}, then the results indicate that saturated water vapor alone can decrease the flame extinction strain rate by 25 %. This enhanced effect is not solely due to dilution, but is partly due to the high thermal capacity of water.

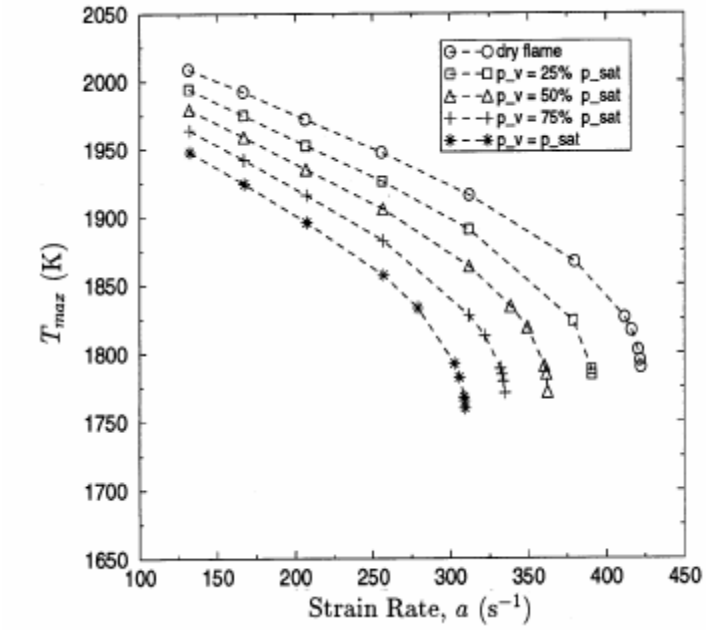

Figure 4-22. Predicted Comparison of the Maximum Flame Temperature, T_{max}, vs. Flow Strain Rate, a, for a Dry Flame and for Four Flames with Different Inflow Water Vapor Partial Pressures.[80]

Dynamics of Water Droplets without Interaction

If the amount of water being injected into the air stream is greater than $p_{H2O,sat}$ = 0.0351 atm (or Y_{H2O} > 0.0222), then the excess water will be in condensed form, i.e., in the form of droplets. The mass fraction of water associated with such droplets leaving the air nozzle can be defined using

$$Y_0 = \frac{m_{d0} n_{d0} v_{d0}}{m_{d0} n_{d0} v_{d0} + \rho_u v_u} \tag{4-7}$$

where m_{d0} is the initial mass of the droplet, n_{d0} the initial number density, v_{d0} the initial velocity of the droplet, and ρ_u and v_u are the density and velocity of air leaving the nozzle, respectively. All the results shown here are obtained by assuming that the droplet velocity leaving the air nozzle is same as that of the gas, i.e., $v_{d0} \equiv v_u$, but other inflow conditions can be easily analyzed with the model as developed.

Various monodisperse water mists for three different fixed water mass fractions in air (Y_0 = 0.01, 0.02, and 0.03) were considered. Table 4–3 shows the number density of water droplets leaving the air nozzle, n_0 (number/cm^3), for three different values of Y_0 and for the three different monodisperse droplet sizes selected.

For all the combinations of water mass fraction in condensed phase and droplet sizes, the ratio of droplet separation length to the droplet diameter, l_0/d, was fairly large (>20) and was of uniform order. It was thus reasonable to neglect droplet–droplet interactions for all the cases considered. Further justification is

presented below.[ii] For dilutely loaded droplets, the gas displacement by water droplets can also be neglected because of the large density ratio between the condensed water and the gas. Under such conditions, the only interaction between the droplets and the gas is from source terms due to mass, momentum and enthalpy transfer per unit volume from the droplets to the gas. (See Equations 2 through 5 in Reference 80.) When these terms are included in the numerical calculations, the flame structure and extinction strain rate are affected dramatically, depending on the amount of condensed water added and the droplet sizes. Thus, for the purpose of illustrating and comparing the trajectories of various droplet sizes in the counterflow field and their associated source terms, a fixed, low strain rate case (a = 130 s^{-1}) where the droplet source terms are excluded (or the source terms turned "off" in the numerics) is considered first. It should be mentioned here that the profiles of droplet trajectories and source terms presented below remain essentially the same for high-strain rates as well.

Table 4–3. Number Density and Droplet Separation Lengths for Some Selected Water Mass Fractions.[80]

Y_o	d (μm)	N_o (cm^{-3})	$N_o^{1/3}$ (cm^{-1})	l_o (cm)	l_o/d
0.01	5	178,000	56.3	0.0177	35
	20	2,790	14.1	0.0711	36
	50	178	5.6	0.178	35
0.02	5	360,000	71.2	0.0141	28
	20	5,630	17.8	0.0562	28
	50	360	7.1	0.141	28
0.03	5	546,000	81.7	0.0122	24
	20	8,530	20.4	0.0485	24
	50	546	8.2	0.122	24

Figure 4-23 shows a comparison of the axial velocity along the axis of symmetry of the gas and droplets of different sizes for the selected low-strain rate case. Although the coupling arising from the droplet source terms on gas-phase structure was neglected, in solving equations for droplet trajectory shown in Figure 4-23, the droplet vaporization effects were included. (See Equations 18 through 23 in Reference 80.) In Figure 4-23, the 5 μm droplets followed the gas fairly closely, whereas large droplets deviated considerably. The droplet lag became slightly worse for high-strain rates, especially near extinction conditions. The 5 μm droplets were completely vaporized soon after they entered the hot mixing layer, whereas 50 μm droplets penetrated through the flame and also the stagnation plane and then reversed their direction somewhere in the fuel stream. When the droplet vaporization was suppressed, then the penetration of 50 μm droplets became much more pronounced, with multiple crossings at the stagnation plane. These predictions are consistent with those reported earlier by Chen et al. [64]

[ii] In actual water mist systems, it is highly unlikely that the water droplets generated are monodisperse. However, the predictions performed here with monodisperse droplets provide a better mechanism to analyze and understand the basic droplet dynamics and interactions with the gas-phase processes, which can be easily extended to polydisperse droplet flows in the future.

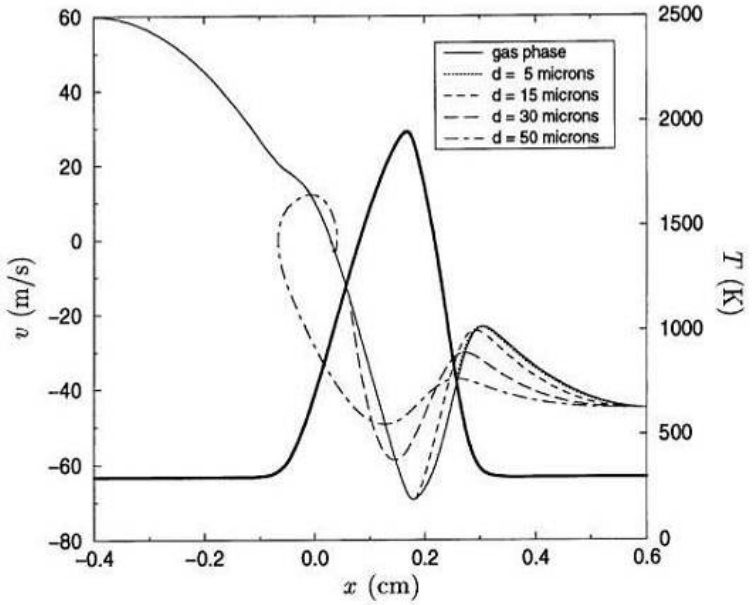

Figure 4-23. Calculated Gas Velocity, Velocities for Varied Water Droplet Diameters, and Gas Temperature (thick solid line) in a 130 s^{-1} Methane/air Flame with Droplet Source Terms turned "off."[80]

The droplet response to the variation in gas-phase flow conditions was characterized by the Stokes number, S_t. By defining the flow residence time in the outer air flow as $t_f = 1/a$, and deriving an expression for the droplet response time (t_d) based on Stokes drag, the following expression was derived for S_t:

$$S_t = \frac{18\mu}{a\rho_d d^2} \tag{4-8}$$

where μ is the gas viscosity, d is the aerodynamic diameter of the drop and ρ_d is the drop density. For the strain rate of 130 s^{-1} considered in Figure 4-23 the variation of S_t for different droplet sizes in the outer oxidizer flow is shown in Table 4–4. The 5 μm droplets have truly small S_t number, consistent with the results shown in Figure 4-23. As the droplet size approaches about 15 μm, the S_t number approaches about 0.1, indicating slower response of the droplet to the gas, as seen in Figure 4-23.

Figure 4-24 through Figure 4-26 show the variation of other variables associated with the droplet, (evaluated from Equations 20, 21, and 23 in Reference 80), along the axis of symmetry. These results were obtained under the same conditions as in Figure 4-23. Figure 4-24, for example, shows that U_d was always less than U, which is expected, as the gas was accelerating radially from the axis of symmetry and is consistent with experimental measurements of methanol droplets in a counterflow by Li et al.[104]

Figure 4-25 shows that the temperature of 5 μm droplets (T_d) followed that obtained assuming thermal equilibrium (solid line), whereas other droplets showed a small thermal lag. However, this lag had insignificant effect on the flame structure and extinction condition considering the small temperature difference and the energy associated with it. The variation of flux fraction, $\mathcal{F}$, as a function of the axial location, shown in Figure 4-26, however, played a very important role in the droplet source terms (see Equation 17 in Reference 80), and therefore the state of the flame. The reduction in $\mathcal{F}$ seen as the droplet approached the stagnation plane was because of the flow divergence or straining effect.

Table 4–4. Stokes Number (S_t) for Different Droplet Sizes for a = 130 s^{-1}.[80]

d (μm)	t_d (s^{-1})	t_f (s^{-1} x 10^2)	S_t
5	0.75 x 10^{-4}	0.77	0.0098
10	0.30 x 10^{-3}	0.77	0.039
15	0.68 x 10^{-3}	0.77	0.089
20	0.12 x 10^{-2}	0.77	0.16
25	0.19 x 10^{-2}	0.77	0.25
30	0.27 x 10^{-2}	0.77	0.35
40	0.48 x 10^{-2}	0.77	0.63
50	0.75 x 10^{-2}	0.77	0.99
60	0.108 x 10^{-1}	0.77	1.42

If the droplet vaporization were neglected, the curves shown for different droplet sizes would shift somewhat, but the dramatic reduction of $\mathcal{F}$ seen with droplet location does not change. Similar results for axial liquid methanol volume flux were observed experimentally by Li et al.[104] with and without a flame.

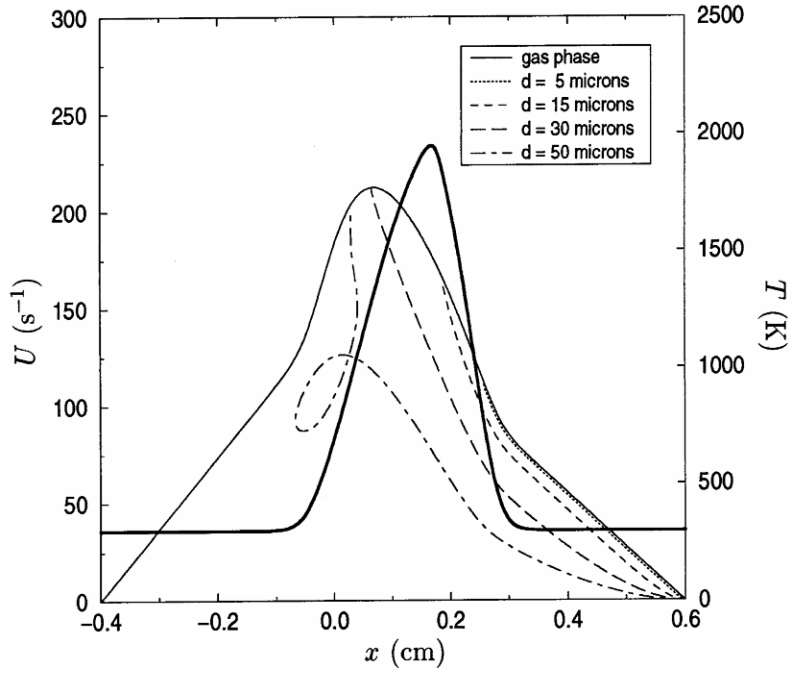

Figure 4-24. Comparison of U of Gas and U_d of Different Droplet Diameters, with Droplet Source Terms Turned "off."[80] Thick line: gas temperature.

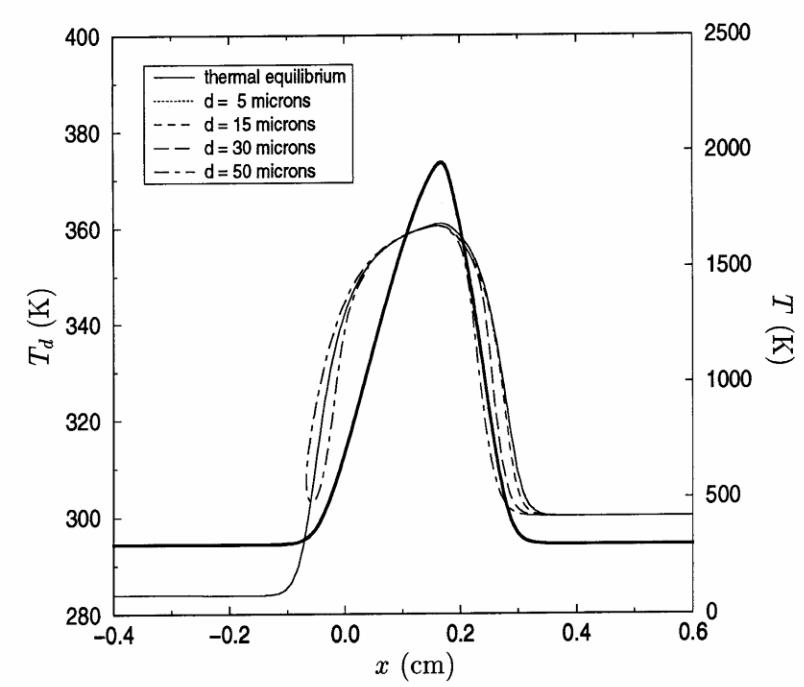

Figure 4-25. Comparison of Droplet Temperature, *Td*, of Different Droplet Diameters, with Droplet Source Terms Turned "off."[80] Thick line: gas temperature.

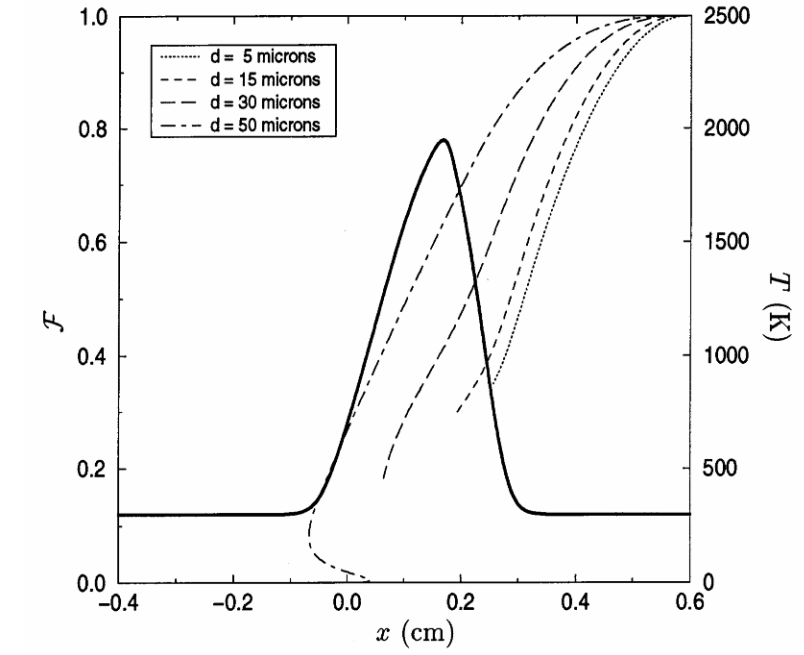

Figure 4-26. Comparison of Flux Fraction Function, $\mathcal{F}$, of Different Droplet Diameters, with Droplet Source Terms Turned "off."[80] Thick line: gas temperature.

SOURCE TERMS WITHOUT INTERACTION. Once the solution of droplet variables was obtained (i.e., d, v_d, U_d, T_d, and $\mathcal{F}$), the source terms contributing to the gas phase were evaluated. (See Equation 17 in Reference 80.) Here, such contributions were shown, once again by turning "off" the interaction of such source terms with the gas-phase calculations to keep the flame structure condition the same for

different droplet sizes considered further in the next section. Figure 4-27 through Figure 4-29 show the variation of mass, momentum, and energy source terms, i.e., S_m, S_U -US_m, and S_h 2 h_iS_m, along the axis of symmetry for different droplet sizes. Figure 4-27 shows apparently strange profiles, especially on the air side before the flame, where evaporation effects were negligible. It is seen that smaller droplets exerted a greater radial force per unit volume on the gas than larger droplets. This is, however, easily explained by the fact that larger droplets shoot through that region faster than smaller droplets, so that they have much shorter residence times. Comparison of Figure 4-28 and Figure 4-29 indicates the profiles of S_m and S_h - h_iS_m to be very similar (except for the change of the sign). This suggested that heat transfer to the droplets and evaporation were well correlated; the implications of such correlations are discussed further in the next section.

EFFECT OF WATER DROPLETS ON FLAME EXTINCTION. An important question that was probed by the two-phase model developed here was the effect of water droplets (i.e., their size and mass loading) on the flame extinction condition, with the source terms turned "on." Such effects were shown by plotting the variation of maximum flame temperature as a function of the flow strain rate, as shown in Figure 4-30. Figure 4-30 also shows the effect of water vapor. Profiles for T_{max} are plotted for a single mass fraction (Y_0) of 0.01 for different droplet sizes. For comparison, the saturated water vapor at room conditions is shown as a solid line.

Figure 4-30 indicates that 50 μm droplets were the least effective of those sizes studied, with a relatively high extinction strain rate. They were still more effective than air saturated with water vapor (mass fraction of 0.022). The 15 μm droplets were the most effective, with the lowest extinction strain rate. As the diameter of monodisperse droplets was decreased below 15 μm, they became less effective. The lowest size considered was 5 μm, as the mass and enthalpy source terms approached a δ-function, as seen in Figure 4-27 and Figure 4-28, introducing severe convergence problems of the numerical model.

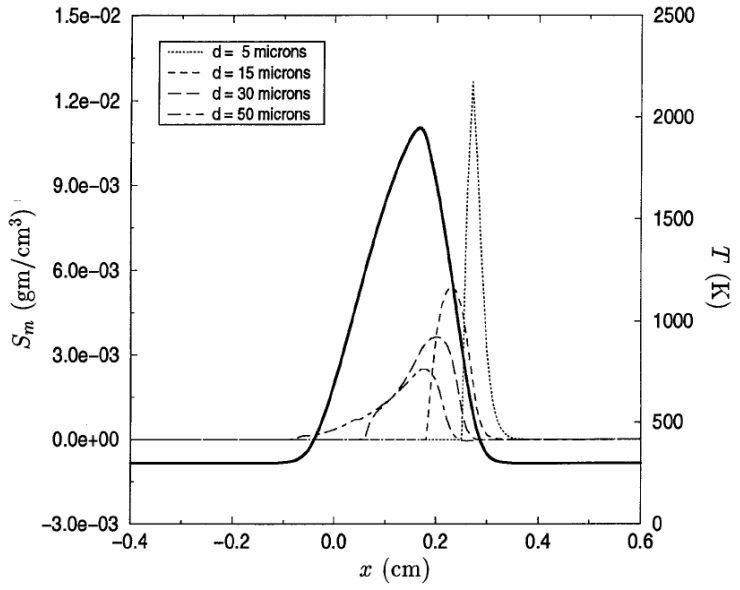

Figure 4-27. Typical S_m Profiles of Different Droplet Diameters, with Y_0 = 0.02 and Droplet Source Terms Turned "off." Thick line: gas temperature. [80]

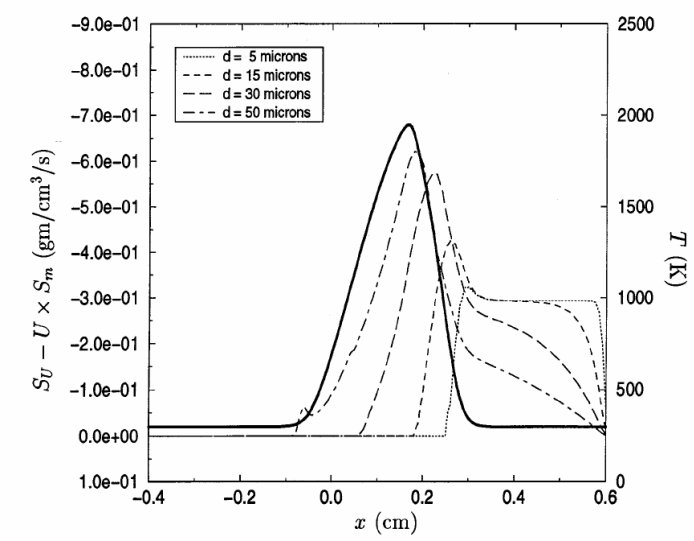

Figure 4-28. Typical S_U - US_m Profiles of Different Droplet Diameters, with Y_0 = 0.02 and Droplet Source Terms Turned "off." Thick line: gas temperature. [80]

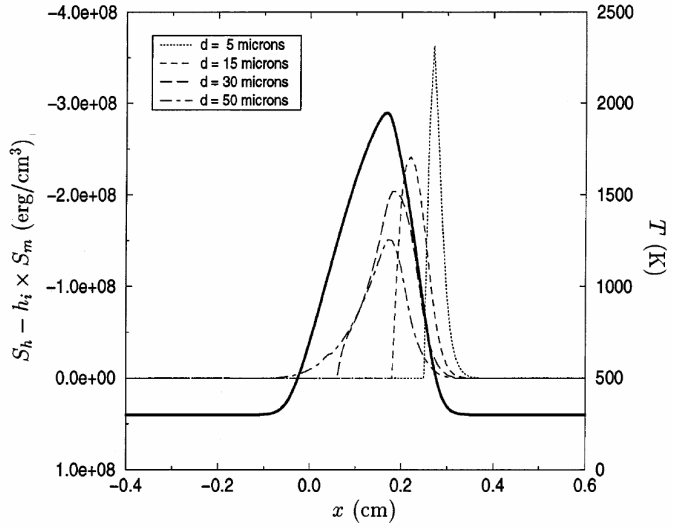

Figure 4-29. Typical S_h - h_iS_m Profiles of Different Droplet Diameters, with Y_0 = 0.02 and Droplet Source Terms Turned "off." [80] **Thick line: gas temperature.**

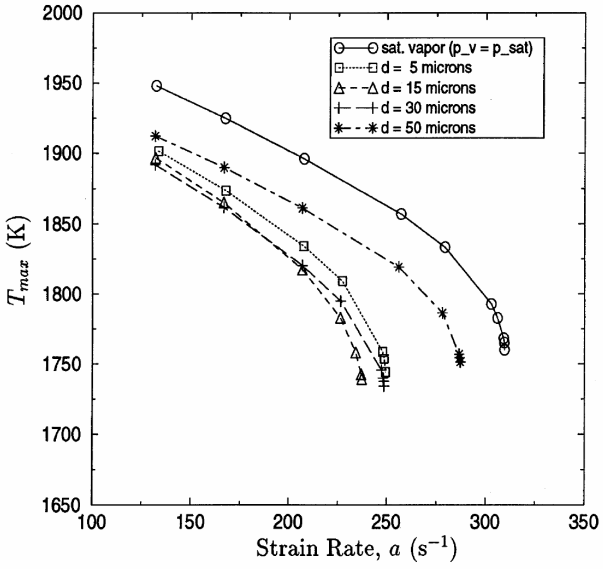

Figure 4-30. Comparison of T_{max} vs. strain rate *a*, for Different Droplet Diameters, with *water mass fraction* = 0.01. [80]

In fact, droplets of 5 μm and below should approach the limit where all the water considered is in the vapor phase at the air side boundary of the mixing layer, provided the inflow temperature of air is not affected. Irrespective of this difficulty, this most interesting nonmonotonic effect of droplet diameter was captured well by the two-phase model developed here for steady, laminar, counterflow, nonpremixed flames.

For higher water mass fractions in the condensed phase, similar profiles were obtained for T_{max} as a function of flow strain rate, as shown in Figure 4-31 and Figure 4-32. The extinction strain rate decreased significantly with increasing water droplet loading.

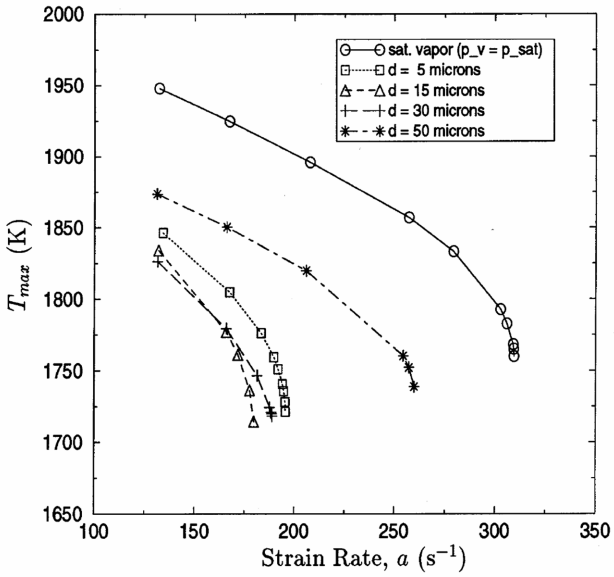

Figure 4-31. Comparison of T_{max} vs. strain rate *a*, for Different Droplet Diameters, with water mass fraction = 0.02. [80]

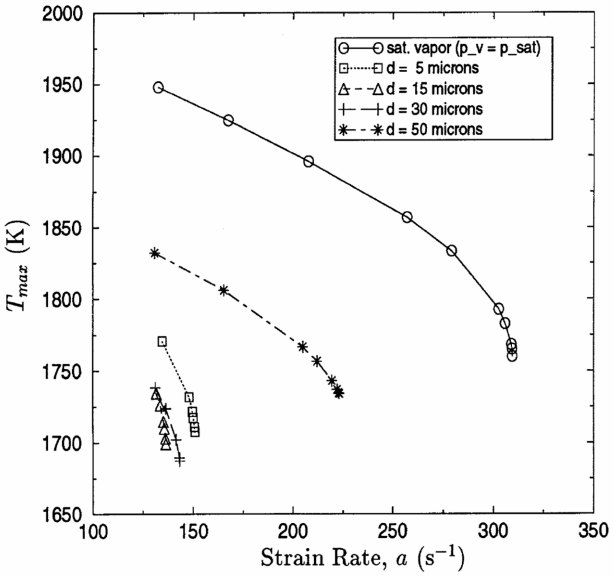

Figure 4-32. Comparison of T_{max} vs. *strain rate a* , for Different Droplet Diameters, with water mass fraction = 0.03. [80]

For the mass fractions considered here, the nonmonotonic effect of droplet diameter on the extinction strain rate can be better illustrated by Figure 4-33. For all the conditions considered here, 15 μm to 20 μm droplets were the most effective.

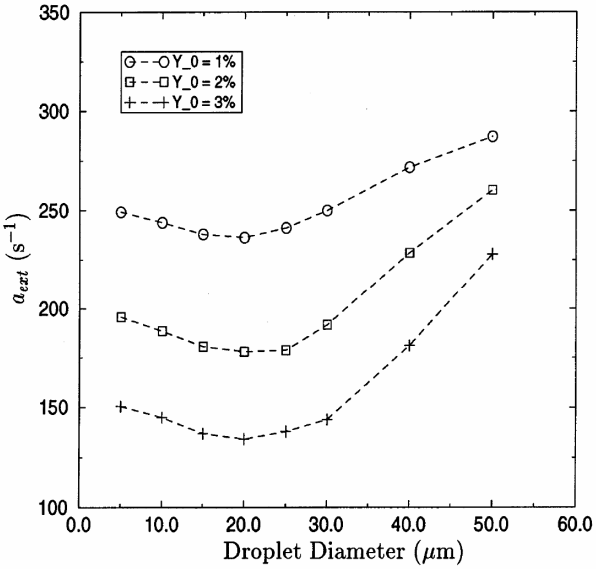

Figure 4-33. Comparison of a_{ext} vs. Droplet Diameter for Different Droplet Mass Fractions in the Condensed Phase at Inflow. [80]

This superior effectiveness of 15 μm to 20 μm droplets can be explained by the location of the mass source term seen in Figure 4-27. In the case of 15 μm droplets, the peak value of S_m, and also of S_h - $h_i S_m$, occurs at the oxygen consumption or radical production layer. The effect of S_h - $h_i S_m$ on flame temperature resulted in lower radical production and hence early flame extinction.[105,106] The exact physical, thermal, and chemical contributions responsible for flame extinction condition in the presence of water droplets are being investigated separately, with comparison to that of traditional chemical agents, such as halon 1301.

The concept of flow strain rate as defined here, i.e., $a = -d_v/d_x$, is strictly applicable to constant density or nonreactive mixing layer flows. However, it is a useful fluid dynamical parameter for comparison with near extinction experimental velocity data obtained with nonintrusive laser Doppler velocimetry techniques.[103] For theoretical studies, a more useful fluid dynamical parameter is the diffusion time scale defined by the inverse of the scalar dissipation rate:[106,107]

$$\chi = 2D\left|\nabla Z\right|^2 \tag{4-9}$$

where D is an appropriate diffusion coefficient (e.g., $D = \lambda/(\rho c_p)$ for unity Lewis number) and Z is the mixture fraction. For small stoichiometric mixture fractions, Z_s, an analytical expression relating the stoichiometric scalar dissipation rate, χ_s, with a taking into account the thermal expansion effects, has been derived by Kim and Williams.[108] Instead of using such an analytical expression, the scalar dissipation rate at the stoichiometric point at extinction was directly computed here by solving for a conservation equation for mixture fraction.

The resulting variation of $(\chi_s)_{ext}$ as a function of the initial droplet size and water mass fraction in condensed phase is shown in Figure 4-34, indicating a trend similar to that of a_{ext} shown in Figure 4-33.

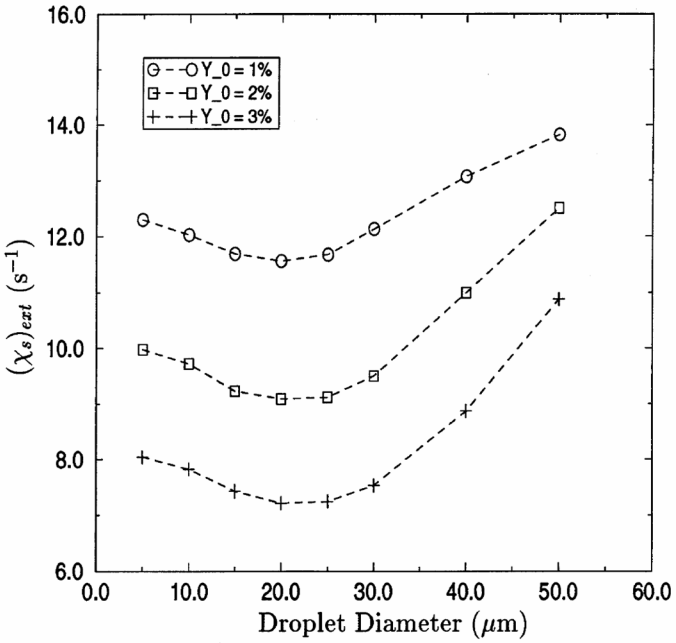

Figure 4-34. Comparison of $(\chi_s)_{ext}$ vs. Droplet Diameter for Different Droplet Mass Fractions in Condensed Phase at Inflow. [80]

The results presented here need to be validated with careful experimentation. Furthermore, the generation of truly monodisperse droplets is a challenging task, and methods of extending the present modeling work to polydisperse droplets also need to be pursued.

DROPLET-DROPLET COLLISIONS. A key assumption in the numerical model developed was that droplets are transported without collision with other droplets. This assumption allowed for a fairly simple description of the droplet flow field and derivation of a self-similar solution for both droplets and the gas phase. It relied on the idea that the droplets leaving the air nozzle were monodisperse with the same exit velocity (n_{d0}) and, hence, similar dynamics in the counterflow field. Although such ideal conditions are difficult to accomplish in experimental situations, if the initial droplet separation distance to droplet diameter is large, as seen in Table 4–3, the fraction of droplets colliding before evaporation can be neglected.

It is valuable to test the validity of this assumption under the worst case for this type of laboratory configuration. This occurs when large droplets at high droplet loading penetrate the stagnation plane and reverse their trajectory, creating a region where opposed flow of droplets exists near the axis of symmetry. Such a region existed for 50 μm droplets considered here, as seen in Figure 4-23.

Figure 4-35 shows the calculated trajectory of 50 μm droplets along the x-axis as a function of time and the corresponding flux fraction function for $Y_0 = 0.03$. With $v_{d0} \approx 60$ cm/s and an average distance $l_0 = 0.12$ cm (see Table 4–3), each droplet was estimated to be preceded and followed by a droplet before and after a time 1.8×10^{-3} s. Thus, assuming that droplets were leaving the air nozzle at every 1.8×10^{-3} s, then the region between points 1 and 2 (the region where each droplet group would see a group of droplets flowing in the opposing direction) in Figure 4-35 consists of ≈ 17 layers. By taking the average value of droplet flux fraction, $\mathcal{F}$, in region 1 → 2 as 1/2 and in region 2 → 3 as 1/4, the probability of droplet collision in this worst case region was roughly estimated as

$$P_{coll} < 17\frac{1}{2}\frac{1}{4}\left(\frac{d}{l_o}\right)^2 \approx 0.4\% \tag{4-10}$$

This estimate for collision probability was even smaller for smaller droplets because of evaporation and the increased straining of droplet flux. Hence, the assumption of negligible droplet collision was reasonable.

Several other simplifications and approximations were also used in the development of the analytical model. The implication of the approximations introduced and possible inaccuracies arising from these approximations were addressed in detail in Reference 80.

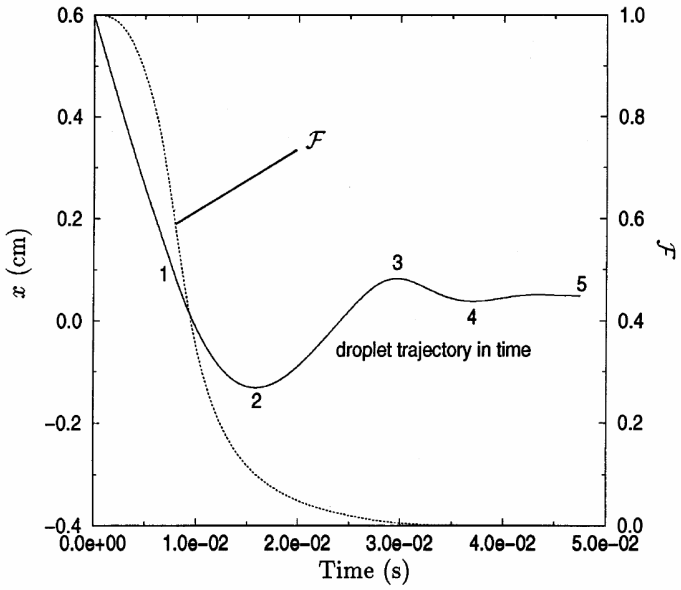

Figure 4-35. Calculated Droplet Trajectory as a Function of Time, for d = 50 μm and Y_0 = 0.03. [80]

SUMMARY FOR MODELING AEROSOL SUPPRESSANTS IN COUNTERFLOW FLAMES. This work developed a new two-phase numerical model to analyze the effectiveness of monodisperse, condensed phase fire suppressants in extinguishing counterflow flames. The model overcame the singularities associated with solving the droplet number density equation in a counterflow field accurately and in a very robust manner. This was achieved using a hybrid Eulerian–Lagrangian formulation for the gas-droplet flow, with the introduction of droplet flux fraction to describe the droplet number density equation. The model was applied to a case where monodisperse water droplets were introduced with the air stream to a nonpremixed counterflow methane/air flame. Several cases with droplet diameters ranging from 5 μm to 50 μm and mass loadings of liquid water in the air stream from 0.01 to 0.03 were considered. The model predicted that small droplets (< 20 μm) tended to follow the gas closely and went through rapid evaporation in the hot mixing layer, never crossing the stagnation plane. The 50 μm droplet crossed the stagnation plane several times before being completely vaporized. The important finding was that the flame extinction strain rate showed nonmonotonic behavior for different monodisperse droplet sizes considered for several water mass loadings. Assuming that the droplets were introduced with the air stream at the same velocity as the gas, 15 μm droplets were predicted to be the most effective. Addition of 3 % of water by mass in condensed phase (in addition to 2.22 % as water vapor due to saturation) was shown to reduce the extinction strain rate to 130 s^{-1} from ≈ 400 s^{-1} for the dry air case. The nonmonotonic

suppression effect of droplet size favoring 15 μm droplets was attributed to the droplet dynamics in the counterflow field and to the large mass evaporation and heat sink observed near the oxygen consumption layer. Sensitivity analyses of the approximate analytical models used to simplify the numerical integrations showed that mass evaporation and heat transfer terms needed to be more accurately modeled. Methods of improving the accuracy of these models were left for future pursuits.

Non-Premixed Counterflow Flame Studies

Experimental Setup

NRL researchers quantified water mist suppression effectiveness in non-premixed flames by determining the extinction strain rate in counterflow propane/air flames.[109] A schematic of the experimental configuration is shown in Figure 4–36.

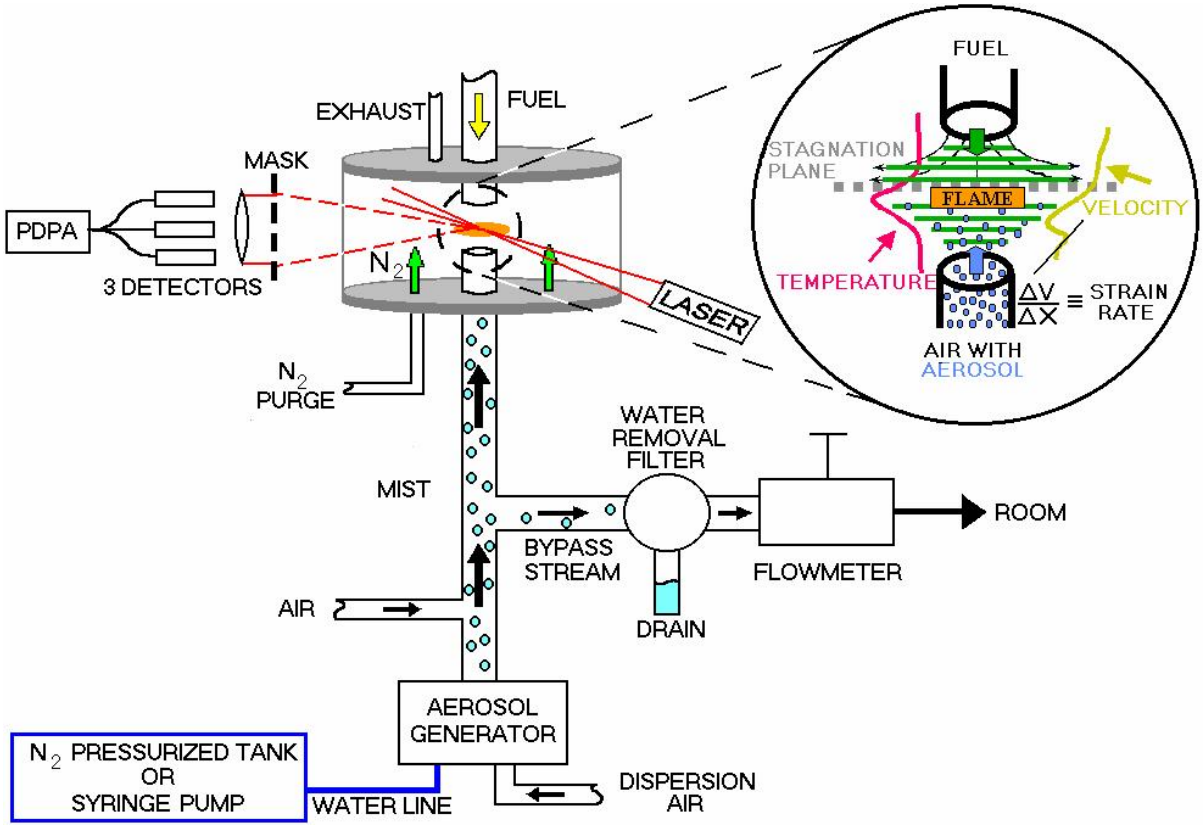

Figure 4-36. Apparatus for Aerosol-inhibited, Non-premixed Counterflow Flames.[75]

The burner consisted of two 50 cm long stainless steel tubes (1 cm inner diameter), with outer concentric tubes for a co-flow. The upper tube had a jacket for cooling water. The two tubes were aligned vertically and collinearly with a separation of 1.00 cm ± 0.05 cm. Air or fuel exited from a single tube with a parabolic velocity profile. Flow straighteners were not used. The air and fuel velocity profiles near the tube exits when opposing each other were flattened slightly from a parabolic profile due to the presence

of the other opposing flow. In the configuration used for the experiments, the luminous flame zone was fairly flat. The end of the each tube was plumbed through the center of stainless steel plates on the top and bottom of a 22 cm inner diameter, 19 cm long acrylic tube. The acrylic tube had flat windows for good optical access. These windows were critical to both the position of the laser beam overlap for the aerosol velocity and sizing measurements and the detection angle of the scattered light. A ≈ 4 SLPM purge flow of nitrogen was introduced into the bottom of the chamber. All gases exited through the top plate of the combustion chamber through a 5 cm diameter exhaust port. Representative centerline temperature and axial velocity profiles are indicated in the "blow-out" section of Figure 4–36, as is the strain rate. For gaseous reactants in this configuration, a relationship between the local strain rate (i.e., the maximum gradient of axial velocity on the air side of the reaction zone), the burner gap size distance, reactant velocities and densities were determined.[110] This burner-specific relationship was used to calculate local strain rates, and had been previously shown to remain valid for the addition of gaseous agents of high molecular weight to the air stream. For a condensed phase agent, the situation became more complicated, because under some conditions the condensed phase comprised a substantial fraction of the total momentum of the flow, and did not have the same velocity as the surrounding gas. In determining strain rates in the present study, it was assumed that the gas flow field was unchanged by the presence of the water mist. This approximation is only valid if the mass fraction of water in the air stream is small. For larger water mass fractions, the gas flow field must be measured in the presence of the water drops. The velocities of the water droplets themselves could not be used to determine the gas flow velocity, however, because they were too large to follow the gas flow field. For these reasons, the water mass fractions in the air stream were no larger than 0.03.

Liquid mist aerosols were generated and seeded in the air flow in the lower tube. Air side introduction of the mist is relevant to real fire, total flooding fire suppression scenarios. Fuel was introduced from the top, water-cooled tube. Flames were started using an arc igniter for a standard fuel and air flow configuration and stabilized in a 1 cm gap between the two tubes. For hydrocarbon fuels burning in air, stoichiometry dictates that the non-premixed flame reside on the air side of the stagnation plane. Phase Doppler Particle Anemometry was used to measure droplet size distribution, number density, and droplet velocities through the flow field by vertically translating the burner assembly. The aerosol generator required a ≈ 1 L/min to 1.5 L/min flow of air for proper operation. In order to examine flames of lower strain rate, part of the air stream containing droplets was diverted from the burner. Droplets from the excess stream were removed by filtering, and the resulting air flow was measured to determine the amount of air sent to the burner.

The mists were produced using a vibrating orifice aerosol generator (TSI Inc. Model 3450), based on the design of Berglund and Liu.[111] A schematic of the droplet generator is shown in Figure 4-13. Water was forced through a pinhole that was acoustically excited by a piezoelectric ceramic. At specific resonant frequencies, the water jet broke up into a monodisperse droplet stream. This stream exited the generator through a hole in the dispersion cap. By forcing air to exit through this same hole, the droplet stream was dispersed into a cloud as it exited the droplet generator and entered the counterflow burner's bottom tube. Measurements of droplet number density as a function of radial position at the tube exit indicated that the droplets were evenly distributed except near the tube wall. The mass flow of water was adjusted primarily by controlling the backing pressure of water entering the orifice. The use of the small orifice in this type of droplet generator placed limitations on the achievable water flow. In general, the smaller the orifice used, the smaller the maximum flow of water that could be obtained.

To obtain flame conditions of high strain and low water mass fraction, the aerosol was mixed with a secondary (dry) air stream. The mixture was then introduced up the tube toward the reaction zone. For low strain rate conditions, the air flow through the droplet generator required to accomplish droplet dispersal often exceeded the desired total air flow to the burner. Under these conditions, a portion of the air/droplet stream was diverted to bypass the burner. The analysis below assumes that no collisions between droplets occurred. The volume fraction occupied by droplets for these operating conditions was typically $\approx 2 \times 10^{-5}$. The assumption that a significant number of collisions did not occur is consistent with the droplet size histograms, which did not show appreciable droplet growth, as would be the case if collisions were to occur.

The aerosol generator used in the present study produced droplets having very narrow size distributions. When the dispersion air is used, 95 % of the droplets had diameters within $\pm$ 2.5 μm of the mean. (The size distribution was even narrower in the absence of dispersion air.)

Droplet size and velocity distributions were monitored using a Phase Doppler Particle Anemometer (PDPA-Dantec Measurement Technology). For the mists studied, all droplets in the original droplet stream were characterized by a single 4 μm wide PDPA bin size. In order to distribute the stream into a mist, a dispersion cap and entrainment assembly were employed. Mist dispersion and air entrainment of the highly-monodisperse droplet stream into a mist in the burner tube degraded the monodispersity slightly. As shown in Table 4–5, > 50 % of the water mass for each mist was still contained in three 4 μm wide bins, centered on the title bin. For the 14 μm mist, this value was 90 %.

Table 4–5. PDPA Derived Diameter Information for the Experimental Mists Studied Measured at 2 mm from the Air Tube Exit. [113]

Mist Name	% Water Droplets within ± 2 μm of Nominal Diameter	% Water Mass within ± 2 μm of Nominal Diameter	% Water Mass within ± 6 μm of Nominal Diameter
14 μm	63	47	90
30 μm	61	60	72
42 μm	53	38	51

One disadvantage of this generator was that the droplet diameter could not be continuously adjusted: monodisperse droplets could only be produced at specific sizes, corresponding to piezoelectric driver frequencies that match acoustic resonances of the orifice. Using a 5 μm diameter pinhole, for example, monodisperse droplet streams with a size distribution peak at diameters of 14 μm, 18 μm, and 24 μm were produced. With a 10 μm diameter pinhole, monodisperse streams of 25 μm, 30 μm, and 37 μm droplets were obtained. If the piezoelectric driver frequency were nonresonant, a bimodal or multimodal droplet size distribution was generally produced.

Using the PDPA, droplet diameters, axial velocities, and number densities were measured at discrete points at a single point in the flame by recording each droplet which crossed the laser probe volume during a specified time period. Laser light scattered by the droplets was collected through a window mounted in the Plexiglas chamber. The burner was mounted on a three-axis translation stage, such that the laser probe volume could be positioned anywhere in the gap between the opposed tubes to record droplet characteristics as a function of position. The axial position of the flame was determined by centering the PDPA probe volume in the middle of the flame's visible emission zone.

The droplet size distribution was monitored during the experiments to ensure that the piezoelectric driving frequency was correctly chosen to yield a monodisperse droplet distribution. The droplet volume density determined by the PDPA was the primary determination of the amount of liquid water delivered to the flame. Comparison runs between the PDPA determination of the water delivery rate, and direct measurements of the accumulated mass of water exiting the droplet generator, yielded agreement within a few percent. The PDPA system was capable of acquiring data at higher droplet loadings than those reported here. This was verified in the case of the larger droplet sizes (the achievable mass fraction of the smaller droplets was limited by the generator). The limit imposed on the water mass fraction was due to the effect of the water droplets on the strain rate, not a limitation of the PDPA diagnostic.

Droplet Behavior

Figure 4-37 and Figure 4-38 show the evolution of the droplet size distribution, in these propane/air counterflow flames, of initially monodisperse water mists of 30 μm and 18 μm, respectively. The figures plot number densities of droplets in various size ranges as a function of axial position (x) along the burner's axis (r = 0 mm). The local axial strain rate, *a,* imposed on the flames corresponds to approximately 30 % of the extinction strain rate measured in the present apparatus[110] for the uninhibited flame (a_{ext} = 608 s^{-1}± 65 s^{-1}). The air and droplets exited the lower tube at x = 0 mm; the propane exited the upper tube at x = 10 mm. The luminous zones of the flames were located at x = 5.0 mm and 4.5 mm, respectively, in the experiments employing 30 μm and 18 μm mists. For both initial sizes, the diameter of the droplets changed very little until the flame was reached, with the 30 μm or 18 μm droplets dominating the size distribution.

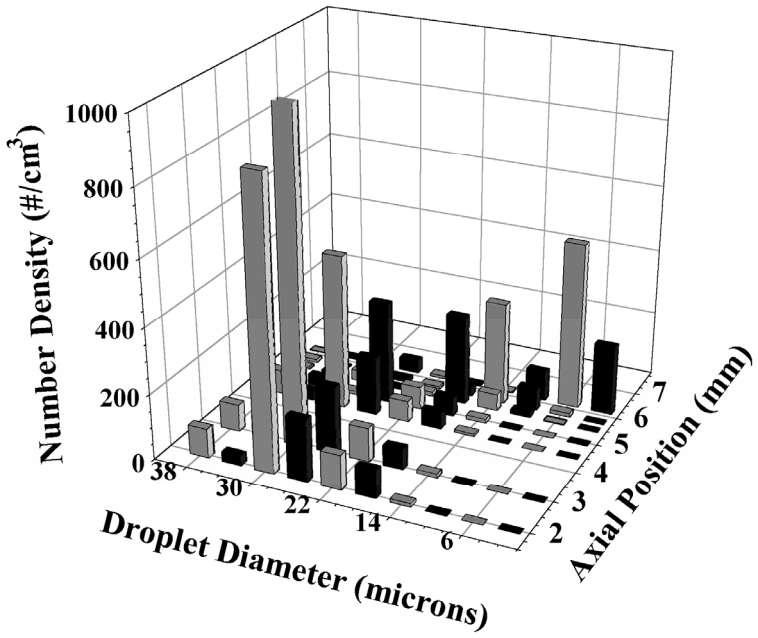

Figure 4-37. Droplet Diameter Distribution Evolution of a 30 μm Mist in a 170 s^{-1} Strain Rate Flame; the luminous flame is centered at 5 mm. [109]

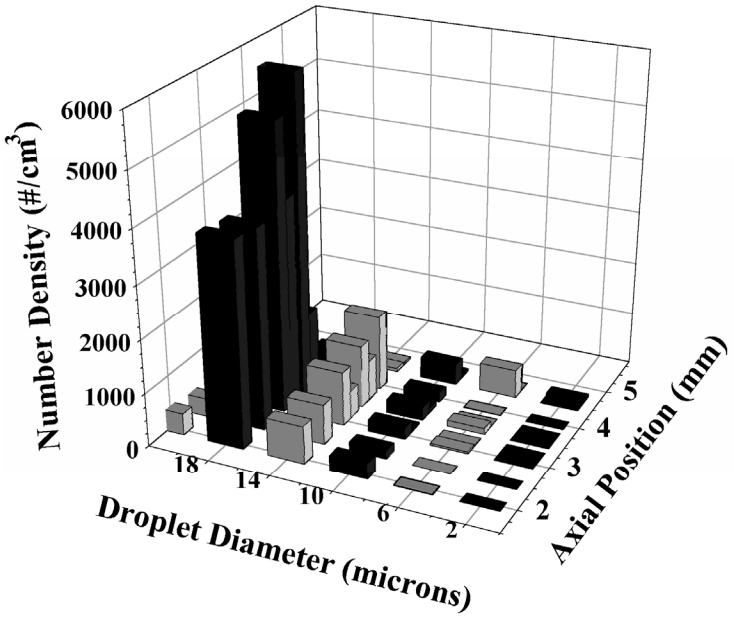

Figure 4-38 Droplet Diameter Distribution Evolution of an 18 μm Mist in a 170 s^{-1} Strain Rate Propane/air Counterflow Flame. The luminous flame is centered at 4.5 mm. [109]

In the flame region, the two droplet sizes showed somewhat different behaviors. In both cases, the droplets evaporated; and the total number density of droplets, summed over all size ranges, decreased. For the 18 μm initial droplet size, virtually no droplets of any size were detected once the flame was reached. For the 30 μm initial size, the total number density decreased, though not as dramatically, in passing through the flame zone. The droplets that were detected in or beyond the flame zone had a broad size distribution and a much smaller average size than did the incident drops. These observations indicate that, for this flame condition, the 18 μm mist underwent essentially complete vaporization once it entered the reaction zone, while the 30 μm mist appeared to be near the threshold size above which droplets were not completely evaporated. When incident droplets of 42 μm diameter were used, a larger number of droplets were detected beyond the flame zone, supporting the assertion that 30 μm is close to the minimum size capable of just penetrating the flame.

Figure 4-39 and Figure 4-40 focus specifically on the number density profiles of the 30 μm and 18 μm droplets respectively. Number density is plotted vs. axial position. In both experiments, the density first increases with axial position; then quickly drops in the flame region.

Three effects combine to explain the shape of the number density profiles. The main effect is related to the velocity profiles of the 30 μm and 18 μm drops, provided in Figure 4-39 and Figure 4-40, respectively. At the lower tube exit, the droplets had roughly the same velocity as the gas stream. As the gas stream's axial velocity changed in the counterflow field, the equilibrium in velocity between the liquid and gas phases was lost, and the drag forces acted to reestablish it. The droplet velocity profile therefore followed that of the gases; the velocity initially dropped as the gases moved towards the stagnation plane. It then increased when the hot gases expanded in the reaction zone, before it dropped down again, close to the stagnation plane. In regions where the droplets were decelerating, faster droplets caught up to slower ones, and the number density tended to increase. In the flame region, the droplets accelerated, which tended to reduce their number density. Figure 4-39 and Figure 4-40 show that the impact of axial velocity gradients on droplet number density was significant, with variations in number density well correlated with variations in velocity.

Furthermore, as the air exited the lower tube, the flow streamlines began to diverge in the counterflow field, producing radial drag forces on the mist. Due to this effect, the droplets moved away from the burner axis. The divergence of the air flow therefore acted to reduce the droplet number density along the centerline. The third effect is evaporation in the flame region, which caused the droplet size to decrease, and thus also contributed to the decrease in the number densities of the 30 μm and 18 μm droplets.

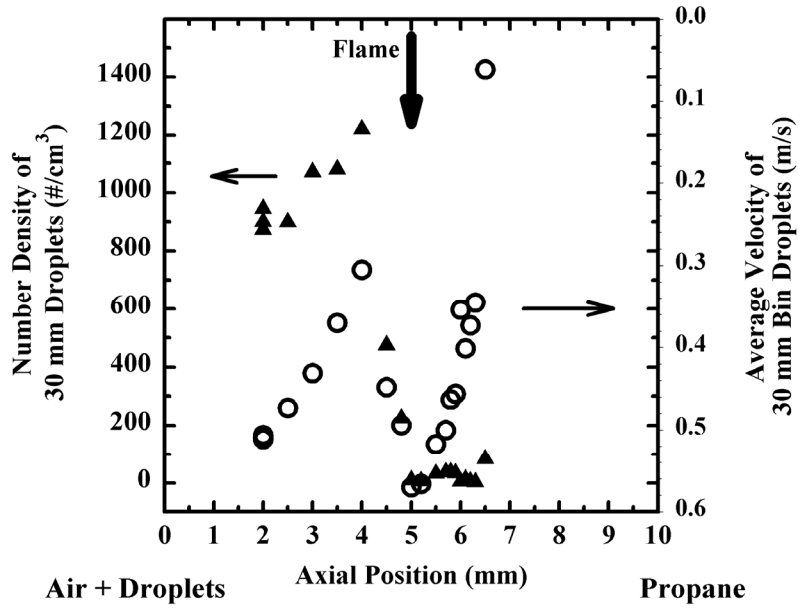

Figure 4-39. Profiles of Number Density (triangles) and Velocity (circles) of 30 μm Droplets vs. Location in a 170 s^{-1} Strain Rate Propane/air/30 μm Mist Counterflow Flame. [109]

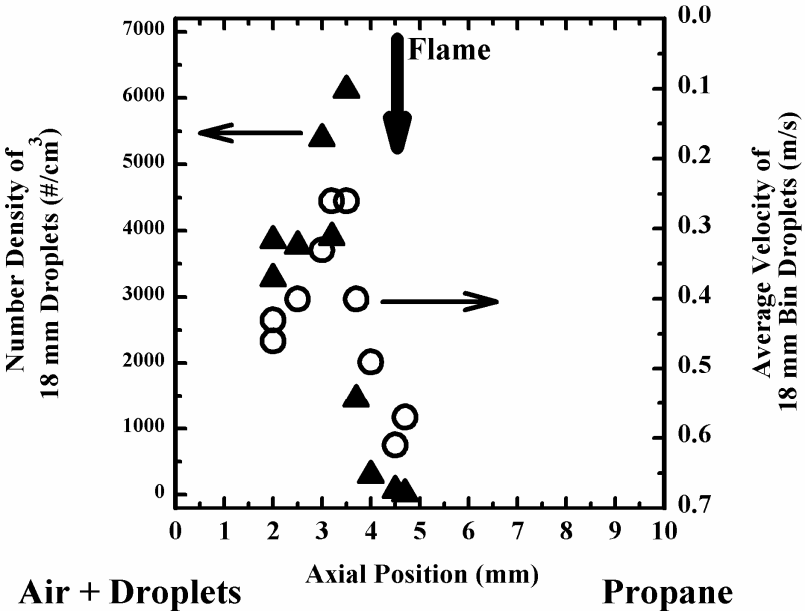

Figure 4-40. Profiles of Number Density (triangles) and Velocity (circles) of 18 μm Droplets vs. Location in a Propane/air/water mist Counterflow Flame. [109]

When the data of Figure 4-39 and Figure 4-40 are plotted in terms of droplet flux rather than number density, the peak just before the reaction zone is not present. Figure 4-41 shows the droplet flux profile for the 30 μm mist. The flux was determined from the PDPA software by summing over all droplets detected within the measurement time, with the sum weighted by the velocity of each drop. The droplet

flux decreased slightly as the flame was approached, under the effects of the diverging flow and evaporation. The flux then decreased dramatically in passing through the high temperature zone. For the 18 μm incident droplet size, the plot of flux vs. position is qualitatively similar to that of the 30 μm drops, except that the flux is reduced to essentially zero once the reaction zone is reached. In the plots of droplet flux, scatter in the data was attributed in part to experimental uncertainties, in the PDPA concentration measurements in particular. Slight variations in the position of the flame over the course of the experiment also contributed to the scatter.

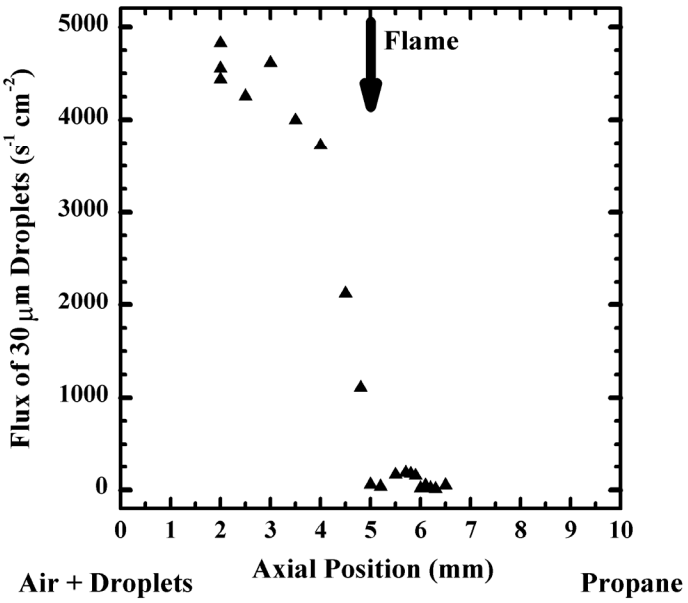

Figure 4-41. Droplet Flux Profile for a 30 μm Mist in a 170 s^{-1} Strain Rate Propane/air Flame.

Flame Extinction

The core data set comprised measurements of the extinction strain rates of non-premixed propane/air counterflow flames at various water mass fractions (up to 0.03) at droplet sizes of 14 μm, 30 μm, and 42 μm. Droplet fluxes were measured by the PDPA instrument along the burner axis 2.0 mm from the air tube exit, at strain rates within 10 % of extinction. Local strain rates were determined from the gas flows as discussed above. The results are plotted in Figure 4-42. For comparison, extinction mass fractions of halon 1301 (CF_3Br) vs. local strain rate in the propane/air counterflow flame[110] are also plotted. The 42 μm water droplets were clearly much less effective in reducing the extinction strain rate than were the 14 μm or 30 μm droplets. The 14 μm droplets were slightly more effective than the 30 μm, but direct comparison was difficult because only a very limited mass fraction of water was obtainable in the 14 μm droplet size with the present generator. Both of the smaller droplet sizes appeared to be more effective in reducing the extinction strain rate than was halon 1301.

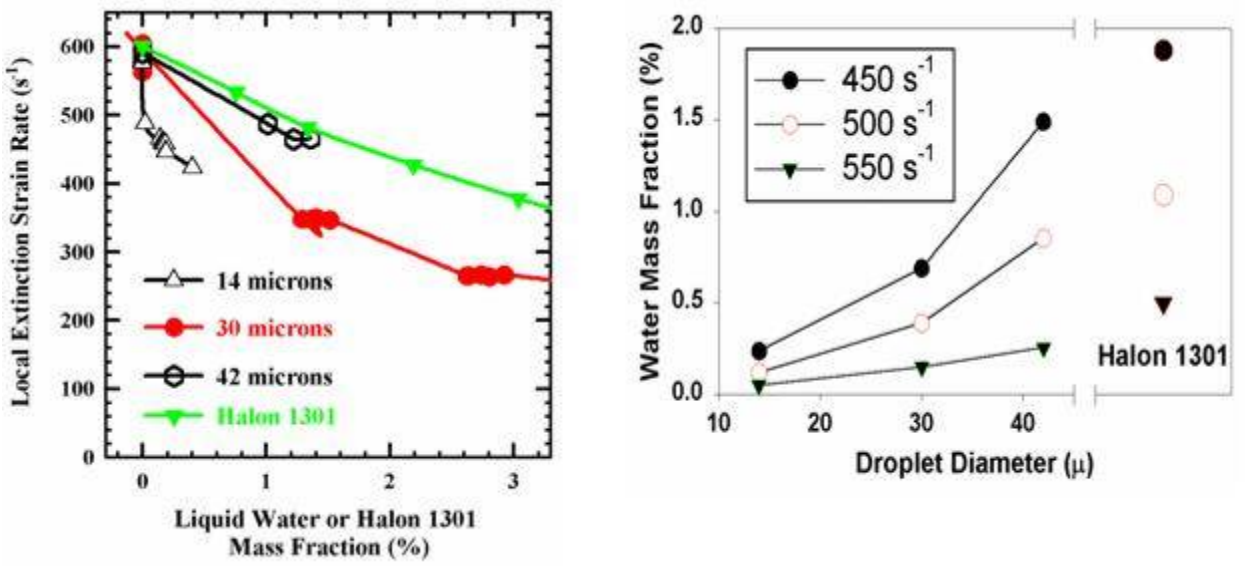

Figure 4-42. Water Mist Effects on the Extinction of Non-premixed, Counterflow Propane/air Flames: (a) Flame Extinction Strain Rate as a Function of Mass of Water or Halon 1301 in the Air Flow; (b) Mass Fraction of Water Needed to Extinguish the Flames as a Function of Droplet Diameter, Compared to Mass of Gas-phase Halon 1301. [75]

Maximum Droplet Evaporation Diameter

Li, Libby, and Williams[104] performed both numerical and analytical modeling, as well as experimental measurements, of the behavior of methanol droplets in opposed flows, both in the presence and absence of a flame. Clearly, there are differences between the interaction of a fuel droplet with a flame and that of a suppressant droplet. Nevertheless, the effects of evaporation and of viscous drag imparted by the local gas flow field have analogies between the two cases. Li et al.[104] analyzed the phenomenon of "pushback" previously described by Chen et al.[64] in which droplets in certain size ranges exhibited oscillatory motion in the vicinity of the stagnation plane. For a given flow field, large droplets tended to oscillate, while small droplets asymptotically approached an equilibrium position slightly below the stagnation plane. Under the assumptions of the Stokes drag law, neglect of evaporation, and an axial strain rate independent of axial position, the minimum droplet radius for oscillation to occur is given by

$$R_{\min} = \left(\frac{9\mu}{8\rho K} \right)^{\frac{1}{2}} \tag{4-11}$$

where μ is the absolute viscosity of the surrounding gas, ρ is the droplet density, and K is the axial strain rate. For a water droplet in air at a strain rate of 150 s^{-1}, the minimum diameter for oscillation to occur was approximately 30 μm. In practice, this threshold represents a lower bound because all droplets lose mass by evaporation, and water droplets with initial sizes smaller than the oscillation threshold usually undergo complete vaporization upon entering the flame zone.[80] The size ranges of droplets investigated in the present study bracketed the threshold size for oscillation for the flow field conditions. Furthermore, the threshold size was similar to the size predicted by Lentati and Chelliah to be most effective at

suppression, although this could be a consequence of the relative importance of viscous drag and evaporation for water in particular.

The experimental results were consistent with the numerical predictions of Lentati and Chelliah[80] for monodisperse droplet streams in a number of respects. For a methane/air counterflow flame with a local strain rate of 130 s^{-1}, Lentati and Chelliah[80] predicted that a 30 μm water droplet should just pass through the reaction zone before evaporating completely, while droplets having diameters 15 μm or less should completely evaporate before reaching the location of maximum temperature. The data shown in Figure 4-37 and Figure 4-38 were taken with a different fuel (propane vs. methane) and at a slightly higher strain rate (165 s^{-1} to 175 s^{-1} vs. 130 s^{-1}), but show the same qualitative behavior as a function of droplet size. Furthermore, Lentati and Chelliah[80] predicted that appropriately sized water droplets could be more effective on a mass basis than halon 1301 in suppressing combustion, but that the effectiveness of water was likely to decrease significantly with increasing droplet size for diameters >30 μm. Both of these predictions were consistent with the data presented in Figure 4-42. There were approximations made in the modeling as well as non-ideality in the present experiment. Nevertheless, the results of these experiments supported the predictions of Lentati and Chelliah[80] in those aspects for which there was an adequate comparison.

The degree of evaporation (or decomposition) of an aerosol particle or droplet in a flame depends on the residence time of the aerosol in the high temperature environment. In the flame, the evaporation rate and droplet size are spatially dependent since the aerosol is moving in a non-uniform temperature field. Solution of the problem requires full consideration of the flow field. However, the evaporation model can be used to estimate a droplet size in the premixed and opposed flame configurations for the onset of complete droplet evaporation. In the flame temperature field, droplets begin to evaporate at the lower temperature and the resulting smaller drop, traveling into the higher temperature region, will experience a higher evaporation rate and consequently a shorter total evaporation time.

Consideration of the burning velocity and flame thickness of the methane-air premixed flames reported earlier in this section suggested that the water droplets should experience a residence time in the range of 1 ms to 2 ms. Consideration of the temperature field and the results of Figure 4-6 indicated a droplet size limit for complete evaporation (and the corresponding onset of water droplet limiting effectiveness) at ~ 15 μm in premixed flames. This upper limit estimate was consistent with the water droplet size profiles observed in the premixed flame and with predictions of the multiphase model.

For counterflow flames, transit time in the flame was estimated from the inverse of the strain rate.[80] For a strain rate of 450 s^{-1} (high strain rate for methane, mid strain rate for propane) the residence time was ≈ 2.2 ms. The estimated droplet size for the onset of complete evaporation was ≈ 25 μm. This value agreed with the experimental water droplet size survival properties in propane-air flames[63] and was consistent with the modeling predictions for methane-air flames.[80]

Modeling the Effect of Water Vapor

NRL staff collaborated with Chelliah and co-workers to understand the observed suppression behavior of water vapor and water droplets on propane-air non-premixed counterflow flames. Comparison of the predictions of the model described in Section 3.5.1 with experimental results provided valuable insights regarding the experimental observations.[112] The collaboration also served to validate the multi-phase flame suppression model further.

During the application of water mist to a fire or a laboratory flame, an enclosed or semi-enclosed chamber will be saturated with water vapor. The time required to attain the saturation condition depends on several factors, including the air temperature, original humidity level, and the total surface area of the droplets applied. For the same condensed water mass, smaller droplets have a higher surface area per unit volume (or mass), leading to a more rapid saturation of the initially dry air, while larger droplets with lower surface area/volume are expected to take considerably longer. Consequently, different levels of water vapor content in air are realizable (i.e., saturated to partially saturated), depending on the droplet size, droplet number density or mass added, gas temperature, and the elapsed time.

The model assumed that the room temperature was constant at 300 K and that the air feed stream was completely saturated with water vapor. The latter implied that droplets traveled with the air stream long enough to attain equilibrium conditions. At 300 K, the mole fraction of water vapor in saturated air is 0.0352; the mass fraction is 0.0224. This corresponds to mole fractions of oxygen of 0.2026, nitrogen of 0.762, and water of 0.0352 in the oxidizer stream.

Results of the two-phase model for non-premixed counterflow propane-air flames are shown in Figure 4-43. Indicated in the figure are flame temperature vs. strain rate curves for flames with dry 300 K air, saturated 300 K air, and saturated 300 K air containing a 14 μm, 30 μm, or 42 μm diameter monodisperse water mist. The water masses for the individual aerosols were based on the experimental determinations shown in Table 4–5. The extinction condition is defined by the curve turning point; the value of the strain rate at the turning point is the predicted extinction strain rate for each suppressed flame condition.

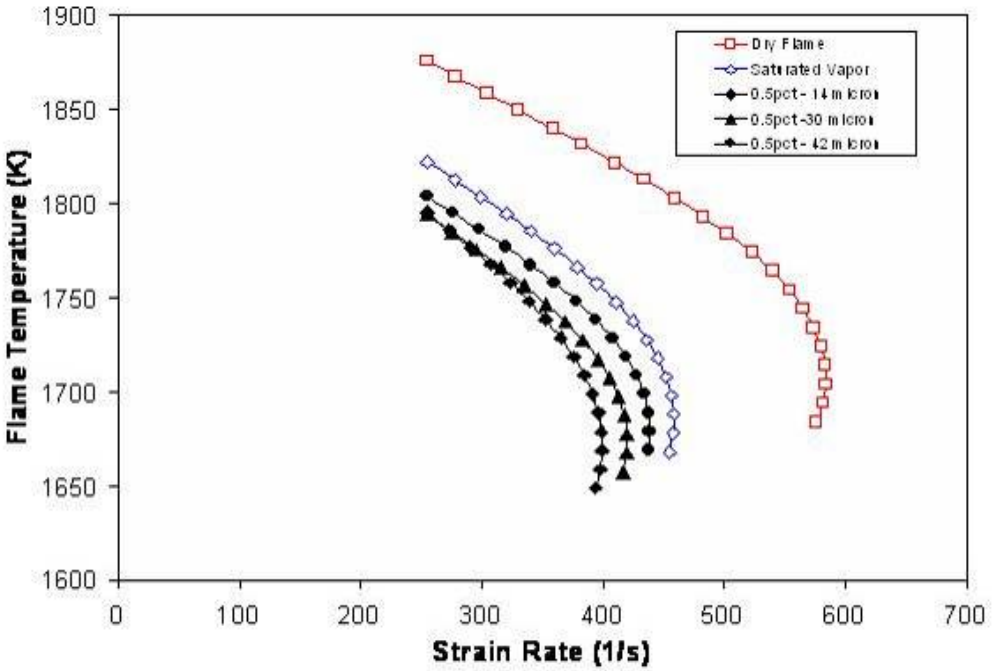

Figure 4-43. Variation of the Predicted Flame Temperature as a Function of the Flow Strain Rate for Propane-air, Non-premixed Counterflow Flames for Dry Air, Air Saturated with Water Vapor, and Saturated Air with Monodisperse Water Droplets. [113]

The reduction of oxygen mole fraction from 0.209 (dry air) to 0.2026 (saturated air) due to displacement by water vapor at 300 K yields a decrease in the predicted flame extinction strain rate from 584 s^{-1} to 458 s^{-1}, a 22 % reduction in the extinction condition, as shown in Figure 4-43. At elevated oxidizer stream temperatures, assuming complete saturation, the increase in partial pressure of water vapor and the resulting decrease in oxygen concentration would lead to an even lower flame extinction strain rate. Likewise, a lower level of humidification in the incoming air stream would result in a smaller reduction in the extinction strain rate than that of the completely saturated air condition.

Modeling the Effects of Condensed Water and Droplet Size

When condensed water droplets were added to an already saturated air stream, the interaction of droplets with the flame front reduced the flame extinction condition further, as seen in Figure 4-44. However, the degree of reduction of the flame extinction condition depended on the droplet size, consistent with previous modeling and experiments involving the methane-air system.[80] Unlike the methane-air counterflow system where the optimal droplet size was predicted to be between 15 μm and 20 μm, the present predictions and experiments indicated that the optimal droplet size for the propane-air counterflow system was below 15 μm. The difference in optimal size was related to the higher flame extinction condition of propane-air flames, about 50 % greater than that of methane-air counterflow flames. The lower flow residence times at higher strain rates provided less time for a given droplet size to completely evaporate. For higher strain rates, droplets need to be correspondingly smaller to optimally interact with the flame front.

A comparison of the modeling and experimental results is presented in Figure 4-44.

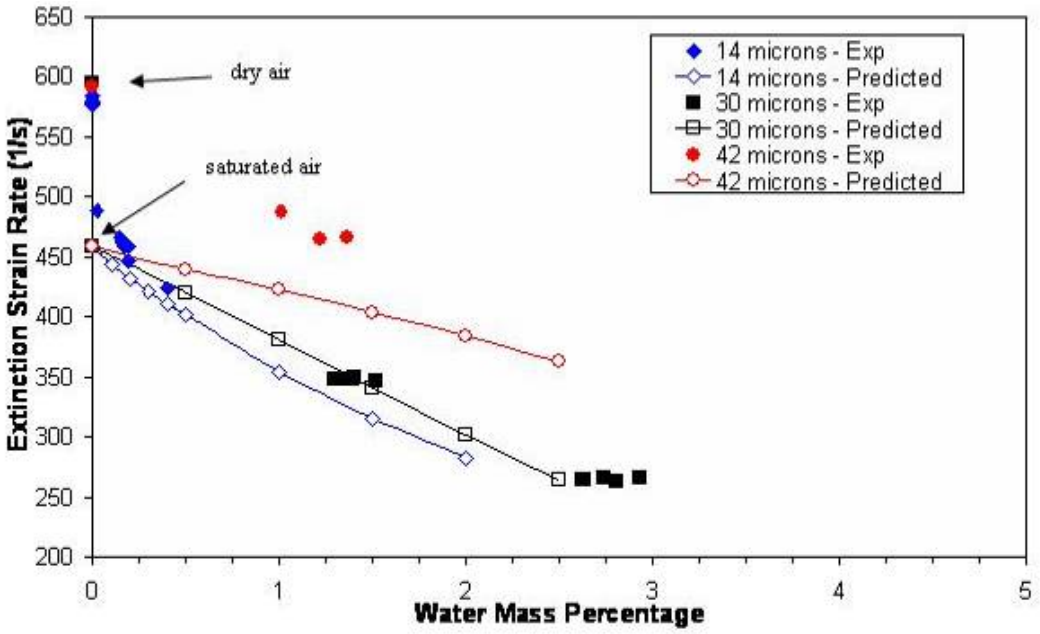

Figure 4-44. Measured Extinction Strain Rate for Water Mist Suppressed Propane-air, Non-premixed Counterflow Flames vs. % Mass of Condensed-phase Water in the Air[109] and Calculated Results for 14 μm, 30 μm, and 42 μm Diameter Monodisperse Water Mists in Saturated Air at 300 K. [113]

Comparison of the results for the three different mists suggests the occurrence of several phenomena. In the experiments, droplets were entrained into dry air. The very rapid reduction in extinction strain rate with only a very small mass of water droplets at the flame, followed by a less dramatic fall off with subsequent water droplet addition suggested a fair degree of humidification. This was particularly noticeable for the 14 μm mist. The experimental data for 14 μm mist at greater than 0.005 mass fraction of added water and for the 30 μm mist data at greater than 0.015 mass fraction of added water droplets were in very good agreement with the model predictions. The 42̃ μm data were ≈ 12 % higher than the calculation predicted at 0.015 mass fraction of added water drops. This disagreement was consistent with the degree of humidification for this larger droplet size. A quantitative prediction of the degree of air saturation expected for the experimental conditions follows below.

Humidification Effects of Air Stream

In order to quantify the degree of droplet evaporation for the different droplet sizes and the effect on flame extinction, evaporation times for the 14 μm, 30 μm, and 42 μm diameter droplets were calculated. The calculation incorporates the droplet evaporation equations given in Chin and Lefebvre.[113] Droplet evaporation times in air at 296 K were determined for a range of relative humidity for each of the experimental droplet sizes. For each droplet size, the variation in droplet evaporation times between 0 % and 100 % relative humidity was fit to a second order polynomial.

The evaporation over time of an ensemble of monodisperse droplets at a specified initial mass fraction in dry air was determined by direct time integration. For each 1 ms time step, the amount of vaporization was calculated based on the instantaneous relative humidity, the droplet number density, and the D-squared evaporation law. The amount of water vaporized impacted the relative humidity and consequently the evaporation rate for the next time step.

The predictions of the total amount of evaporation for a residence time of 750 ms are shown in Figure 4-45.

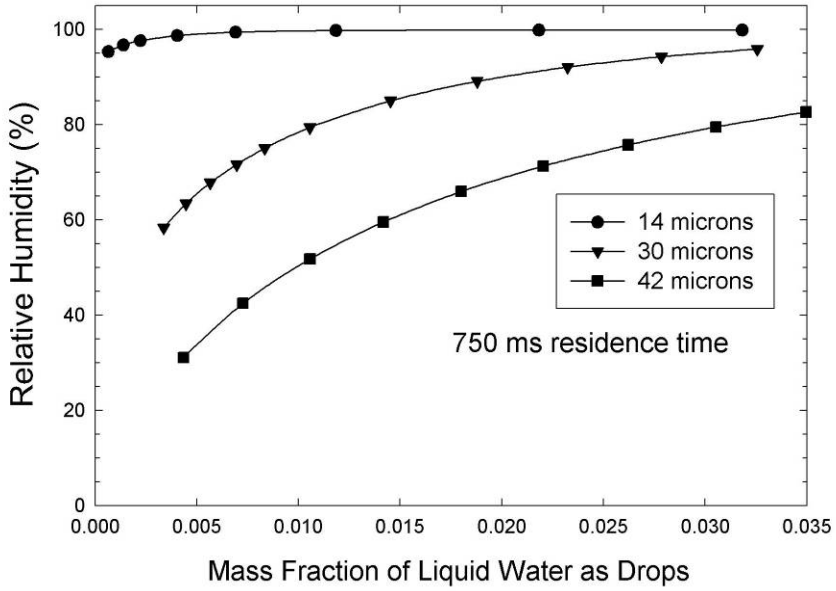

Figure 4-45 Calculated Humidification Levels of a 296 K Air Stream Containing 14 μm, 30 μm, or 42 μm droplets, Following a Residence Time of 750 ms Starting in Dry Air, as a Function of the Mass Fraction of Liquid Water Remaining after Droplet Evaporation. [113]

The residence time considered here was the time required to transport the mist after entrainment in originally dry air up the 50 cm long inlet tube. A residence time of 750 ms is the shortest value studied and corresponds to the air exit velocity necessary to produce flames with a local strain rate of ≈ 600 s^{-1}. The shortest residence time provided a lower bound for the degree of humidification. Figure 4-45 plots the relative humidity (saturated air having a water mass fraction of 0.018 at the experimental temperature of 296 K) against the mass fraction of liquid water remaining after the specified residence time. The liquid water delivered to the flame as determined via PDPA measurements 2 mm above the air tube exit was reported by Zegers et al.[110], rather than the initial mass fraction of water introduced by the droplet generator. Figure 4-45 shows that in the case of 14 μm drops, for any liquid water to remain after 750 ms, the air stream relative humidity must be at least 95 %. Thus, the assumption of saturated air in the extinction calculation was valid and was consistent with the rapid reduction in extinction strain rate observed for this droplet size. For the 30 μm drops, two sets of experimental points were collected, clustered at liquid mass fractions of 0.015 and 0.028. For the 0.015 mass fraction tests, the relative humidity after a 750 ms residence time was predicted to be approximately 85 %, while for the 0.028 mass fraction tests it was 95 %. Since the extinction strain rates for the flames inhibited by the 30 μm droplets were approximately 350 s^{-1}, this implies a droplet residence time in the air stream prior to arrival at the flame of approximately 1250 ms. The degree of saturation for a 0.015 mass fraction of residual liquid at 1250 ms was predicted to be 96 % (data not shown). For the 42 μm droplets the experimental measurements all had liquid mass fractions in the vicinity of 0.012. For this condition, the calculation predicted a relative humidity of only 55 %; assumption of a residence time of 1000 ms, based on the measured extinction strain rate, gives a relative humidity of 66 %. The calculation assuming 100 % relative humidity was expected to overpredict the extinction strain reduction (lower extinction strain rate), due to the additional heat capacity from the water vapor that was not present in the experiment. This underestimate in the extinction strain rate was in quantitative agreement with the results for the 42 μm mist, as shown in Figure 4-44.

Conclusions

Using piezoelectric generation of aerosol drops, NRL investigated the evolution of velocity and size distributions of initially monodisperse, 30 μm and 18 μm water mists in non-premixed propane/air counterflow flames. For both size mists, the peak in the droplet size distribution did not change until the flame zone was reached. The peak then shifted to smaller diameters due to evaporation. Variations in number density with axial position were strongly correlated with variations in droplet axial velocity. The fluxes of both 30 μm and 18 μm droplets decreased between the air tube exit and the stagnation plane, due to the effects of the diverging flow and evaporation. None of the 18 μ droplets and very few of the 30 μm droplets survived the flame, suggesting that for this range of droplet sizes in a counterflow flame at moderate strain rate, most of the suppression potential of the mist is used.

On a mass basis, both 14 μm and 30 μm diameter mists were found to be more effective than halon 1301 at suppressing non-premixed propane/air counterflow flames. The flame inhibition properties of the 42 μm diameter mist were considerably poorer than those of the 14 μm or 30 μm mists. The lower suppression efficiency of the 42 μm mist paralleled previous predictions of numerical modeling, and appeared to be caused by incomplete droplet vaporization during passage through the reaction zone. Comparison of the computational extinction strain rates with the reported experimental measurements showed good agreement in consideration of the degree of mist evaporation in the experimental air stream entering the flame. These results explained the observed droplet dependent suppression behavior in the

range of 14 μm to 42 μm in suppressing counterflow propane air flames. The agreement between the predictions and experiments was remarkable, considering the high effectiveness of the small amount of water mass introduced to the flame with the air stream. The hybrid Eulerian-Lagrangian multi-phase flame suppression model and chemical kinetic propane combustion mechanism well predicted the measured local propane-air extinction strain rate. Water droplet suppression modeling of the flames and consideration of the amount of humidification of the air stream for the reported experimental mists quantitatively accounted for the observed response of the flames to the added liquid water mass as well as the effect of water droplets in this size range. Because of the higher strain rate at extinction, the optimum size water droplet was $\leq$ 15 μm, somewhat smaller than for methane air flames. This smaller optimum size may be anticipated for other fuels considering the similarity of the extinction properties of propane to that of many other higher hydrocarbon "typical" fuels. The present findings indicated that, if the delivery issues inherent to a condensed phase fire suppressant were successfully addressed, aerosols of water composed of fairly small droplets have the potential to be comparable to that of CF_3Br.

4.5.2 Alkali Metal Bicarbonates, Chemically Active Fire Suppressants

Fire suppression by chemically active particulates such as the alkali metal bicarbonates had been investigated for a number of years prior to the NGP.[1,2,3,4] $NaHCO_3$ powder (effective diameter < 10 μm) was known to be far more effective than any other gaseous chemical agent being considered to replace halon 1301, but the exact physical and chemical mechanism was unquantified. Explicit understanding of the suppression behavior was also lacking. Two NGP projects explored the suppression behavior of these powders in counterflow flames, providing quantitative information that contributed to the development of suitable chemical and physical models describing the behavior of these aerosols.

Study I: Extinguishment of Flames with $KHCO_3$ and $NaHCO_3$

Experimental

NRL staff examined the fire suppression effectiveness of solid aerosols of sodium bicarbonate ($NaHCO_3$) and potassium bicarbonate ($KHCO_3$) in extinguishing non-premixed counterflow propane air flames using the counterflow burner described in Section 4.5.1 and shown schematically in Figure 4–36.[114,115] For the powder aerosol suppression studies, air was supplied through the top tube and propane through the bottom tube as is shown in Figure 4-46. This figure also shows the location, relative to the stagnation plane, of the visible flame, and predicted profiles of the temperature and the flame radicals H, O and OH. Experimental strain rates were evaluated using laser Doppler velocimetry (LDV) following the procedure outlined by Zegers et al.[109] Uninhibited propane/air flames had an extinction strain rate of $\approx$ 600 s^{-1}. Powder suppression efficiency was evaluated by adding powder to flames whose uninhibited strain rates were 180 s^{-1}, 305 s^{-1}, and 475 s^{-1}, referred to as low, medium, and high. The flows and strain rates are summarized in Table 4–6.

The powder delivery system provided a steady flow of agent, with controlled variability from $\approx$ 10 mg/min to 300 mg/min. The system, shown in Figure 4-47, consisted of a glass metering valve with an adjustable orifice and a tee above the valve where the powder could be introduced. The valve was made from a tapered brass rod inserted into a matching tapered glass orifice. The system was airtight and the orifice could be changed by screwing the tapered rod in or out. A hose clamp holding a piece of teflon was fastened to the glass metering valve at about the position of the valve. The teflon was used to

contact a rotating wheel of variable frequency. A modulated helium-neon laser beam, monitored with a lock-in detector, was used to measure the powder flow. The laser beam was positioned perpendicular to the flow of powder just below the top tube exit. Scattered laser light created by the powder flow was collected by a photomultiplier tube and collection lens at 90°. The intensity of the scattered light was calibrated to the powder flow by collecting and massing powder with no flame. Because the particle scattering intensity is a function of the air velocity and the size distribution of the particles, a calibration was obtained for each powder size and at each flow tested.

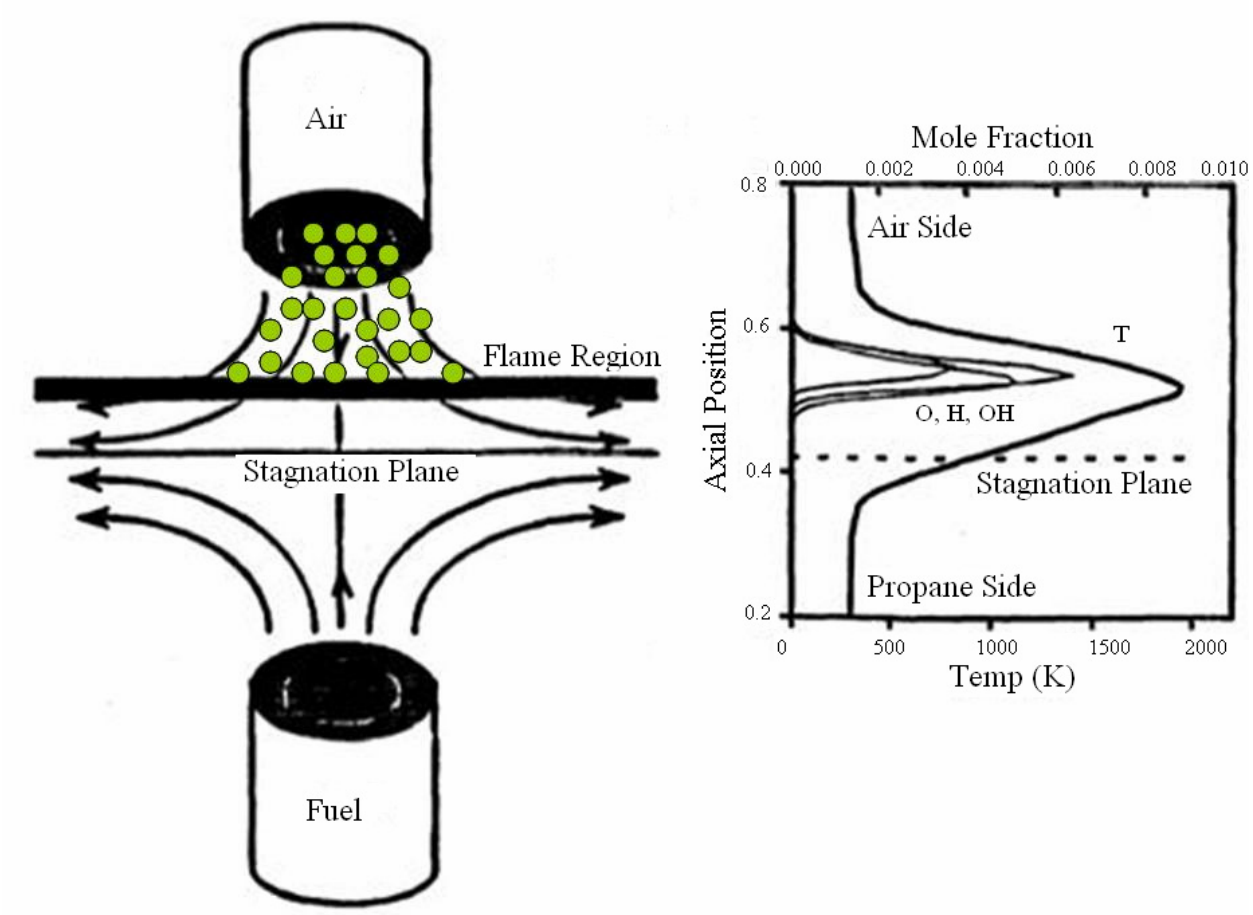

Figure 4-46. Schematic of the Non-premixed Counterflow Burner and Calculated Temperature, O, H, and OH Profiles for the Low Strain Flame. [114]

Table 4–6. Flow and Strain Rate Conditions for Extinction Experiments. [114]

	Low Strain Flame	Medium Strain Flame	High Strain Flame
Air Flow (L/min)	1.5	2.4	3.5
Fuel Flow (L/min)	1.0	1.7	2.8
Global Strain Rate[a] (s^{-1})	110	180	290
Measured Strain Rate (s^{-1})	180	305	475

[a] Calculated strain rate following Zegers et al.[110]

A video system was used to determine the exact time that the flame was extinguished. Using a fiber optic positioned on the video screen, the intensity of a portion of the flame was monitored and recorded simultaneously with the powder scattering intensity using a LabView controlled A/D board. The addition of powder to the flame dramatically increased the excited C_2 emission from the flame. A suitable optical filter was used to block this emission from the video monitor. Extinction of the flame was evidenced by a dramatic change in light intensity from the video signal. The corresponding powder scattering signal was evaluated to determine the powder flow rate at extinction.

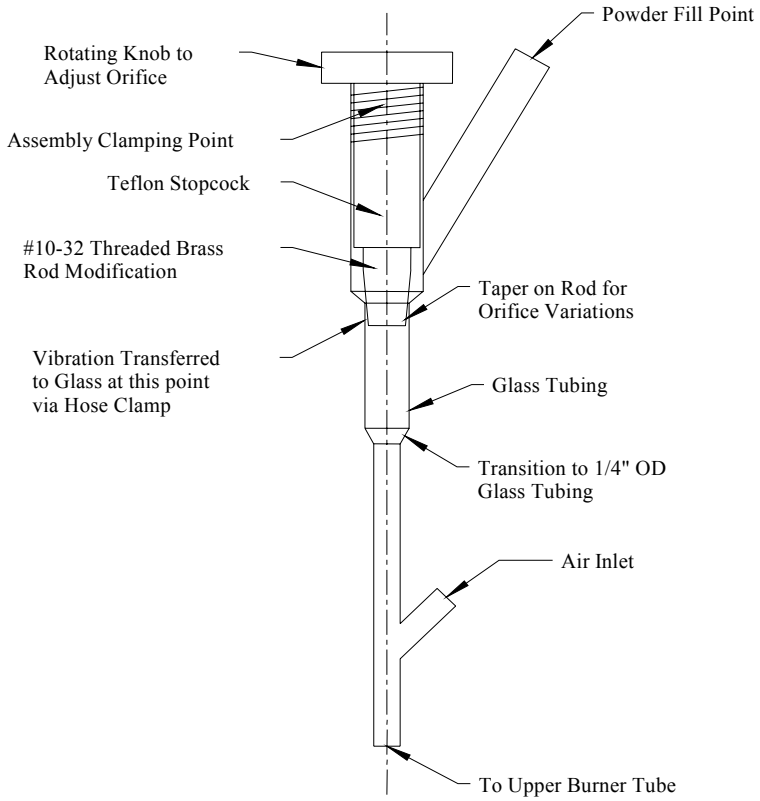

Figure 4-47. Powder Delivery System. [115]

Prior to each test, the chamber and tubes were cleaned to remove any excess powder. The flame was ignited and established midway between the two tubes, and the flows adjusted to produce the desired strain rate per Table 4–6. Once the system was acquiring data, the powder was turned on, mixing into the air stream from above the flame to simulate total flooding agent delivery systems. Particle delivery from the top also minimized any size dependent particle entrainment/flow issues. The flow was gradually ramped up until the flame extinguished. In this flow configuration (air on top, fuel on bottom) the propane/air flames tended to extinguish only along the centerline, leaving an annular flame attached to the upper tube. However, the extinction strain rates determined from the centerline extinction were consistent with other studies and have been shown to be valid.[110] Total extinguishment occurred for the propane/air flames only after an excessive amount of powder was delivered to the flame to sufficiently overwhelm it. The flat horizontal burning region of the flame was centered along the axis and positioned at the location determined by the momenta of the flows. However, the flame was rounded at the edges and had a bowl-like shape. The top of the flame curved around and attached to the outer rim of the upper burner tube. Upon extinction, the flat horizontal region of the flame disappeared, but the upper curved region of the flame remained stabilized to the upper burner tube. The flame would continue to burn in the annular

configuration even after the flow of powder was stopped as the flame had attached and stabilized itself on the upper tube. The air and fuel flows were decreased to destabilize the annular flame and recover the original flame structure. The process was repeated until 8 to 10 extinction points were obtained. This procedure was repeated for the same powder at the remaining two strain rates.

Tests were conducted with both sodium bicarbonate ($NaHCO_3$) and potassium bicarbonate ($KHCO_3$). Both powders were mechanically sieved into size ranges of <38 μm, 38 μm to 45 μm, 45 μm to 53 μm, 53 μm to 63 μm, and 63 μm to 75 μm using a commercial sieving unit. Silica was added to the powder samples (2 % by mass) as a drying additive. Both powders seemed to flow very freely with almost no agglomeration noticed. Representative micrographs of the $NaHCO_3$ powders are shown in Figure 4-48; micrographs for the $KHCO_3$ powders, ground and sieved at 45 μm to 53 μm are shown in Figure 4-49.

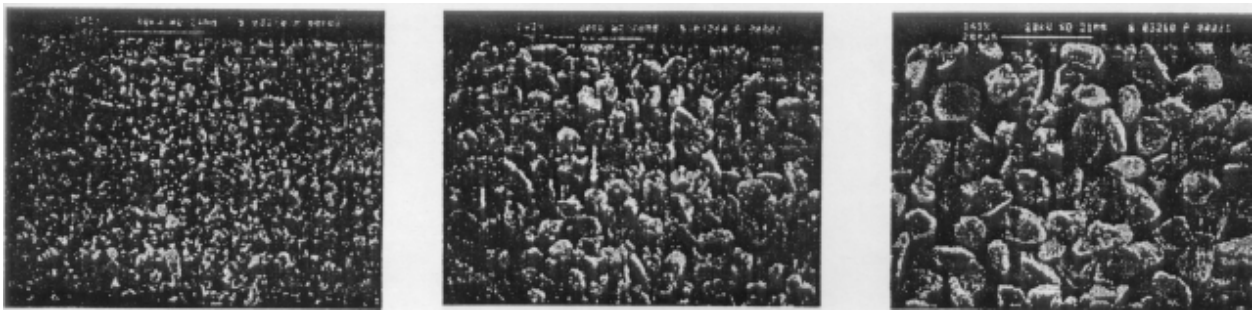

38 μm 45 μm to 53 μm 63 μm to 75 μm

Figure 4-48. Typical Micrographs of $NaHCO_3$ Powder Samples. [115]

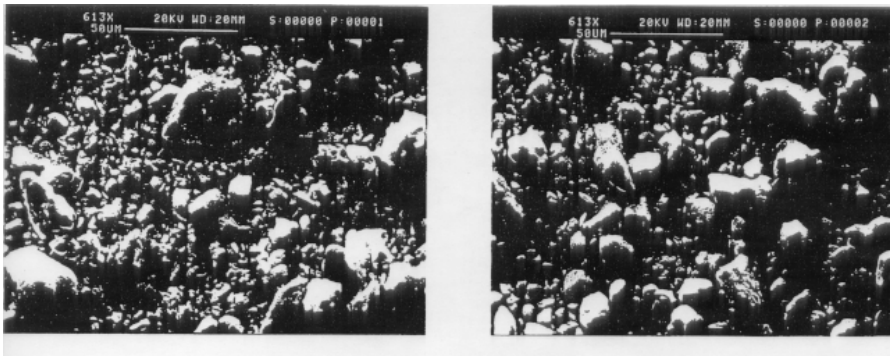

Figure 4-49. Typical Micrographs of $KHCO_3$ Powder. [115]

Results and Discussion

Extinction mass concentration measurements as a function of the measured strain rate and particle size bin are tabulated in Table 4–7 and plotted in Figure 4-50. The halon 1301 data were derived from Zegers et al.[109]

Table 4–7. Propane-air Counterflow Non-premixed Flame Extinction Mass Concentrations for Powders and Halon 1301. [114]

Chemical	Measured Strain rate (s^{-1})	Extinction Mass Concentration for Specified Size Bin (g/m^3)				
		< 38 µm	38 µm to 45 µm	45 µm to 53 µm	53 µm to 63 µm	63 µm to 75 µm
$NaHCO_3$	180	70	52	150	270	730
	310	8	15	53	56	80
	480	4	1	7	7	4
$KHCO_3$	180	12	18	70	100	370
	310	3	12	20	18	51
	480	1	6	3	1	2
Halon 1301	180	110				
	310	56				
	480	15				

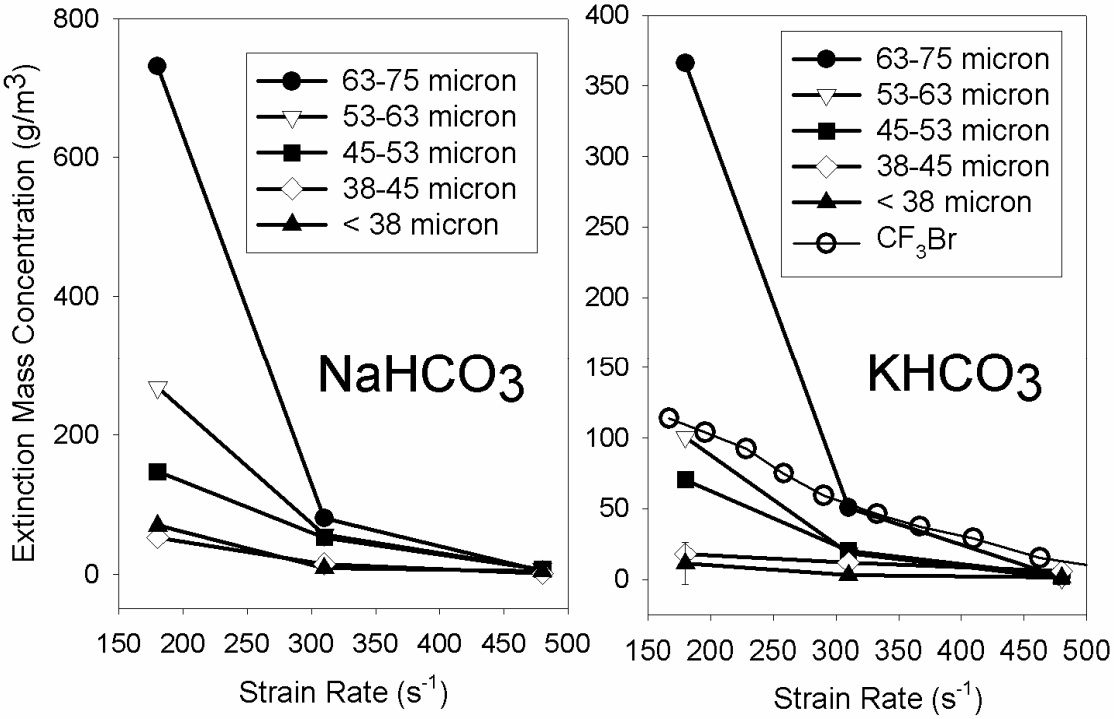

Figure 4-50. Extinction Mass Concentration as a Function of Strain Rate for Various Particle Sizes Ranges of $NaHCO_3$ and $KHCO_3$ Powders in a Propane/air, Counterflow, Non-premixed Flame. [114]

In general, the extinction mass concentration varied inversely with the strain rate of the flame and directly with the particle size of the powder. $KHCO_3$ was approximately 2.5 times more effective than $NaHCO_3$ on a mass basis in extinguishing the flame (3 times more effective on a molar basis). The data in Figure 4-50 are replotted in Figure 4-51, showing the extinction mass concentration vs. average particle

diameter for each strain rate flame for $NaHCO_3$ and $KHCO_3$. The most dramatic increase in performance for the smaller particles was observed for the low strain rate flame.

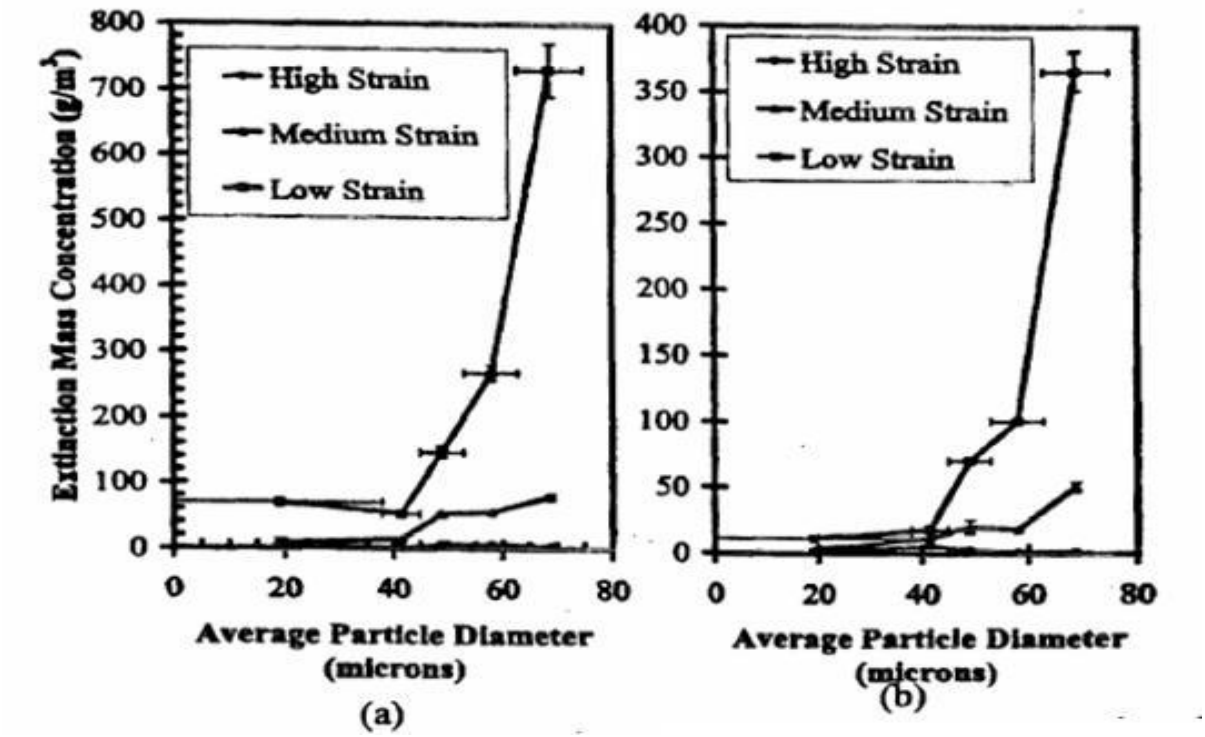

Figure 4-51. Data from Figure 4-50 Plotted to Show Extinction Mass Concentration as a Function of Particle Size Range for Each Flame Strain Rate and Added Powder. [114]

A number of factors have been postulated to contribute to the inhibition of fires by powders although the exact mode of the alkali metal bicarbonates' effectiveness is still not completely understood. The powder adds a great deal of heat capacity to the flame, and solid particles are often effective infrared radiators, leading to radiation cooling of the flame zone. In addition, the alkali metal bicarbonates undergo endothermic decomposition at elevated temperatures, releasing carbon dioxide. The residual alkali hydroxide vaporizes and decomposes at a much higher temperature. The difference in effectiveness between sodium and potassium is also partially due to differences in decomposition temperatures and enthalpies, and possibly to differences in catalytic scavenging cycles between the two elements. The possibility of free radical scavenging processes involving either the solid surface of the particle (heterogeneous) or gaseous by-products of the decomposition (homogeneous) have been postulated. Catalytic reactions would involve the alkali metal ion (i.e., Na, K) and proceed as $A + R + M \rightarrow AR + M$ followed by $AR + R' \rightarrow A + RR'$ where A is the alkali metal ion, R and R' are H, O, or OH, and M is a third body. These reactions are exothermic and add heat to the flame. However, under favorable thermochemistry, scavenging of the radicals inhibits the flame more than the additional heat promotes it. The possibility of catalytic recombination on the surface of the solid particle has also been suggested.[11,116]

Plots of the extinction mass concentration as a function of average particle diameter and surface area can be found in Figure 4-52a and Figure 4-52b, respectively, for the medium strain rate flames for both powders. The average particle diameter was calculated as the arithmetic mean of each particle size bin,

assuming an even distribution. This average particle diameter was then used in the calculation of the average particle surface area.

Ewing et al.[16] concluded that the fire extinguishing effectiveness of dry chemicals could be fully explained on the basis of particle size and distribution. They found that the effectiveness of the agent increased gradually as the particle diameter decreased until reaching a critical diameter. At this diameter there was a dramatic increase in the flame suppression efficiency and the effectiveness remained constant for all particles below the limit size. The limit sizes reported were 16 μm and 22 μm for $NaHCO_3$ and $KHCO_3$, respectively. NRL noticed a dramatic increase in the efficiency at about 45 μm for the $NaHCO_3$ sample at medium strain rate. A sizable increase was also noted for $KHCO_3$, but at a much larger particle size of about 65 μm. The higher value found for $KHCO_3$ may be influenced by the large percentage of very small particles in all size bins of this agent, as evidenced in representative photomicrographs of the various size bins.

Figure 4-52a shows that the measured extinction concentration increases with the diameter, although a linear correlation between extinction mass concentration and diameter was not found at the medium strain rate. There did appear to be a linear correlation at the medium strain rate case for the extinction mass concentration vs. average particle surface area as seen in Figure 4-52b. For this strain rate, the particle surface area available to interact with the flame more closely correlated with suppression effectiveness than particle diameter.

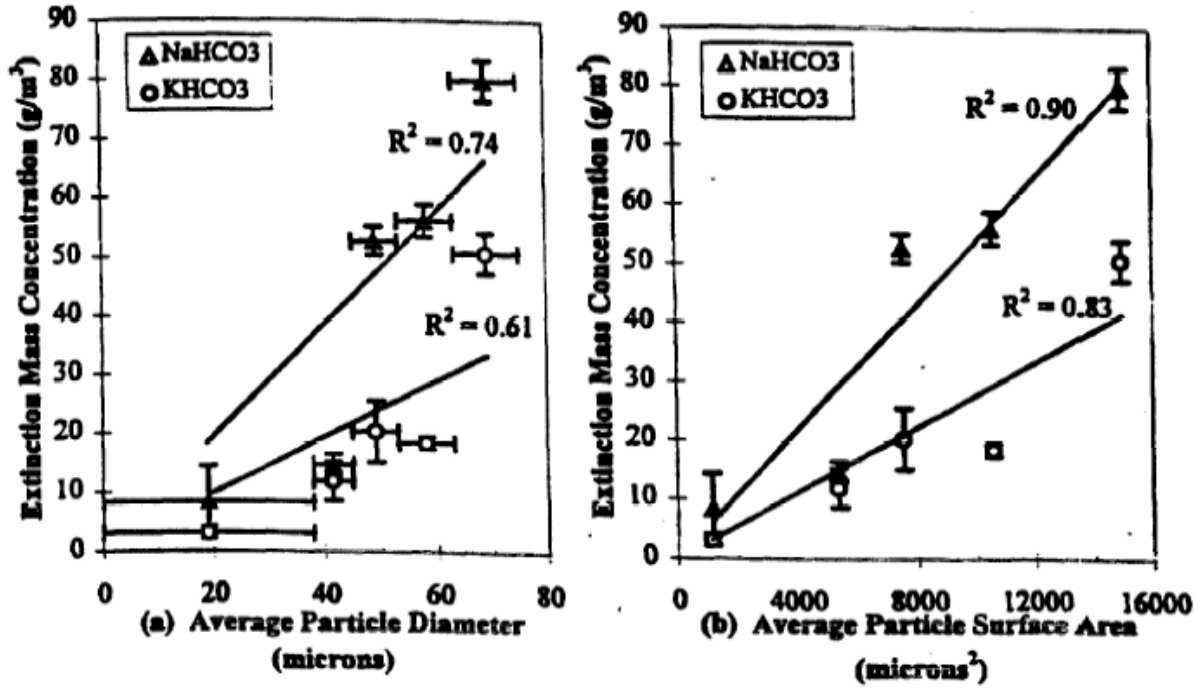

Figure 4-52. Extinction Mass Concentration as a Function of (a) Average Particle Diameter and Average Particle Surface Area for $NaHCO_3$ and $KHCO_3$ Powders in a Medium Strain Rate (310 s^{-1}) Propane/air Counterflow Non-premixed Flame. [114]

For the high and low strain rate cases, the correlation between surface area and effectiveness was less clear. For the low strain rate flame, the largest particles fell directly through the flame and into the bottom tube, as they were too large to remain suspended near the stagnation plane by the opposing fuel flow. A dramatic falloff in effectiveness was observed for the two largest particle bins, which likely resulted from the reduced residence time near the flame for these particle sizes. For the high strain rate case, the amount of powder required to extinguish the flame was so small that the particle delivery was difficult to accurately measure and control with our seeding apparatus, leading to a larger uncertainty. It was thus difficult to quantify a relationship between particle size or nominal surface area and extinction effectiveness for these two strain rates, although smaller particles were more effective in both cases. Effectiveness appeared to correlate more closely with surface area than with diameter. The determination of surface area in this study was based on the assumption of a spherical particle of the average diameter for the sieve fraction. A more accurate determination of the effect of surface area on suppression requires direct measurement of surface area (e.g., by gas adsorption), and a more monodisperse size distribution would be useful. However, the extinction results for the 1-D flames of uniform strain rate are consistent with "real world" observations that smaller particles are preferable presumably due to the increased surface area.

Suppression effectiveness should scale with particle surface area for most powder suppression modes. This includes heat transfer, radiation, decomposition/vaporization, and surface catalysis. Therefore, for a specified total powder mass, small particles are expected to be more effective at fire suppression, in accord with our experimental observations. Any dependence on surface area does not, however, allow determination of the primary means by which these particles extinguish fires, due to the interrelated operating suppression modes.

Sodium bicarbonate and potassium bicarbonate have different decomposition temperatures. $KHCO_3$ has a decomposition temperature between 100 °C and 200 °C, whereas $NaHCO_3$ decomposes at approximately 270 °C. Thus, $KHCO_3$ would require less time to reach its decomposition phase than $NaHCO_3$, under similar strain rate and particle size distribution. Also, according to data compiled by Ewing, Hughes, and Carhart[15], the reaction heat sinks, those associated with the decomposition, vaporization and dissociation, are reported to be 59.7 kcal/mole and 128.6 kcal/mole for $NaHCO_3$ and $KHCO_3$, respectively, based on vaporization of non-decrepitating solids. Non-decrepitating solids are defined as those which decompose or vaporize without breaking up. The sensible enthalpies of the decomposition/vaporization products of the two powders over a temperature range from ambient to the extinction temperature of a methane fire, were reported by Ewing, Hughes, and Carhart[15] to be 57.3 kcal/mole and 47.2 kcal/mole for $NaHCO_3$ and $KHCO_3$, respectively. The total sensible enthalpies (phase change and heating of the decomposition/evaporation products) are 117.0 kcal/mole for $NaHCO_3$ and 175.8 kcal/mole for $KHCO_3$. On a mass basis, the values are 1.39 kcal/g for $NaHCO_3$ and 1.76 for $KHCO_3$. For comparable powder sizes based on this thermal analysis, $KHCO_3$ should be some 30 % more effective than $NaHCO_3$. The comparable suppression effectiveness of small particles of sodium or potassium bicarbonate compared to halon 1301 and the much higher effectiveness of potassium vs. sodium shown in Figure 4-50 can be attributed to the chemical effectiveness of alkali metal bicarbonates.[117]

For the counterflow flame configuration, *where* the particles reside as they decompose is very important. As the particles exit the top tube of the burner, they position themselves in the counterflowing field at different locations based on their size and mass and the magnitude of the velocity field. Assuming that the particles behave as spherical bodies, the smaller, less massive particles are expected to follow the flow

field as it changes direction to flow radially outward because of the matching opposed fuel flow. Li, Libby, and Williams[104] mathematically examined the behavior of droplets in an opposed flow field. They observed that large droplets fall through the stagnation plane and are turned around by the opposing flow, if the drag force is greater than the gravitational force. The smallest particles always followed the gas velocity streamlines (assuming minimal thermophorectic effects). Slightly larger particles penetrated the stagnation plane and could be "pushed back" by the opposing flow and could exhibit a decaying oscillatory behavior near the stagnation plane. The amplitude for this oscillation was a function of the particle size. Lentati and Chelliah[80] calculated different trajectories for water droplets as a function of size in a counterflow burner. Their calculations indicated that the oscillatory amplitude is essentially zero for a 30 μm (non-evaporating) water drop. For smaller drops, the resulting oscillatory motion was essentially confined to a plane. It should be noted that these calculations are valid only for the particular conditions (e.g., strain rate, spherical drops, fuel density) of the models used. However, comparison to particles is qualitatively similar.

The proximity of the oscillatory "plane" to the stagnation plane depends on the particle shape and size and the strain rate of the flow but not on the original direction of the particle trajectory. Figure 4-53 shows the axial positions of the oscillatory planes relevant to bicarbonate spheres, 10 μm to 70 μm in diameter, in a potential non-reacting counterflow field model assuming the experimental flows for the medium strain rate flame studied. The drag forces on the particles were assumed to obey Stokes law. The 0 cm and 1 cm positions corresponded to the propane and air tube exits, respectively. Ratios of experimental flow to tube cross section were used as model exit velocities, yielding a stagnation plane at 0.39 cm.

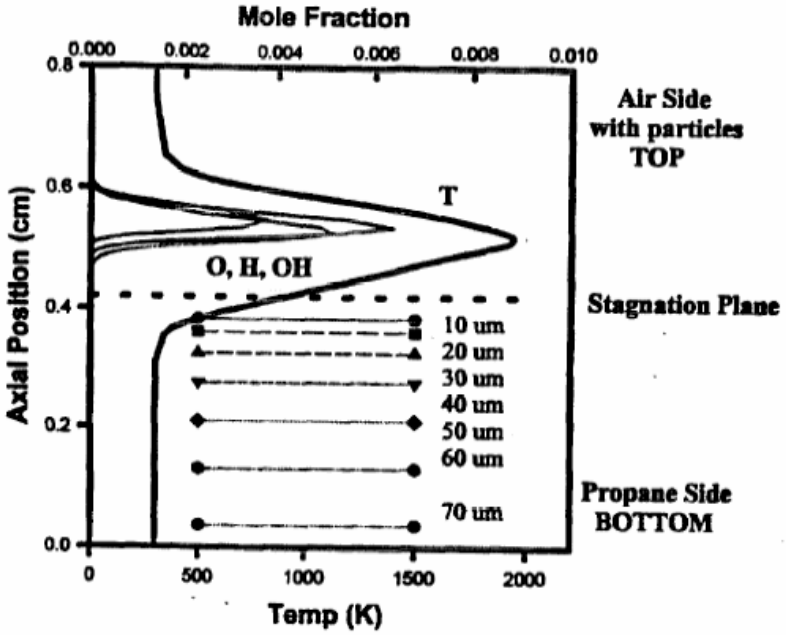

Figure 4-53. Calculated Particle Asymptotic Location as a Function of Particle Diameter for the Flow Conditions of the Low Strain Propane/air Flame. [114]

Also shown in Figure 4-53 are calculated axial temperature and O, H, and OH radical profiles for the propane/air flame at the medium strain rate. For particles introduced into the upper flow *or* the lower flow, the contribution of gravity dictates that the particle will asymptotically oscillate in a plane below the stagnation plane. Smaller particles were predicted to lie closer to the stagnation plane. The location of the oscillatory plane becomes significant if the opposing flow supports a flame. Stoichiometry dictates that the propane/air non-premixed flame be located on the air side, as shown in Figure 4-53. With air

(and powder particles) on the top and propane on the bottom, the flame is located above the stagnation plane. All particles will then pass through the flame and those particles within a certain range of diameters (~ 20 μm to 60 μm for the low strain rate flows) can oscillate below the stagnation plane and hence below the center of the flame but still in an elevated temperature region. As the particles decompose, they become smaller, and the opposing flow will move them closer to the stagnation plane, but never in the flame center if delivered with the air from the top.

With propane on top and air on the bottom, the flame is located below the stagnation plane on the air side. In this configuration, some of the particles oscillate at the flame maximum temperature, and hence also at the peak of the key flame radicals. This oscillatory location should lead to greater decomposition because the particle would experience a greater residence time in the higher temperature region and ultimately generate a higher inhibitor concentration closer to the maxima of the key flame radicals. Following this analysis, one might expect that there should be an optimum delivery particle size which would allow the particle to locate at the flame maximum. Since the distance of the flame center to the stagnation plane is a function of the strain rate, one might predict that the optimum particle size might also vary with strain rate. Experimentally, delivering powders via the lower tube is more complicated than delivering powders from the top. Top delivery is essentially "dropping" the particles on the flame; there is no restriction on how big a particle can be and entrainment is straightforward. Bottom, upward delivery, for the gas velocities and particles in this study, cannot deliver the largest particles to the flame since these particles cannot be supported and carried "up" by the entrainment flow velocity.

Flame extinguishment by dry chemical agents is due to a combination of both thermal and chemical mechanisms. The relative contribution of each mechanism is difficult to determine since effectiveness depends on the nature of the particle *and* the particle size and the flame conditions. Both suppression mechanisms rely on the degradation of the solid particles to achieve the maximum effect on the flame. The degree of degradation is a function of the particle size which with the gas velocity determines eventual location of the particles in and near the flame. Smaller particles decompose faster and this degradation increases suppression effectiveness in two ways: heat abstraction due to highly endothermic processes, including decomposition and vaporization; and production of gas-phase atoms that can promote scavenging of the important flame propagation radicals. Since all of the flow is forced to go through the flame, the location of the thermal extraction in the flow is probably less important than where the chemical players (if any) are released.

Conclusions

In propane/air counterflow non-premixed flames, $KHCO_3$ was shown to be more effective at extinguishment on a mass basis than $NaHCO_3$ for all particle sizes tested. The effectiveness of the powder agent varied inversely with the particle size for the size range tested; smaller particles were more effective in suppressing the flames than the larger ones. Model predictions addressing the behavior of particles in counterflowing fields were consistent with the observed behavior for the suppression effectiveness when the fuel is on the bottom. An explanation of the high effectiveness observed for the alkali metal bicarbonate particles required a significant contribution from a chemical suppression mechanism.

Study II: Modeling and Flame Extinguishment Measurements of $NaHCO_3$

Contrary to the extinction behavior observered for $NaHCO_3$ reported in the prior section, Trees and Seshadri[118] found a non-monotonic variation of $NaHCO_3$ particle mass fraction with particle size required to extinguish a non-premixed counterflow flame for the size range ≈ 0 μm to 30 μm. Chelliah and co-workers conducted NGP studies to address the uncertainties regarding the effect of $NaHCO_3$ particle size on flame extinction and developed a rigorous method of quantifying various physical, thermal, and chemical contributions.[119]

Flame Suppression with $NaHCO_3$

Figure 4-54 shows the apparatus for generating non-premixed, methane air counterflow flames. The $NaHCO_3$ particles were separated into five size ranges: <10 μm, 10 μm to 20 μm, 20 μm to 30 μm, 30 μm to 40 μm, and 40 μm to 60 μm using a vortex separation technique. Particles of a given size were introduced with the air stream at a relatively steady rate. The typical particle mass fraction was about 0.01, corresponding to a particle flow of about 0.1 g/min. For a selected $NaHCO_3$ loading, the flame extinction effectiveness of $NaHCO_3$ particles was characterized by the extinction flow strain rate, measured by two methods: a global formula based on the nozzle exit velocities and nozzle separation distance[81] and local velocity field measurements using laser Doppler velocimetry (LDV).

Because of the need to establish the accuracy of previously reported data with $NaHCO_3$ particles, considerable attention was devoted to the development of a particle seeder that could deliver steady feed rates of particles of specified sizes. Two approaches were used.

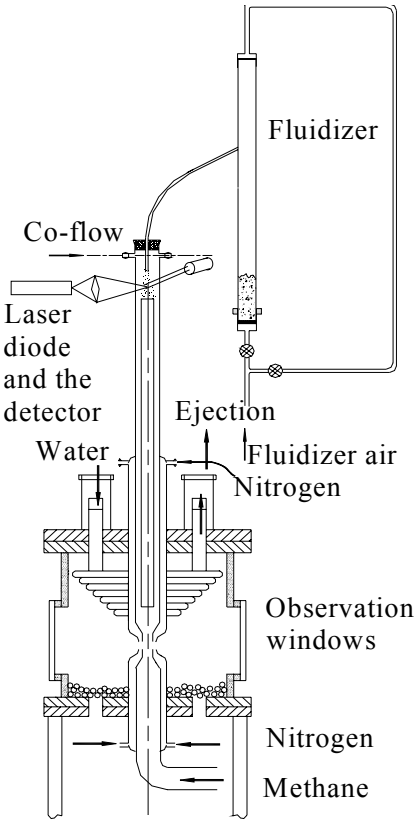

Figure 4-54. Schematic of the Counterflow Flame Apparatus with the Particle Seeder. [119]

For the small air flows (typically 0.1 L/s), the fluidized bed approach shown in Figure 4-54 gave satisfactory seeder performance, but only for particles less than 30 μm. The fluidized bed seeder consisted of a 19 mm diameter glass tube with two porous plugs connected at either end. The air inflow to the seeder, controlled through a mass flow controller, was split into two streams and connected to either end of the glass tube. The flow passing through the bottom, which controlled the fluidization level, was monitored through another flow controller. The fluidized particles and the total air entering the fluidization tube were ejected through a small tube located toward the middle of the tube. By maintaining the total air flow through the fluidizer tube constant, the mass fraction of particles attained a steady state. The particle feed rate was continuously monitored using a Mie scattering detection system located at the exit of the seeder air, as shown in Figure 4-54. This detection system consists of a laser diode operating at 671 nm, a Thor Labs DET1-SI High Speed Silicon Detector with collection by a 3 cm focal length lens, background radiation filtering using an Edmund Scientific 671 nm interference filter, and a Hewlett-Packard Model 7132 strip chart recorder. Because the seeder air flow was held fixed, the scattering signal was independent of the total air flow exiting through the air nozzle and was primarily dependent on the particle delivery rate of the seeder. The scattered signal was observed to decay slightly over 20 min to 30 min periods, but could be controlled by shifting part of the bottom fluidizing air to the top. Different particle flows were obtained by controlling the fraction of seeder air flowing through the top and the bottom. The actual mass fraction of the particles in the air stream was determined by calibrating the recorded scattering signal by a separate gravimetric analysis, usually performed before and after each flame extinction experiment.

For particles greater than 20 μm, a positive feed auger system (not shown) was employed. This seeder arrangement consisted of a multi-start Teflon screw (7 mm outer diameter and 5 mm inner diameter) in a high-precision stainless steel tube, where the screw was driven by speed-locked variable speed motor. This seeder was vibrated pneumatically to assist the particle flow, but the particle feed rate was primarily controlled by the motor speed. Part of the total air flow was diverted through a screw-driven particle seeder and was then mixed with the remaining air prior to exiting through the air nozzle. As before, air flow through the seeder was held constant while the total air flow through the nozzle was varied to attain different flame strain rates. For particle sizes above 20 μm, the Mie scattering signal varied less than ± 10 %. Particles smaller than 20 μm had a tendency to clump, and consequently significant variation of the scattering signal was observed. Hamins et al.[20] had overcome such clumping by adding about 1 % by mass of 10 nm silica particles to the $NaHCO_3$ particles. Due to the uncertainty of the effect of adding the silica particles and the associated safety issues, no silica was added.

Without particles, the measured global flame extinction strain rate was about 470 s^{-1}, while the measured local LDV strain rate was about 390 s^{-1}. These values are consistent with those reported previously by Chelliah et al.[103] As $NaHCO_3$ particles were added to the air stream, the flame extinction strain rate was expected to decrease because of the physical, thermal, and chemical effects of the particles.

The measured variation of flame extinction strain rate vs. the $NaHCO_3$ particle mass fraction in the air stream is shown in Figure 4-55 for the five particle size groups. All five groups demonstrated a clear decrease in the extinction strain rate with increasing particle loading. For a given particle mass fraction, the smallest particles (0 μm to 10 μm and 10 μm to 20 μm, which gave indistinguishable results) produced the lowest extinction strain rate, indicating their highest effectiveness as a flame suppressant.

Trees and Seshadri [118] had reported a similar variation of the mass of particle required with varying extinction strain rate, for each size group. However, they found that while 0 μm to 10 μm particles were the most effective, 10 μm to 20 μm particles were the least effective, with 20 μm to 30 μm particles showing an intermediate effectiveness. There were two differences between the studies that could have affected the results: (a) The fuels were different. Seshadri used a liquid heptane fuel pool, while the present experiments used gaseous methane. (b) Seshadri added about 1 % by mass of 10 nm silica particles to minimize the clumping of particles and help fluidize the smaller particles.

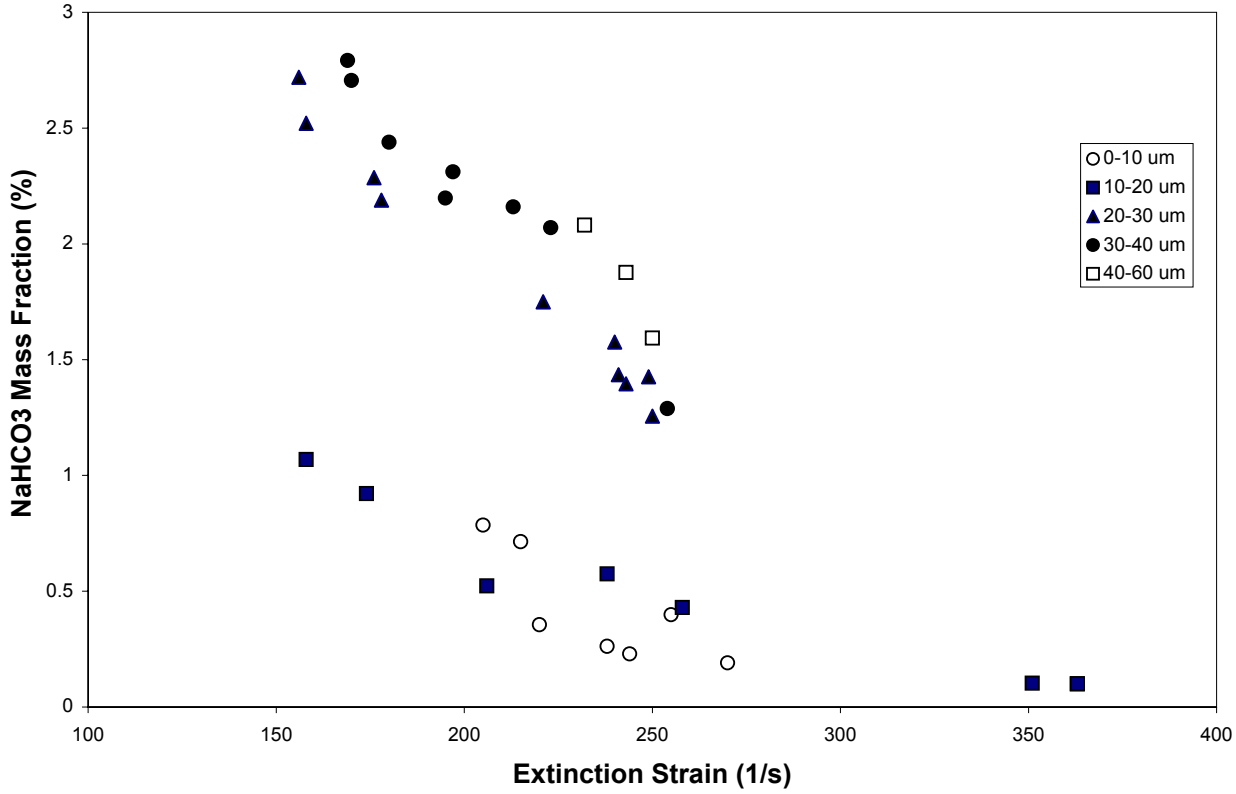

Figure 4-55. % $NaHCO_3$ by Mass in air as a Function of Extinction Strain Rate for Different Size Groups of Particles. [119]

When sodium bicarbonate particles are heated, they are known to decompose into oxides of Na in two stages. In the first stage, $NaHCO_3$ decomposes to solid sodium carbonate (Na_2CO_3), H_2O, and CO_2 around 543 K. (Note that the global decomposition temperature can vary depending on the particle heating rate, e.g., smaller particles are expected to heat rapidly when exposed to the flame environment because of their higher surface area/volume ratios than the larger particles.) In the second stage, Na_2CO_3 is known to decompose at 1170 K, leading to formation of Na_2O and CO_2. In the presence of water, however, Na_2CO_3 and Na_2O are known to react to form sodium hydroxide (NaOH).[120] The NaOH formed promotes catalytic recombination of the radicals species needed for flame propagation, causing the flame to extinguish readily.[121]

Numerical Simulation of $NaHCO_3$ Particle Effects

The numerical model described earlier in Section 4.5.1 was extended to include the effects of sodium bicarbonate particle transport, heating, decomposition and subsequent interaction of decomposed gaseous species with the homogeneous flame chemistry. The detailed gas-phase kinetic model for methane-air was augmented with a 20-step elementary mechanism for Na from Jensen and Jones.[121] The model developed for sodium bicarbonate particles involved considerable additional uncertainties. These included the non-spherical nature of the particles, the transient heating effect of the particles, the heterogeneous decomposition mechanism of sodium bicarbonate, and the gas-phase chemical inhibition mechanism by intermediate species formed from the decomposition.

Previous studies had indicated that sodium bicarbonate decomposes at a low temperature of about 543 K to form sodium carbonate through the reaction:[10]

$$2\,(NaHCO_3)_s \rightarrow (Na_2CO)_s + CO_2 + H_2O.$$

For particle temperatures above 1124 K, the sodium carbonate formed can decompose further to form other reaction intermediates of Na. Based on these observations, Friedman and Levy[120] had postulated that NaOH is the primary inhibiting compound responsible for flame extinction and proposed the following reaction pathways leading to formation of NaOH

$$(Na_2CO_3)_s \rightarrow (Na_2O)_{liq} + CO_2,$$

$$(Na_2O)_{liq} + H_2O \rightarrow 2NaOH,$$

$$(Na_2O)_{liq} \rightarrow Na_2O,$$

followed by the homogeneous reaction:

$$Na_2O + H_2O \rightarrow 2NaOH.$$

Once the alkali metal hydroxide was formed, the following catalytic radical scavenging cycle was known to be responsible for reduction of the radical pool

$$NaOH + H \rightarrow H_2O + Na,$$

$$Na + OH + M \rightarrow NaOH + M,$$

$$NaOH + OH \rightarrow H_2O + NaO.$$

The relative importance of these reactions was not well established and the literature indicates some conflicting results.[117,120,121,122]

In the initial NGP simulations, a fast global decomposition reaction of the form,

$$2(NaHCO_3)_s \rightarrow 2NaOH + 2CO_2$$

was employed. The particle temperature at which the decomposition occurred (defined here as T_{decomp}) was varied to obtain the sensitivity of the particle size. Although such a global model can be fine tuned to a narrow range of conditions (e.g., narrow particle size range), it should be cautioned that extension of such models to a wider range of conditions may lead to physically unrealistic results. For the homogeneous chemistry associated with NaOH, a detailed reaction model involving 6 species in 20 elementary reactions proposed by Jensen and Jones[121] was employed, in conjunction with the detailed chemistry model for methane oxidation.[80]

Figure 4-56 shows the predicted variation of $NaHCO_3$ mass fraction as a function of flame extinction strain rate, for selected $NaHCO_3$ particle size groups. For comparison, a plot of equivalent NaOH mass fraction for different extinction strain rates is also shown. The predicted curve with NaOH indicates the absolute maximum inhibition possible, based on the homogeneous model employed. Different NaOH reaction mechanisms were expected to modify this curve, but the predicted trends were not expected to change. The results clearly indicate that particles above 20 μm have a small effect on flame extinction, but as the particle size decreased below 20 μm, the extinction strain rate decreased significantly, indicating a remarkable increase in the effectiveness. This effect was attributed to the rapid heating of the particle and fast decomposition processes.

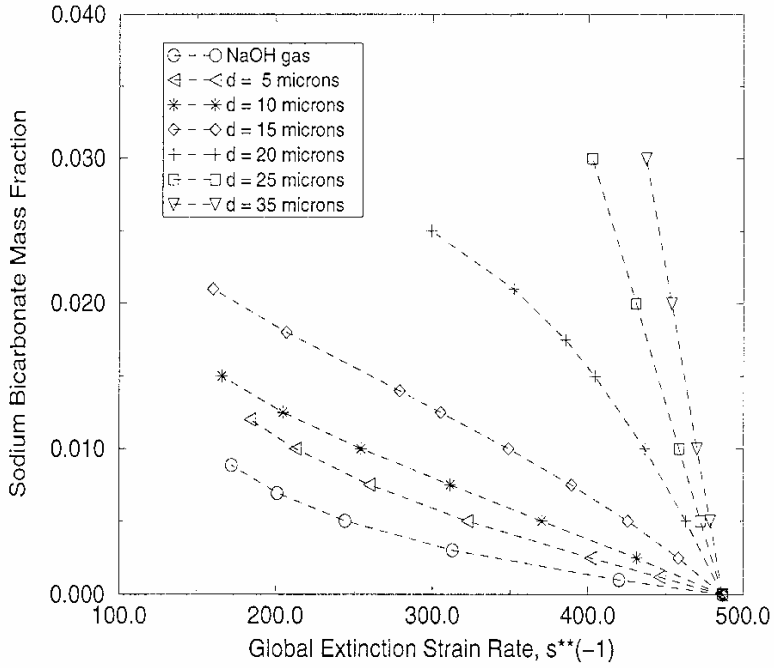

Figure 4-56. Numerical Prediction of $NaHCO_3$ Mass Fraction as a Function of Extinction Strain Rate, for Selected Particle Sizes. [119]

By varying the T_{decomp} described earlier, the location at which these particles were rapidly decomposing in the flow field was varied. As a consequence, the amount of Na released to the homogeneous phase is affected, leading to a varying degree of chemical inhibition. To quantify the contributing thermal and chemical effects, the source terms were selectively turned "off" in the model. Unlike previously reported fine-water droplet simulations, these results indicated a significant chemical effect in the presence of $NaHCO_3$ particles. For the dilute particle loading considered here, the physical effects were found to be negligible. Improved methods of treating the particle heating and subsequent heterogeneous particle decomposition need to be developed in order to provide more accurate flame extinction predictions.

Conclusions

All the $NaHCO_3$ particle sizes considered (< 10 μm, 10μm to 20μm, 20μm to 30μm, and 40μm to 60 μm) indicated a decrease in flame extinction strain rate with increasing particle mass fraction, consistent with the NRL results. The effectiveness of flame suppression (quantified here based on the $NaHCO_3$ mass fraction needed) varied monotonically with particle size, with the smallest size group being the most effective. Two independent approaches to particle seeding yielded identical results for the overlapping particle size range of 20 μm to 30 μm, providing considerable confidence in the measured results.

Numerical predictions taking into account the detailed homogeneous chemistry and global particle decomposition model indicated a trend in particle effectiveness very similar to that obtained from the experiments. By varying the temperature at which the particles decompose to gaseous products, the predictions showed that the smallest particles are more effective because of their rapid heating, leading to complete decomposition of the particles. By manipulating various source terms in the model, the superior effectiveness of $NaHCO_3$ particles was attributed to the homogeneous catalytic radical scavenging by NaOH formed, while thermal effects associated with particle heating played a minor role.

Co-flow, Non-premixed Flames – Cup Burners

The effectiveness of aerosol agents in a cup burner apparatus was not explicitly investigated under the NGP. What was investigated and is reported in Chapter 3, was the role of particle *formation* in the flame after agent introduction which limits the effectiveness of chemical agents. This is a fundamental thermodynamic limitation regardless of whether the agent enters the flame as a gaseous species or a condensed liquid or solid. The cup burner flame still remains a challenging yet relevant configuration for understanding aerosol effectiveness in general. Thus, work continues in a number of labs including the NRL[84] to understand the behavior of aerosols agents in a cup burner apparatus and other co-flow flame configurations.

4.5.3 Aqueous Metal Salt Solutions, Combined Chemical and Physical Suppression

Non-Premixed Flames

Introduction

Chelliah and coworkers, using both experimental and modeling approaches, examined the interactions of small droplets of water and water/NaOH solutions with steady, laminar counterflow methane/air non-premixed flames.[98] To compare to the experimental studies, the previously developed hybrid Eulerian-Lagrangian numerical model for monodisperse droplet distributions was generalized to account for more realistic, polydisperse size distributions.

Experimental Method

The counterflow burner, shown in Figure 4-57, was similar to that described in Study II in Section 1.5.2. A steady, planar, non-premixed flame was established in the mixing layer of counter flowing methane and air streams. The fuel and air nozzles (Pyrex glass) each had an area contraction ratio of 6.5 and an exit diameter of 1.5 cm, producing nearly plug flow velocity profiles at their exits. Co-flowing nitrogen streams on both fuel and air sides helped to maintain a very stable planar flame disk. The nozzles were enclosed in a cylindrical burner chamber, in which water cooling coils and air dilution of the post combustion gases eliminated secondary flames. The nozzle tubes entered the chamber through vacuum fittings which permitted easy adjustment of the nozzle separation distance, which is typically set to 12 mm. An air-driven mass flow ejector evacuated the product gases, while a differential pressure gauge monitored the chamber pressure, which was typically 120 Pa (12 mm water) below atmospheric pressure.

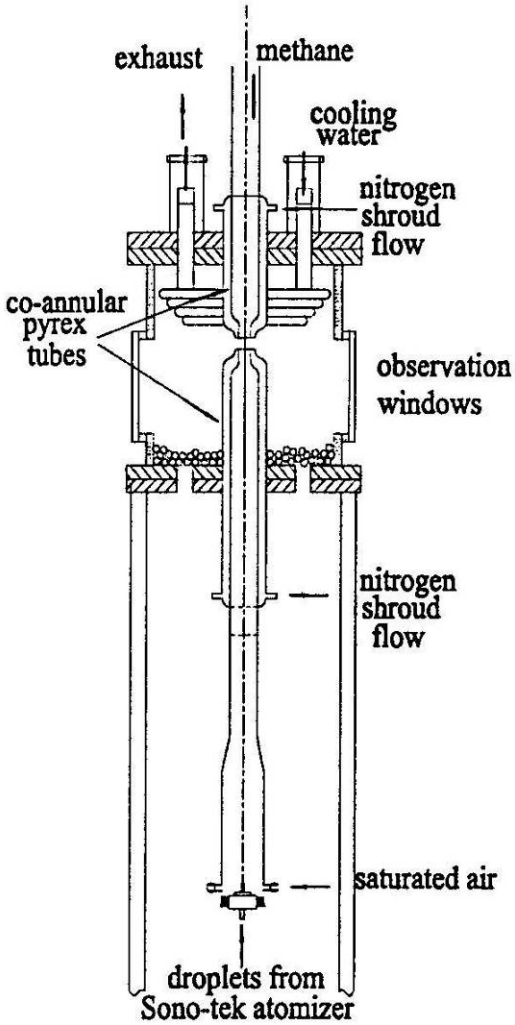

Figure 4-57. Schematic of the Counterflow Burner Configuration with the Water Droplet Atomizer.[98]

An oil-free shop compressor followed by a series of desiccant beds provided the air; the fuel gas was methane (BOC grade 4.0, 99.99% purity). Mass flow meters (Teledyne Hastings–Raydist, factory calibrated with a reported accuracy of ± 1% of full-scale reading) indicated the volumetric flows of the methane and air. For experiments involving water vapor or water droplets, the metered dry air was saturated with water vapor prior to the nozzle exit by bubbling the air through a water bath. A bath

heated to 5 ºC above ambient produced an air stream at the nozzle exit at ambient temperature and at least 97 % relative humidity (verified with a hygrometer, Testo 605-H1).

The droplet atomizer was located at the base of the bottom (air) tube, and the droplets were entrained in the airflow. The glass tubes allow easy detection of any water condensation on the tube walls. The droplet size distribution is measured using a PDPA (Aerometrics, two-component; model, DSA).

Two types of droplet generators were tested: (1) a piezoelectrically excited fluid jet atomization system (Fluid Jet Associates)[123] and (2) an ultrasonic fluid surface breakup system (Sono-Tek, Model 8700-120). The first atomizer was capable of generating truly monodisperse droplets (variable by changing the orifice diameter), but the small, 10 μm holes needed for generating 20 μm droplets proved susceptible to clogging and erosion. The second atomizer was found to be relatively simple to use and did not clog, but the droplets generated had a much wider size distribution. The median droplet size was varied by selecting a different length nozzle tip and resonance frequency. All the experimental flame extinction data were obtained using the ultrasonic droplet generator.

The ultrasonic droplet generation system consisted of the ultrasonic nozzle and a broadband ultrasonic frequency generator. A syringe pump (Instech Model 2000) with a plastic 10 cc syringe fed water to the atomizer. In the experiments, the water mass flow was fixed, and the air and fuel flows were increased until the flame extinguished. The flame was found to be very stable until the extinction point. The water mass flow at the nozzle exit was measured gravimetrically by carefully collecting all of the saturated air stream (with droplets) and impinging the droplets on a collection surface. These tests showed that while only about 70 % of the mass of water injected to the atomizer reached the nozzle exit, the operation of the droplet injection system was very consistent over the entire range of water and air flows of the tests.

The droplet number distribution (f) as a function of size (d) in the vicinity of the ultrasonic atomizer nozzle was characterized by the manufacturer and was believed to follow a log-normal distribution:

$$f(d) = \frac{1}{\sqrt{2\pi}d\sigma}\exp\left[-\frac{\ln d - \ln \mu}{2\sigma^2}\right] \tag{4-12}$$

with a median diameter (l) of about 20 μm and a Sauter mean diameter (SMD) of about 30 μm (for σ = 0.6). This normalized distribution, separated into 12 discrete sections for modeling purposes, is shown in Figure 4-58a. Nonetheless, based on the estimated settling velocities of different droplet sizes and the flow velocities in the air tube, it was found that not all the droplets produced by the atomizer would be convected out of the air nozzle. For example, for an airflow corresponding to a flow strain rate of about 285 s^{-1}, the estimated maximum droplet size that could be carried in the air stream was about 75 μm, whereas for a strain rate of 160 s^{-1}, the corresponding maximum droplet size was about 55 μm. Thus, the air flow velocity up the air-nozzle would modify the generated droplet size distribution. PDPA measurements verified the droplet sizes at the air nozzle exit. Figure 4-58b shows the measured droplet size distribution for a high strain rate of 285 s^{-1}, and Figure 4-58c shows a similar plot for a lower strain rate of 160 s^{-1}. The shift in maximum size of droplets was consistent with estimates, and the general shape of the distribution remained log-normal.

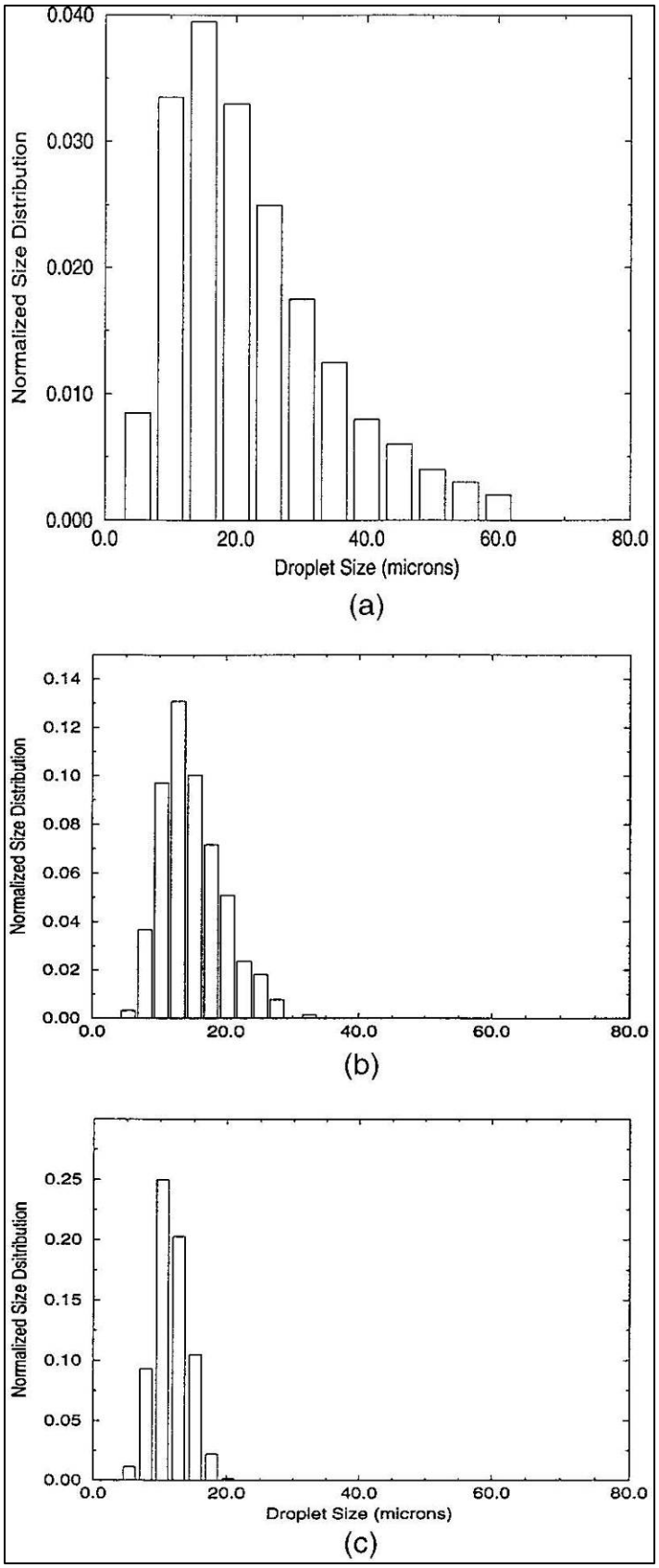

Figure 4-58. (a) Normalized Droplet Diameter Distribution of the Ultrasonic Atomizer as Reported by the Manufacturer; (b) and (c) Normalized Water Droplet Diameter Distributions Measured Using a PDPA at the Exit of the Air Nozzle for an Air Flow Corresponding to Counterflow Strain Rates of 285 s^{-1} and 160 s^{-1}, respectively. [98]

Flame extinction experiments were conducted by increasing the air and methane nozzle exit velocities such that the momentum of the two streams was balanced, that is,

$$\left(\rho v^2\right)_{air} = \left(\rho v^2\right)_{CH_4} \tag{4-13}$$

where ρ is the density and v is the axial velocity. Knowing the nozzle separation distance L, the flow strain rate was defined by the global formula[81]

$$a = 4\frac{|v_{air}|}{L} \tag{4-14}$$

For non-premixed methane/air flames, the measured global flame extinction strain rate of 470 s^{-1} was obtained, while the measured local flow velocity using a laser Doppler velocimetry system yielded a local flow strain rate of about 390 s^{-1}. Both of these numbers were highly reproducible and consistent with previous experiments and modeling efforts.[103] The experimental flame extinction results are all based on the global strain rate formula unless otherwise noted.

Results

The presence of condensed-phase water implied that at equilibrium, the air stream was saturated with water vapor, and this was verified using a hygrometer. At atmospheric pressure and a room temperature of 300 K, the saturated water vapor mole fraction in air is 0.0351 (mass fraction Y_{vap} = 0.0224). The saturated water vapor can have a significant effect on the flame extinction condition. Previously, detailed modeling efforts had indicated that the predicted local flame extinction strain rate reduced from 420 s^{-1} for a methane/air flame to 365 s^{-1} for methane and air saturated with water vapor (a reduction in extinction strain of 12 %).[80] Present experiments with saturated water vapor in the air stream yielded a global extinction strain rate of 405 s^{-1} (i.e., a reduction of 13 % from 470 s^{-1} measured for methane and dry air), in excellent agreement with the predictions.

Lazzarini et al.[98] also examined the effect of water droplets of 20 μm median diameter on the extinction condition for the flames. With increasing droplet number density (or mass fraction of water droplets in the air stream), it was expected that flame extinction would occur more readily, resulting in a lower extinction strain rate. Figure 4-59 plots the mass fraction of water in the condensed phase (Y_0) as a function of the flame extinction strain rate.

Note that the zero water droplet mass fraction corresponds to the case where the air stream is saturated with water vapor (i.e., Y_{vap} = 0.0224). The predicted variations of water droplet mass fraction as a function of global extinction strain rates assumed 20 μm monodisperse droplets. Irrespective of the assumption of monodisperse droplet size distribution in the simulations, the predicted trend is seen to be in reasonable agreement with experiments.

The experiments and predictions agreed well for pure water vapor. The agreement grew poorer with increasing droplet mass loading. In predictions, relaxation of the monodisperse size distribution approximation based on the measured distributions shown in Figure 4-58 was not expected to rectify this difference because 20 μm monodisperse droplets have been predicted to be the most effective. As discussed later in the numerical section, any broadening of the size distribution about 20 μm led to predicted higher mass fraction of water in the condensed phase for the same flame extinction strain rate. Thus, differences seen in Figure 4-59 between experiments and modeling were likely due to other causes.

In experiments, calibration of the water droplet mass flow through gravimetric analysis introduced errors; however, considerable care was taken to address uncertainties associated with the approach adopted.

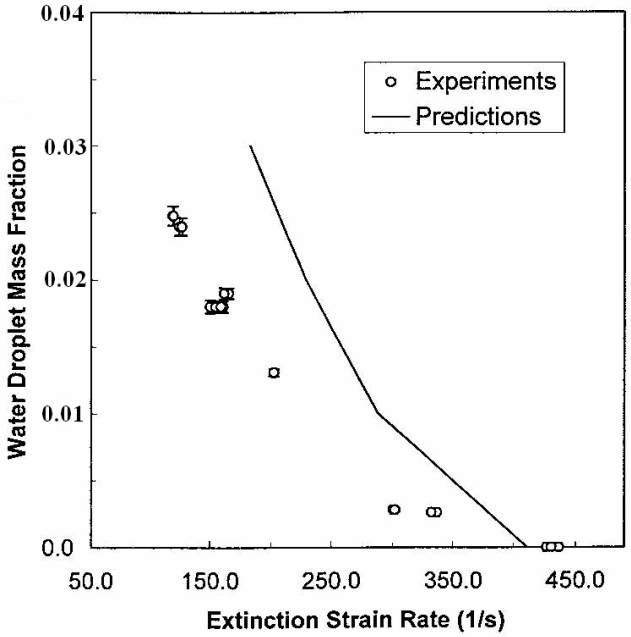

Figure 4-59. Variation of Water Droplet Mass Fraction in the Condensed Phase as a Function of Flame Extinction Strain Rate. [98]

Experiments and simulations also examined the effect of the addition of NaOH to the water droplets. The primary mechanism of flame extinction by pure water droplets is through the thermal cooling of the flame front, leading to slower chemical reaction rates. For example, in a counterflow field of methane and air, the 20 μm droplets were shown to be most effective because most of the droplet mass was predicted to evaporate near the oxygen consumption or radical species production region.[105,106] This thermal effect of water droplets can be considerably enhanced by including a chemically active fire-suppressing compound in water. NaOH was selected, as it was known to be the primary compound in the catalytic radical recombination path of sodium bicarbonate fire suppression.[121] Since the solubility of NaOH in cold water is about 30 % of the total mass,[124] a significant amount of NaOH can be released at the flame front, provided that the droplets consisting of water/NaOH are completely vaporized. As noted earlier in this chapter, 20 μm droplets were fully evaporated in this flame system. The same ultrasonic was used to deliver various aqueous solutions of NaOH and investigate their effect on suppressing counterflow methane/air flames.

Figure 4-60 plots the experimentally measured water/NaOH mass fractions as a function of the flame extinction strain rate. As before, the air flowing into the nozzle tube was saturated with pure water vapor. Because the NaOH vapor pressure is very small, less than 130 kPa (1 mm Hg) at room temperature[124], air saturated with pure water vapor was not expected to affect the evaporation of NaOH. The measured results indicated that with increasing NaOH mass fraction in water, the amount of water/NaOH mass fraction needed for flame extinction decreased significantly - almost a factor of 5 for 17.5 % NaOH by mass in water at the lowest strain rate considered. Combining thermal and chemical suppression effects leads to a significant increase in fire suppression ability, as shown in Figure 4-60.

For a selected extinction strain rate, Figure 4-60 also shows an interesting nonlinear decrease in total water/NaOH mass fraction with increasing NaOH fraction in the solution. Such a phenomenon may be related to saturation of NaOH in the vapor phase and must be addressed through future modeling efforts.

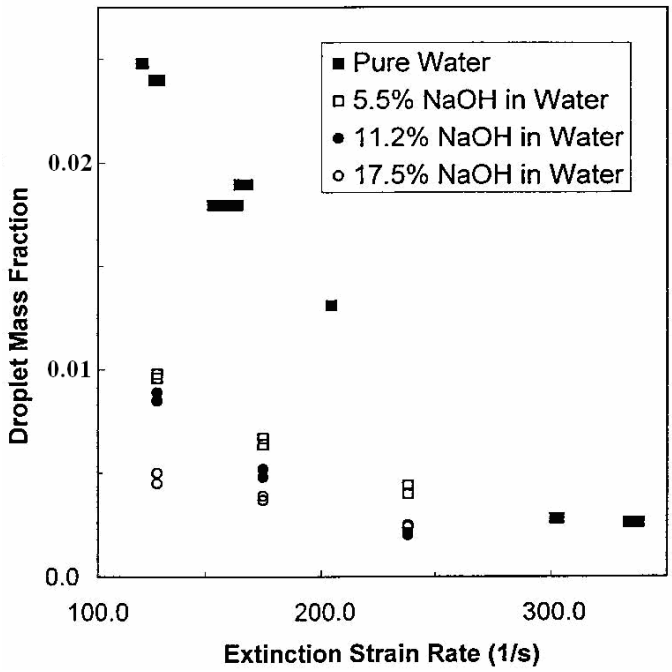

Figure 4-60. Droplet Mass Fraction in the Condensed Phase as a Function of Flame Extinction Strain Rate for Different Mass Loadings of NaOH in Water. [98]

Numerical Predictions

The hybrid Eulerian-Lagrangian formulation for gas and liquid phases described in Section 4.5.3 was used here.[80] This model includes a detailed reaction model for methane oxidation and transport of species and energy across the mixing layer. In this approach, knowing the gas-phase solution, the Lagrangian equations for mass, momentum, energy, and particle flux fraction (normalized by that at the air nozzle exit) were integrated in time to determine the droplet location and source terms contributing to the gas-phase conservation equations. With these new source terms, the Eulerian equations describing the gas phase were then integrated using a standard approach.[125] Finally, the two sets of coupled equations were iterated until a predetermined convergence criterion was reached.

As described in the experimental section, the flame extinction was realized by increasing the flow of methane and air (saturated with water vapor), while the mass flow of condensed water droplets ($m_{H2O,c}$) was held constant by the syringe pump. During this process, the mass fraction of water droplets

$$Y_0 = \frac{m_{H_2O,c}}{m_{air} + m_{H_2O,c}} \tag{4-15}$$

in air changed because of the varying air mass flow (m_{air}). In previous numerical predictions, it was assumed that the condensed phase water mass fraction (Y_0) was held constant at all strain rates. The predicted flame temperature variation as a function of flow strain rate for constant $m_{H2O,c}$ and for constant Y_0 are shown in Figure 4-61 for 20 μm monodisperse droplets. In the absence of radiative losses, usually only one extinction condition is realized for constant Y_0. Two flame extinction points are predicted if strain rate is changed in a proportional manner to keep the momentum balanced as depicted in Figure 4-61. Changing the strain rate by varying only the air and fuel flows for a constant $m_{H2O,c}$ = 2.65 mg/s/cm^2 generated the innermost closed oval in Figure 4-61. Starting at some strain rate away from extinction (e.g. point P), extinction conditions were predicted depending on whether strain rate was

increased (point E1) or strain rate was decreased (point E2). This phenomenon was purely a consequence of the two-phase system considered, and its occurrence was observed for water/NaOH solutions. In practice, this second extinction point (E2) can be realized by decreasing the oxidizer transport while the droplet transport is held constant.

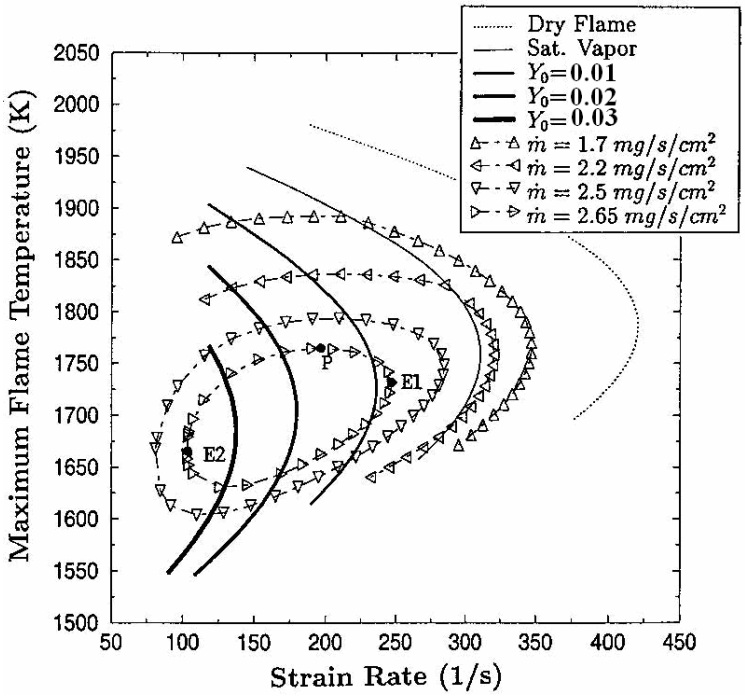

Figure 4-61. Variation of the Maximum Flame Temperature as a Function of Local Flow Strain Rate for Constant Droplet Mass Fractions (lines) and Constant Water Mass Flux Rates (Lines with Symbols). [98]

The model developed previously to simulate the interaction of fine water droplets with the counter flow flame assumed monodisperse droplets.[80] This assumption made the computations less demanding, but more importantly, the analyses of the results on droplet size effects became considerably simpler. Because of the experimental difficulties in realizing truly monodisperse water droplets, the above model was generalized here to include the polydisperse size effects. It was shown previously that for water mass loadings similar to those considered here, the ratio of droplet-to-droplet separation distance to droplet size was over 20. Under such conditions, the equation for droplet mass flux ($\mathfrak{I}$) (i.e., the spray equation), written in the form for the present quasi-one-dimensional counterflow field[80]

$$\frac{d\mathfrak{I}}{dt} + 2\mathfrak{I}U_d = \Gamma \tag{4-16}$$

was simplified by setting the droplet collision source term $\Gamma = 0$. Thus, by treating the droplet size distribution as composed of several discrete size groups[126,127], the simulation simplified to solving several Lagrangian equations for these discrete droplet size groups, with initial conditions corresponding to each discrete size group specified at the air nozzle exit.

For 0.01 mass fraction of water in the condensed phase, flame extinction calculations were performed with the three different discrete polydisperse size distributions shown in Figure 4-58. A comparison of these flame extinction results with the ideal 20 μm droplet size for this flow configuration is shown in Table 4–8. The predicted extinction strain rates indicate that any broadening of the size distribution of droplets from the ideal 20 μm size led to a higher flame extinction strain and a further deviation from the

experiments. At higher water mass loadings and decreasing flow strain rates, the thermal radiation effects are known to increase and may also have an influence in the present predictions. However, the strain rates indicated in Table 4–8 are rather moderate, and it is unlikely that the significant differences between experiments and modeling can be solely attributed to radiation heat loss effects.

Table 4–8. Experimental and Predicted Global Flame Extinction Strain Rates (s^{-1}) for Different Droplet Size Distributions and Water Droplet Mass Fraction of 0.01. [98]

	Experiment	20 μm Monodisperse Droplets	Distribution from Figure 4-58a	Distribution from Figure 4-58b	Distribution from Figure 4-58c
Global strain rate (s^{-1})	180	286	297	291	292

Conclusions and Summary

The main purpose of the work reported in this section was to provide experimental data to validate predictions of the effectiveness of fine water droplets in extinguishing counterflow non-premixed flames. On a mass basis, the predicted ability of fine water mist to suppress gaseous fires with similar or better effectiveness than halon 1301 was verified. Although the original goal was to obtain results using monodisperse droplets as assumed in previous theoretical investigations, this task became rather challenging because of difficulties associated with clogging of very small orifices (≈ 10 μm). Instead, an ultrasonic water atomizer generating log–normal distribution of droplet sizes, with a median droplet size of about 20 μm, was employed. The actual droplet size distribution was expected to deviate from the prescribed distribution at the atomizer depending on the convective velocity in the air tube in the counterflow burner, and this variation was characterized using a PDPA. The hybrid Eulerian–Lagrangian numerical model was extended to include such polydisperse droplet size distributions, subject to the assumption that the droplet collisions were negligible based on the large separation distance between droplets compared to their diameter.

When the air stream was saturated with water vapor only, the counterflow non-premixed flame extinction condition measurements agreed well with the corresponding numerical predictions. With addition of condensed phase water droplets, the trends agreed well; however, considerable quantitative differences exist between the experimental results and the modeling predictions. The observed differences were shown to be mildly affected by the polydispersivity of the atomizer employed. This led to the conclusion that other submodels in the numerical model, including radiative heat losses, need to be evaluated.

Addition of NOH to water complemented the thermal fire suppression effectivenss of water. At low strain rates (≈ 125 s^{-1}), 17.5% by mass of NaOH in the solution reduced the flame extinction strain rate by almost a factor of five. Inclusion of alkali metal compounds to water mist may not be desired in many applications because of corrosive effects. Yet combining the chemical-acting powder agent with the physical-acting liquid can enhance the suppression effectiveness of the liquid and provide a potentially more convenient delivery method for the powder agent.

Comparing Non-Premixed and Premixed Flame Suppression Behavior

Flame inhibition and extinguishment have been studied in a wide variety of laboratory flames, often with conflicting results. Chelliah and co-workers examined the effectiveness of water droplets and droplets of

water with three alkali metal compounds in both premixed and non-premixed opposed flow flames, with the intent of constructing a unified phenomenology.[128,129]

Experimental

Two apparatus were used, producing non-premixed and premixed methane/air flames. The burners were designed to be modular, so that the same water-generation and gas-supply systems could be used with either. The counterflow burner was as described in the previous section.[98] As before, the water mass flow was fixed, and the air and methane flows were increased together until the flame was extinguished. The fuel and air flows were adjusted so as to balance their momentum; according to Equation (4-13). The global flow strain rate was defined by Equation (4-14) providing a suitable parameter that describes the non-premixed flame extinction condition.[81] The total water (or solution) droplet mass fraction in the air + saturated water vapor stream was denoted as Y_0, while the mass fraction of the additive (i.e., NaOH, KOH, NaCl, or $FeCl_2$) was denoted as y_{add}. In the experiments, variation of a_{ext} with Y_0 as well as y_{add} were measured.

The premixed burner consisted of a straight-sided conical flame established at the exit of a Mache-Hebra-type nozzle. A schlieren imaging system provided the flame cone angle, which was used to determine the burning velocity.[77] The nozzle exit flow profile was characterized by laser Doppler velocimetry measurements. The typical half-cone angle of the flame was about 20^o. With addition of the solution droplets, the flame height was maintained constant at about 2.0 cm by adjusting the total flow of reactants while maintaining the equivalence ratio at the desired value. For the present data, the expanded uncertainties (with a coverage factor of 2) in the burning velocity were ± 6.0 %.

The inhibition of a laminar premixed flame was characterized by the relative decrease in the burning velocity (denoted here by S_L) with respect to that of an uninhibited flame (S_L).The simple conical premixed flame stabilized above the Mache-Hebra nozzle, and the associated flame cone angle measurement technique adopted here is one of many traditional methods of obtaining the laminar flame speed.[77] While curvature and stretch effects did exist in the flame, they were considered minor, particularly since all results were reported as normalized flame speed, S/S_0. The uninhibited methane and air flame speed obtained from the present burner was 35 cm/s ± 1.2 cm/s. Because the ultrasonic atomizer and the length of the Pyrex tube delivering the reactant gas mixture were the same as in the counterflow burner, the median droplet diameter was not expected to be different from that of the counterflow flames.

The ultrasonic atomizer was that described above. Droplets of pure water and water containing NaOH, KOH, and $FeCl_2$ were generated with a diameter range of 10 μm to 20 μm, except as noted.

Extinction of Non-Premixed Flames with Water Solutions

Figure 4-62 shows a comparison of droplet mass fraction in air (Y_0) as a function of the global extinction strain rate (a_{ext}), with varying NaOH mass fraction in water (y_{NaOH}). Similar results were reported above for NaOH mass fractions in water of y_{NaOH} = 0.055, 0.112, and 0.175.[98] Earlier experiments at the lowest flow strain rate of 125 s^{-1} and 0.175 NaOH in water showed a significantly higher effectiveness over the 0.055 and 0.112 NaOH cases (i.e., Y_0 = 0.005 for y_{NaOH} = 0.175 vs. Y_0 = 0.010 for y_{NaOH} = 0.055 and 0.112). However, for higher extinction strain rates (>125 s^{-1}), the earlier experiments showed a negligible differences in extinction condition with varying NaOH mass fraction.

The difference between the new y_{NaOH} = 0.175 data and previous results was found to be caused by a temperature dependence of the ultrasonic nozzle performance. When the nozzle tip was allowed to reach a steady operating temperature, typically about 40 ºC after about 15 min of continuous operation, the resulting flame extinction data were consistent and reproducible. While the revision of y_{NaOH} = 0.175 data can be attributed to ultrasonic atomizer nozzle performance, the observation that the mass fraction of NaOH above 0.055 yields no apparent increase in flame suppression is rather interesting. The differences in the effectiveness with varying NaOH mass fractions pointed to the importance of the residence time in the flow field and the requirement that both the droplets evaporate *and* the residue particles evaporate or decompose. Only after the drops have evaporated can the residue particles begin to decompose in order to release the chemical suppression agent. Higher concentration of additives for the same drop size resulted in a larger particle after drop evaporation. At a fixed strain rate (i.e. drop and resulting particle residence time) higher additive concentrations were expected to take longer to release all of the chemical agent.

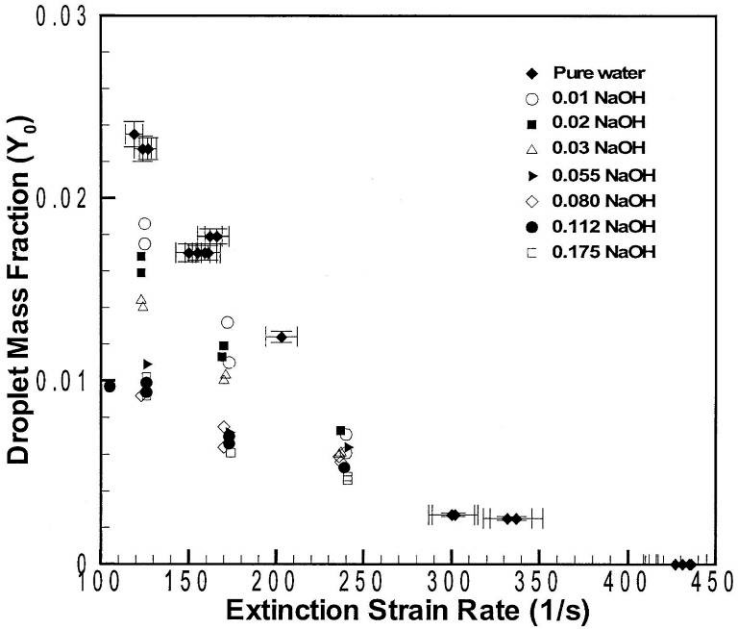

Figure 4-62. Droplet Mass Fraction as a Function of Extinction Strain Rate of a Methane/air Non-premixed Flame for Several NaOH Mass Fractions in Water. [129]

Also important to the degree of suppression effectiveness was a thermodynamic limit to the amount of resposnsible chemical catalytic scavenger that could be achieved in the gas phase at the flame conditions. Agent saturation behavior has been reported in premixed flames with iron, manganese, and tin organometallic compounds[130,131] and metal salts added as particles.[13] For sodium compounds, NaOH is the active chemical catalytic species for Na-based chemical suppression. Thus, the gas phase concentration of NaOH controlled the amount of suppression achievable. The flame extinction results shown in Figure 4-62 at the strain rate of 125 s^{-1} are replotted in Figure 4-63, according to the variation of droplet mass fraction (Y_0) vs. NaOH mass fraction in water (y_{NaOH}). As the y_{NaOH} in the water was increased above 0.08, the total droplet mass fraction (Y_0) needed for flame extinguishment became invariant with the NaOH mass fraction in the droplets. Also shown in Figure 4-63 is the mole fraction of NaOH in air (X_{NaOH}), *assuming* that all of the NaOH in the water droplets was completely released to the gas phase. As pointed out above, the amount of additive released is controlled by the residence time. In addition, the maximum X_{NaOH} that can exist in the gas phase is controlled by temperature and thermodynamics.

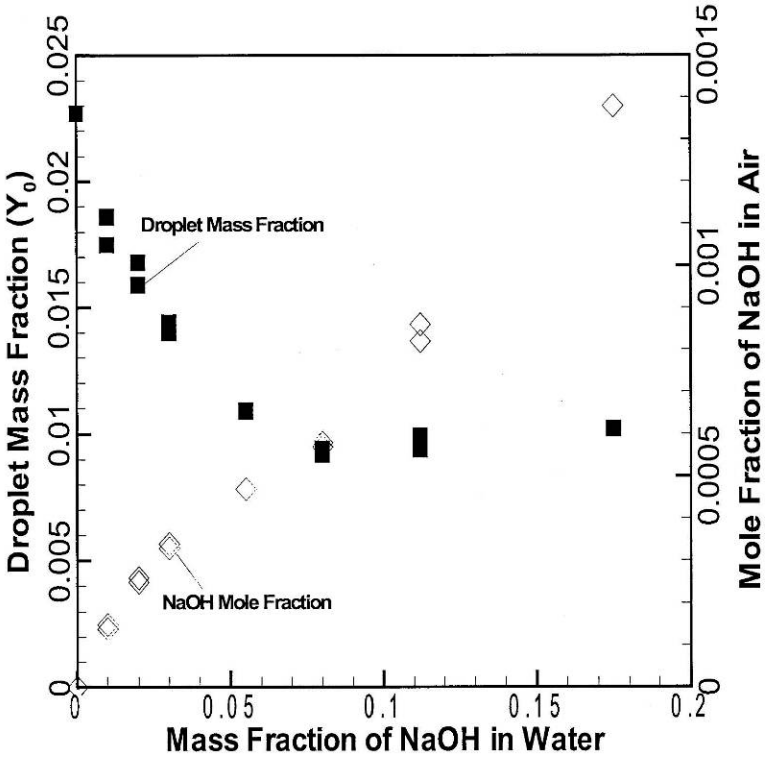

Figure 4-63. Y_0 and Mole Fraction of NaOH in Air as a Function of y_{NaOH} for the Extinction Strain of 125 s^{-1} in Figure 4-62. [129]

Thermochemical data for NaOH were used to estimate the maximum amount of gas phase NaOH achievable. Assuming that NaOH exists as a monomer in the gas phase, an equilibrium liquid-vapor calculation based on the Clausius-Clapeyron equation yielded an NaOH saturation temperature of 1125 K.[132] This vapor-liquid equilibrium temperature is about 400 K to 500 K below the characteristic temperature within the rate-limiting oxygen-consumption, radical-production region of the flame.[106] Because of the thermal boundary layer surrounding each evaporating droplet, it is conceivable that an effective temperature below the flame temperature may control the saturation of excess NaOH vapor. Alternatively, loss of active inhibiting species to condensation may be controlled by a compound with a lower vapor pressure than NaOH. In experiments, resolving the appropriate effective temperature that controls saturation of condensation of the relevant species is perhaps impossible, and therefore, only detailed numerical simulations can provide better understanding of the saturation phenomenon occurring. Although numerical simulations that include detailed interactions between the condensed phase and the gas phase have recently been developed to describe water droplet interactions,[80] analytical models for droplet evaporation of binary mixtures in flames have not. In this case, modeling the evaporation of binary liquid droplets with highly disparate boiling temperatures (373 K for water vs. 1663 K for NaOH) may require further simplifications. Only experimental results are presented here.

Besides NaOH, other alkali metal compounds are known to be chemically effective fire suppressants. In particular, potassium-containing compounds have been shown to be more effective than sodium.[13] Figure 4-64 shows experimental extinction strain rates of a methane/air non-premixed flame with similar sized water/KOH droplets containing varying mass fractions of KOH. For the lowest extinction strain rate considered (i.e., 125 s^{-1}), the data show increasing flame suppression up to about y_{KOH} = 0.112. Further increase in the KOH mass fraction in water up to 0.175, however, yielded no further increase in the flame suppression ability of the water/KOH solution. Following the analysis of water/NaOH saturation vapor conditions, current water/KOH results indicated that KOH saturates at a gas-phase mole

fraction of about $x_{KOH} = 0.0003$ for $y_{KOH} = 0.112$. Liquid-vapor equilibrium data for KOH indicated that this mole fraction corresponds to a gas temperature of about 1025 K, which is about 100 K lower than that obtained for the NaOH case. The lower effective saturation temperature for KOH was consistent with the lower boiling temperature of KOH (1597 K) compared to that of NaOH (1663 K).

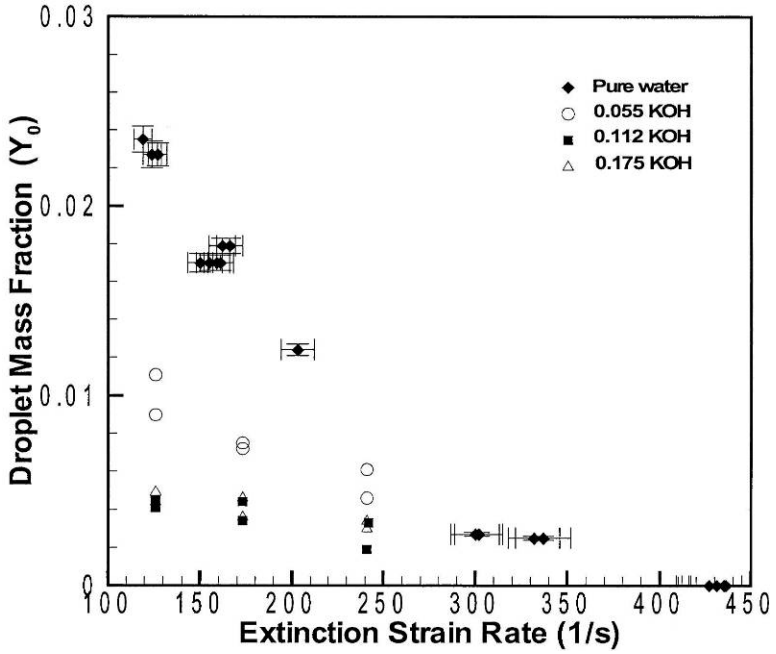

Figure 4-64. Droplet Mass Fraction as a Function of Extinction Strain Rate of a Methane/air Non-premixed Flame for Several KOH Mass Fractions in Water. [129]

Non-premixed methane/air flame extinction experiments were also conducted with NaCl. Water/NaCl droplets have been considered previously by Zheng et al.,[42] but only in the context of extinction of counterflow premixed flames as a function of fuel-air equivalence ratio. The flame suppression trends shown in Figure 4-64, with increasing NaCl mass fraction in water, were consistent with previous data with NaOH and KOH.

Compounds containing the metal Fe has previously been shown to be very effective at flame inhibition.[133] Here, exploratory experiments were conducted to test the efficacy of an Fe^{2+} compound dissolved in water. An $FeCl_2$ mass fraction of an $y_{FeCl2} = 0.15$ in water was tested, and this water/$FeCl_2$ solution clearly indicated a chemical inhibition effect, as seen in Figure 4-65. Although $FeCl_2$ was not as effective as NaCl on a mass basis, experiments with lower mass fractions of $FeCl_2$ must be performed to evaluate the occurrence of saturation phenomenon, as observed in water/NaOH solutions.

In order to relate the chemical inhibition of the agents considered here to previous studies, the non-premixed flame extinction results were analyzed on a molar basis of the additive. To avoid uncertainties related to saturation effects, only additive mass fractions below the saturation condition were considered. Since water/NaOH extinction results showed saturation of NaOH vapor was approached for additive mass fractions above 0.055, the molar comparisons between NaOH and KOH were performed at $y_{add} = 0.055$. For the extinction data points considered, the mole fraction of alkali metal hydroxide (AmOH) was evaluated and is plotted as a function of flame extinction strain rate, as shown in the upper panel of Figure 4-66.

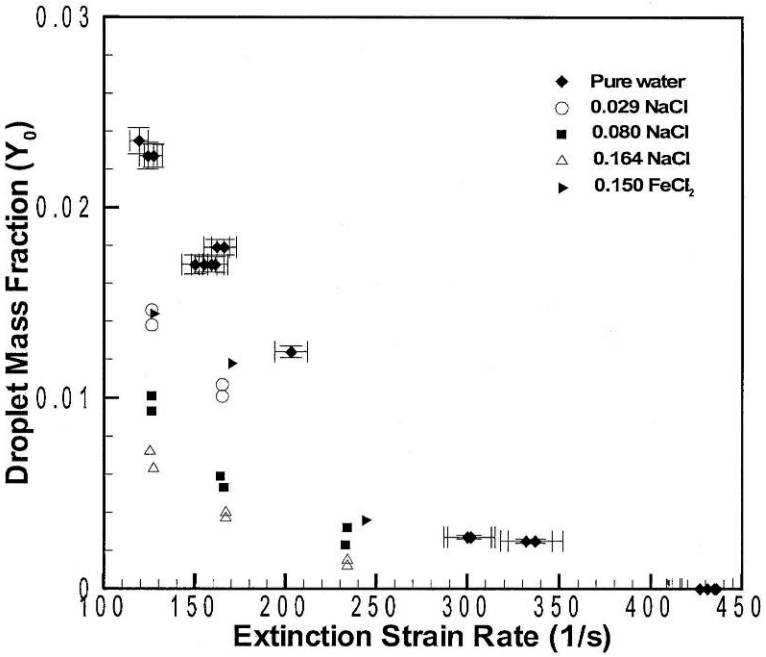

Figure 4-65. Droplet Mass Fraction as a Function of Extinction Strain Rate of a Methane/air Non-premixed Flame for NaCl and $FeCl_2$ in Water. [129]

These molar comparisons indicated a roughly double performance benefit of KOH over NaOH as an additive to water droplets, similar to what has been reported based on flames inhibited with particulates.[13] Kinetic studies indicated that recombination of K with OH is about 30 % faster than Na with OH and that recombination of K with O_2 is in fact 2 to 3 times faster than Na with O_2.[134] Thus, differences in the reaction kinetics was perhaps the primary reason for the more effective flame suppression of KOH over NaOH.[117]

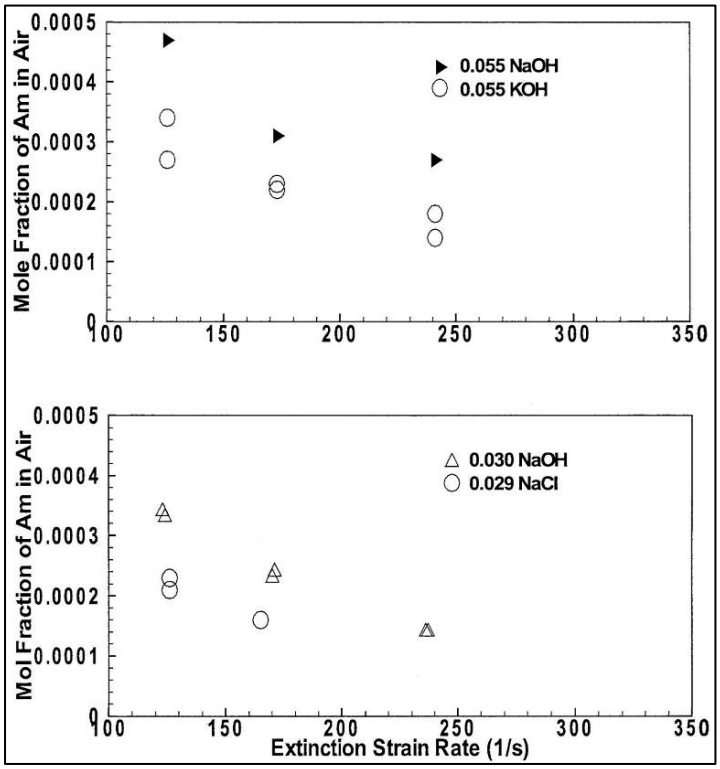

Figure 4-66. Upper panel: Mole Fraction of Alkali Metal atom in Air as a Function of Non-premixed Methane/air Flame Extinction Strain Rate for NaOH and KOH Mass Fractions of 0.055 shown in Figure 4-63 and. Lower panel: Mole Faction of Am in Air as a Function of Non-premixed Methane/air Flame Extinction Strain Rate for NaOH and NaCl Mass Fractions of 0.03 Shown in Figure 4-63 and Figure 4-66 (upper panel). [129]

Comparison of molar plots of NaCl vs. NaOH, shown in the lower panel of Figure 4-66, indicates a surprisingly superior flame suppression ability of NaCl over NaOH. The difference in effectiveness is not due to the vapor pressure of the parent compounds, since NaCl has a lower vapor pressure than NaOH. Although Cl can display an inhibiting effect similar to Br, a quantitative comparison between NaCl and NaOH requires additional studies and more detailed modeling to understand their suppression differences.

For a droplet mass loading of Y_0 =0.014 and an extinction strain rate of 125 s^{-1}, a comparison of the mole fraction of chemical agent needed in air (Xi) yielded the following order: X_{KOH} = 0.00021 < X_{NaCl} = 0.00023 < X_{NaOH} = 0.00034 < X_{FeCl2} = 0.00056 (assuming linear interpolation between available data). These values indicated that on a molar basis KOH is the most effective chemical agent, followed by NaCl and NaOH. For water/$FeCl_2$, the interpolation assumed that y_{FeCl2} = 0.15 is unsaturated at this high molar loading, which is certainly questionable. If $FeCl_2$ does condense at a lower additive mass fraction (e.g., y_{FeCl2} < 0.05), then on a molar basis water/$FeCl_2$ would be the most effective solution as X_{FeCl2} would approach 0.00018 (instead of 0.00056 above).

Extinction of Premixed Flames with Water Solutions

The inhibition of premixed flame propagation with various chemical fire-suppressing agents is well documented.[130,135,136] Chelliah and coworkers[129] investigated the inhibition of a conical premixed flame with fine water/NaOH droplets. Based on phenomenological reasoning,[137] it is well known that the burning velocity is proportional to the square root of the chemical reaction rate.

$$S = \left(\frac{S_L}{S_L^0} \right)^2 \tag{4-17}$$

Consequently, Figure 4-67 shows the square of normalized burning velocity vs. droplet mass fraction (Y_0) for varying the NaOH mass fraction in water (y_{NaOH}). With increasing y_{NaOH}, these results do not show any significant increase in flame inhibition compared to the inhibition with pure water droplets. This was a rather unexpected finding because of the close similarities (described below) between the premixed and non-premixed flames considered.

The insensitivity of higher NaOH mole fractions in water droplets in the premixed flame configuration can be explained by considering the droplet residence times in the flame. Because of the vast difference in the boiling temperature between water and NaOH (373 K vs. 1663 K), water is expected to evaporate first. If the flow residence time of droplets through the premixed flame were less than that through a counterflow flame, a partially vaporized droplet (smaller than the initial ~ 20 μm at the inflow boundary) with a much higher concentration of NaOH would emerge. Therefore, the lack of chemical inhibition observed in the premixed experiments with water/NaOH solutions may be caused by partially vaporized droplets. To test this hypothesis, the flow residence times of droplets through premixed and non-premixed flames, inhibited with pure water droplets, were investigated.

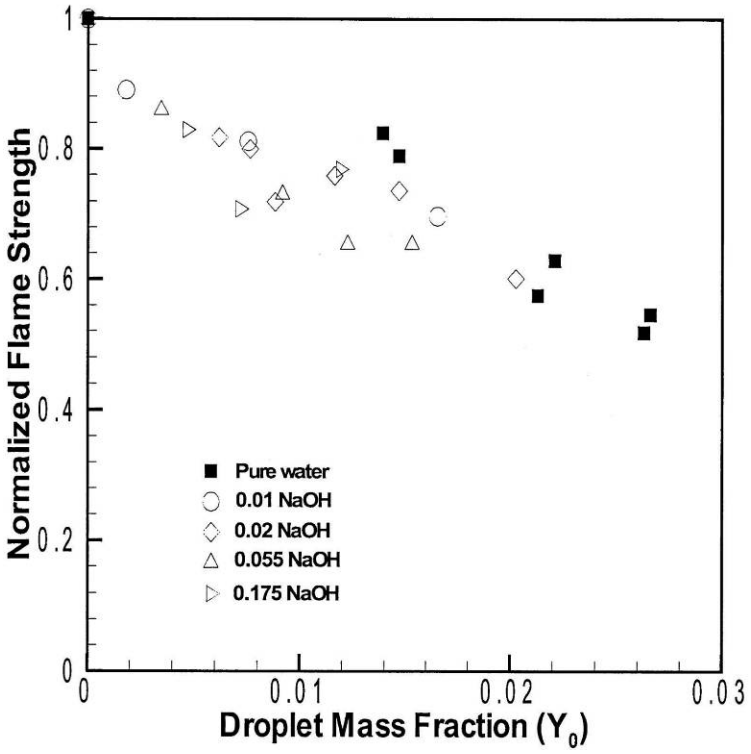

Figure 4-67. Square of the Normalized Burning Velocity of a Premixed Flame Inhibited with Fine Droplets of Water Solution for Several NaOH Mass Fractions in Water. [129]

Comparison of Premixed and Non-Premixed Flames with Pure Water Droplets

As described above, the premixed flame burning velocity is proportional to the square root of the overall chemical reaction rate. The non-premixed flame extinction strain rate, however, is directly proportional to the chemical reaction rate. A formal asymptotic analysis,[107] assuming that the overall reaction of the form fuel + oxidizer → products is applicable to both premixed and non-premixed flames, yielded the following relationship between the burning velocity and extinction strain rate

$$\left(\rho_0 S_L^0\right)^2 \propto \left(\frac{\rho\lambda}{c_P Z^2}\right)_{st} a_{ext} \tag{4-18}$$

where Z_{st} is the stoichiometric mixture fraction (assumed to be a small parameter), k the thermal conductivity, and c_p the specific heat. Based on this relationship and assuming that the mixture fraction, transport, and thermodynamic properties were not affected by the small fraction of condensed-phase agent added,[138] a direct comparison of the extinction/inhibition of non-premixed and premixed flames was accomplished by defining normalized flame strength as

$$S = \left(\frac{S_L}{S_L^0}\right)^2 = \left(\frac{a_{ext,inhib}}{a_{ext,uninhib}}\right) \tag{4-19}$$

Its applicability for droplets of pure water was examined in Figure 4-68, which shows the normalized flame strength for the premixed and non-premixed flames as a function of the mass fraction of water. The data indicate that the 13 μm median diameter droplets are not equally effective in inhibiting the premixed flame. (Note that for proper normalizations, S_L^0 corresponds to a case in which the premixed methane/air stream is saturated with water vapor, and $a_{ext,uninhib}$ to a case in which the non-pre-mixed air stream is saturated with water vapor.)

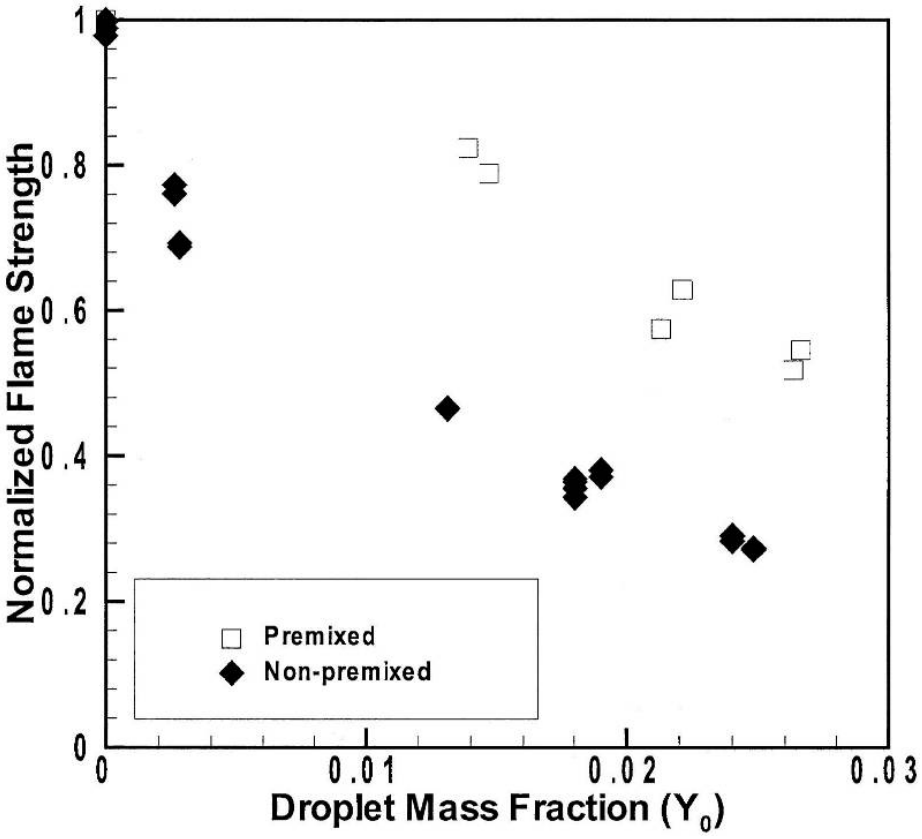

Figure 4-68. Normalized Flame Strength of Non-premixed and Premixed Methane/air Flames Inhibited with Droplets of Water with a Median Diameter of 20 μm. [129]

The aforementioned differences between the inhibition of non-premixed and premixed flames by pure water droplets, as well as the disparate results for droplets of water/NaOH in premixed flames, was explained based on the flow residence time as associated with each flame structure and its effect on the evaporation of fine water droplets. Figure 4-69 shows the numerically obtained flame structure of a premixed and a non-premixed flame, corresponding to conditions in which the flame was inhibited by 13 μm droplets with a droplet mass fraction of $Y_0 = 0.01$.

The estimated flow residence time of these droplets through the thermal layer, from the cold boundary up to the peak flame temperature, differed substantially: 4 ms for the premixed vs. 14 ms for the non-premixed. This implied that the time available for the droplets to vaporize in premixed flames was considerably less, and that the 13 μm droplets were not necessarily the ideal size for inhibiting the premixed flame considered. Consequently, the maximum thermal cooling was not achieved compared to the counterflow flame, resulting in the lower flame inhibition observed in Figure 4-68 for premixed flames.

Residence time considerations may also explain the much poorer relative effectiveness of either NaOH or KOH at $a = 240\ s^{-1}$ vs. $a = 125\ s^{-1}$, as shown in Figure 4-62 and Figure 4-64. The higher strain flames present lower residence times, possibly preventing release of all of the additive to the gas phase.

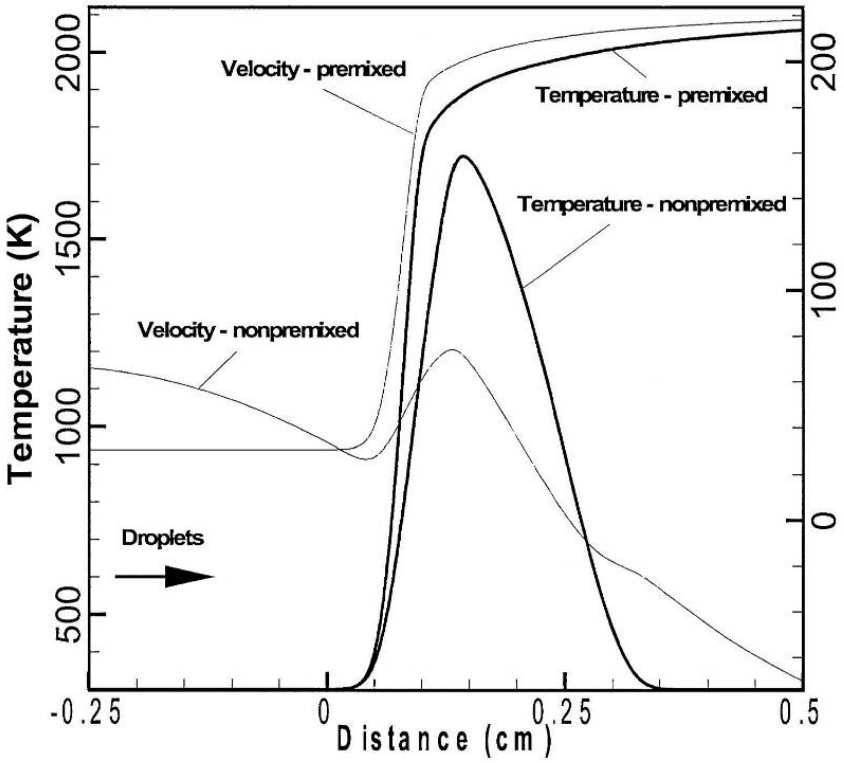

Figure 4-69. Non-premixed and Premixed Flame Structures Corresponding to Inhibited Conditions of Water Droplet Mass Fraction of Y_0 = 0.01. [129]

Conclusions and Summary

The low vapor pressure of alkali metal salts at normal room temperature requires their delivery to a flame as a powder or as a droplet spray, if suppression is to be efficient. However, efforts to combine the thermal fire suppression ability of fine water droplets with the chemical inhibition of alkali metal compounds indicated the existence of an upper limit for agent effectiveness perhaps due to condensation of some intermediate inhibitor species. Inclusion of NaOH in water (up to 17.5 % by mass) significantly enhanced the fire suppression ability of water by complementing its thermal effects with chemical catalytic radical recombination effects of NaOH. When the mass fraction of an alkali metal hydroxide in water was below this condensation limit, comparison of the chemical effectiveness indicated that KOH was twice as effective as NaOH on a molar basis for a wide range of flow strain rates. Comparison of the effectiveness of water/NaOH with water/NaCl on a molar basis indicated the superior effectiveness of NaCl over NaOH.

The relationship between droplet size and flow residence time was found to be important, both for comparing the behavior of condensed-phase agents between flame types, as well as for evaluating the efficacy of chemically active additives. Comparison of the effects of water/NaOH droplets on the extinction of non-premixed and inhibition of premixed flames implied that if the droplets were not completely evaporated before reaching the chemical reaction layer (because of non-optimal droplet size or insufficient droplet residence times), then the full chemical effectiveness of the agent was not realized. When the same water droplets were introduced to non-premixed and premixed flames, with no velocity lag between the droplets and the gas phase, the characteristic flame extinction/inhibition conditions of the two flames differed. Flame structure analysis revealed a distinct flow residence time of droplets (with a median diameter of 13 μm) through each flame structure: 14 ms for the non-premixed flame, 4 ms for the premixed flame. This time difference was the cause for the observed differences in the two flames.

The predicted results for polydisperse size distributions were consistent with previous monodisperse predictions. However, differences observed between experiments and modeling could not be explained solely on the basis of the size distribution effects.

The results illustrate the importance of understanding the particular reacting flow field and temperature conditions in order to assess the intricate coupling between droplet size and its residence time through the flame structure. In real fires with turbulent flow fields, the flow residence times of droplets can be quite varied; optimum droplet sizes might be different than the 10 μm to 20 μm observed in these studies. Therefore, design of optimal fire-suppression systems using droplets of water solutions must consider the flow residence times and flame structures of each application carefully.

4.5.4 Dendrimers, Combined Chemical and Physical Flame Suppression[iii]

Introduction

At the beginning of the NGP, dendritic polymers or dendrimers were a new polymer technology coming to fruition as commercial products. They are ultra-branched, three-dimensional polymeric molecules possessing a low-density core surrounded by a crowded, high density surface.[139,140] Typical dendrimers were of the order of 5 nm to 10 nm in diameter. The interior of the dendrimer has tens to hundreds of branching junctions, depending on the overall degree of polymerization of the dendrimer. In the chemistries most commonly synthesized, these branching points were tertiary amines. Thus, the nitrogen at the branch junction has a lone pair of electrons that could be used for "complexation." The ends of these branching paths are located on the dendrimer's surface and may also number in the tens to hundreds. The chemistry of these end groups is easily tailored to incorporate a desired chemical moiety or to encourage complexation with a specific ion.

Previous research had shown that transition metal complexes and alkali metal salts may act as super-agents for fire suppression, performing as much as 60 times more efficiently than halon 1301.[141,142] Unfortunately, the most effective of the complexes also suffer from such problems as high toxicity and reactivity with metal surfaces. By encapsulating the metal ion inside the dendrimer or by attaching it to a dendrimer surface, it might be possible to create a super-effective agent encapsulated in an inert, bio-compatible shell that would decompose upon contact with flame.

Beck Tan *et al.*[143] of the Army Research Laboratory (ARL) assessed the applicability of aqueous aerosols of dendritic polymerics for fire suppression effectiveness on gaseous laboratory flames (using the dispersed liquid agent fire fighting screen described in Chapter 8) and on liquid pool fires.

Materials

Poly(amidoamine) dendrimers were purchased from Dendritech, Inc., of Midland, Michigan. Two types of dendrimers were used in this study. The G3.5-ONa dendrimers had 64 -COONa end groups per molecule and a nominal molecular weight of 14,000 g/mole. These materials were used in the as-received condition. Four derivatives of G4.0 dendrimers were synthesized and tested. They were designated G4.SA (no metal added) or G4.SA-X, where X indicated the added metal ion: Cr, Fe, or K. Each of the

[iii] Text and figures in Section 4.5.4 are taken mainly from Reference 143 unless otherwise noted.

added ions had indicated significant flame inhibition potential (Chapter 3). The base molecular weight of the G4.SA dendrimer was 19,300 g/mole. Each potassium dendrimer contained 64 potassium ions; each other metal dendrimer contained 21 metal ions. Elemental analyses of the five dendrimers are given in Table 4–9.

Table 4–9. Elemental Composition of Pure Dendrimers and Dendrimer Salt Complexes.

Element	Quantity	Dendrimer				
		G4.SA	G4.SA-Cr	G4.Sa-Fe	G4.SA-K	G3.5-ONa
H	Mass %	8.08	6.94	6.81	6.7	7.38
	Atom %	53.09	51.2	51	50.9	52.5
C	Mass %	48.03	42.07	37.9	42.2	43.37
	Atom %	26.7	25.6	23.7	26.7	25.7
N	Mass %	14.7	12.76	16.63	12.61	12.9
	Atom %	7.0	6.72	7.29	6.84	6.55
O	Mass %	29.1	33.6	37.3	28.7	29.4
	Atom %	12.5	15.5	17.5	13.6	13.1
Cr	Mass %	--	4.63	--	--	--
	Atom %	--	0.66	--	--	--
Fe	Mass %	--	--	4.37	--	--
	Atom %	--	--	0.6	--	--
K	Mass %	--	--	--	9.8	--
	Atom %	--	--	--	1.9	--
Na	Mass %	--	--	--	--	13.1
	Atom %	--	--	--	--	2.14

Fire Suppression Experimentation

The fire suppression effectiveness for aqueous solutions of the five dendrimers was evaluated using two techniques.

One set of tests involved the dispersed liquid agent fire suppression screen (DLAFSS) apparatus developed at NIST for screening experimental fire suppressants; it is described fully in Chapter 8. Briefly, the apparatus consists of a cylindrical, opposed flow, propane burner located in a vertical wind tunnel. A nebulizer was used as a droplet generation device. Liquid agents were entrained into the air flow in the wind tunnel and traveled upward where they impinged on the propane flame. When the air velocity reached a critical value, the stable, blue enveloped flame at the burner was blown off, forming a wake flame. The transition to a wake flame was equivalent to extinguishing the fire. All experiments using the DLAFSS apparatus were conducted with the propane flow set at 2.0 L/min and the nebulizer air flow at 0.25 L/min.

Some data were collected for solutions of 25 % (by weight) dendrimer in water and a sample delivery rate of 0.3 mL/min. However, due to the high viscosity of the solutions, the sample delivery pump stalled repeatedly. The remainder of the tests were conducted using more dilute solutions (15 % by weight) and increased sample delivery rate of 0.5 mL/min. These settings allowed for the same delivery rate of sample without causing the sample delivery device to stall.

Although this was by far the best method found for screening experimental liquid fire suppression agents, the dendrimer residue frequently clogged the burner pores, necessitating changing the burner. This also added substantial variation to the test results. (The blow-off velocity for air alone was 220 cm/s. The range of scatter between runs and for the different burners was about ± 20 cm/s. For water droplets, the blow-off velocity was 200 cm/s, with scatter of ± 20 cm/s.) To improve the ability to discern differences among the tested aerosols, data for air blow-off velocity and water blow-off velocity for a given burner collected on a given day were averaged and used in calculating blow-off velocity ratios of water to air, sample to air, and sample to water for samples that were evaluated using that same burner. Then, the ratios calculated for each sample were averaged. These average ratios were the parameters used to evaluate the candidate suppressant's performance.

The second method used was a modification of the JP-8 fuel fire suppression agent screening method developed by Finnerty at ARL.[144] A test involved spraying a stream of the agent directly onto a 160 mm diameter pan containing 200 mL of JP-8. A Binks Model 15 paint spray gun was used as the agent delivery device, with a 1.58 mm nozzle operating at a pressure of 275 kPa (40 psi). This gun produced a fine stream of fluid droplets entrained in a forced air flow from a relatively small volume (50 mL) of fluid. The apparatus was adjusted so that the droplet spray distribution pattern covered the entire surface of the fuel container. For water, the flow out of the spray gun was 4.6 mL/s, while the rate of collection in the fuel container was 1.7 mL/s.

The time to extinguish the fire was the criterion used to evaluate the effectiveness of various agents. Additional data included the volume of agent fluid remaining in the spray gun, and the volume of fluid remaining in the fuel pan. All experiments were recorded using a video camera, and exact fire-out times were extracted from the recordings. A photograph of an experiment in progress is shown in Figure 4-70.

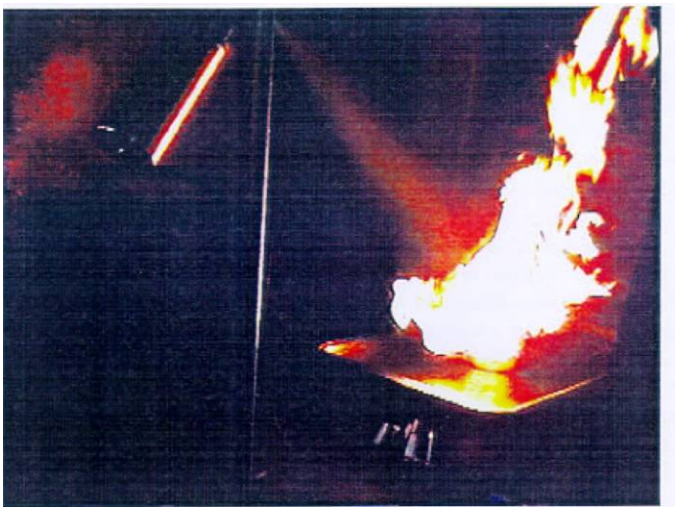

Figure 4-70. Setup for JP-8 Fire Suppression Experiments.

DLAFSS Results

Fire suppression screening experiments were conducted on water and aqueous solutions of pure dendrimer, dendrimer Na salts, dendrimer K salts, dendrimer Fe complexes, dendrimer Cr complexes, NaAc, K_2CO_3, chromium (+3) chloride hexahydrate, and ammonium iron (+2) sulfate hexahydrate. In the case of the salt solutions, the salt concentrations were adjusted so that the atom concentration of the metal

ion was either equivalent to that in the corresponding dendrimer-metal complex solution (Na, Fe, and Cr salts) or set at 10 times the equivalent weight (K salts).

The values of average blow-off velocities calculated for each agent screened are shown in Table 4–10. These values are similar to those collected by Yang et al.[145,146] for a variety of potassium and sodium small molecule salts. A lower blow-off velocity indicates a more efficient flame suppressant.

Table 4–10. Average Blow-off Velocities for of Various Candidate Agents.

Agent	Blow-off Velocity (cm/s) @ 0.3 mL/min	Blow-off Velocity (cm/s) @ 0.5 mL/min	Sample-to-water Blow-off Ratio
Water			1.00
10 % G4.SA	170		0.91
25 % G4.SA-K	152		0.82
4.8 % K_2C0_3	189		0.98
15 % G4.SA		193	0.96
15% G4.SA-K		180	0.94
3.23 % K_2C0_3		204	0.98
15 % G3.5-ONa		152	0.78
0.65 % CH_3C0_2Na		171	0.87

The results of the DLAFSS flame suppression experiments are summarized in Figure 4-71 and Figure 4-72. To avoid misinterpretation of the data, the water-to-air blow-off velocity ratio measured during the same conditions as the sample-to-air blow-off velocity ratio is given in each case. The effectiveness of the agent should be interpreted based on that reference.

Figure 4-71 summarizes the results of fire suppression experiments conducted with a sample delivery rate of 0.3 mL/min. The most interesting result from the 0.3 mL/min experiments was from comparison of the 25 % G4.SA-K and the 4.8 % K_2C0_3 solutions. Although the K_2CO_3 aerosol contained 10 times the K ions of the G4.SA-K dendrimer salt solution, the dendrimer solution was more efficient as a fire suppression agent. Another important finding was that the pure dendrimer solution, 10 % G4.SA, had fire suppression capacity that was comparable to pure water. This was significant because there were initial concerns that the polymer might act as a fuel and thereby be detrimental to fire suppression effectiveness.

The DLAFSS results for the 15 % solutions and a sample delivery rate of 0.5 mL/min are summarized in Figure 4-72. The results from small molecule K and Na salts are also included for comparison. The results for the 15 % G4.SA solution indicate that once again, the addition of the pure dendrimer to water was not detrimental to fire suppression effectiveness. The fire suppression effectiveness of the 15 % G4.SA and the 15 % G4.SA-K samples was the same as water, within experimental uncertainty. Comparison of G4.SA-K to the K_2C0_3 solution showed that the dendrimer salt solution was perhaps a little better than the pure salt, but the former contains one-tenth the K ion concentration.

The agent that showed the most significantly enhanced fire suppression capability was the G3.5ONa dendrimer K salt. The blow-off velocity of the dendrimer-sodium salt was reduced nearly 20 % relative to the blow-off velocity ratio for water measured under the same conditions. The 0.65% NaAc, which had the same Na ion concentration as the G3.5-ONa dendrimer salt, also showed promise for enhancing the fire suppression effectiveness of water, but to a lesser extent than the dendritic salt solution.

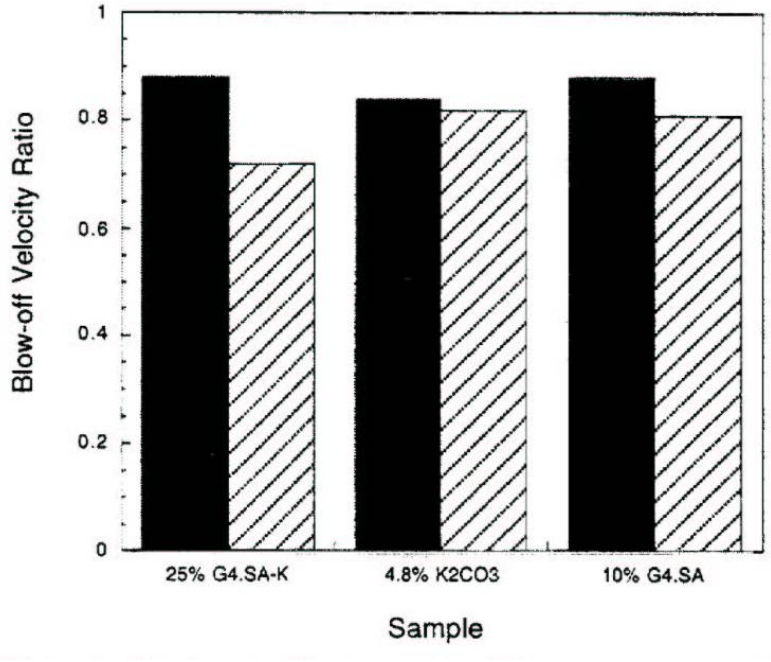

Figure 4-71. Blow-off Velocity Ratios for Various Candidate Agents to Air, and Reference Ratios for Water to Air Measured under the Same Conditions. Solid bars: water to air; lined bars: sample to air.

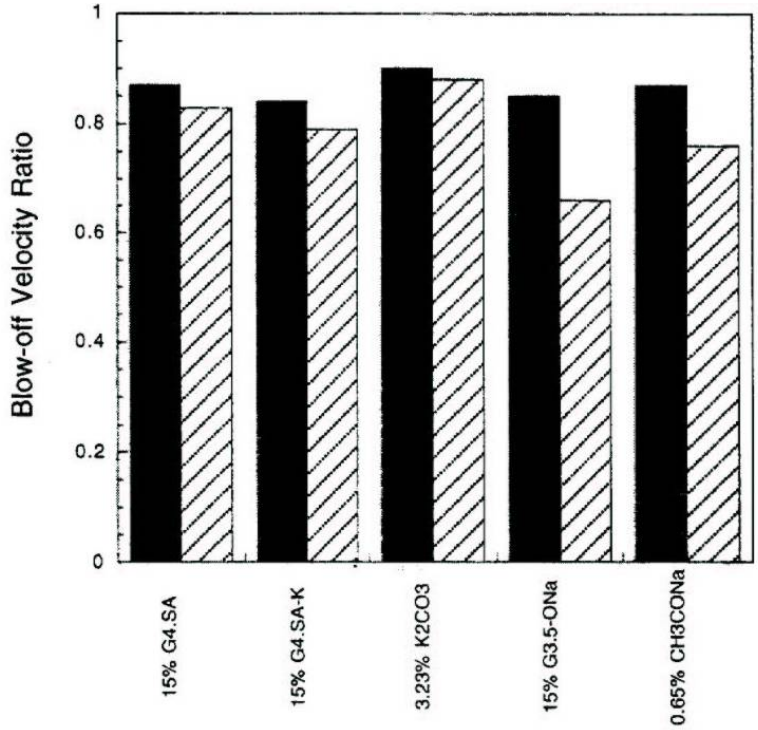

Figure 4-72. Blow-off Velocity Ratios for Various Candidate Agents to Air, and Reference Ratios for Water to Air Measured under the Same Conditions. Solid bars: Water to air; lined bars: sample to air.

The blow-off velocity ratios of sample fire suppression effectiveness to water fire suppression effectiveness measured when the same conditions were used are tabulated in Table 4–10. All ratios were comparable to or less than 1.0, indicating that all the experimental agents performed at least as well as water. In particular, the Na salts (both dendrimer and small molecule) and the dendrimer-potassium salt delivered at 0.3 mL/min from 25% solution were considerably more effective than water.

In the case of the Na salts, it appears that the Na cation was the active species. Both the small molecule salt and the dendrimer salt showed promise as fire suppression agents. It is noteworthy that the NaAc showed an effect when present at only ≈ 0.65 % by weight. Since this salt is inexpensive, non-hazardous and readily available, it may be prudent to investigate its fire suppression effectiveness more fully. The G3.5-ONa dendrimer performed somewhat better than the small molecule salt solution of equivalent Na ion concentration. A similar effect was observed in comparing the 25 % G4.SA-K and the 4.8 % K_2CO_3 solutions. Since the pure dendrimer solutions were not found to be significantly more effective than water, the observed effect must be related to the combination of the cation with the dendrimer "carrier." This is the type of effect that motivated the project and offers some proof of the concept that the use of dendritic polymers as carriers for active fire suppressant species could be beneficial.

The mechanism responsible for observed enhancement in the fire suppression effectiveness of the Na and K through coupling with the dendrimer carrier cannot be easily extracted from the data. One possibility was that the organization of the cations on the dendrimer surface, which resulted in an extremely high local concentration of them, had a beneficial effect on the kinetics of the radical recombination reaction believed to be responsible for flame suppression. This type of kinetic effect had been observed for other situations in which an active species was localized on the surface of a dendrimer.[147] A second possibility was that the size and size distribution of the droplets being delivered to the flame were altered by the dendrimers in such a way as to improve the fire suppression effectiveness of the fluid, based on purely geometrical considerations. The droplet diameter from a nebulizer, which was the sample delivery device incorporated into the DLAFSS device, is known to be related to the properties of the nebulizing fluid, such as density, surface tension, and viscosity.[148] The density of the dendrimer solutions was not substantially different from that of water, and the surface tension of polymer and salt solutions was generally not changed by more than about 10 % to 20 %. However, the viscosity of dendrimer solutions was much greater than that of water. Other recent work on poly(amidoamine) dendrimers[149] indicated that the viscosity of 15 % to 25 % dendrimer solutions at room temperature should be on the order of tens of centipoise, an order of magnitude greater than that of pure water (~1.0 cP).[150] A third possibility may the thermodynamic saturation limits to the amount of inhibitor species permitted in the gas phase discussed in Section 4.5.3.

The idea that the viscosity effects may alter the fire suppression effectiveness through changes in the delivery spray may explain the apparent discrepancy between the fire suppression effectiveness observed for 25 % G4.SA-K dendrimer solution delivered at 0.3 mL/min and the 15 % G4.SA-K solution delivered at 0.5 mL/min (Figure 4-71 vs. Figure 4-72). The mass flow of polymer into the flame was identical, but the fire suppression effectiveness of the 25 % solution was considerably better than the 15 % solution. This may have been a reflection of the viscosity difference between the two fluids, which could be as much as a factor of 6 to 8, and its effect on the droplet size and distribution in the sample delivery spray. Although results by Yang et al.[151] indicated that the droplet size and distribution generated in the DLAFSS experiment are not strongly dependent on fluid viscosity in low viscosity solutions (~1cP to 4 cP), they did not measure droplet size distributions in polymer solutions that have viscosities that are much greater than that of water.

Although it is likely that viscosity played a role in the determination of apparent fire suppression effectiveness, in the sodium salt and sodium dendrimer systems, chemical mechanisms are also probably contributing significantly. Both the 15 % pure dendrimer solution and the 15 % G4.SA-K solution were much less effective than the 15 % G3.5-ONa solution, though the viscosities should be of similar

magnitude (see Table 4–10). Given this evidence of chemical interaction, it is in the sodium-containing systems where the kinetic benefits of localizing the active species on the surface of a dendrimer should be most readily apparent. The results from the G3.5-ONa solution provide the most concrete evidence that using a dendrimer carrier to deliver active species into a flame can have a positive effect on the fire suppression effectiveness of that active species.

Pan Fire Suppression Results

The analysis of data from the JP-8 fuel fire screening experiments was straightforward. The relevant parameters recorded were the time to extinguish the fire and the mass of agent that was dispersed in extinguishing the fire. Because a relatively large mass of agent was required to perform each experiment and the results were not found to be highly reproducible, these experiments were used only for the dendrimer-iron complexes that could not be studied using the DLAFSS apparatus because of their high viscosity. The associated transition metal salt and pure dendrimer controls were also studied (chromium [III] chloride hexahydrate, ammonium iron [II] sulfatehexahydrate, and G4.SA). The dendrimer chromium complexes could not be studied because the supply of material was insufficient.

The results from the JP-8 fuel fire screening experiments are summarized in Figure 4-73 and Figure 4-74.

Although the masses of the various agents required to extinguish the JP-8 fires varied from 40 g to 65 g (Figure 4-74), the measurement uncertainty precluded drawing definitive conclusions regarding the relative fire-out times for any of the agents studied. It was not possible to judge the relative efficiency of the agents from these experiments also due to the discrepancy in the agent delivery rates. These rates were calculated from the mass deployed and the time of deployment and are plotted in Figure 4-75. The paint sprayer was delivering higher viscosity solutions at slower rates. This difficulty in uniform agent dispersion for solutions of varying viscosity is a challenge to be addressed during the development of screening techniques for experimental fire suppression agents.

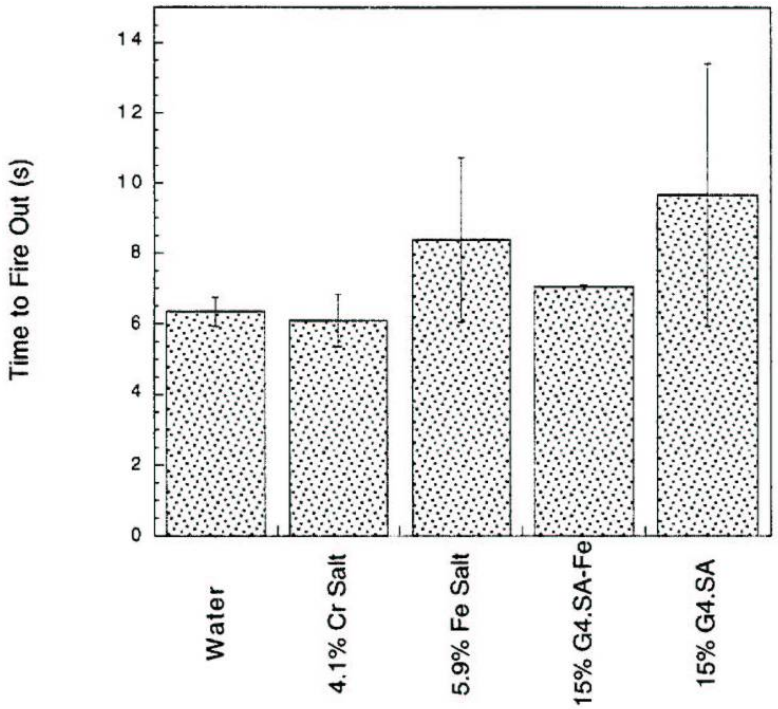

Figure 4-73. Times for Various Experimental Fire Suppressants to Extinguish a 200 mL JP-8 Pan Fire. The error bars represent ± one standard deviation.

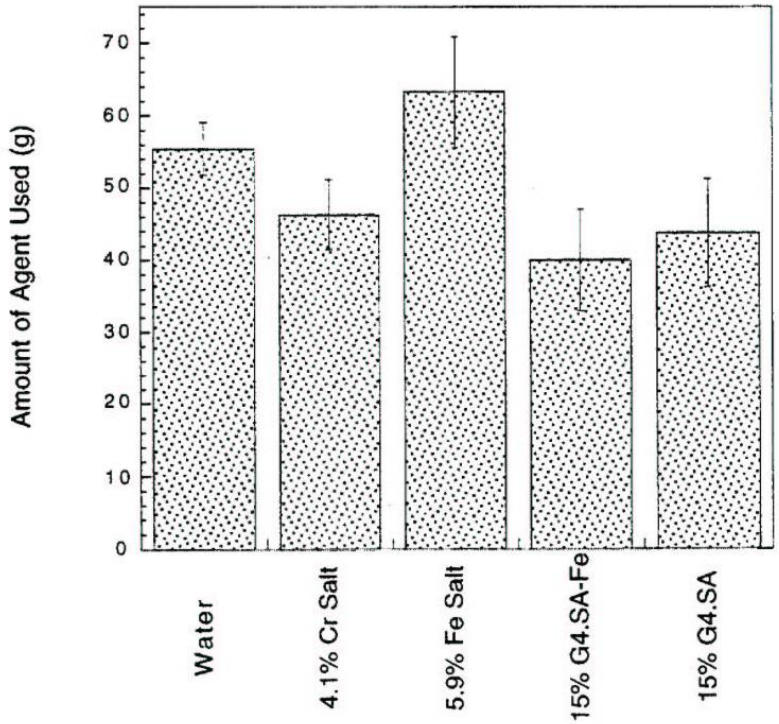

Figure 4-74. Mass of Various Experimental Fire Suppressants to Extinguish a 200 ml JP-8 Pan Fire. The error bars represent ± one standard deviation.

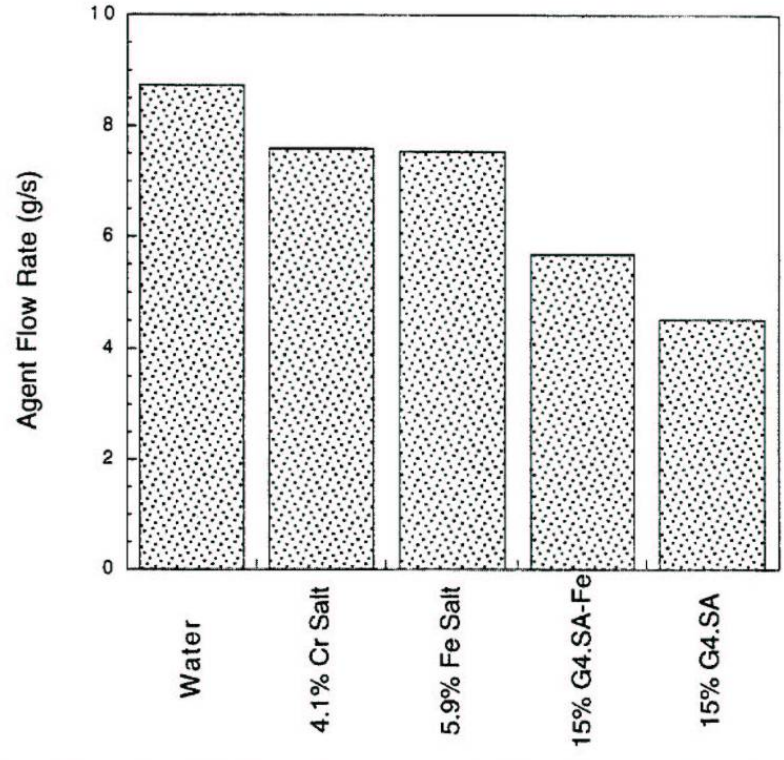

Figure 4-75. Mass flows for Various Fire Suppressants Deployed during JP-8 Screening Experiments.

Because of the difficulties encountered in investigating the transition metal complexes using the JP-8 fuel fire experiments, it was not possible to draw any strong conclusions regarding the fire suppression effectiveness of the dendrimer-transition metal complexes. However, the experiment was sensitive enough so that the effect of a super-agent would have been noticeable. This study indicated that the dendrimer-iron complexes did not exhibit the super-agent performance previously observed for iron pentacarbonyl and other volatile transition metal complexes.[143]

Important Findings

This exploratory study found that:

- Poly(amidoamine) dendrimers added to water at substantial concentrations have no deleterious effect on the fire suppression effectiveness of water and can marginally improve the flame suppression effectiveness of water. Any contribution of polymer combustibility was at least offset by the flame suppression contribution.
- The use of dendritic polymer carriers to deliver agents containing potassium and sodium ions can increase the effectiveness of these agents on laboratory flames.
- Dendrimer-sodium salts were more effective flame suppression agents than dendrimer potassium salts. This is in contrast to the geater observed effectiveness of potassium over sodium in all other (non-dendrimeter delivery) suppression studies and may be due to saturation limits in the dendrimeter experiments.
- The addition of sodium acetate to water improved its flame suppression effectiveness significantly, even at loadings of less than 1 % by weight.
- Potassium carbonate did not significantly improve the flame suppression effectiveness of water at concentrations as great as 5 % by weight for the droplet size and flow conditions studied.
- More work is needed in the development of versatile experiments for screening experimental aerosol fire suppressants.

4.6 SURFACE COOLING[iv]

4.6.1 Introduction

When liquid suppressant droplets released from a discharge port approach a fire, several things can happen.[152] Droplets with sufficient momentum to penetrate the flame, depending on their sizes, can either be consumed in the flame (participate directly in the suppression processes through physical and/or chemical mechanisms) or reach the fuel surface. Droplets with little momentum (e.g., very small droplets) may not penetrate the fire and will be deflected away by the rising hot plume.[153] These deflected droplets will eventually evaporate or strike adjacent objects. For droplets landing outside the burning area, the cooling of the adjacent and surrounding surfaces could mitigate or contain the flame spread. Therefore, droplet interaction with surfaces is an integral part of the overall suppression process.

[iv] Large portions of the text of Section 4.6, as well as the figures , have been used from Reference 152 without further attribution. The reader should consult the original document for additional details.

Surface heat extraction and burning surface area reduction are generally regarded as the dominant mechanism for extinguishment of burning solid fuels by water sprays.[154] The cooler liquid droplets can interact with the relatively hot fuel surface, extract heat during vaporization, and thereby reduce the surface temperature. With surface cooling, the burning rate falls, which leads to a decrease in heat feedback to the fuel surface. Eventually, a critical burning rate is reached beyond which combustion can no longer be sustained. The deposited droplets also reduce the mass transfer area on the fuel surface, which also causes a reduction in burning rate.

In order to understand surface cooling without resorting to a detailed analysis of the coupling between the transient thermal response of the fuel bed as a result of the application of liquid agent and the heat feedback from the flame to the fuel, the transient coupling process is considered as a series of quasi-steady steps. At any instant in time, a steady-state energy balance at the fuel surface can be written as:

$$\dot{m}''_{fuel}\Delta H_{fuel} = Q''_{cond} + Q''_{conv} + \varepsilon_{flame}\sigma T^4_{flame} - \varepsilon_s \sigma T^4_{surf} - q'' \tag{4-20}$$

where $\dot{m}''_{fuel}$ is the fuel burning mass flux, ΔH_{fuel} is the effective heat of gasification of the fuel, Q''_{cond} is the conductive heat flux to the fuel surface, Q''_{conv} is the convective heat flux to the fuel surface, ε_{flame} is the flame emissivity, σ is the Stefan-Boltzmann constant, T_{flame} is the average flame temperature, ε_s is the surface emissivity, T_{surf} is the fuel surface temperature, and q'' is the heat flux removal from the fuel surface due to surface cooling.

The surface cooling heat flux, q'', depends on the interaction of the liquid droplets with the surface. There are many different scenarios of droplet impact on a surface. The impacting processes depend on the thermophysical and geometrical properties of the droplet and of the target surface and on the magnitude and direction of the impact velocity vector. In addition, for a flaming surface, the droplet will traverse through an environment different from that of a non-burning surface before impact. However, in the literature, droplet/surface interaction studies focus almost exclusively on non-burning surfaces.

When relatively cool liquid droplets impact a solid surface, cooling of the surface occurs as a result of heat transfer between the surface and the droplets. A liquid droplet impacting a solid surface has been extensively studied in the literature.[155,156,157,158,159,160,161,162,163] Maps that identify the various impact and heat transfer regimes over a wide range of experimental conditions have been constructed. Spray cooling or quenching of hot metallic surfaces has also been extensively studied.[164,165,166,167,168,169] Many empirical heat transfer correlations for spray cooling applications exist.

For a liquid droplet interaction with a *liquid* surface, several scenarios need to be considered. The impact dynamics are complicated by the ability of the liquid surface to deform and to displace in response to the impinging droplet. There is also internal fluid motion of the liquid pool initiated by the impact processes.[170] If the droplet has a very high impact velocity, it can cause a crater in the liquid pool and a splash upon impact. For a burning liquid pool, the splash may result in a sudden increase in burning rate due to an increase in the liquid surface area caused by the splash droplets. If the droplet is soluble in the liquid, mass transfer between the penetrating droplet and the liquid will occur. Depending on droplet impact parameters, differences in miscibilities and physical properties (surface tension and viscosity) between the droplet and the target liquid, and the depth of the liquid layer, several phenomena are likely following impact. The droplet may float on the surface, may coalesce into the liquid pool with little or no splashing and produce a vortex ring, may rebound or splash forming a crater and a small jet or column of liquid at the surface, or may dissolve into the liquid pool. Most work in the literature has examined the

isothermal impact of a liquid droplet onto a surface of the same liquid (e.g., see the review article of Rein[170] and the references therein). In a fire suppression scenario, the impacting droplet encounters a different liquid target (suppression fluid vs. fuel) with different physical properties. The temperature of the droplet can be much lower than that of the liquid surface (especially, in the case of burning), and the contact between a cold droplet with a hot liquid may sometimes results in vapor explosion, [171] an unwanted situation. All of these complicated interactions render the study of heat transfer processes between liquid droplets and a liquid surface an arduous and daunting task. Appropriate heat transfer correlations do not exist in the literature; therefore, liquid surface cooling calculations, in spite of the importance of the process, are not attempted here.

This section discusses droplet evaporation and solid surface cooling by droplets, an integral part of the surface cooling problem. If the droplets evaporate completely before reaching the fuel surface, the heat removal from the surface will decrease significantly due to the fact that the liquid latent heat of vaporization does not play a role. Under this circumstance, the surface will only be cooled by a vapor jet, which is not an effective cooling mechanism.

Another important aspect in surface cooling is the ability of the droplets to reduce the surface temperature of components in the vicinity of a fire to prevent re-ignition, which is a potential problem in suppressing aircraft engine nacelle fires. If sufficient cooling of any hot surfaces in the vicinity does not occur, re-ignition of residual fuel vapor/air mixture may result.

In the following discussion, the five fluids (water, lactic acid, $C_3F_5H_3O$, HFE-7100, and R338mccq) identified in Pitts et al.[152] as having the highest mass-based ΔH^{total} (total heat absorbed including enthalpy of evaporation in going from room temperature to 1400 K) were considered to evaluate their droplet vaporization and surface cooling characteristics. Low boiling-point fluids were not considered because under typical operating conditions, these fluids flash-vaporize soon after they leave the discharge opening and arrive at the surface in the form of a vapor.

4.6.2 Evaporation of Liquid Droplets

The estimation of liquid droplet evaporation is based on the classical d^2-law, which gives the droplet diameter as a function of time as

$$D^2 = D_o^2 - Kt, \tag{4-21}$$

where D is the instantaneous droplet diameter, D_o is the initial droplet diameter, t is the time, and K is the evaporation constant. The evaporation constant was calculated by

$$K = \frac{8k_g \ln(1+B)}{\rho_F C_{pg}}, \tag{4-22}$$

where B is the transfer number, k_g is the gas-phase thermal conductivity, C_{pg} is the gas-phase heat capacity, and ρ_F is the liquid density. The B number based on mass transfer considerations is given by

$$B_M = \frac{Y_{FS} - Y_{F\infty}}{1 - Y_{FS}}, \tag{4-23}$$

where Y_{FS} and $Y_{F\infty}$ are the vapor-phase mass fraction at the droplet surface and ambiance, respectively. The mass fraction, Y_{FS}, was evaluated by

$$Y_{FS}=\frac{P_{FS}M_F}{P_{FS}M_F+(P-P_{FS})M_A}, \tag{4-24}$$

where P_{FS} is the liquid vapor pressure at the droplet surface, P is the ambient pressure, which is equal to the sum of the liquid vapor pressure and partial pressure of air at the droplet surface, and M_F and M_A are the molecular weights of liquid and air, respectively.

The B number based on heat transfer considerations was given by

$$B_T=\frac{C_{pg}(T_\infty-T_s)}{\Delta H_{vap}}, \tag{4-25}$$

where T_∞, T_s, and ΔH_{vap} are the ambient temperature, droplet surface (wet-bulb) temperature, and latent heat of vaporization of the liquid, respectively. Under steady-state conditions, $B_M = B_T$, and either Equation (4-23) or Equation (4-25) may be used to calculate the evaporation constant in Equation (4-22).

If T_s is known, the calculation of the evaporation constant is straightforward; however, under normal circumstances it is necessary to determine T_s in order to evaluate B and K. The calculation procedure can be found in References113, 172 and 173. The basic idea was to find T_s such that $B_M = B_T$. Spalding[172] and Kanury[173] used a graphical approach. By plotting B_M and B_T against T_s, the intersection of these two curves defined the wet-bulb temperature and the corresponding B. An iterative method was used by Chin and Lefebvre.[113] The calculations presented here used the latter approach.

To calculate K, the reference temperature (T_r) and mass fractions (Y_{Fr} and Y_{Air} for the fluid and air, respectively), based on the one-third rule,[113] were used to estimate the gas phase thermophysical properties.

$$T_r=T_s+\frac{T_\infty-T_s}{3} \tag{4-26}$$

$$Y_{Fr}=Y_{FS}+\frac{Y_{F\infty}-Y_{FS}}{3} \tag{4-27}$$

$$Y_{Air}=1-Y_{Fr}. \tag{4-28}$$

The equation for calculating the gas-phase heat capacity, C_{pg}, was given by

$$C_{pg}(T_r)=Y_{Air}C_{pA}(T_r)+Y_{Fr}C_{pF}(T_r) \tag{4-29}$$

where C_{pA} is the heat capacity of air and C_{pF} is the gas-phase heat capacity of the fluid, all evaluated at T_r. The thermal conductivity of the gas phase was estimated using the following equation,

$$k_g(T_r)=Y_{Air}k_A(T_r)+Y_{Fr}k_F(T_r), \tag{4-30}$$

where k_A is the thermal conductivity of air and k_F is the gas-phase thermal conductivity of the liquid, all evaluated at T_r.

The conditions used in the calculations were: (1) T_∞ = 1400 K (to simulate a flaming ambiance), (2) $Y_{F\infty}$ = 0, and (3) P = 0.101 MPa. The thermophysical properties of air, water, and lactic acid were obtained from the database of the Design Institute for Physical Properties I.[174] The properties of $C_3F_5H_3O$, HFE-7100, and R338mccq were estimated by methods described in Reid et al.,[175] the modified Rackett technique was used for ρ_F, the method of Joback for C_{pF}, the method of Lee and Kesler for P_{FS}, the method of Pitzer's acentric factor correlation for ΔH_{vap}, and the method of Ely and Hanley for k_F.

Figure 4-76 shows droplet evaporation times, t_b, as a function of initial droplet diameter. The droplet evaporation time was easily obtained by assigning D = 0 in Equation (4-21) once K is known,

$$t_b = \frac{D_o^2}{K}. \tag{4-31}$$

For a given initial droplet diameter under the same ambient conditions, the evaporation time for a water droplet was the longest and for a R338mccq droplet the shortest. For the five fluids examined, the ranking based on droplet evaporation times was

$$t_{b,R338mccq} < t_{b,HFE7100} < t_{b,C_3F_5H_3O} < t_{b,lacticacid} < t_{b,water}. \tag{4-32}$$

How fast a droplet evaporates determines whether it will still remain as a droplet upon reaching the surface. However, if *flame cooling* is the dominant fire suppression mechanism, then it would be better to have the droplet completely vaporized in the flame.

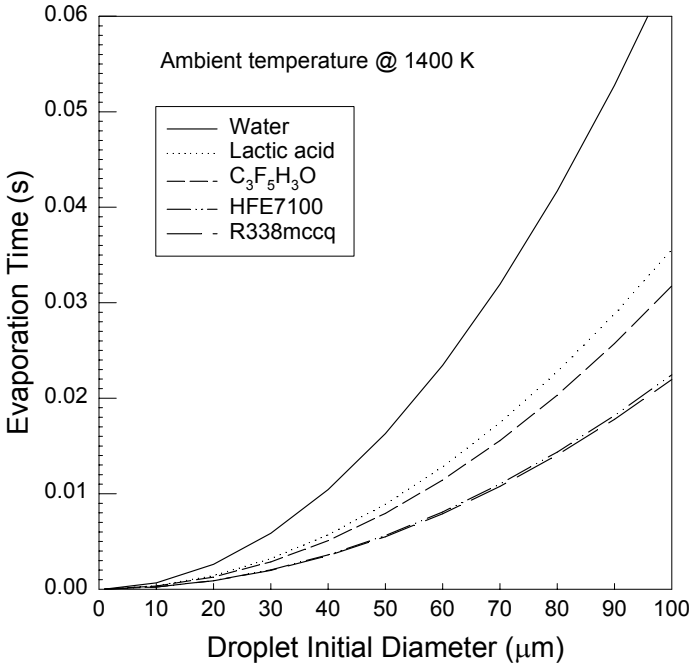

Figure 4-76. Droplet Evaporation Time as a Function of Initial Droplet Diameter for Five Fluids.

4.6.3 Spray Cooling

In order to assess surface cooling, we consider the literature on spray cooling and quenching of hot metallic surfaces. The application of spray-cooling correlations to fuel surface cooling is only appropriate when the fuel surface is solid (e.g., a PMMA or wood slab). Even in this case, care should be exercised because subtle differences in cooling mechanisms exist. A burning PMMA surface in reality is in a molten state, and wood forms a porous char layer. The interactions of droplets with molten and porous surfaces remain very difficult problems to tackle. Differences also arise between fuel surface cooling and quenching of metallic surfaces. In the latter, radiative heat transfer to the droplets only occurs from the heated surface; however, in the former, it also occurs from the flame. Strictly speaking, the following calculations are more applicable to the cooling of a hot surface to prevent re-ignition than to the cooling of a burning fuel surface.

Depending on the surface temperature, when a hot surface is being quenched by a liquid spray, it will experience several distinct heat transfer regimes which can be followed along the "boiling curve." Such a curve is a plot of surface heat flux vs. surface temperature and represents the strong relationship between heat flux and surface temperature during quenching. The characteristics of the boiling curve are classified as (with increasing surface temperature): (1) convective, (2) nucleate boiling, (3) critical heat flux, (4) transition boiling, (5) Leidenfrost point, and (6) film boiling. Detailed descriptions are available.[164,165] Figure 4-77 is an illustration of a boiling curve associated with spray cooling of a hot surface. The general features of the curve are similar to those for a pool boiling curve.

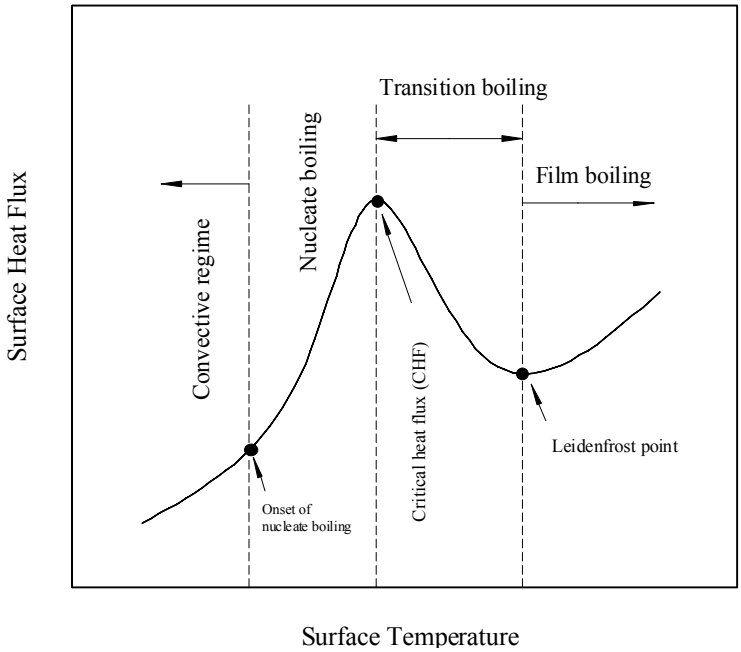

Figure 4-77. Typical Boiling Curve Associated with Quenching of a Hot Surface by Liquid Droplets.

Since the boiling curve of one fluid may differ from that of other fluids, there are several important assumptions that have to be made in the following analysis.

- When a comparison of surface heat fluxes is made, it is assumed that for the prevailing surface temperature, these fluids are in the *same* regime on the boiling curve. This assumption may not be valid because, for example, the surface temperatures at which the critical heat flux and Leidenfrost phenomena occur may be significantly different among the fluids studied; therefore, while one fluid may be at the critical heat flux, the other fluid may be in the nucleate boiling regime at the prevailing surface temperature. Unfortunately, in most cases, it is not possible *a priori* to determine the demarcation point (surface temperature) from one cooling regime to another without resorting to experimental observations.
- The second assumption is that the dimensionless heat transfer correlations obtained in the literature using water (in most cases) are applicable to the other fluids considered here.
- A third assumption is that the effect of surface roughness on surface heat flux is not considered. Furthermore, the spray parameters used in the following calculations were chosen to be within the range of applicability of the empirical correlations. These operating parameters, though encountered in spray quenching applications, may not be identical to those appropriate for fire fighting applications. In addition, since different droplet generation techniques (sprays *vs*. mono-dispersed droplet streams) have been used to obtain the heat transfer correlations in various regimes, it is imperative that a comparison among the calculated surface heat fluxes should be made with these fluids in the *same* regime.

4.6.4 Convective Regime

Mudawar and co-workers[164,165] had performed extensive studies on cooling of metal surface in this regime using water sprays. Their heat transfer data were correlated using the Nusselt number (Nu), the Reynolds number (Re), and the Prandtl number (Pr) by the following expression,

$$\frac{hD_{32}}{k_f} = Nu = 2.512\left[\frac{Q''D_{32}}{\nu_f}\right]^{0.76}\left[\frac{C_{pf}\mu_f}{k_f}\right]^{0.56} = 2.512Re^{0.76}Pr^{0.56}, \qquad (4\text{-}33)$$

where h is the heat transfer coefficient, k_f is the thermal conductivity of the liquid, ν_f is the liquid kinematic viscosity, C_{pf} is the liquid heat capacity, and μ_f is the liquid viscosity. The Reynolds number is based on the volumetric spray flux, Q'', and the Sauter mean diameter, D_{32}, of the spray. All the liquid properties are evaluated at $(T_{surf} + T_f)/2$ where T_f is the droplet temperature before impact.

Figure 4-78 shows the calculated heat flux as a function of $T_{surf} - T_f$. The calculations were performed using Q'' = 0.005 m^3/m^2-s, T_f = 295 K, and D_{32} = 0.5 mm. The thermophysical properties of water and lactic acid were obtained from the DIPPR.[174] The properties of $C_3F_5H_3O$, HFE-7100, and R338mccq were estimated by methods described in Reid et al.,[175] the boiling point method of Sato was used for k_f, the corresponding states method of Rowlinson for C_{pf}, and the method of Brule and Starling for μ_f. In this regime, water removed heat from the surface more efficiently than the other four fluids. It may not be feasible in practice to maintain the same D_{32} with a fixed Q'' (the conditions used in the calculations) for the five fluids because the atomization characteristics at the spray nozzle would be vastly different among the fluids owing to their thermophysical properties, thus resulting in different D_{32}.[66]

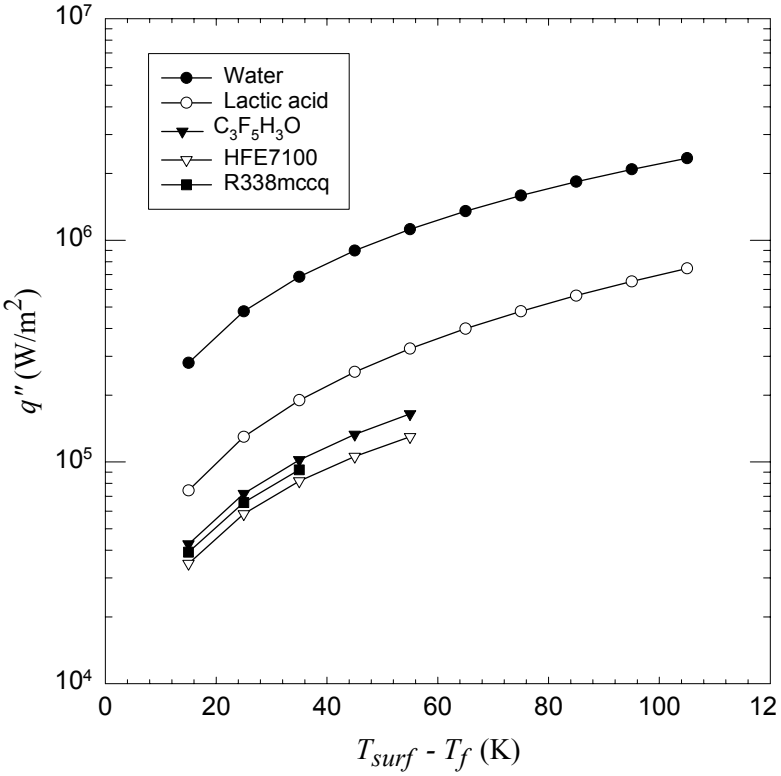

Figure 4-78. Calculated Boiling Curves in the Convective Regime for Five Liquids.

4.6.5 Nucleate Boiling Regime

Compared to other regimes on the boiling curve, the nucleate boiling regime in spray cooling has probably been the least studied. In this regime, the heat flux removal from the surface was found to scale only with T_{surf}-T_f in the studies by Mudawar and co-workers[164,165] where a water spray was used. The heat flux, q'', was correlated in the form of

$$q''=1.87\times10^{-5}(T_{surf}-T_f)^{5.55}. \tag{4-34}$$

In the work of Qiao and Chandra[176] on nucleate boiling enhancement using a surfactant/water solution, the heat flux measurements could also be correlated well by scaling with T_{surf} - T_f in a form similar to Equation (4-34),

$$q''=0.56\times10^{-5}(T_{surf}-T_f)^{6}. \tag{4-35}$$

Assuming that the proportionality constant and the power in the scaling law do not change significantly among the five chemical compounds and that the heat flux can be scaled with (T_{surf} - T_f), then the heat flux removal from the surface in the nucleate boiling regime using these five liquids should be similar for a given T_{surf}.

4.6.6 Critical Heat Flux

The dimensionless correlation developed by Mudawar and Valentine[164] for water spray cooling over a wide range of flows was used to estimate the critical heat flux (*CHF*),

$$\frac{CHF}{\rho_g \Delta H_{vap} Q''} = 122.4\left\{1+0.0118\left[\frac{\rho_g}{\rho_F}\right]^{1/4}\left[\frac{\rho_F C_{pf}(T_{sat}-T_f)}{\rho_g \Delta H_{vap}}\right]\right\}\left(\frac{\sigma_f}{\rho_F Q''^2 D_{32}}\right)^{0.198}, \quad (4\text{-}36)$$

where ρ_g is the vapor density of the fluid, T_{sat} is the saturation temperature of the fluid, and σ_f is the surface tension of the fluid. All the fluid properties were evaluated at the fluid saturation temperature.

Using Q'' = 0.005 m^3/m^2-s, T_f = 295 K, and D_{32} = 0.5 mm, the resulting *CHF*s for water, lactic acid, $C_3F_5H_3O$, HFE-7100, and R338mccq are 0.63 × 10^7 W/m^2, 0.86 × 10^7 W/m^2, 0.33 × 10^7 W/m^2, 0.23 × 10^7 W/m^2, and 0.21 × 10^7 W/m^2, respectively. In the calculations, surface tensions of water and lactic acid were obtained from the DIPPR,[174] while those of $C_3F_5H_3O$, HFE-7100, and R338mccq were estimated using the method of Brock and Bird.[175] Although lactic acid and water have the highest and second highest *CHF*s, respectively, under the conditions used in the calculations, it should be noted that it is inappropriate to compare the *CHF*s unless they occur at the same surface temperature for the five fluids, a situation highly unlikely given the differences in the thermophysical properties of these fluids.

4.6.7 Transition and Film Boiling Regimes

Based on dimensional analysis, Deb and Yao[177] statistically derived an equation for heat transfer effectiveness (ε) in terms of droplet Weber number (*We*), dimensionless wall superheat (B_w) and vapor parameters (K_d), and surface factor (*SF*) for surface material effect,

$$\varepsilon = 0.027\exp\left[\frac{0.08\sqrt{\ln\left(\frac{We}{35}+1\right)}}{\left(B_w+\frac{SF}{60.5}\right)^{1.5}}\right]+0.21K_d B_w \exp\left[-\frac{90}{We+1}\right], \quad (4\text{-}37)$$

with

$$We = \frac{\rho_F V_i D_o}{\sigma_f} \quad (4\text{-}38)$$

$$B_w = \frac{C_{pF}\left(T_{surf}-T_{sat}\right)}{\Delta H_{vap}} \quad (4\text{-}39)$$

$$K_d = \frac{k_F}{C_{pF}\mu_v} \quad (4\text{-}40)$$

and

$$SF=\sqrt{\frac{k_s \rho_s C_{ps}}{(k\rho C_p)_{steel}}}-1, \tag{4-41}$$

where V_i is the droplet impact velocity, K_d is the dimensionless vapor parameter, μ_v is vapor viscosity, and k_s, ρ_s, and C_{ps} are the thermal conductivity, density, and heat capacity of the surface material, respectively. All liquid and vapor properties are evaluated at T_{sat}. The heat transfer effectiveness is defined as the ratio of actual heat transfer from the hot surface to the total heat transfer required for complete evaporation of the droplets. Therefore, the heat flux from the surface is

$$q''=\varepsilon G[\Delta H_{vap}+C_{pf}(T_{sat}-T_f)], \tag{4-42}$$

where G is the liquid mass flux. ε was obtained from Equation (4-37) by fitting data mainly from experiments using a single stream of droplets. The experimental conditions covered the film boiling regime and to some extent the adjacent transition boiling regime and Leidenfrost point.

Figure 4-79 shows the calculated heat fluxes for the five fluids as a function of the surface temperature. The calculations were performed using T_f = 295 K, V_i = 2.5 m/s, D_o = 0.3 mm, and G = 0.5 kg/m^2-s. For illustration, a stainless steel, SS 304, was used as the target surface. Under the conditions used in the calculations, the resulting droplet *We* were 31, 97, 181, 297, and 339 for water, lactic acid, $C_3F_5H_3O$, HFE-7100, and R338mccq, respectively. The range of surface temperatures used in the calculations was chosen so that the calculated ε did not exceed 1. The three boiling regimes (transition boiling, Leidenfrost condition, and film boiling) are apparent in Figure 4-79. If it is assumed that at $T_{surf} \geq$ 800 K, all five fluids exhibit film boiling, and lactic acid has the highest surface heat flux.

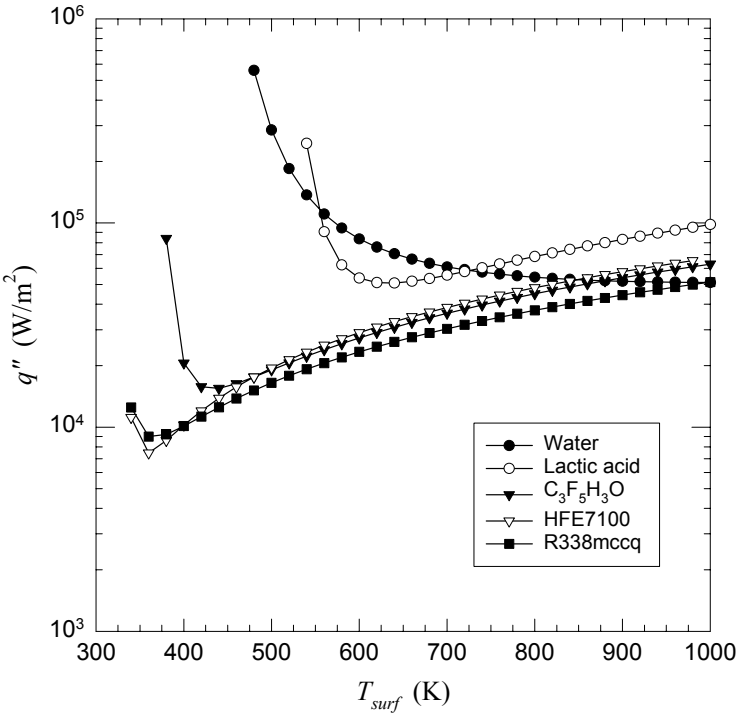

Figure 4-79. Calculated Boiling Curves for Five Liquids for the Transition and Film Boiling Regimes.

Figure 4−79 also demonstrates again the difficulty in comparing the heat fluxes at a given surface temperature. For example, at T_{surf} = 550 K, $C_3F_5H_3O$, HFE-7100, and R338mccq are in the film boiling regime, whereas, water and lactic acid are in the transition boiling regime. As stated above, unless the surface temperature at which the onset of a particular boiling regime is known a priori, it is not possible to know which heat flux correlation pertaining to which boiling regime should be applied in the estimation.

4.6.8 Summary

A suppression mechanism possibility for aerosol agents (and not generally for gaseous agents) is the potential to cool any burning surfaces or hot surrounding surfaces. Surface cooling by liquid droplets is a very complicated heat transfer process because it depends on so many parameters: the thermophysical properties (surface tension, density, viscosity, heat of vaporization, etc.) of the liquid, droplet size, droplet impact velocity, spray mass flux, and surface properties. Even for non-burning, smooth surfaces, calculations of surface heat fluxes from first principles are not possible without resorting to experimental observations. Empirical heat transfer correlations under conditions encountered in fires are lacking, and the quantification of surface cooling as a means to extinguish the burning fuel remains elusive, especially when the fuel is a liquid. Nonetheless, the greatest benefit will arise from those agents that are efficient thermal agents, particularly aerosols that have large heats of vaporization per gram of agent.

4.7 AEROSOLS AND BURNING SURFACES

There are four key physical phenomena involved in the interaction of aerosols with burning surfaces: (1) buoyancy effect on the trajectory of the aerosol particles, (2) evaporation/decomposition effect on the trajectory of the particles, (3) cessation of reaction and reduction in flame spread caused by the aerosol on flaming surface combustion, and (4) reduction in surface temperature caused by the particle impingement, spreading, and evaporation/decomposition on surface. The NGP study on the interaction of aerosol with burning surfaces addressed the interactions of liquid droplets with surfaces. The NGP study experimentally determined the key water droplet properties, such as surface loading and droplet diameter, that affect flame spread rate, and through numerical and experimental comparison sought to determine the effect of droplet size and velocity on droplet buoyancy and evaporation as the droplets approach a hot surface or fire. The work is summarized here and can also be found in References 178, 179, 180 and 181.

Monte Carlo methods are widely used to solve for the heat transfer in a wide variety of problems[182,183] due to their simplicity and accuracy. There are many methods to improve the accuracy of Monte Carlo simulations including improved sampling,[184] weighing and biasing,[185] and the discrete probability function method.[186] Therefore, the simulation of the problem utilizing Monte Carlo methods is straightforward, once the important rates that govern the physical processes are understood.

The different components that describe both the droplet trajectory and the temperature distribution over the surface as a function of time are studied in detail in this project by separating the various physical processes and integrating them to obtain an experimentally validated model that can be used in Monte Carlo simulations. Experiments were conducted with non-evaporating and evaporating particles of controlled density injected at controlled velocities towards a variably heated surface. Particle velocity as a function of the impressed buoyancy forces were measured, thereby determining the likelihood of a particle reaching a burning surface. Evaporation effects were also examined. Both monodisperse and polydisperse droplets were injected over PMMA flames or over heated polyurethane foam, using droplet

loading, delay time after ignition, and location of the spray from the leading edge as parameters. Such conditions provided data for examining any correlation between spray characteristics and flame spread. Surface temperature changes as a function of aerosol impingement were determined using a Two Color Planar Pyrometer. Finally, Monte Carlo simulations of the mist/surface interactions were investigated to develop fuller understanding of the dominant processes and identify the key aerosol properties that impact efficient suppression of the fire.

4.7.1 Flame Spread Studies

Experimental

Flame spread experiments were carried out in a wind tunnel, whose photograph is shown in Figure 4-80. The wind tunnel measured 45 cm high, 76 cm wide, and 175 cm long. The roof had three rectangular slots 7.6 cm wide x 28 cm long for observation of the flame by means of a video camera. The slots were covered with 1.25 cm thick glass windows during the experiments. The velocity inside the tunnel was controlled by an exhaust fan.

Honeycomb flow straighteners of polycarbonate, placed at the mouth of the duct, were used to remove large scale turbulent eddies and create uniform flow conditions in the test section. Each flow straightener had a diameter of 0.64 cm and is 25 cm in length. This L/D ratio, yielded a maximum Reynolds number of 64 and was sufficient to establish a fully developed laminar flow in the straighteners.[187] A 0.16 cm thick ceramic paper was applied to the interior of the tunnel to reduce heat transfer to the walls.

Figure 4-80. Wind Tunnel Used for Fire Spread Studies.

PMMA sheet was used as the fuel. PMMA supports surface combustion, and the flame spread rate over it is steady and well characterized. The properties of PMMA, such as density, specific heat at constant pressure, and heat of combustion, are consistent and well known. PMMA test specimens were 30 cm x 20 cm sheets of thickness 0.32 cm or 0.64 cm. The PMMA sheets were ignited with a small methanol trough before placing them into the wind tunnel. The experiments were carried out at four opposing wind speeds of 69 cm/s, 84 cm/s, 121 cm/s, and 153 cm/s. Three air flows, ranging from 9.5 cm^3/min to 15.5 cm^3/min, and three inlet pressures (880 kPa, 1375 kPa, and 2115 kPa) were used to vary the mass loading and the droplet size of the water spray used for suppression.

Initially, the fire suppression experiments were carried out with one surface in contact with an insulating ceramic material. This is the conventional method, called here "with backing" mode or one-sided combustion mode. When fire suppression experiments were begun, it was realized that the ceramic backing was quick to absorb water and was instrumental in extinguishing the flame almost as soon as the water spray was turned on. Therefore, the present studies were carried out with the PMMA sample supported along its sides with air flowing above and below the specimen. A photograph of the flame suppression experiment with the water mist applied is shown in Figure 4-81.

Figure 4-81. Flame Spread Experiment with Water Mist.

Calculations showed that the Blasius boundary layer thickness over the surface of the aluminum platform has a maximum value of about 1.4 cm. A 6 cm gap between the bottom surface of the PMMA specimens and the support platform ensured that free stream conditions existed on both the top and bottom and that the flame spread was unaffected by the boundary layer on the support platform.

A hollow cone spray was generated using a pressure atomizer which delivered good atomization quality over a large range of flows at the same inlet pressure. The nozzle was mounted on a bracket at a distance of about 60 cm upstream of the sample and at a height of about 17.5 cm above the surface of the PMMA. The droplets were carried downstream and onto the flame by the airflow present in the wind tunnel.

To obtain local surface loading of the water spray, pieces of absorbent tissue paper were taped onto the surface of a PMMA sample in a 4 x 4 grid. The spray was established at a given test condition and the difference in weight of the tissues was determined after a suitable interval of time. A Phase Doppler Particle Analyzer was used to obtain the droplet size and droplet mean velocity data. The PDPA was operated in forward scatter mode (θ =30"). The probe volume was 14 cm downstream of the nozzle exit.

A black-and-white 8-bit CCD camera was used to track the motion of the flame. The camera was mounted on a bracket above the observation window and looked down perpendicularly onto the burning samples. It was observed that the edges of the PMMA samples burned faster than the center. In order to avoid erroneous estimates of flame spread rate on account of edge effects, the camera focused on the central 23 cm of the flame.

During a typical experiment, the flame spread images were obtained 8 s apart. The location of the flame was assigned to be the pixel of maximum intensity. The difference in location of the flame in a particular row of pixels between two frames (that were separated by a known time interval) yielded the flame spread rate for that row. To reduce the discretization errors, the flame spread was calculated from images separated by 160 s. The mean velocity of the flame calculated for all the rows was designated to be the velocity of the flame at that time.

The reduction in flame temperature due to droplet loading was obtained using a two-color planar pyrometer (TCPP). A schematic diagram of the two color planar pyrometer is shown in Figure 4-82. The TCPP had an imaging lens that was used to collect broad band radiation from the fire. The radiation was split into two beams that were spectrally differentiated using band pass filters. An array imaging camera was used to obtain the spectral image of the flame at two wavelengths. The band pass filters were centered at approximately 900 nm and 1000 nm, and each had a band width of 80 nm. The TCPP was calibrated using a standard laboratory black body source.

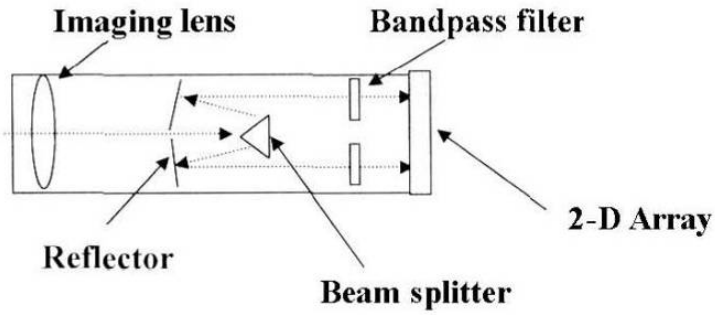

Figure 4-82. Schematic of the Two-color Planar Pyrometer.

Results and Discussion

The first issue addressed was the measurement uncertainty. If x is the position of the flame and t is the time interval between measurements, the velocity is given by $v = x/t$. The uncertainties in the measurement of flame position (w_x) and time (w_t) were used to estimate the uncertainty in the flame spread rate (w_V) [188]

$$w_V = \left[\left(\frac{\partial v}{\partial T} w_V \right)^2 + \left(\frac{\partial v}{\partial x} w_x \right)^2 \right]^{\frac{1}{2}} \tag{4-43}$$

For the imaging system, the uncertainty in position was ± 1 pixel, and that in time (provided by the camera timer) was 1 μs. Therefore, for a typical flame event lasting 160 s, with the flame moving about 12 pixels, the uncertainty in velocity was:

$$\frac{w_V}{V} = \frac{w_X}{X} = 8.3\% \tag{4-44}$$

Typical flame velocity data obtained using the imaging system is shown in Figure 4-83. The imaging system started recording at a rate of 1 image every 8 s immediately following flame ignition. During the first few minutes, the flame spread rate rapidly decreased until a steady state was reached. At steady

state, the flame spread velocity changed approximately 10 % due to the small-scale fluctuations in the flame front and the uncertainty of the measurement.

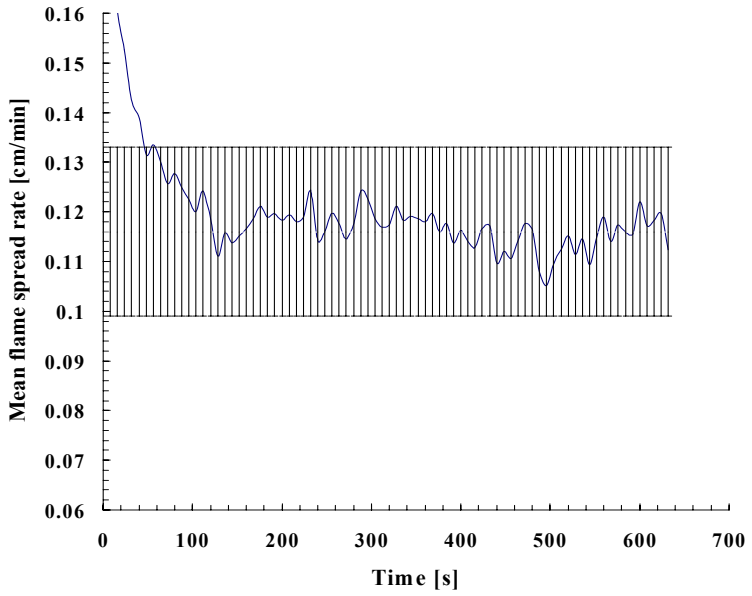

Figure 4-83. Typical flame spread time trace obtained using Focal Plane Array Imaging.

The flame spread rate as a function of opposing wind speed is shown in Figure 4-84. The vertical bars represent one standard deviation in the statistical variation of the data on each side of the mean (approximately 60 points per run). The experimental uncertainty is less than 10 % of the mean.

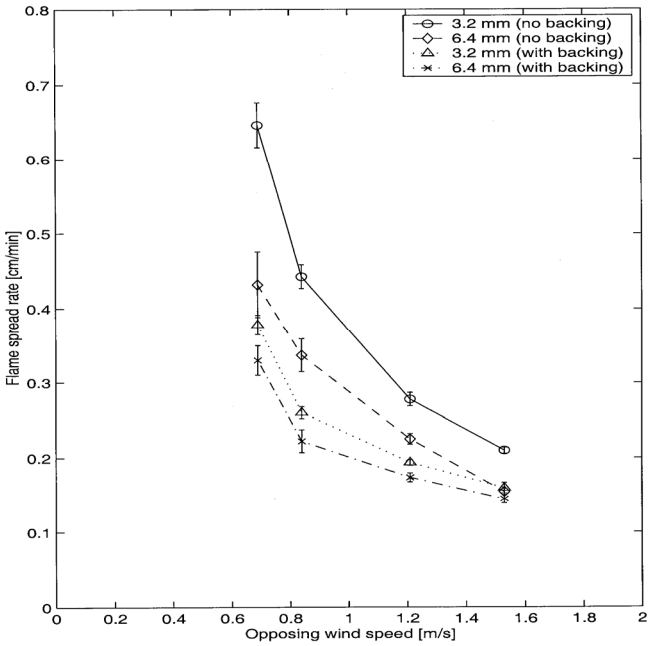

Figure 4-84. Flame Spread Rates without Water Mist.

As expected, the flame spread rate without backing was higher than that with backing for the same sample thickness, since burning was allowed to take place on both sides in the 'without backing' mode. Also in 'with backing' mode, some amount of heat loss occurred to the supporting aluminum plate since the ceramic paper (on which the PMMA is burned) was not a perfect insulator.

Another observation is that the flame spread rate decreased as the opposing wind speed increased. This can be explained by realizing that the forward heat transfer by gas-phase conduction from the flame to the unburned fuel decreased. Convective heat transfer from the unburned fuel surface also increased. This result is therefore expected. It was also found that the flame spread rate was higher for the thinner fuel than the thicker fuel. Since the heat transfer required to raise the temperature of the unburned fuel to its vaporization temperature is less for a thin fuel, this finding was also expected. These three results were consistent with the observations reported by previous investigators.

The flame spread rate results found in this work were approximately 20 % greater than the findings of Fernandez-Pello et al.[48] for the 0.64 cmm thickness PMMA at 70 cm/s opposed flow velocity. At flow velocities of 85 cm/s and 120 cm/s, the results in the present work were lower than the findings of Reference 48 by about 9 % and 6 %, respectively. The results at the two higher flows were within the limits of experimental uncertainty.

Differences at the lower flow velocity were outside of the experimental uncertainty and can be explained as follows. At the lower opposed wind speeds, the flame stand-off height was more than at the higher opposed wind speeds. As the width of the sample in the present work (30 cm) was much greater than that in Reference 48, there was greater radiation heating of the unburned fuel surface by the flame. Hence the measured flame spread rate was greater.

At the higher opposing wind speeds the flame stand-off height was much less. At these high wind speeds, radiation from the flame was much lower, due to a small view factor. It is believed that it was the size of the experimental facility that was responsible for differences in the measured flame spread velocities between this study and the work of Reference 48. In particular, the wind tunnel duct used by Reference 48 was 5 cm x 4 cm in cross-section and 100 cm long, while the duct used in the present work had a cross-section of 45 cm x 76 cm and was 175 cm long. The greater re-radiation from the walls of the duct in the work of Reference 48 was believed to be the reason for the difference in the findings.

Another reason for the differences between the current measurements and those of Reference 48 could be different diagnostic and analytical techniques used to determine the flame spread rate. The progress of the flame in the experiments of Reference 48 was measured visually as it passed over previously ruled marks on the PMMA surface, whereas in the present work a CCD camera tracked the flame motion. The data analysis method used by Reference 48 is not known, but in the present work the estimate of flame spread rate is over a rather large length of time (160 s) rather than being “instantaneous.”

The flame spread rate as a function of surface loading for the 0.32 cm thickness sample is shown in Figure 4-85. Similar results for the 0.64 cm thick PMMA are shown in Figure 4-86. The systematic decrease in flame spread rate with increasing surface loading on the PMMA can be clearly seen in all cases.

The effect of surface loading was greatest in the case of low opposing wind speeds, viz. 69 cm/s and 84 cm/s. The reason may be that the flame spread rate was low to begin with at the higher opposing wind speeds and with increasing loading there was a practical limit to the flame spread rate that can exist and still be measurable. It was conjectured that a threshold value of flame spread rate exists, between 0.15 cm/min and 0.20 cm/min, below which the flame would be rapidly extinguished.

The role of surface loading on the flame spread rate was explained in terms of heat transfer effects. On account of surface cooling, there was a reduction in pyrolysis of the fuel ahead of the flame front. As the rate of fuel vapor production decreased, less heat was liberated in the exothermic chemical reaction between the fuel vapor and oxygen. This resulted in a net decrease in heat transfer to the unburned PMMA ahead of the flame. As a result, the flame spread rate dropped.

In order to determine the effect of spray operating parameters on the droplet size, namely the atomizer inlet pressure and flow, measurements of droplet size and velocity were performed using a Phase Doppler Particle Analyzer. Droplet size and velocity data are presented in Figure 4-87.

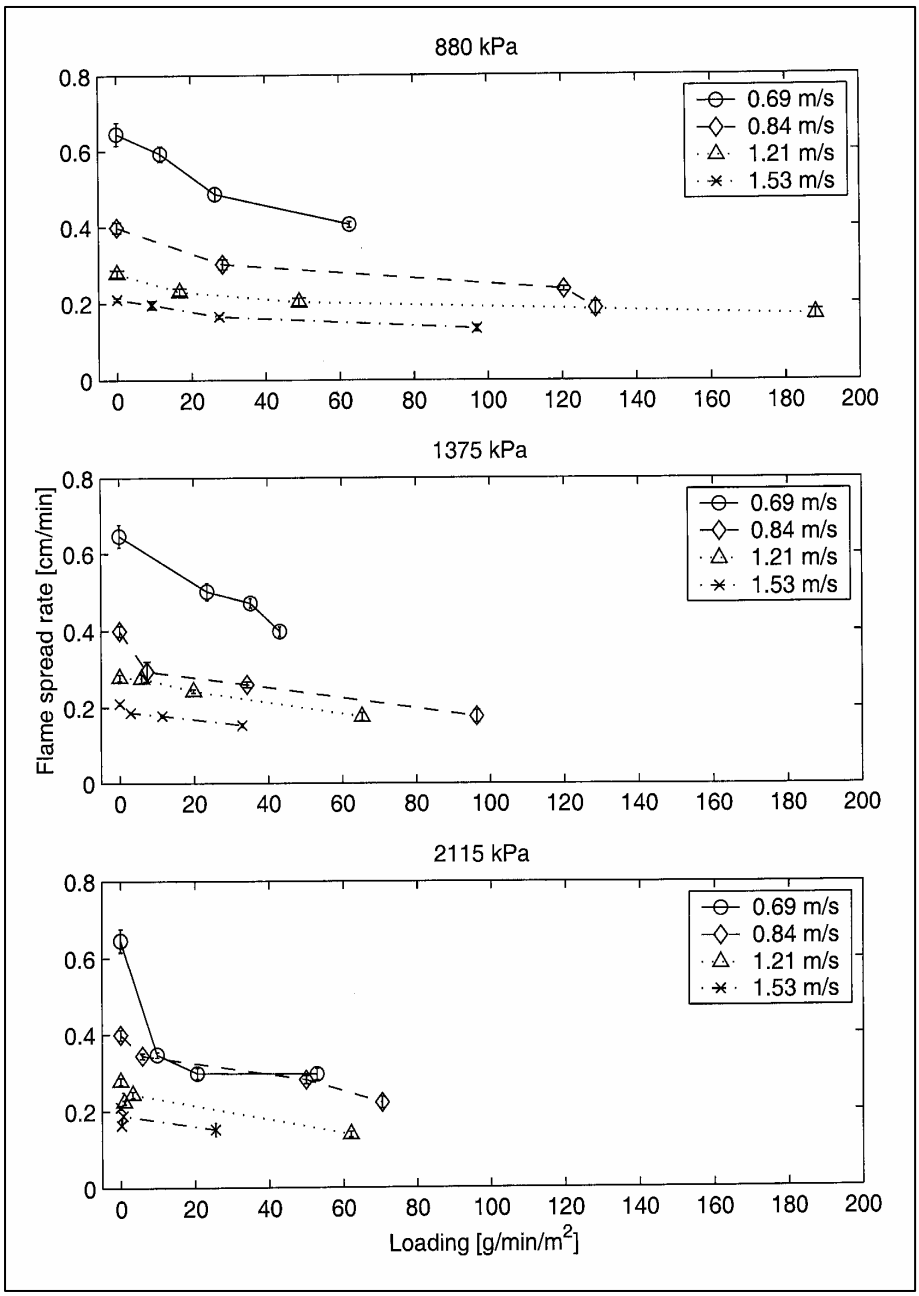

Figure 4-85. Flame Spread Rate as a Function of Surface Loading for 3.2 mm Thick PMMA.

From Figure 4-87, it is seen that both the droplet size and the mean velocity increased as the mass flow rate through the nozzle increased for a constant inlet pressure. At the same flow through the nozzle, the droplet size was smaller and the mean velocity greater at the higher pressure. The difference in the mean droplet diameter at 10 cc/min flow at the three different pressures was approximately 2.5 μm; at 15 cc/min flow rate it was approximately 1 μm. By the d^2-law of droplet evaporation the ratio of evaporation times of droplets 27.5 μm and 25 μm in diameter is 1.2. Therefore, a notable impact due to evaporative cooling in the flame vicinity cannot be expected. Consequently, the droplet size variation should not be a significant factor in flame spread rate variations for the conditions considered here.

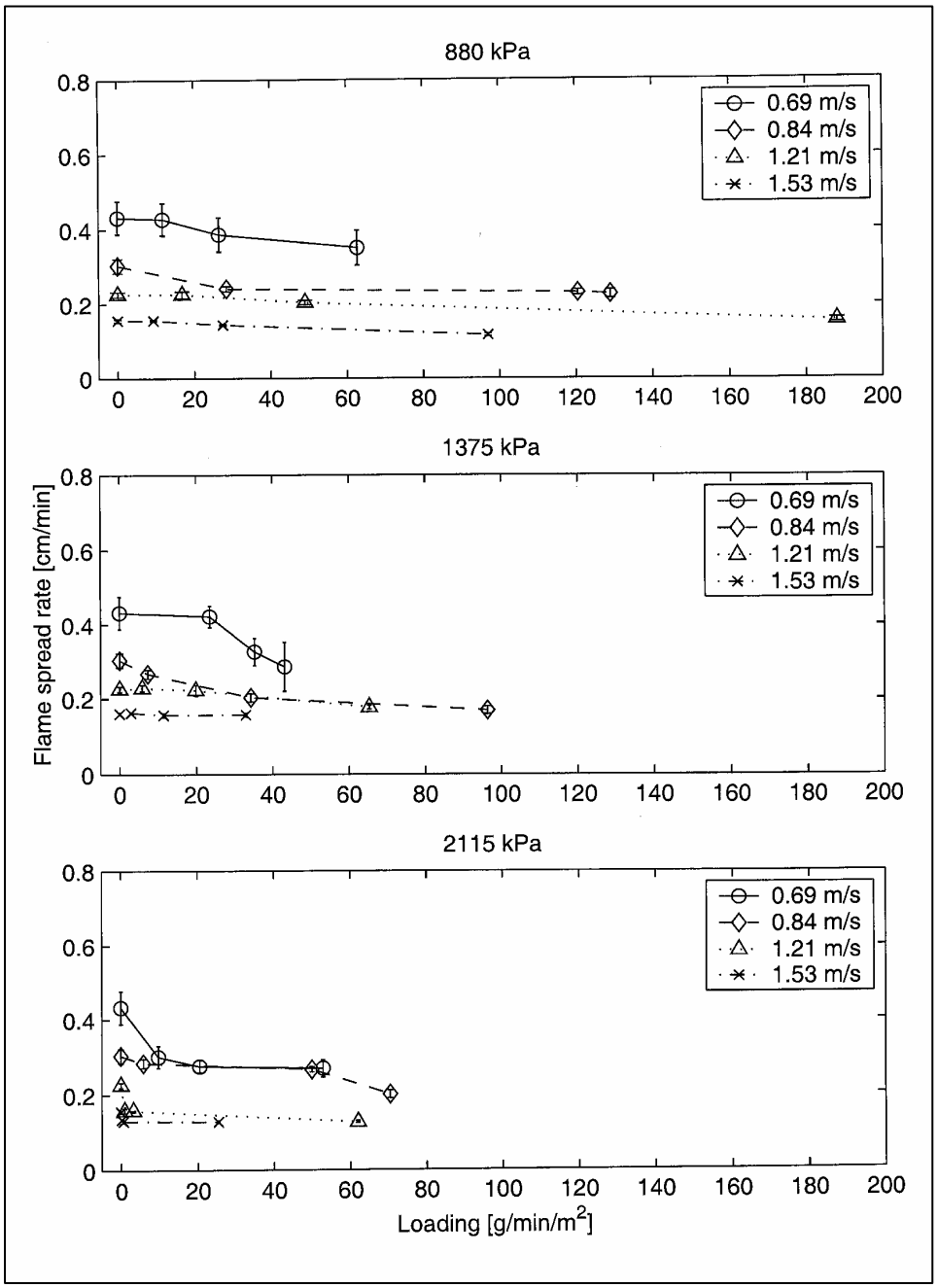

Figure 4-86. Flame Spread Rate as a Function of Surface Loading for 0.64 cm Thick PMMA.

The droplet mean velocity measurements provided an explanation as to why the flame spread rate increased with increasing nozzle discharge rate at low opposing wind speeds. The reason is that the droplet mean velocity increased as the flow rate increased. This reduced drift due to the cross-wind and led to deposition of the spray in the collection pan (placed below the spray nozzle) upstream of the target. The surface loading on the PMMA was thus reduced and, consequently, the flame spread rate increased. The data obtained from all tests were used to develop an empirical correlation. The normalized flame spread rates for all conditions are shown in Figure 4-88. Three different injection pressures (corresponding to different droplet diameters), two different PMMA thicknesses, and four different opposed flow velocities were used in developing the empirical correlation.

Data represented by open symbols shown in Figure 4–87 were obtained with 0.32 cm thick PMMA, and those represented by closed symbols were obtained with 0.64 cm thick PMMA sheets.

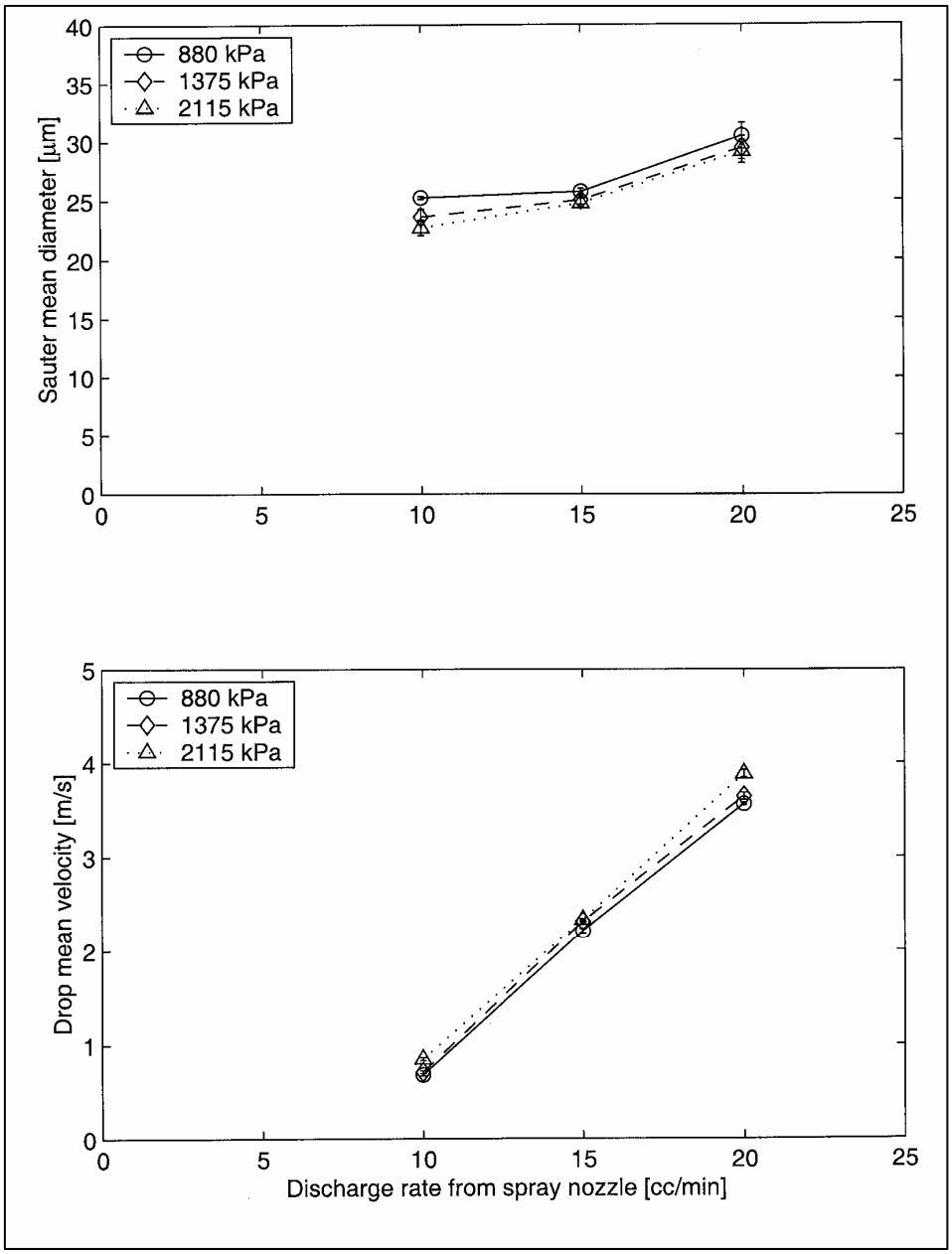

Figure 4-87. Mean Droplet Size and Velocity as a Function of Spray Nozzle Discharge Rate.

The regression analysis for the normalized flame spread in the thinner samples provided an approximately 85 % correlation with liquid mass loading. For the thicker samples, the correlation of the normalized flame spread with the liquid mass loading was approximately 75 %. The correlation obtained for all twenty-four conditions showed that the normalized flame spread rate was roughly a function of the local liquid mass loading alone. Correlations for flame spread rates with zero liquid mass loadings are readily available in the literature.

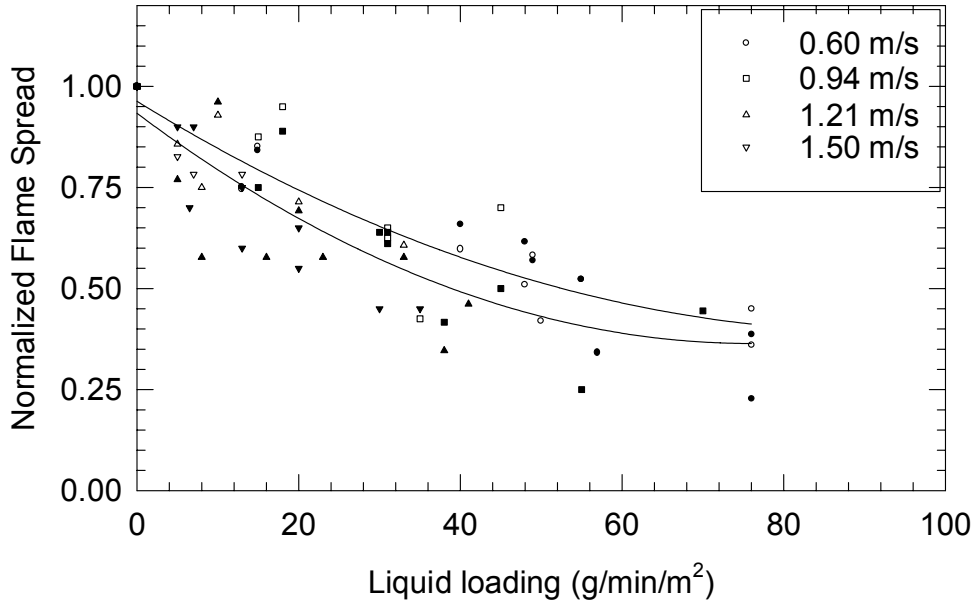

Figure 4-88. Variation in Normalized Flame Spread with Liquid Loading.

Therefore, the current results can be used to estimate (within a factor of two) what the local liquid mass flux should be to achieve extinction. This information is useful, since it provides a direct estimate of the optimal suppressant mass required to extinguish the fires. The effect of water loading on the decrease in the mean flame temperature is shown in Figure 4-89. The mean temperature of the flame without any water loading varied between 1200 K and 1400 K depending on the opposing wind velocity. The temperature dropped rapidly with increasing water loading, and the flame was extinguished at approximately 1000 K.

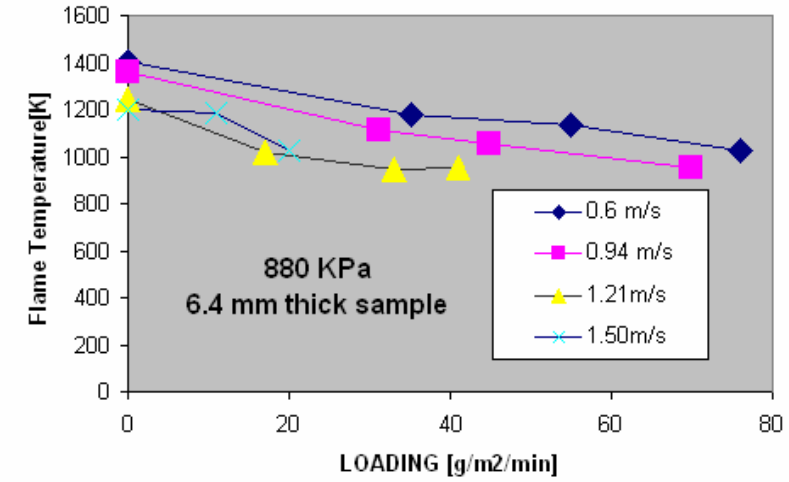

Figure 4-89. Mean Flame Temperature Obtained Using the TCPP. (880 kPa, 0.64 cm thick PMMA)

4.7.2 Droplet Interaction with a Hot Surface

Experimental

Schematics of the experimental arrangement are shown in Figure 4-90 through Figure 4-93. The experimental apparatus consisted of six main parts: the liquid supply system, the piezoelectric ceramic atomizer and its power supply system, the heater assembly and its power supply system, the temperature data acquisition system, the Phase Doppler Particle Sizer (PDPA) spray characterization system, and the spray imaging system.

Compressed shop air was reduced to an appropriate pressure by a regulator then introduced into a thick-walled plastic reservoir in which the liquid was stored. Liquid flowed out of the reservoir and passed through a filter and a rotameter, before finally reaching the piezoelectric ceramic atomizer. The filter had a pore size of 10 μm. The mass flow ranged from 0.1 g/s to l.0 g/s, and the inlet pressure ranged from 27.6 kPa to 82.7 kPa. They were adjusted simultaneously using the rotameter. Distilled water was used for evaporation experiments. Dow Corning 510, a non-evaporative fluid, was used for the buoyancy experiments.

A piezoelectric atomizer (purchased from Universitat Erlangen-Nurnberg, Germany) was used to produce monodisperse droplets with flows up to 4 g/s.[189] A schematic of the atomizer is shown in Figure 4-91. A 2 MHz function generator (Wavetek, Model 19) was used with an amplifier to supply square wave signals (approximately 30 V peak to peak) to the atomizer. The output frequencies ranged from 3 kHz to 2 MHz.

Three round stainless steel plates with orifices of different diameters made by laser drilling were used as nozzles in the atomizer. The plates were 50 μm thick, and were supported by a 1 mm thick stainless plate with a 1 mm hole in the center. The orifice diameters were 100 μm, 50 μm, and 20 μm. The atomizer was placed above the center of the heater in a fixture that allowed 360 º rotation. In addition, the atomizer was capable of being moved in both the vertical and horizontal direction.

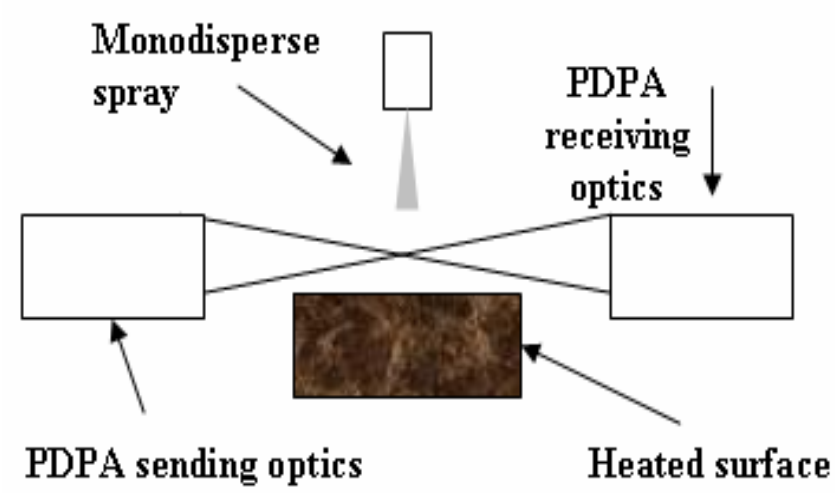

Figure 4-90. Experimental Arrangement for the Measurements.

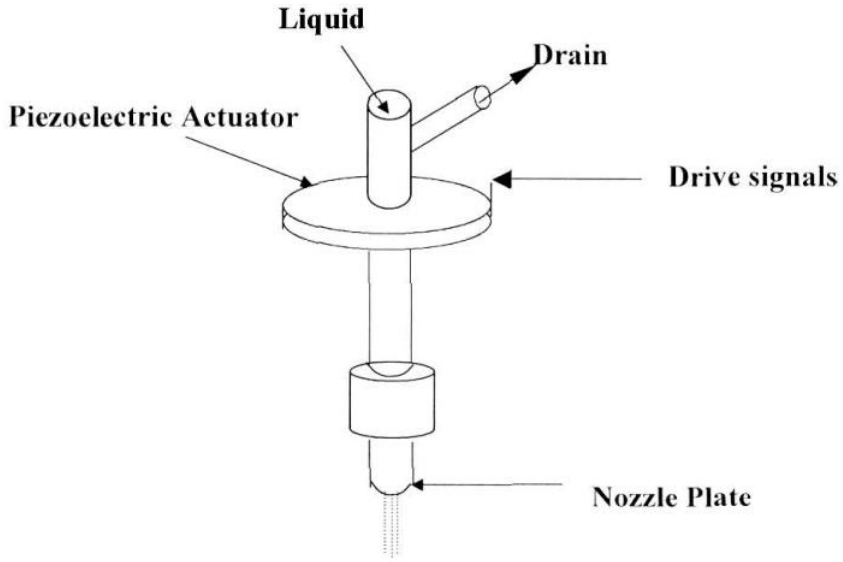

Figure 4-91. Configuration of the Piezoelectric Atomizer.

A heat source was necessary to provide a surface temperature as uniform as possible. A modified design of a hot plate was used in the experiments.[190] A schematic of the heater assembly is shown in Figure 4-92. The main components were an exterior aluminum ring with top and bottom cover plates, a copper block with inside cartridge heaters, and insulation material. To reduce oxidization of the heated surface and clogging in the orifices and pipes, distilled water was used. The plate used was taken out of the atomizer after each experiment and cleaned using an ultrasonic cleaner before the next test.

The arrangement of the oxygen-free copper block and the thermocouples is shown in Figure 4-93. The block was 10 cm in diameter. The exposed surface was nickel-plated to a thickness of 50 μm. Twenty-three cartridge heaters were obtained from OMEGA, each rated at 100 W maximum. They were arranged to heat the block as uniformly as possible. Twelve type K subminiature thermocouples were inserted into the copper block at 4 radial locations. There were 3 in each group, located at different depths to extrapolate the surface temperature. Holes for the cartridge heaters were 0.94 cm in diameter, and a total of 23 were arranged in three concentric circles as shown in Figure 4-93. The holes for the thermocouples were 0.16 cm in diameter, and a total of 12 were located as shown in Figure 4-93.

The copper block was surrounded by Cotronics Rescor 360 Ceramic Board insulation. This insulation was selected for low thermal conductivity (0.055 W/m-K at 260 ºC, 0.108 W/m-K at 600 ºC), resistance to high temperature (continuous operating temperature limit of 1260 ºC), rigidity, and machinability. There was a center hole in each insulation layer below the copper block to allow the thermocouples and cartridge heater leads to pass through.

A square, 1.59 mm thick Macor machinable ceramic cover was placed above the uppermost piece of the insulation layer, with a hole 10.16 cm in diameter in it for the exposed nickel-plated copper surface. The Macor sat on a ridge machined into the top aluminum cover plate. The exposed heater surface was maintained flush with the surrounding Macor plate by adjusting three screws beneath the insulation at the very bottom of the assembly. High temperature sealant 906 (Megnesia Adhesive from Cotronics) was used to fill the gap between the Macor and the aluminum cover plate. Excess water flowed down along the exterior surface of the aluminum ring and was drained out through a hole in the slot, which was formed by the cylinder and the short ring mounted on the bottom plate.

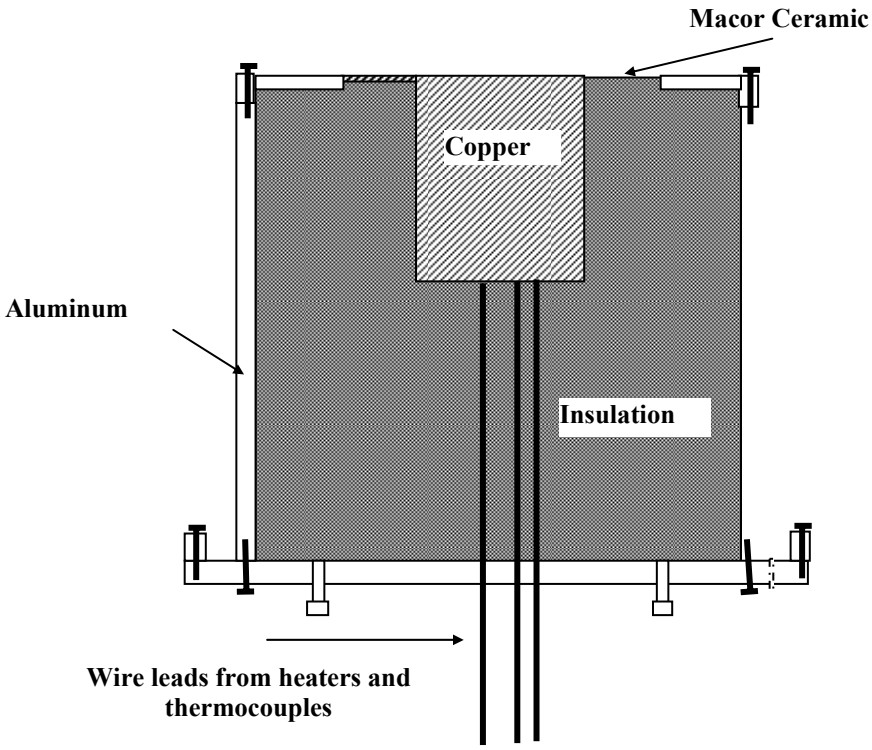

Figure 4-92. Schematic Diagram of the Heater Assembly.

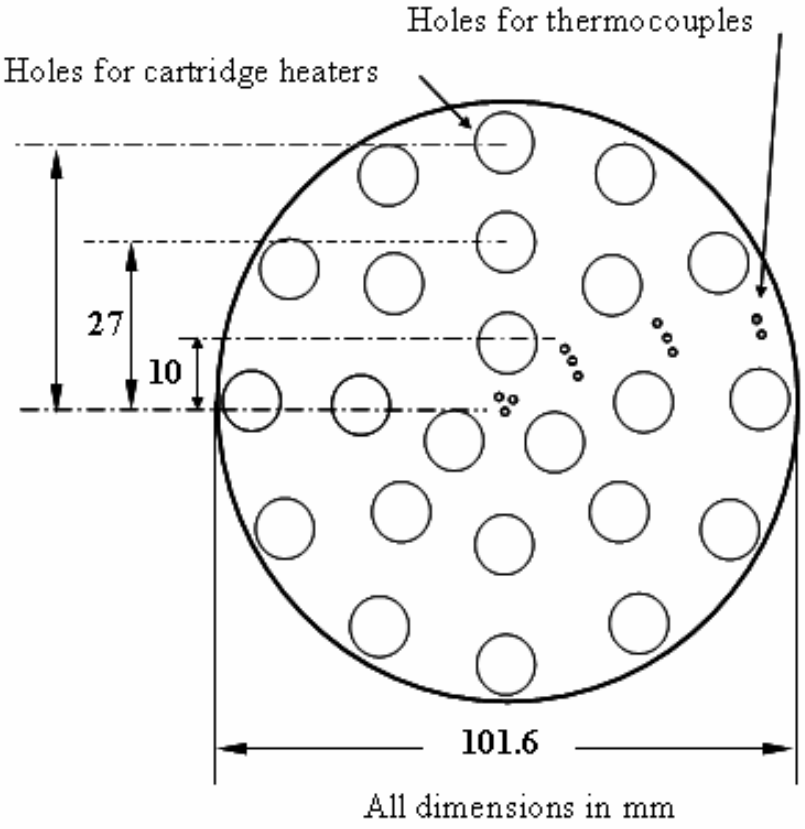

Figure 4-93. Temperature Measurement Locations on the Heater.

A PDPA was used to measure the sizes and velocities of the droplets (See Section 4.3.4). The PDPA transmitter (Model 11 00) contained a 10 mW, polarized Helium-Neon laser. The collimating lens was 300 mm, and the receiver lens was 1000 mm to permit the largest range for measuring droplet sizes. The forward scattering mode was used to obtain data. The position of the Phase Doppler Particle Analyzer (PDPA) was fixed. The heater and the atomizer were moved together to measure droplets at different axial and radial locations. A three-dimensional motor controller was used to provide accurate relative positioning of the laser probe volume.

The 12 voltage signals from the thermocouples were received by the EXP-16 board (Computer Boards) and multiplexed into a single signal for amplification. A gain of 100 was used to achieve the largest voltage measurable and programmable by the CIO-DAS1402/12 board (Computer Boards). The EXP-I6 also contained a CJC (cold junction compensation) circuit for correcting thermocouple readings.

Experiments were performed for different liquids, nozzle plates, flows, and operating frequencies. The initial surface temperature of the copper was chosen to be 600 ºC for water and 250 ºC for Fluid 510. In addition, a base line data set with the heater at 25 ºC was also obtained. For a given a nozzle plate and a given flow, the operating frequencies were changed to get different droplet sizes and velocities. A frequency was chosen by visually observing the jet shape and ensuring that there were no satellite droplets breaking away from the main stream. A plastic curtain was used in the experiments to reduce the ambient disturbances. Measurements at different axial and radial locations within the spray were obtained by moving the heater and the nozzle assembly using a slide.

Modeling

For designing suppression systems, models are routinely used to calculate droplet trajectories. Since droplets arriving at a fire location have to pass through a hot environment, the models also have to account for buoyancy and evaporation. The data obtained using the PDPA can be used for assessing the accuracy of these models. During the course of the project, a model based on Lund et al.[191] that accounts for coalescence and evaporation of droplets was evaluated using the data.

The influence of evaporation was evaluated through use of the d^2 law as described by [192]

$$\frac{dm}{dt} = 2\pi D_V \frac{p_v}{RT} ShD \tag{4-45}$$

where m is droplet mass, t is time, D_V is the mass diffusion coefficient, p_v is the vapor pressure, R is the ideal gas constant for the vapor, T is the temperature, Sh is the Sherwood number, and D is the droplet diameter.

A change of variables converted the change in mass with respect to time in Equation (4-45) to a change in diameter with respect to axial location. The resulting equation was:

$$\frac{dD}{dz} = \frac{4 D_V p_v Sh}{\rho_L DRTV} \tag{4-46}$$

The remaining unknown variable, the Sherwood number, was calculated using the correlation found in Ranz and Marshall:[193]

$$Sh = 2 + 0.6\,\mathrm{Re}^{0.5}\,Sc^{0.33} \tag{4-47}$$

where *Re* is the Reynolds number and *Sc* is the Schmidt number.

Calculations were made using Equations (4-46) and (4-47), plus the definitions of *Re* and *Sc*, to determine the change in droplet diameter with axial location for a particular size class. Since droplet diameter was found to decrease by only 0.015 μm for every 1 cm of axial distance, it was concluded that the influence of evaporation was negligible for the hydrocarbon oil used in this investigation.

The extent to which droplet coalescence played a role in increasing SMD was determined via a kinetic theory-based model. The model neglected viscous, gravitational and pressure forces. It was based on the coalescence of a droplet of size-velocity class *i* with a droplet of size-velocity class *j* to yield a droplet of size-velocity class k:

$$D_i + D_j \rightarrow D_k \tag{4-48}$$

From this relationship the rate equation for change in number of droplets of class *i* was:

$$\frac{dn_i}{dz} = \varepsilon\left(-\sum\frac{k_{ij}\eta_i\eta_j}{V_i} + \sum\frac{k_{ij}\eta_i\eta_j\alpha_{ij}}{V_i}\right)V_p \tag{4-49}$$

where n_i, the counts per unit volume for droplet class *i*, was defined as

$$\eta_i = \frac{n_i}{A_p t_{run} V_i} \tag{4-50}$$

The collision frequency for droplets of class *i* colliding with those of class *j*, was defined as:

$$k_{ij} = \frac{\pi}{4}\left(D_i + D_j\right)^2 V_{ij} \tag{4-51}$$

The probability of a collision leading to coalescence, ε, was determined by extrapolating the work of Jiang et al.[194] to the fluids studied here, and then approximating the impact parameter vs. Weber number curves as straight lines. Such a procedure overestimated the probability of a collision leading to coalescence.

In Equations (4-49) through (4-51), n_i represents the number of droplets in class *i*, A_p is the PDPA probe area normal to the flow, t_{run} is the run time, V_i is the velocity of class *i*, V_p is the PDPA probe volume, and a_{ij} represents the diameter D_k that results from coalescence in Equation (4-48).

Equations (4-49) through (4-51) were used to calculate the change in number of droplets for a particular class *i* with respect to axial location. Care was taken when distributing the product mass and momentum over the appropriate size-velocity bins. The coarse-grained PDF technique of Sivathanu and Gore[186] was employed to keep computational evaluation of Equation (4-49) tractable while ensuring spray mass and momentum conservation. Having calculated dn_i/dz in this fashion, $dSMD/dz$ was determined by taking the derivative of *SMD* with respect to *z*.

$$\frac{dSMD}{dz} = -\frac{\left(\sum D_i^2 \frac{dn_i}{dz}\right)\left(\sum n_i D_i^3\right)}{\left(\sum n_i D_i^2\right)^2} \tag{4-52}$$

Equation (4-52) was then used to calculate a change in the *SMD* due to coalescence of droplets with axial location. The results were compared with those obtained using the PDPA instrument.

Results and Discussion

The temperature field above the hot plate is shown in Figure 4-94. The temperature was 600 ºC just above the hot plate and rapidly decreased due to buoyancy induced entrainment. At an axial distance of 100 mm, the temperature was less than 200 ºC at the center line. The buoyancy induced velocity field was unsteady. (The time-resolved velocity field was not quantified.) The injector was located 250 mm above the hot plate in the centerline.

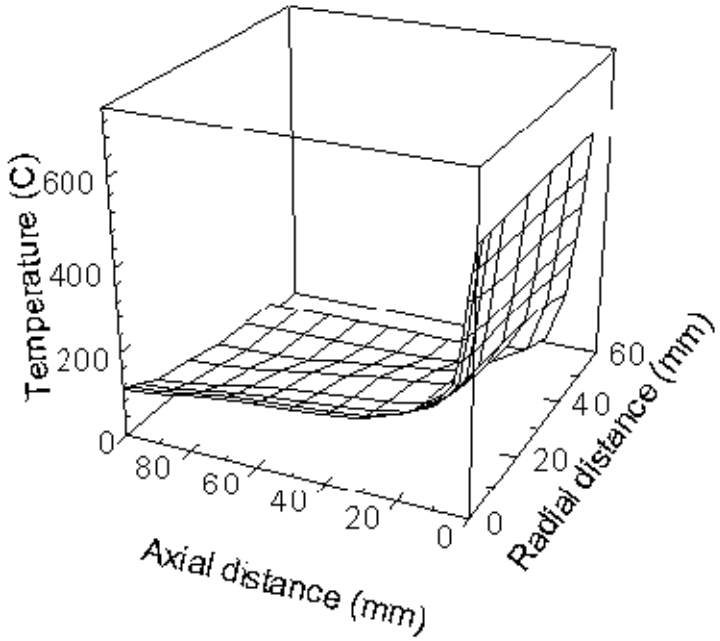

Figure 4-94. Steady State Temperature Field above the Hot Plate.

A steady state k-ε-g model, assuming a boundary layer flow, was used to try to predict the temperature field. However, even under steady state conditions, the local velocity field had both positive and negative values. The model did not have a mechanism to account for flow reversals. Therefore, the model predictions showed very large divergence from the experimental observations and are not provided here. A 3-D large eddy simulation code is needed to improve the model predictions.

The change in droplet diameter with distance from the injector is shown in Figure 4-95. The PDPA results obtained using a cold plate and a hot plate are also shown. The effects of coalescence are readily apparent. For both cases, the mean diameter of the droplets increased by approximately a factor of three by the time they arrived at the hot plate. For the hot surface, the droplet diameter increased only by a factor of two. The smaller droplet diameters in the hot environment are likely due to evaporation. They may also be due to decreased coalescence. If the buoyancy induced flow field affects the local velocities

significantly, this could lead to lower coalescence and reduce the SMD. These two effects can be separated using non-evaporating droplets.

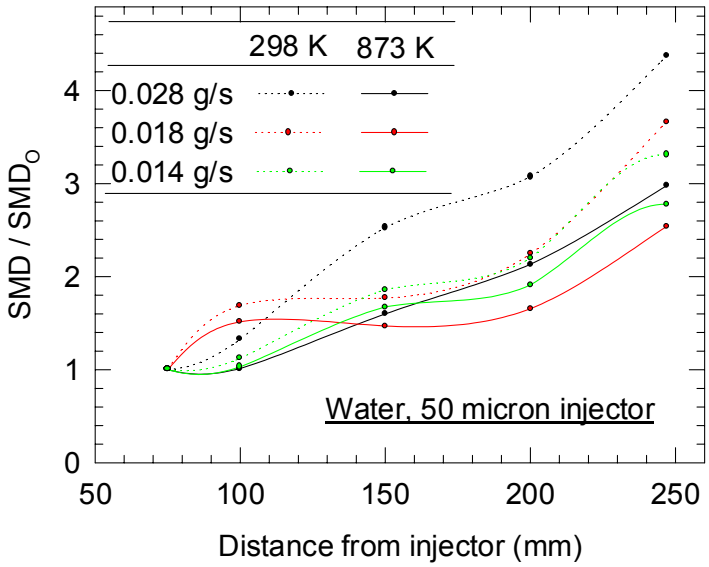

Figure 4-95. Change in Sauter Mean Diameter of the Water Droplets with Axial Distance.

Fluid 510 was used to determine evaporation effects on the droplet size history. When the fluid was sprayed onto the surface at 600 ºC, a thick smoke was formed. This smoke prevented the PDPA from obtaining droplet velocity and size data. In addition, the fluid formed a very hard coating on the copper plate. Therefore, the plate was cleaned, and the temperature reduced to 250 ºC (below the flash point of Fluid 510).

The change in droplet diameters with axial locations for Fluid 510 is shown in Figure 4-96. Two different excitation frequencies, representing two different droplet diameter distributions were used for the experiments. For both cases, it was found that the variation in SMD was identical, irrespective of the temperature of the plate. Therefore, the buoyancy induced flow field did not significantly affect the coalescence of droplets. It was evaporation that was responsible for the lower SMD when the plate was hot.

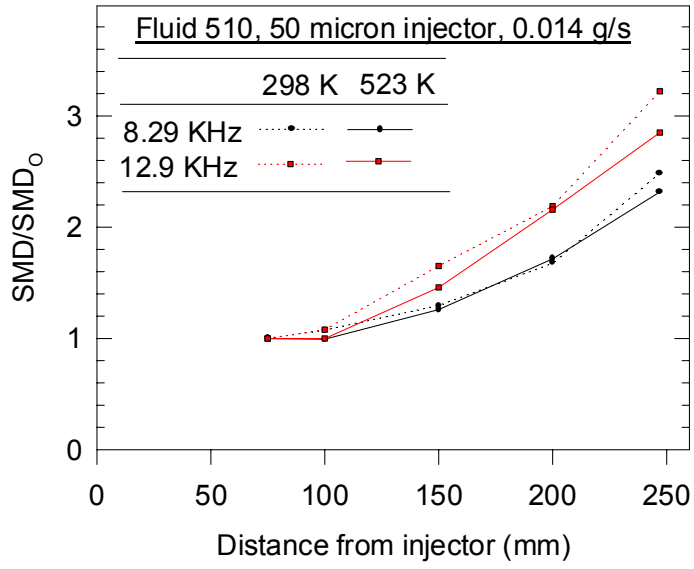

Figure 4-96. Change in Sauter Mean Diameter of the Droplets with Axial Distance for Fluid 510.

To evaluate the coalescence model, the velocity and number density of the droplets was required. The velocity of the water droplets is shown in Figure 4-97. It is clearly evident that the velocity of droplets was affected significantly by buoyancy. The velocities are much lower when the plate was hot. This usually increased the droplet SMD since the lower velocities provided a longer time interval for coalescence.

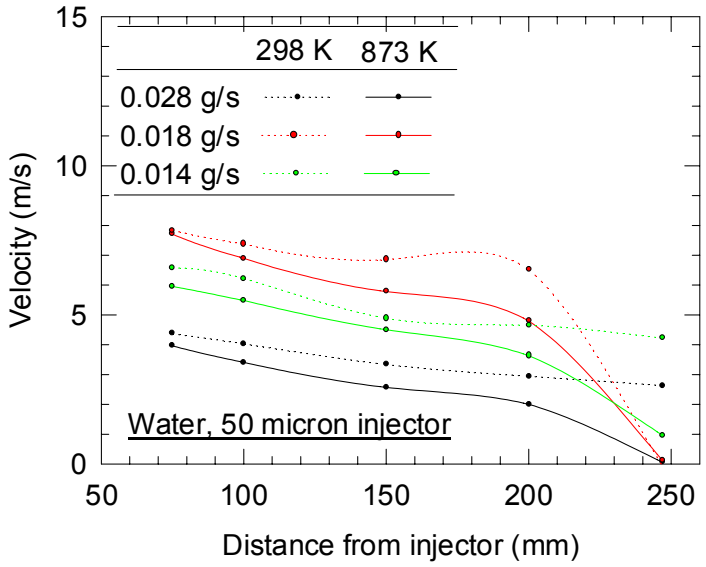

Figure 4-97. Variation in Velocity with Axial Distance for Water Spray.

The change in velocity with axial distance for three conditions using Fluid 510 is shown in Figure 4-98. Due to the lower temperatures attained, the change in velocity due to the buoyancy induced upward velocity of air was minimal. Similar results were obtained for the 20 μm nozzle. In all cases, the droplet diameter increased a factor of two or higher with downstream distance. Coalescence was the primary reason for the increase in droplet diameter.

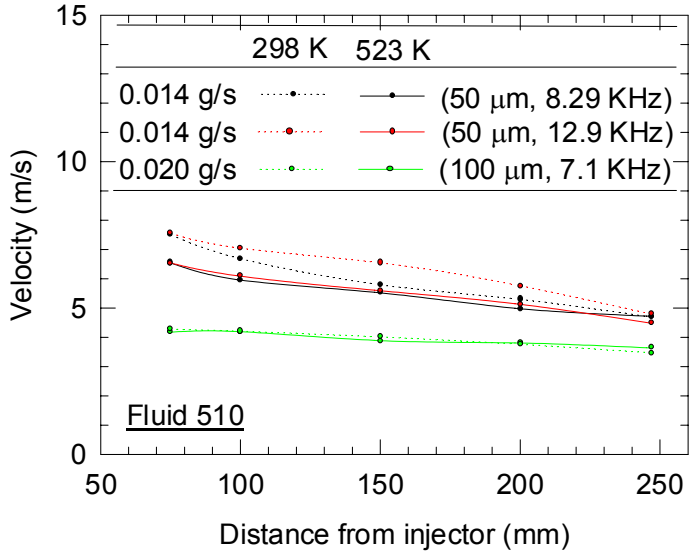

Figure 4-98. Variation in Velocity with Axial Distance for Fluid 510.

Modeling results of the change in SMD with diameter using Equation (4-46) for coalescence and Equation (4-52) for droplet evaporation differed significantly from the experimental data. The coalescence model predicted approximately two orders of magnitude lower changes in SMD with axial distance. The evaporation model suggested that the SMD of droplets would change by less then 2 % in all cases.

Improvements in the model using a Monte Carlo-based approach are needed to delineate the effects of coalescence and evaporation. Also needed is a more rigorous method of predicting the temperature field above the hot surface to implement the Monte Carlo simulations. Finally, wake effects are important in this study and should be incorporated into the models.

4.7.3 Summary and Conclusions

This research examined the effect of water mist on the reduction in the flame spread velocity into an opposing wind. Flame spread velocities with and without water mist were obtained for a solid fuel, polymethylmethacrylate (PMMA), using Focal Plane Array Imaging. PMMA sheets of different thickness were burned in an opposed flow configuration, with varying wind velocities. The flame spread rate for the 'without backing' tests was found to be greater than for the 'with backing' tests due to flame spread on both sides in the ‘without backing’ case. At ambient oxygen concentration, the heat transfer effect on the fuel vapor evolution rate was the dominant factor controlling the flame spread rate.

A spray nozzle, suspended over the PMMA sheets, was used to vary the water loading at the flame front. Flame spread in the presence of a water mist indicated a strong influence of surface loading in reducing flame spread rate. The effect was more pronounced at low values of opposing wind speeds. The flame spread rate for a given liquid loading decreased slightly for smaller droplets. Water loading, rather than the droplet size, is the more important parameter for reducing flame spread. The reduction in flame spread rate in the presence of the mist can be modeled empirically using the experimental parameters.

Droplet diameter and velocity measurements from a monodisperse spray onto a hot plate showed that buoyancy had a significant impact on both droplet velocities and diameters. A non-evaporating spray (Dow Thermal Fluid 510) was used to assess the effects of buoyancy and an evaporating spray (water) was used to study the combined effects of buoyancy and evaporation on the droplet trajectories. For both fluids, coalescence was the dominant mechanism by which droplets changed size during their flight to a hot surface. For the temperature range achieved during the study, the change in water droplet diameters due to evaporation was much smaller than due to coalescence. Two coalescence and evaporation models developed were not successful in predicting droplet coalescence and evaporation. The models need to be improved significantly before they can be used in fire suppression studies. Temperature reduction of burning surfaces inhibited with water mist has to be measured for more conditions to obtain a more accurate assessment of the optimal water loading required for fire extinguishments.

The results of the study are applicable to design considerations for aerosol-based fire suppression devices to ensure optimum operation.

4.8 THE NEW STATE OF KNOWLEDGE OF THE MECHANISM OF FLAME EXTINGUISHMENT BY AEROSOLS

NGP research has greatly advanced the understanding of the processes by which aerosols in the form of solid particles or liquid droplets suppress flames, the aerosol properties that control these processes, and the values of the properties that promote efficient extinguishment. The interrelated dependencies of particle size and flame conditions explain why seemingly contradictory suppression results appeared in the earlier literature exploring the effectiveness of aerosols in differing flame systems. Experimental quantification of the aerosol particle size distributions, number densities, and particle velocities actually delivered to the flames was key to establishing valid correlations between observed suppression effectivenesses with modeling predictions. Comparison of experimental data in combination with modeling predictions permitted the exploration of suppression in aerosol parameter space that would have been much more difficult to explore solely with either approach alone.

- Rosser and co-workers summarized the extinction mechanism of powders of metal compounds based on experiments in the 1960s.[13] NGP assessment of subsequent works combined with detailed NGP experimental and modeling studies concluded that with some modification these conclusions can be extended to qualify the suppression mechanism of aerosols in general.
- To achieve maximum suppression effectiveness, individual components of an aerosol must pass through a succession of steps: I - Heating; II - Evaporation/decomposition; II - Generation of the chemical inhibitor specie(s) for chemical agents; IV - Flame inhibition.
- Evaporation/decomposition leads to dilution of the available oxygen and lowers the temperature which alters the flame chemistry (dominates for those aerosols with no chemical inhibitor).
- Any generated chemical inhibitor species must directly participate in the flame radical chemistry.
- Small particles are favored; evaporation/decomposition must be close to or in the flame.
- The transition diameter from effective, small particles to larger, less effective larger ones depends on the time to complete steps I and II (i.e., complete evaporation of the aerosol material).
- Suppression effectiveness is controlled by the time required for the aerosol particles to progress through each step AND the amount of time allowed, i.e. the residence time.
- For premixed flames, higher flame temperatures imply higher burning velocities and shorter particle residence times.
- For non-premixed counterflow flames, the particle residence time is related to the inverse of the strain rate; particles can oscillate near the stagnation plane and lengthen the effective residence time for certain particle sizes and strain rates.
- For non-premixed co-flow flames with air-stream entrainment of the aerosol (e.g. cup burner flames), the residence times are dictated by the air stream velocity through the flame.
- Residence time requirements are greater for liquid aerosols with a chemical inhibitor additive than for the pure liquid; liquid with additive aerosols must complete steps I and II for the liquid followed by steps I and II again for the additive residue.

- For chemical inhibitor species, thermodynamic limitations can impose restrictions on the gas phase chemical inhibitor specie(s) (see Chapter 3); complete evaporation/decomposition and/or longer residence times may offer no advantage.
- Aerosols are generally less effective in premixed flames than in non-premixed flames of the same fuel.
- For achievable aerosol suppression effectiveness there is a tradeoff between flame temperature, flow field velocity, particle residence time, and particle physical and chemical properties; this tradeoff can lead to non-monotonic effectiveness behavior with particle size.
- Specific flame type, nature of fuel, and aerosol properties ultimately determine the magnitude of the aerosol suppression effectiveness.

4.9 RELATION OF FINDINGS TO PRACTICAL FIRES

The conclusions in this chapter are based for the most part on observations in laboratory-scale flame suppression studies. Aerosol particles were typically injected directly into the flame. For real-scale fires, the conclusions outlined above will include a critical additional first step; the aerosol must first get to the fire to begin the process. The type of aerosol generation system and what happens in aerosol transport to the fire will also impact suppression performance. Thus, in addition to answering what aerosol properties are optimum at the fire, one must also address what properties should the aerosol exhibit when generated in order to achieve the optimum suppression properties at the fire. The required set of aerosol characteristics can change as the fire changes, especially as the fire grows in size involving more of its surroundings. Transport and delivery topics are presented and discussed in Chapter 8.

Spaces where real fires occur are generally distinctly larger than the dimensions of a laboratory flame apparatus. Aerosol travel distances are longer; changes will occur in the size distribution and particle velocities from generation point to the fire location. This location is not known in advance so there is also a need to consider the effective dispersion throughout the area requiring protection. Higher aerosol densities need to be generated in order to fill the space adequately. This often impacts the resulting particle size distributions.

Small fires in large spaces, especially small, obstructed fires, are particularly challenging for gaseous agents. These fires are even more challenging for aerosol suppression agents. Smaller fires generate less heat, resulting in lower overall tempeatures and lower aerosol evaporation or decomposition rates. Entrainment currents around smaller fires are less intense and less likely to draw large amounts of aerosol into the fire. For a given aerosol, the smaller particles are more likely to follow the weaker airstream trajectories than the larger particles, but smaller particles evaporate more quickly. A bi-modal aerosol distribution (or other combination) may address this issue. A bi-modal distribution may also address the aerosol requirements for protecting a wider range of fire threats and protecting against fires in varying stages of development.

4.10 REFERENCES

1. Braidech, M.M., Neale, J.A., Matson, A.F., and Dufour, R.E., *The Mechanism of Extinguishment of Fire by Finely Divided Water*, Underwriters Laboratories lnc. for the National Board of Fire Underwriters, N.Y., 1955.

2. Rasbash, D.J., Rogowski, Z.W., and Stark, G.W.V., "Mechanisms of Extinction of Liquid Fires with Water Sprays," *Combustion and Flame* **4**, 223–234, (1960).

3. Lugar, J.R., "Preliminary Test Results of Fine Water Mist Fire Protection Systems Study," David W. Taylor Naval Ship Research and Development Center, MD, 1980.

4. Coppalle, A,, Nedelka, D., and Bauer, B., "Fire Protection: Water Curtains," *Fire Safety Journal* **20**, 241-255, (1993).

5. Mawhinney, J.R., Dlugogorski, BZ., and Kim, A.K., "A Closer Look at the Fire Extinguishing Properties of Water Mist," *Proceedings of the Fourth International Symposium on Fire Safety Science*, The International Association for Fire Safety Science, pp. 47–60, 1994.

6. Seshadri, K., "Structure and Extinction of Laminar Diffusion Flames Above Condensed Fuels with Water and Nitrogen," *Combustion and Flame* **33**, 197-215, (1978).

7. McCaffrey, B.J., "Momentum Diffusion Flame Characteristics and the Effects of Water Spray," *Combustion Science and Technology* **63**, 315-335, (1989).

8. Fielding, G.H., Williams, F.W., and Carhart, H.W., *Fire Suppression – Why Not Water?,* NRL Memorandum Report No. 3435, Naval Research Laboratory, Washington, DC, February 1977.

9. Friedman, R., "On the Mechanisms of Flame Extinguishment by Dry Powders," *Journal of Fire Protection Engineering* **5**, 290-318, (1993).

10. Dolan, J.E., and Dempster, P.B., "The Suppression of Methane-Air Ignitions by Fine Powders," *Journal of Applied Chemistry* **5**, 510-517, (1955).

11. DeWitte, M., Verbosch, J., and van Tiggelen, A., "Inhibition and Extinction of Premixed Flames by Dust Particles," *Combustion and Flame* **8**, 257-266, (1964).

12. Birchall, J.D., "On the Mechanism of Flame Inhibition by Alkali Metal Salts," *Combustion and Flame* **14**, 85-96, (1970).

13. Rosser, W.A., Jr., Inami, S.H., and Wise, H., "The Effect of Metal Salts on Premixed Hydrocarbon-Air Flames," *Combustion and Flame* **7**, 107-119, (1963).

14. G. Fischer and J. T. Leonard, *The Effectiveness of Fire Extinguishing Powders Based on Small Scale Fire Suppressant Tests*, Internal NRL Progress Report, 1984.

15. Ewing, C.T., Hughes, J.T., and Carhart, H.W., "The Extinction of Hydrocarbon Flames Based on the Heat-Absorption Processes which Occur in them," *Fire and Materials* **8**, 148-156, (1984).

16. Ewing, C.T., Faith, F.R., Hughes, J.T., and Carhart, H.W., "Flame Extinguishment Properties of Dry Chemicals: Extinction Concentrations for Small Diffusion Pan Fires," *Fire Technology* **25***,* 134-149, (1989).

17. Fischer, G., and Leonard, J.T., *Effectiveness of Fire Extinguishing Powders Based on Small Scale Fire Suppression Tests*, Naval Research Laboratory, NRL/MR/6180-95-7778, Washington, D.C., 1995.

18. Chattaway, A., Dunster, R.G., Gall, R., and Spring, D.J., "The Evaluation of Non-Pyrotechnically Generated Aerosols as Fire Suppressants," 1995, in Gann, R.G., Burgess, S.R., Whisner, K.C., and

Reneke, P.A., eds., *Papers from 1991-2006 Halon Options Technical Working Conferences (HOTWC)*, CD-ROM, NIST SP 984-4, National Institute of Standards and Technology, Gaithersburg, MD, 2006.

19. Knuth, E.L., Ni, W.F., and Seeger, C., "Molecular-Beam Sampling Study of Extinguishment of Methane-Air Flames by Dry Chemicals," *Combustion Science and Technology* **28**, 247-262, (1982).

20. Hamins, A., Gmurczyk, G., Grosshandler, W., Rehwoldt, R.G., Vazquez, I., Cleary, T., Presser, C., and Seshadri, K., "Flame Suppression Effectiveness," in *Evaluation of Alternative In-Flight Fire Suppressants for Full-Scale Testing in Simulated Aircraft Engine Nacelles and Dry Bays*, National Institute of Standards and Testing, No. NIST SP 861, pp. 345-465, April 1994.

21. Hamins, A., "Flame Extinction by Sodium Bicarbonate Powder in a Cup Burner," *Proceedings of the Combustion Institute* **27**, 2857-2864, (1998).

22. Wahl, A.M., "Water and Water Additives for Fire Fighting," Section 6, Chapter 1, in *Fire Protection Handbook*, 18th edition, A.E. Cote (editor), National Fire Protection Association, Quincy, MA, 1997.

23. Monson, W.L., Reid, L.J., Schreiner, M., Jr., Bonney, D.T., and Huff, W.J., *Research on Water Additives for Fire Fighting*, Quarterly Report No. 3, U.S. Army Engineer Research and Development Laboratories, Fort Belvoir, Virginia, December 15, 1953.

24. Monson, W.L., Reid, L.J., Schreiner, M., Jr., Bonney, D.T., and Huff, W.J., *Research on Water Additives for Fire Fighting*, Quarterly Report No. 4, U.S. Army Engineer Research and Development Laboratories, Fort Belvoir, Virginia, March 15, 1954.

25. Grove, C.S. et al., "Additives to Improve the Fire-Fighting Characteristics of Water," *Fire Research Abstracts and Reviews* **1**, 18, (1958).

26. Aidun, A.R., Walker, E.J., Gabriel, S., Buckman, W.R., and Grove, C.S., Jr., "Additives to Improve the Fire-Fighting Characteristics of Water," *Fire Research Abstracts and Reviews* **1**, 58, (1958).

27. Walker, E.J., Aidun, A.R., and Grove, C.S., Jr., "Additives to Improve the Fire-Fighting Characteristics of Water," *Fire Research Abstracts and Reviews* **1**, 129, (1958).

28. Walker, E.J., Aidun, A.R., and Grove, C.S., Jr., "Additives to Improve the Fire-Fighting Characteristics of Water," *Fire Research Abstracts and Reviews* **2**, 71, (1960).

29. Aidun, A.R. and Grove, C.S., Jr., "Additives to Improve the Fire-Fighting Characteristics of Water," *Fire Research Abstracts and Reviews* **3**, 91, (1961).

30. Aidun, A.R. "Additives to Improve the Fire-Fighting Characteristics of Water," *Fire Research Abstracts and Reviews* **3**, 93, (1961).

31. Aidun, A.R.,"Additives to Improve the Fire-Fighting Characteristics of Water," *Fire Research Abstracts and Reviews* **3**, 213, (1961).

32. Grove, C.S., Jr., Grove, S.T., and Aidun, A.R., "Improving the Effectiveness of Water for Fire Fighting," *Fire Research Abstracts and Reviews* **4**, 54, (1962).

33. Aidun, A.R. and Grove, C.S., Jr., "Additives to Improve the Fire-Fighting Characteristics of Water," *Fire Research Abstracts and Reviews* **5**, 34, (1963).

34. Davis, J.B., Dibble, D.L., and Phillips, C.B., "Firefighting Chemicals–New Weapon for the Fire Suppression Crew," *Fire Research Abstracts and Reviews* **5**, 37, (1963).

35. Davis, J.B., Dibble, D.L., Phillips, C.B., and McBride, R.S., "Viscous Water and Algin as Fire Control Materials," *Fire Research Abstracts and Reviews* **5**, 37, (1963).

36. Friedrich, M., "Fire Extinguishing Experiments with Aqueous Salt Solution Sprays," *Fire Research Abstracts and Reviews* **6**, 44, (1964).

37. Elkins, G.H.J., "Use of Anti-Freeze in Water Extinguishers," *Fire* **57**, 448, (1965).

38. Kida, H., "Extinction of Fires of Liquid Fuel with Sprays of Salt Solutions," *Fire Research Abstracts and Reviews* **11**, 212, (1969).

39. Ball, D.N., Spring, D.J., and Davis, S.J., "Fire Extinguishing Substance," UK Patent GB 2,233,226A, June 21, 1990.

40. Finnerty A.E., McGill, R.L., and Slack, W.A., *Water-Based Halon Replacement Sprays*, ARL-TR-1138, Army Research Laboratory, Aberdeen Proving Ground, July, 1996.

41. Yang, J.C., Donnelly, M.K., Prive, N.C., and Grosshandler, W.L., *Dispersed Liquid Agent Fire Suppression Screen Apparatus*, NISTIR 6319, National Institute of Standards and Technology, Gaithersburg, MD, July 1999.

42. Zheng, R., Bray, K.N.C., and Rogg, B., "Effect of Sprays of Water and NaCl-Water Solution on the Extinction of Laminar Premixed Methane-Air Counterflow Flames," *Combustion Science and Technology* **126**, 389–401, (1997).

43. Mitani, T., and Niioka, T., "Extinction Phenomenon of Premixed Flames with Alkali Metal Compounds," *Combustion and Flame* **55**, 13-21, (1984).

44. Edwards, M., Watkins, S., and Glockling, J., "Low Pressure Water Mist, Fine Water Spray, Water Source and Additives: Evaluation for the Royal Navy," *Proceedings of the 8th International Fire Science and Engineering Conference, Interflam '99,* Edinburgh, Scotland, Vol. 1, pp. 639-650, 29 June-1 July, 1999.

45. De Ris, J.N., "Spread Of A Laminar Diffusion Flame," *Proceedings of the Combustion Institute* **12**, 241-252, (1969).

46. Lastrina F.A., Magee R.S., and McAlevy III, R.F., "Flame Spread Over Fuel Beds: Solid-Phase Energy Considerations," *Proceedings of the Combustion Instisute* **13**, 935-948, (1971).

47. Fernandez-Pello, A.C., Ray, S.R., and Glassman, I. "Downward Flame Spread In An Opposed Forced Flow," *Combustion Science and Technology* **19** (1-2), 19-30, (1978).

48. Fernandez-Pello, A.C., Ray, S.R., and Glassman, I., "Flame Spread in an Opposed Forced Flow: The Effect of Ambient Oxygen Concentration," *Proceedings of the Combustion Institute* **18**, 579-589, (1981).

49. Apte, V.B., Bilger, R.W., Green, A.R. and Quintiere, J.G., "Wind-Aided Turbulent Flame Spread and Burning Over Large-Scale Horizontal PMMA Surfaces," *Combustion and Flame* **85**, 169-184, (1991).

50. Loh, H.-T. and Fernandez-Pello, A.C., "A Study Of The Controlling Mechanisms Of Flow Assisted Flame Spread" *Proceeding of the Combustion Institute* **20**, 1575-1582, (1984).

51. Perzak, F.J. and Lazzara, C.P., "Flame Spread Over Horizontal Surfaces of Polymethylmethacrylate," *Proceedings of the Combustion Institute* **24**, 1661-1668, (1992).

52. Kwok, K.C., *A Fundamental Study of Air-Spray Painting*, Ph. D. Thesis, Mechanical Engineering Department, University of Minnesota, 1991.

53. Hicks, P.G., and Senser, D.W., "Simulation of Paint Transfer in an Air Spray Process," *Journal of Fluids Engineering* **117**, 713-719, (1995).

54. DiMarzo, M.. Kavoosi, and Klassen, M., *Transient Cooling of a Hot Surface by Droplets Evaporation*, Report prepared for the National Institute of Standards and Technology, NISTGCR- 89-559, University of Maryland, College Park, MD, 1989.

55. DiMarzo, M., and Evans, D.D., *Evaporation of Water Droplet Deposited on a Hot High Thermal Conductivity Solid Surface*, NBSIR 86-3384, National Insitute of Standards and Technology, Gaithersburg, MD, 1986.

56. Sheinson, R.S., Maranghides, A., Eaton, H., Barylski, D., Black, B., Friderichs, T., Peatross, M., Salmon, G., and Smith, W., "Total Flooding Agent Distribution Considerations," 1995, in Gann, R.G., Burgess, S.R., Whisner, K.C., and Reneke, P.A., eds., *Papers from 1991-2006 Halon Options Technical Working Conferences (HOTWC)*, CD-ROM, NIST SP 984-4, National Institute of Standards and Technology, Gaithersburg, MD, 2006.

57. Carhart, H.W., Sheinson, R.S., Tatem, P.A., and Lugar, J.R., "Fire Suppression Research in the U.S. Navy, "Proceedings - First International Conference on Fire Suppression Research, Stockholm and Boras, Sweden, May 5-8, 1992.

58. Ewing, C.T., Faith, F.R., Romans, J.B. Hughes, J.T. and Carhart, H.W., "Flame Extinguishment Properties of Dry Chemicals: Extinction Weights for Small Diffusion Pan Fires and Additional Evidence for Flame Extinguishment by Thermal Mechanisms," *Journal of Fire Protection Engineering* **4**, 35-52, (1992).

59. Ewing, C.T., Faith, F.R., Romans, J.B., Siegmann, C.W, Ouellette, R.J., Hughes, J.T., and Carhart, H.W., "Extinguishing Class B Fires with Dry Chemicals: Scaling Studies," *Fire Technology* **31**, 1-16, (1995).

60. Sheinson, R.S., Eaton, H.G., Black, B.H., Brown, R., Burchell, H., Salmon, G., St. Aubin, J., and Smith, W.D., "Total Flooding Fire Suppressant Testing in a 56 m^3 (2000 ft^3) Compartment," 1993, in Gann, R.G., Burgess, S.R., Whisner, K.C., and Reneke, P.A., eds., *Papers from 1991-2006 Halon Options Technical Working Conferences (HOTWC)*, CD-ROM, NIST SP 984-4, National Institute of Standards and Technology, Gaithersburg, MD, 2006.

61. Sheinson, R.S., Eaton, H.G., Zalosh, R.G., Black, B.H., Brown, R., Burchell, H., Salmon, G.,and Smith, W.D. ,"Intermediate Scale Fire Extinguishment By Pyrogenic Solid Aerosol," 1994, in Gann, R.G., Burgess, S.R., Whisner, K.C., and Reneke, P.A., eds., *Papers from 1991-2006 Halon Options Technical Working Conferences (HOTWC)*, CD-ROM, NIST SP 984-4, National Institute of Standards and Technology, Gaithersburg, MD, 2006.

62. Discussions between R.S. Sheinson and A. Baratov, 12 April, 1994.

63. Zegers, E.J.P., Williams, B.A., Sheinson, R.S., and Fleming, J.W., "Dynamics and Suppression Effectiveness of Monodisperse Water Droplets in Non-Premixed Counterflow Flames," *Proceedings of the Combustion Institute* **28**, 2931-2937, (2000).

64. Chen, N.H., Rogg, B., and Bray, K.N.C., "Modelling Laminar Two-Phase Counterflow Flames with Detailed Chemistry and Transport," *Proceedings of the Combustion Institute* **24**, 1513-1521, (1992).

65. Prasad, K., Li, C., Kailasanath, K., Ndubizu, C., Ananth, R., and Tatem, P.A., "Numerical Modeling of Water Mist Suppression of Methane-Air Diffusion Flames," *Combustion Science and Technology* **132**, 325-364, (1998).

66. Lefebvre, A.H., *Atomization and Sprays*, Hemisphere Publishing Corporation, pp. 91-92, 1988.

67. Sirignano, W.A., *Fluid Dynamics and Transport of Droplets and Sprays*, Cambridge University Press, Cambridge, United Kingdom, pp. 5-6, 1999.

68. Black, D.L., McQuayt, M.Q., and Bonint, M.P., "Laser-Based Techniques for Particle-Size Measurement: A Review of Sizing Methods and their Industrial Applications," *Progress in Energy and Combustion Science* **22**, 267-306, (1996).

69 Durst, F., Brenn, G., and Xu, T.H., "A Review of the Development and Characteristics of Planar Phase-Doppler Anemometry," *Measurement Science and Technololgy* **8,** 1203–1221, (1997).

70. Chigier, N., "Optical Imaging of Sprays," *Progress in Energy and Combustion Science* **17**, 221-262, (1991).

71 Rafel, M., Willert, C.E., Kompenhans, J., *Particle Image Velocimetry: A Practical Guide,* Spring-Verlag Berlin, 1998.

72. Turns. S, *An Introduction to Combustion: Concepts and Applications*, 1st ed., McGraw Hill, Inc., New York, p. 314, 1996.

73. Kays, W.M. and Crawford, M.E., *Convective Heat and Mass Transfer*, 2nd ed., McGraw-Hill Book Company, New York, p 388, 1980.

74. Perry, R.H., Green., D.W., Maloney, J.O., *Perry's Chemical Engineers' Handbook*, Seventh Edition, The McGraw-Hill Companies, Inc., New York, p. **6**-51, 1997.

75. Fleming, J.W., Williams, B.A., Sheinson, R.S., Yang, W., Kee, R.J., "Water Mist Fire Suppression Research: Laboratory Studies", *Proceedings of the Second National Research Institute for Fire Disaster Symposium: Technology Standards for Fire*, Tokyo, Japan, Paper 23, 17-19 July 2002.

76. Noto, T., Babushok, V, Burgess Jr., D.R., Hamins, A., Tsang, W., and Miziolek, A., "Effect of Halogenated Flame Inhibitors on C1-C2 Organic Flames," *Proceedings of the Combustion Institute* **26**, 1377-1383, (1996).

77. Andrews, G.E., and Bradley, D., "Determination of Burning Velocities: A Critical Review," *Combustion and Flame* **18**, 133-153, (1972).

78. Continillo, G., and Sirignano, W.A., "Counterflow Spay Combustion Modeling", *Combustion and Flame* **81**, 325-340, (1990).

79. Lacas, F., Darabiha, N., Versaevel, P., Rolon, J. C., and Candel, S., "Influence of Droplet Number Density on the Structure of Strained Laminar Spray Flames," *Proceedings of the Combustion Institute* **24**, 1523- 1529, (1992).

80. Seshadri, K. and Williams. F.A., "Laminar Flow Between Parallel Plates with Injection of a Reactant at High Reynolds Number," *International Journal of Heat and Mass Transfer* **21**, 251-253, (1978).

81. Lentati, A.M. and Chelliah, H.K., "Dynamics of Water Droplets in a Counterflow Field and their Effect on Flame Extinction," *Combustion and Flame* **115**, 158-179, (1998).

82. Yang, J.C., Donnelly, M.K., Prive, N.C., Grosshandler, W.L., An Apparatus For Screening Fire Suppression Efficiency Of Dispersed Liquid Agents," *Fire Safety Journal* **36**, 55-72, (2001).

83. Hirst, R. and Booth, K., "Measurement of Flame-Extinguishing Concentrations," *Fire Technology* **13**, 296-315, (1977).

84. Fisher, B.T., Awtry, A.R., Sheinson, R.S., and Fleming, J.W., "Flow Behavior Impact on the Suppression Effectiveness of sub-10-μm Water Drops in Propane/Air Co-flow Non-Premixed Flames", *Proceedings of the Combustion Institute* **31**, 2731-2739, (2007).

85. Fuss, S.P., Chen, E.F., Yang, W., Kee, R.J., Williams, B.A., Fleming, J.W., "Inhibition of Premixed Methane/Air Flames by Water Mist," *Proceedings of the Combustion Institute* **29**, 361-368, (2002).

86. Mitani,T., "A Flame Inhibition Theory by Inert Dust and Spray," *Combustion and Flame* **43**, 243-253, (1981).

87. Blouquin, R. and Joulin, G., "On the Quenching of Premixed Flames by Water Sprays: Influences of Radiation and Polydispersity", *Proceedings of the Combustion Institute* **27**, 2829-2837, (1998).

88. Kee, R.J., Grcar, J.F., Smooke, M.D., and Miller, J.A., *A Fortran Program for Modeling Steady Laminar One-Dimensional Premixed Flames*, Sandia National Laboratories, SAND85-8240, 1987.

89. Yang, W. and Kee, R.J., "The Effect of Monodispersed Water Mists on the Structure, Burning Velocity, and Extinction Behavior of Freely Propagating, Stoichioetric, Premixed, Methane-Air Flames," *Combustion and Flame* **130**, 322-335, (2002).

90. Kee, R.J., Grcar, J.F., Smooke, M.D., and Miller, J.A., *A Fortran Program for Modeling Steady Laminar One-Dimensional Premixed Flames*, Sandia National Laboratories, SAND85-8240, 1987.

91. Lutz, A.E., Kee, R.J., Grcar, F.M. and Rupley, F.M., *OPPDIF: A Fortran Program for Computing Opposed-Flow Diffusion Flames*, Sandia National Laboratories, SAND96-8243, 1997.

92. Smith, G.P., Golden, D.M., Frenklach, M., Moriarty, N.W., Eiteneer, B., Mikhail Goldenberg, M., Bowman, C.T., Hanson, R.K., Song, S., Gardiner, Jr., W.C., Lissianski, V.V., and Qin, Z., *GRI-Mech 3.0*, http://www.me.berkeley.edu/gri_mech/, 2001.

93. Fuss, S.P., Chen, E.F., Yang, W., Kee, R.J., Williams, B.A., Fleming, J.W., "Inhibition of Premixed Methane/Air Flames by Water Mist," *Proceedings of the Combustion Institute* **29**, 361-368, (2002).

94. Parks, D.J., Alvares, N.J., and Beason, D.G., "Fundamental Flame-Speed Measurements in Combustion Gases Containing CF_3Br," *Fire Safety Journal* **2**, 237-247, (1979/80).

95. Chase Jr., M.W., Davies, C.A., Downey Jr., J.R., Frurip, D.J., McDonald, R.A., and Syverud, A.N., *JANAF Thermochemical Tables*, 3rd Edition, *Journal of Physical And Chemical Reference Data* **14**, 927-1856, Suppl. 1, 1985.

96. Noto, T., Babushok, V., Hamins, A., and Tsang, W., "Inhibition Effectiveness of Halogenated Compounds," *Combustion and Flame* **112**, 147-160, (1998).

97. Davis, M.P., Fleming, J.W., Williams, B.A., and Ladouceur, H.D., "Flow Field Considerations for Counter Flow Burners", *Proceedings of the Eastern States Section*, The Combustion Institute, Pittsburgh, PA, pp. 200-203, Oct 1999.

98. Lazzarini, A.K., Krauss, R.H., Chelliah, H.K., and Linteris, G.T, "Extinction Conditions of Non-Premixed Flames with Fine Droplets of Water and Water/NaOH Solutions," *Proceedings of the Combustion Institute* **28**, 2939-2945, (2000).

99. Chelliah, H.K., Lazzarini, A.K., Wanigarathne, P.C., and Linteris, G.T., "Inhibition of Premixed and Non-Premixed Flames with Fine Droplets of Water and Solutions," *Proceedings of the Combustion Institute* **29**, 369-376, (2002).

100. Chelliah, H.K.,Williams, B.A., Mowrey, R.C., and Fleming, J.W., "Water Mist Suppression Of Propane-Air Flames: Modeling And Experimental Study," *Proceedings Of The Eastern States Section*, The Combustion Institute, Pitsburgh, PA, 26-29 October 2003.

101. Davis, S.G., Law, C.K., and Wang, H., "Propene Pyrolysis and Oxidation Kinetics in a Flow Reactor and Laminar Flames," *Combustion and Flame* **119**, 375-399, (1999).

102. H. Wang, U. Delaware, private communication with H.K. Chelliah.

103. Chelliah, H.K., Law, C.K., Ueda, T., Smooke, M.D., and Williams, F.A., "An Experimental and Theoretical Investigation of the Dilution, Pressure and Flow-Field Effects on the Extinction Condition of Methane-Air-Nitrogen Diffusion Flames," *Proceedings of the Combustion Institute* **23**, 503-511, (1990).

104. Li, S.C., Libby, P.A., and Williams, F.A., "Spray Structure in Counterflowing Streams with and without a Flame," *Combustion and Flame* **94**, 161-177, (1993).

105. Seshadri, K., and Peters, N., "Asymptotic Structure and Extinction of Methane-Air Diffusion Flames," *Combustion and Flame* **73**, 23-44, (1988).

106. Chelliah, H.K., and Williams, F.A., "Aspects of the Structure and Extinction of Diffusion Flames in Methane-Oxygen-Nitrogen Systems," *Combustion and Flame* **80**, 17-48, (1990).

107. Peters, N., "Local Quenching due to Flame Stretch and Non-Premixed Turbulent Combustion," *Combustion Science and Technology* **30**(1-6), 1-17, (1983).

108. Kim, J.S., and Williams, F.A., "Structures of Flow and Mixture-Fraction Fields For Counterflow Diffusion Flames With Small Stoichiometric Mixture Fractions," *SIAM Journal of Applied Mathematics* **53**(6), 1551-1566, (1993).

109. Zegers, E.J.P., Williams, B.A., Sheinson, R.S. and Fleming, J.W., "Dynamics and Suppression Effectiveness of Monodisperse Water Droplets in Non-Premixed Flames," *Proceedings of the Combustion Institute* **28**, 2931–2937, (2000).

110. Zegers, E.J.P., Williams, B.A., Fisher, E.M., Fleming, J.W., and Sheinson, R.S., "Suppression of Nonpremixed Flames by Fluorinated Ethanes and Propanes," *Combustion and Flame* **121**, 471-487, (2000).

111. Berglund, R.N. and Liu, B.Y.H., "Generation Of Monodisperse Aerosol Standards", *Environmental Science and Technology* 7(2), 147-153, (1973).

112. Chelliah, H.K, Williams, B.A., and Fleming, J.W., "Water Mist Suppression of Propane-Air Flames: Interpretation of Experimental Results," NRL/MR/6180--05-8853, March 10, 2005.

113. Chin and Lefebvre, "Steady-State Evaporation Characteristics of Hydrocarbon Fuel Drops," *AIAA* **21**(10), 1437- 1443, (1983).

114. Fleming, J.W., Reed, M.D., Zegers, E.J.P., Williams, B.A., and Ronald S. Sheinson, R.S., "Extinction Studies of Propane/Air Counterflow Diffusion Flames: The Effectiveness of Aerosols," *Proceedings of the Halon Options Technical Working Conference*, 403-414, (1998).

115. Reed, Mark D., *A Study of the Behavior of Bicarbonate Powder Extinguishants in a Counterflow Propane/Air Diffusion Flame*, M.S. thesis, Worcester Polytechnic Institute, Fire Protection Engineering, Worcester, MA, (work carried out at the NRL), 1997.

116. Seeger, P.G., "A Laboratory Test Method for Evaluating the Extinguishing Efficiency of Dry Powder," *AGARD Conference Proceedings* Vol. **166**, Paper 24, 1975.

117. Williams, B.A. and Fleming, J.W., "Suppression Mechanisms of Alkali Metal Compounds,"' 1999, in Gann, R.G., Burgess, S.R., Whisner, K.C., and Reneke, P.A., eds., *Papers from 1991-2006 Halon Options Technical Working Conferences (HOTWC)*, CD-ROM, NIST SP 984-4, National Institute of Standards and Technology, Gaithersburg, MD, 2006.

118. Trees, D. and Seshadri, K., "Experimental Studies of Flame Extinction by Sodium Bicarbonate ($NaHCO_3$) Powder," *Combustion Science and Technology* **122**, 215-230, (1997).

119. Wanigarathne, P.A., Krauss, R.H., Chelliah, H.K., and Davis, R.J., "Fire Suppression by Particulates Containing Metallic Compounds," 2000, in Gann, R.G., Burgess, S.R., Whisner, K.C., and Reneke, P.A.,

eds., *Papers from 1991-2006 Halon Options Technical Working Conferences (HOTWC)*, CD-ROM, NIST SP 984-4, National Institute of Standards and Technology, Gaithersburg, MD, 2006.

120. Friedman, R. and Levy, J.B., Inhibition of Opposed-Jet Methane Air Diffusion Flames - the Effects of Alkali Metal Vapors and Organic Halides, *Combustion and Flame* **7**, 195-201, (1963).

121. Jensen, D.E., and Jones, G.A., "Kinetics of Flame Inhibition by Sodium," *Journal of the Chemical Society, Faraday Transactions* I **78**, Part 9, 2843-2850, (1982).

122. McHale, E.T., "Flame Inhibition by Potassium Compounds,'' *Combustion and Flame* **24**, 277-279, (1975).

123. Takahashi, F., Schmoll, W. J., and Dressler, J. L., "Characterization of a Velocity-Modulation Atomizer," *Review of Scientific Instruments* **65**, 3563–3569, (1994).

124. Lide, D.R., ed, *CRC Handbook of Chemistry and Physics*, 81st edition., CRC Press, Boca Raton, FL, p. 8-108, 2000.

125. Smooke, M.D., "Solution of Burner-Stabilized Premixed Laminar Flames by Boundary-Value Methods," *Journal of Computational Physics* **4**, 72-105, (1982).

126. Greenberg, J.B., Silverman, I., and Tambour, Y., "On the Origins of Spray Sectional Conservation Equations," *Combustion and Flame* **93**, 90–96, (1993).

127. D'Angelo, Y., Silverman, I., Gao, L. P., Gomez, A., and Smooke, M. D., "Computational and Experimental Study of Counterflow Spray Diffusion Flames," *Proceedings of the Eastern States Section*, The Combustion Institute, Pttsburgh, PA, 1996.

128. Wanigarathne, P.C., *Fire Suppression in Studies with Particulates Containing Metallic Compounds*,' M.S. thesis, University of Virginia, Charlottesville, VA, 2001.

129. Chelliah, H.K., Lazzarini, A.K., Wanigarathne, P.C., and Linteris, G.Y., "Inhibition of Premixed and Non-premixed Flames with Fine Droplets of Water and Solutions," P*roceedings of the Combustion Institute* **29**, 369-376, (2002).

130. Reinelt, D., and Linteris, G.T., "Experimental Study of the Inhibition of Premixed and Diffusion Flame by Iron Pentacarbonyl," *Proceedings of the Combustion Institute* **26**, 1421-1428, (1996).

131. Linteris, G.T., Knyazev, V., and Babushok, V., "Inhibition of Premixed Methane Flames by Manganese and Tin Compounds," *Combustion and Flame* **29**, 221-238, (2002).

132. *NIST Chemistry WebBook*, no. 69, http://webbook.nist.gov/chemistry/, release July 2001.

133. Vanpee, M., and Shirodkar, P.P., "A Study of Flame Inhibition by Metal Compounds," *Proceedings of the Combustion Institute* **17**, 787-795 , (1978).

134. Patrick, R., and Golden, D.M., "Termolecular Reactions of Alkali Metal Atoms with O_2 and OH," *International Journal of Chemical Kinetics* **16**, 1567-1574, (1984).

135. Lask, G., and Wagner, H.G., "Influence Of Additives On The Velocity Of Laminar Flames," *Proceedings of the Combustion Institute* **8**, 432-438, (1962).

136. da Cruz, F.N., Vandooren, J., and Van Tiggelen, P., "Comparison Of The Inhibiting Effect Of Some Halogenomethane Compounds On Flame Propagation," *Bull. Soc. Chim. Belg.* **97**, 1011–1030, (1988).

137. Williams, F.A., *Combustion Theory*, 2nd ed., Benjamin/Cummings, Menlo Park, CA, 1985.

138. Chelliah, H.K., Yu, G., Hahn, T.O., and Law, C.K., "An Experimental and Numerical Study on the Global and Detailed Kinetics of Premixed and Nonpremixed Flames of Chloromethane, Methane, Oxygen and Nitrogen," *Proceedings of the Combustion Institute* **24**, 1083-1090, (1992).

139. Tomalia, D.A., "Dendrimer Molecules," *Scientific American* **272,** 62-66, (1995).

140. Tomalia, D.A., Naylor, A.M., and Goddard, W.A., "Starburst Dendrimers - Molecular Level Control of Size, Shape, Surface Chemistry, Topology, and Flexibility from Atoms to Macrocopic Matter," *Angewandte Chemie. International Edition* **29,** 138-175, (1990).

141. Tapscott, R.E., "Current Topics on New Halon Replacements," National Industrial Research Institute, Agency of Industrial Science and Technology, Nagoya, Japan, 10 April 1997.

142. Babushok, V.I. and Tsang, W., "Inhibitor Rankings for Hydrocarbon Combustion," *Combustion and Flame* **123,** 488-506 (2000).

143. Beck Tan, N.C., DeSchepper, D.C., and Balogh, L., *Dendritic Polymers as Fire Suppressants*, ARL-TR-2071, Army Research Laboratory, Aberdeen Proving Ground, October, 1999.

144. Finnerty, A.E., McGill, R. L., and Slack, W.A., Technical Report ARL-TR-1138, Aberdeen Proving Ground, Maryland, 1996.

145. Yang, J.C., Donnelly, M.K., Prive, N.C., and Grosshandler, W.L., "An Apparatus for Screening Fire Suppression Efficiency of Dispersed Liquid Agents," 1998, in Gann, R.G., Burgess, S.R., Whisner, K.C., and Reneke, P.A., eds., *Papers from 1991-2006 Halon Options Technical Working Conferences (HOTWC)*, CD-ROM, NIST SP 984-4, National Institute of Standards and Technology, Gaithersburg, MD, 2006.

146. Yang, J.C., Donnelly, M. K., Prive, N.C., and Grosshandler, W.L., *"Dispersed Liquid Fire Suppression Screen Apparatus,"* NISTIR-6319, Gaithersburg, MD, 1999.

147. Chen, C.Z., Beck Tan, N.C., and Cooper, S.L., "Incorporation of Dimethyldedecyclammonium Chloride Functionalities onto Poly(propylene) Dendrimers Significantly Enhances Their Anti-bacterial Properties," *Chemical Communications* **16**, 1585-1586, (1999).

148. Nukiyama and Tanasawa, "Experiments on the Atomization of Liquids in Air-Stream," *Transactions of the Society of Mechanical Engineers* **4,5,6,** (1938-1940).

149. Uppuluri, S. , Dvornic, P. R., Beck Tan, N. C., and Hagnauer, G., *"The Properties of Dendritic Polymers II: Generation Dependence of the Physical Properties of Poly(amidoamine) Dendrimers,"* ARL-TR-1774, Aberdeen Proving Ground, Maryland, 1999.

150. Lide D.R., ed., *CRC Handbook of Chemistry and Physics*, 81st edition, CRC Press, Inc., Boca Raton, FL, p.**6**-3, 2000.

151. Yang, J.C., Prive, N.C., Donnelly, M.K., and Grosshandler, W.L., "Recent Results from the Dispersed Liquid Agent Fire Suppressant Screen," 1999, in Gann, R.G., Burgess, S.R., Whisner, K.C., and Reneke, P.A., eds., *Papers from 1991-2006 Halon Options Technical Working Conferences (HOTWC)*, CD-ROM, NIST SP 984-4, National Institute of Standards and Technology, Gaithersburg, MD, 2006.

152. Pitts,W.M., Yang, J.C., Bryant, R.A., Blevins, L.G., and Huber, M., *Characteristics and Identification of Super-Effective Thermal Fire-Extinguishing Agents*, Final Report, NGP Project 4C/1/890, NIST Technical Note 1440, National Institue of Standards and Technology, Gaithersburg, MD, June 2001.

153. Downie, B., Polymeropoulos, C., and Gogos, G., "Interaction of a Water Mist with a Buoyant Methane Diffusion Flame," *Fire Safety Journal* **24**, 359-381, (1995).

154. Rasbash, D.J., "The Extinction Of Fire With Plain Water: A Review," *Proceedings of the First International Symposium of Fire Safety Science*, C. E. Grant And P.J. Pagni, Editors, Hemisphere, Washington, pp. 1145-1163, 1986.

155. Engel, O. G., "Waterdrop Collisions With Solid Surfaces," *Journal of Research of the National Bureau of Standards* **54**, 281-298, (1955).

156. Chandra, S. and Avedisian, C.T., "On The Collision Of A Droplet With A Solid-Surface," *Proceedings of the Royal Society of London A-Mathematical Physical and Engineering Sciences* **432**, 13-41, (1991).

157. Chandra, S. and Avedisian, C.T., "Observations of Droplet Impingement on a Ceramic Porous Surface", *International Journal of Heat and Mass Transfer* **35**, 2377-2388, (1992).

158. Mundo, C., Sommerfeld, M., and Tropea, C., "Droplet-Wall Collisions - Experimental Studies of the Deformation and Breakup Process," *International Journal of Multiphase Flow* **21**, 151-173, (1995).

159. Yarin, A.L. and Weiss, D.A., "Impact of Drops on Solid-Surfaces - Self-Similar Capillary Waves, and Splashing as a New-Type of Kinematic Discontinuity," *Journal of Fluid Mechanics* **283**, 141-173, (1995).

160. Bernardin, J.D. and Mudawar, I., "Experimental and Statistical Investigation of Changes in Surface Roughness Associated with Spray Quenching," *Inernational Journal of Heat and Mass Transfer* **39**, 2023-2037, (1996).

161. Bernardin, J.D., Stebbins, C.J., and Mudawar, I., "Effects of Surface Roughness on Water Droplet Impact History and Heat Transfer Regimes," *International Journal of Heat and Mass Transfer* **40**, 73-88, (1997).

162. Bernardin, J.D., Stebbins, C.J., and Mudawar, I., "Mapping of Impact and Heat Transfer Regimes of Water Drops Impinging on a Polished Surface," *International Journal of Heat and Mass Transfer* **40**, 247-267, (1997).

163. Bernardin, J.D. and Mudawar, I., "Film Boiling Heat Transfer of Droplet Streams and Sprays," *International journal of Heat and Mass Transfer* **40**, 2579-2593, (1997).

164. Mudawar, I. and Valentine, W.S., "Determination Of The Local Quench Curve For Spray Cooled Metallic Surfaces," *ASME Journal of Heat Treating* **7**, 107-121, (1989).

165. Klinzing, W.P., Rozzi, J.C., and Mudawar, I., "Film And Transition Boiling Correlations For Quenching Of Hot Surfaces With Water Sprays,"*ASME Journal of Heat Treating* **9**, 91-103, (1992).

166. Mudawar, I. and Deiters, T.A., "A Universal Approach to Predicting Temperature Response of Metallic Parts to Spray Quenching", *International Journal of Heat and Mass Transfer* **37**, 347-362, (1994).

167. Hall, D.D. and Mudawar, I., "Experimental and Numerical Study of Quenching Complex-Shaped Metallic Alloys with Multiple, Overlapping Sprays," *International Journal of Heat and Mass Transfer* **38**, 1201-1216, (1995).

168. Estes, K.A. and Mudawar, I., "Correlation of Sauter Mean Diameter and Critical Heat Flux for Spray Cooling of Small Surfaces," *International journal of Heat and Mass Transfer* **38**, 2985-2996, (1995).

169. Mudawar, I. and Estes, K.A., "Optimizing And Predicting Chf In Spray Cooling Of A Square Surface," *ASME Journal of Heat Transfer* **118**, 672-679, (1996).

170. Rein, M., "Phenomena Of Liquid-Drop Impact On Solid And Liquid Surfaces," *Fluid Dynamic Research* **12**, 61-93, (1993).

171. Henry, R.E. and Fauske, H.K., "Nucleation Processes In Large-Scale Vapor Explosions," *ASME Journal of Heat Transfer* **101**, 280-287, (1979).

172. Spalding, D.B., *Some Fundamentals of Combustion*, Butterworths Scientific Publications, London, 1955.

173. Kanury, A.M., *Introduction to Combustion Phenomena*, Gordon & Breach, New York, 1975.

174. *DIPPR Data Compilation of Pure Compound Properties Database*, V9.02, NIST Standard Reference Data Program #11, NIST, Gaithersburg MD, 1995.

175. Reid, R.C., Prausnitz, J.M., and Poling, B.E., *The Properties of Gases & Liquids*, 4th ed., McGraw-Hill, New York, 1987.

176. Qiao, Y.M., and Chandra, S., "Spray Cooling Enhancement by Addition of a Surfactant," *ASME Joournal of Heat Transfer* **120**, 92-98, (1998).

177. Deb, S. and Yao, S.-C., "Analysis on Film Boiling Heat Transfer of Impacting Sprays," *International Journal of Heat and Mass Transfer* **32**, 2099-2112, (1989).

178. Fu, C., Sojka, P.E., and Sivathanu, Y.R., "Water Mist Impingement onto a Heated Surface," *Proceedings of the 5th Joint ASMEIJSME Joint Thermal Engineering Conference*, 1999.

179. Fu, C., Sojka, P.E., and Sivathanu, Y.R., "On the Interaction Between Evaporating Sprays and Heated Surfaces," *Proceedings of the 12th Annual Conference on Liquid Atomization and Spray Systems*, 1999.

180. Oke, H.P., *An Experimental Study of Flame Spread over PMMA Subject to a Water Mist*, M.S. Thesis, School of Mechanical Engineering, Purdue University, November, 1999.

181. Chunming Fu., *Droplet Interactions with a Hot Surface*, M.S. Thesis, School of Mechanical Engineering, Purdue University, March 2000.

182. Howell, J.R, "Application Of Monte Carlo To Heat Transfer Problems Advances in Heat Transfer," in *Advances In Heat Transfer*, Vol. 5, J. P. Hartnett and T. Irvine, Eds., Academic Press, New York, p. 1, 1968.

183. Haji-Sheik, *Handbook of Numerical Heat Transfer*, John Wiley & Sons Inc., NY, 1988.

184. Kahn, H., and Marshall, A. W., "Methods Of Reducing Sample Size In Monte-Carlo Computations," *Journal of the Operations Research Society of America* **1**, 263-278, (1953).

185. Lanore, J.M., "Weighting and Biasing of a Monte Carlo Calculation for Very Deep Penetration Of Radiation," *Nuclear Sciene and Engineering* **45**, 66-72, (1971).

186. Sivathanu, Y.R., and Gore, J.P., "A Discrete Probability Function-Method for the Equation of Radiative-Transfer," *Journal of Quantitative Spectroscopy and Radiative Transfer* **49**, 269-280, (1993).

187. Fox, R.W., and McDonald, A.T., *Introduction to Fluid Mechanics*, John Wiley & Sons (SEA) Pte. Ltd., Singapore, 1995.

188. Kline, S.J., and McClintock, F.A., "Describing Uncertainties In Single-Sample Experiments," *ASME Mechanical Engineering* **75**, 3-8, (1953).

189. Brenn, G., Helpio, T., and Durst, F. , "A New Apparatus for the Production of Monodisperse Sprays at High Flow Rates," *Chemical Engineering Science* **5**, 237-244 , (1997).

190. Dingel, B.E., *An Experimental and Theoretical Study of Air and Water Mist Impingement Cooling*, M.S. thesis, Mechanical Engineering, Purdue University, 1997.

191. Lund, M.T., Sojka, P.E., Lefebvre, A.H., Gosselin, P.G., "Effervescent Atomization at Low Mass Flow Rates. Part I: The Influence Of Surface Tension," *Atomization and Sprays* **3**, 77-89, (1993).

192. Masters, K., *Spray Drying*, 2nd Edition, John Wiley and Sons, New York, 1976.

193. Ranz, W.E., and Marshall, W.R, "Evaporation from Drops," *Chemical Engineering Progress* **48**, 173-180, (1952).

194. Jiang, Y.J., Umemura, A., and Law, C.K., "An Experimental Investigation on the Collision Behavior of Hydrocarbon Droplets," *Journal of Fluid Mechanics* **234**, 171-190, (1992).